Variability within cold air outbreaks and implications for parametrization

A thesis submitted to the **School of Environmental Sciences**
of the **University of East Anglia** in partial fulfilment
of the requirements for the degree of Doctor of Philosophy

Jan Chylik
March 2017
revised version

©This copy of the thesis has been supplied on condition that anyone who consults it is understood to recognise that its copyright rests with the author and that use of any information derived there from must be in accordance with current UK Copyright Law. In addition, any quotation or extract must include full attribution.

©Copyright 2017
Jan Chylik

Abstract

Author: Jan Chylik
Year of Submission : 2015, 2017 (revised)

Title: **Variability within cold air outbreaks and implications for parametrization**

Abstract:
The changing structure of the marginal sea-ice zone (MIZ), together with high temperature gradients between the cold Arctic air and relatively warm sea water, contribute to uncertainty in numerical weather prediction (NWP). Since cold-air outbreaks (CAO) over the MIZ contribute strongly to heat transfer in the polar areas, assessment of variability in them is of a great importance.
This thesis deals with extending our understanding of the variability within CAO by means of large eddy simulations, performed in The Met Office Large Eddy Model (LEM).
The novel approach of this study lies within: firstly, introducing three different patterns of heterogeneity in surface temperatures that represent conditions in MIZs; secondly, investigating both the spatial and temporal variability in the developing boundary-layer convection. A set of idealised scenarios and a case study are analysed. The case study is performed for a weak CAO event observed during ACCACIA field campaign on 21 March 2013.
The study shows a profound impact of the inhomogeneous surface on both the spatial organisation of the boundary-layer convection and the latent heat flux at the surface and the boundary layer. The effect of heterogeneities depends strongly on the wind shear, the size and the orientation of the heterogeneity, and the initial stratification. When active cumuli clouds form, the effect of heterogeneities quickly diminish due to a top-driven mixing. In a stronger stratification that inhibits cumulus formation, the effect of heterogeneity is maintained. Stripes of temperature anomalies parallel to mean wind direction drive the formation of forced convective rolls and facilitate significantly higher latent heat flux. The impact of this heterogeneity usually increases with increased wind-shear, while the impact of other heterogeneities generally decreases. The impact of temperature heterogeneity is generally stronger than the impact of varying ice roughness.
The implications for the parametrization of convective boundary layer are discussed.

Key words: cold-air outbreak, large eddy simulation, parametrization, marginal sea-ice zone, heterogeneous surface, latent heat flux

Acknowledgements

Firstly, I would like to thank National Centre for Atmospheric Science that provided funding for this research project and therefore made it possible. Past few years have been an interesting adventure, full of ups and downs.

I would like to sincerely thank Professor Ian Renfrew, my supervisor, for his time and contribution. In many harsh stages of the project, he has encouraged me to to keep trying and finally overcome the obstacles in the way.

Further I would like to thank other members of the supervisory team, Dr. Glenn Shutts and Dr. Stefano Migliorini for their feedback on my research conclusions. I would also like to thank UEA HPC staff who have invested a great amount of effort into installing the numerical software required for this project on UEA computational cluster. And I cannot forget to thank Dr. Adrian Hill who helped me to gain understanding of this software. Additionally, I would like to thank both examiners, Dr. Bob Beare and Professor Adrian Matthews, for insightful comments that lead to the improvement in this thesis.

I have enjoyed all my years at UEA and although I cannot list all the people who have influenced me during the time here, I would like to thank them at least this way. Last but not least, I would like to thanks my family for their moral support during all the times when I was feeling down.

Contents

List of Tables

List of Figures

List of Symbols

notation	unit	meaning
$\sim$	·	similar - assignment of probability distribution
$\propto$	·	proportional equivalent to; i.e. equivalent up to a constant
$\overline{(\,\cdot\,)}$	·	horizontal averaging
$\overline{\varphi}$	·	mean value of a quantity φ
$\overline{\varphi}^{(l,k)}$	·	mean value of a quantity φ over a subdomain
φ'	·	variant part of a quantity φ
$\overline{(\,\cdot\,)}_u^{(u)}$	·	averaging over the area of strong updraughts
$(\,\cdot\,)_{RE}$	·	resolved values of a term in parenthesis
$\overline{(\,\cdot\,)}_{SG}$	·	statistics of modelled subgrid values of a term in parenthesis
$(\,\varphi\,)_{(\mathrm{sm}),\lambda}$	·	smoothing of a series of variable φ over smoothing length λ
$\triangle_\varphi$	·	perturbation in a quantity φ
a_u	m s^{-1}	fraction of the area taken by strong updraughts
C_p	J kg^{-1} K^{-1}	specific heat capacity at constant pressure (isobaric mass heat capacity)
$d_{(\mathrm{h})}$	m	length of a side of block in a heterogeneity pattern
E_k	J kg^{-1}	kinetic energy per unit of mass
E_w	J kg^{-1}	kinetic energy of vertical motion
$h_i^{(\varphi)}$	·	subgrid scalar flux of the quantity φ
K_h	m^2 s^{-1}	K-profile for eddy difusivity transport of a scalar quantity
L_e	J kg^{-1}	latent heat of evaporation
N	1	number of gridpoints / number of measurements in a time-series
N_x	1	number of gridpoints in the direction of the axis-x
$\mathsf{N}(\mu, \sigma^2)$	·	normal distribution with mean μ and standard deviation σ

notation	unit	meaning
q_v	kg kg^{-1}	specific humidity
q_{cl}	kg kg^{-1}	cloud total water content
q_i	kg kg^{-1}	cloud ice water content
q_l	kg kg^{-1}	cloud liquid water content
q_t	kg kg^{-1}	total water content (total humidity)
q_{tr}	kg^{-1}	content of a passive aerosol tracer
Q_{LH}	W m^{-2}	latent heat flux
Q_{SH}	W m^{-2}	sensible heat flux
$P(A)$	·	probability of an event A
r	kg kg^{-1}	water vapour mixing ratio
r_l	kg kg^{-1}	liquid water mixing ratio
r_φ	·	residua in a series of the variable φ
$\mathbb{S}_{i,j}$	s^{-1}	rate of strain tensor
S	s^{-1}	modulus of the rate of strain tensor
$S_{\varphi,\alpha}$	·	sample quantile of values of variable φ for probability *alpha*
t_0	s	time of transition - when the surface starts warming
T	K	absolute temperature
$\boldsymbol{u}$	m s^{-1}	vector of wind velocity
u	m s^{-1}	component of wind velocity in the direction of x-axis
U	m s^{-1}	wind speed (scalar)
u_*	m s^{-1}	friction velocity scale
$u_\star$	m s^{-1}	friction velocity in LEM surface model
$\mathsf{U}(a,b)$	·	uniform distribution on the interval $[a,b]$
v	m s^{-1}	component of wind velocity in the direction of y-axis
v_f	m s^{-1}	large scale wind forcing in the direction of y-axis
w	m s^{-1}	vertical component of wind velocity
w_*	m s^{-1}	convection velocity scale
w_u	m s^{-1}	vertical velocity in strong updraughts
$\overline{(w'\varphi')}$	·	vertical flux of scalar quantity; general notation
$\overline{(w'\varphi')}_s$	·	vertical flux of scalar quantity at the surface; general notation
$\overline{(w'\theta')}$	·	vertical kinematic heat flux
$\overline{(w'\theta'_v)}$	·	vertical kinematic buoyancy flux
$\overline{(w'q')}$	·	vertical kinematic moisture flux
z_0	m	aerodynamic roughness length
$z_{0,\theta}$	m	aerodynamic roughness length for scalar quantities
z_i	m	height of the mixed boundary layer (MBL)
z_α	1	quantile of the standard normal distribution for probability α

notation	unit	meaning
$\delta_{i,j}$	1	Kronecker delta
$\delta_{(\mathrm{h})}T$	K	temperature scale of a heterogeneity in surface potential temperature
δt	s	length of timestep in a timeseries
Δt	s	length of a timestep of numerical computations
Δx	m	grid resolution in the direction of x-axis
Δz	m	grid resolution in the vertical direction
$\Delta_{(\mathrm{h})}T$	K	temperature scale of a surface anomaly
$\varepsilon_{i,j,k}$	1	Levi-Civita symbol in three dimensions
θ	K	potential temperature
$\theta_\star$	K	scalar scale in LEM surface model
θ_e	K	equivalent potential temperature
θ_l	K	liquid water potential temperature
θ_{surf}	K	surface potential temperature
θ_v	K	virtual potential temperature
κ	1	Von Kármán constant
λ	m	mixing length
λ_0	m	reference mixing length
ν_m	$\mathrm{m^2\,s^{-1}}$	sub-filter eddy-viscosity in a subgrid model
$\nu_{m,s}$	$\mathrm{m^2\,s^{-1}}$	sub-filter eddy-viscosity in the surface exchange model
ν_h	$\mathrm{m^2\,s^{-1}}$	sub-filter eddy-diffusivity in a subgrid model
$\nu_{h,s}$	$\mathrm{m^2\,s^{-1}}$	sub-filter eddy-diffusivity in a surface exchange model
σ_φ	·	standard deviation of a quantity φ
φ	·	scalar quantity; general notation
ρ	$\mathrm{kg\,m^{-3}}$	density of air
τ	$\mathrm{N\,m^{-2}}$	vertical momentum flux; wind stress
$\tilde{\tau}_{i,j}$	$\mathrm{N\,m^{-2}}$	tensor of the subgrid stress
ϕ_m	1	Businger–Dyer function for the momentum
ϕ_h	1	Businger–Dyer function for the heat flux

List of Abbreviations

notation	meaning
AWS	automatic weather station
ABL	atmospheric boundary layer
CAO	cold–air outbreak
CBL	convective boundary layer
CFL	Courant-Friedrichs-Lewy condition
Cu	cumulus
CuL	cumulus layer
CVEL	the largest advective Courant number
CVIS	the viscous stability parameter
EDMF	eddy-diffusivity mass-flux
IBL	internal boundary layer
IFS	ECMWF Integrated Forecasting System
IQR	interquartile range
EZ	entrainment zone
FA	free atmosphere
LES	large eddy simulation
LEM	Met Office Large Eddy Model
LH	latent heat
LW	long-wave infrared radiation
MetUM	Met Office Unified Model
MIZ	marginal sea-ice zone
ML	(well-) mixed layer
P–W	Piascek–Williams
CtS	control set
SBL	stable boundary layer
Sc	stratocumulus
SH	sensible heat
TKE	turbulent kinetic energy

Chapter 1

Introduction

Human civilization has been always dependent on exploiting favourable weather and mitigating against violent weather. Understanding weather patterns and predicting upcoming shifts in weather has always been vital. One of the great achievements of the twentieth century has been numerical weather prediction (NWP) models of the atmosphere, which have enabled useful forecasts of upcoming weather. During past decades, originally simple models have become increasingly more complicated, representing an ever increasing number of phenomena that can affect the development of weather.

However, the majority of simulations have occasionally failed to predict serious weather events just a few days in advance. Although more accurate evaluation of the initial conditions in the atmosphere and further advances in computational power are beneficial, a number of phenomena occur on time scales and spatial scales that are too small to be directly resolved in the NWP simulation. The effect of these phenomena therefore need to be approximated by employing a suitable parametrization. In addition, it has been indicated that a further drive towards more accurate deterministic NWP models alone is not sufficient, and weather prediction should instead be treated in a probabilistic way (Palmer et al., 2005).

An interesting example of the phenomenon which occur on relatively small scales is a turbulence over a heterogeneous surface. This is particularly common when the cold air masses of the Arctic are advected over a warmer surface of a marginal sea-ice zone. This meteorological phenomenon, known as *cold-air outbreak*, is then characterized by a developing convection. This leads to vertical transport of heat, moisture and momentum (Renfrew and Moore, 1999). NWP models usually parametrize the convective boundary layer in a cold-air outbreak as if it was taking place over a homogeneous surface, even though a marginal sea-ice zone consists of a heterogeneous mix of water and segments of sea-ice (Gryschka et al., 2008). However, the heterogeneity in surface conditions is likely to effect the organisation of convective eddies (Gryschka et al., 2014). This is nicely illustrated by a satellite image in the figure 1.1. It is, therefore, a valid question

how heterogeneous surface conditions alter the structure of the boundary layer and the resulting vertical transport of heat, moisture and momentum.

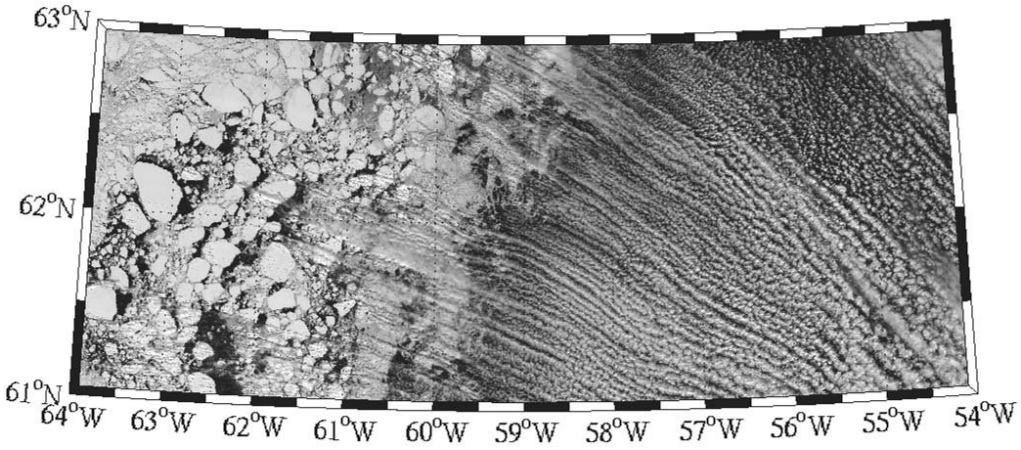

Figure 1.1: Satellite image showing the distinctive organisation of cloud streets in the cold-air outbreak over the marginal sea-ice zone of the Labrador Sea. Reproduced from Liu et al. (2006).

The main purpose of this thesis is to extend our knowledge of atmospheric processes in cold-air outbreaks for the purpose of parametrization in NWP. The central point is examining the influence of a heterogeneous surface forcing on a developing cold-air outbreak. The study then aims to investigate the structure of the convective boundary layer and provide implications for the boundary layer parametrization schemes. We therefore focus on the analysis of vertical fluxes of heat, moisture and momentum, as well as on the variation in their values. The main novelty of this study lies in the introduction of three different types of heterogeneous patterns in surface temperatures.

This introductory chapter explains the motivation behind this study and further narrows down the topic of the study. Firstly, it shows the importance of parametrizing small-scale processes (1.1). Secondly, it points out the importance of parametrizing the underlying variability in weather (1.2). Although there is a wide palette of mesoscale phenomena where the variability is not properly examined, this study needs to only focus on one chosen phenomenon. The motivation for the choice is given in the following part (1.3) — it explains the significance of the phenomenon of cold-air outbreak. The next part (1.4) specifies the main problems and state clearly the thesis objectives. The subsequent part (1.5) will then briefly justify the choice of methods for this study. Finally, the structure of the thesis will be shown in the last section of the introductory chapter (1.6).

1.1 Introduction to the Parametrization of Convective-Scale Phenomena

The atmosphere can be viewed as a highly complex, non-linear dynamical system. In this part of the introduction, we will explain the importance of parametrizing parts of this dynamical system. First, we will briefly review the theory. Secondly, we will describe some examples of the parametrization of convective-scale phenomena. Finally, we will show some persisting issues in indexparametrization parametrization approaches.

The atmosphere could be viewed as an infinite-dimension dynamical system. Using *Palmer's notation*, an evolution of this system $\{\widetilde{\boldsymbol{X}}(t)\}_t$ is schematically described as

$$\dot{\widetilde{\boldsymbol{X}}} = \widetilde{\mathbf{F}}\big[\widetilde{\boldsymbol{X}}\big], \tag{1.1}$$

where $\tilde{F}$ in a non-linear functional. For the purpose of numerical prediction, an approximation includes some form of Galerkin decomposition on a finite-dimension dynamical system described as

$$\dot{\boldsymbol{X}} = \mathbf{F}\big[\boldsymbol{X}\big] + \mathbf{P}\big[\boldsymbol{X}; \beta\big], \tag{1.2}$$

where the finite-dimensional $\mathbf{F}$ is a truncation of $\widetilde{\mathbf{F}}$, the functional $\mathbf{P}\big[\boldsymbol{X}; \beta\big]$ represents the effects of remaining terms in $\widetilde{\mathbf{F}}\big[\widetilde{\boldsymbol{X}}\big]$ that were not preserved, and β are parameters based on physical properties of atmosphere and the form of the decomposition. (Palmer, 2001)

Grid-based models use the premise that the dynamical system can be decomposed on resolved-scale variables and a local remainder. However there is not a clear justification for this assumption, even though the research on cospectra of wind velocities in the atmospheric boundary layer (ABL) indicated an existence of the cospectral gap (Vickers and Mahrt, 2003). Nevertheless, the possible issues arising from a cut-off between the resolved and unresolved scales should be always carefully considered.

Over last few decades, NWP models have, amongst other improvements, seen an increase in the grid resolution. This increased resolution has led to a higher amount of resolved processes. We will show it on examples of paramatrizations for turbulent transport in the ABL used in current NWP models.

1.1.1 Examples of Convective Boundary Layer Parametrization

One of the popular approaches for parametrizing the convective boundary layer (CBL) is *eddy-diffusivity mass-flux* (EDMF) method. It is employed in a number of NWP and

other numerical models, including the Integrated Forecasting System (IFS) of the European Centre for Medium-Range Weather Forecasts (ECMWF). The main idea behind EDMF schemes is that transport of mass and energy within the CBL are modelled as a combination of upward transport inside thermals and a diffusion into the rest of CBL. The CBL parametrization in the operational version of the Met Office Unified Model (**MetUM**) is based on the similar principles, but it differs from the EDMF parametrization. It models the vertical transport as the combination of the effect of a non-local forcing for the transport across the CBL and the local gradient transport by eddy diffusion. The following paragraphs further explain both schemes .

From the **EDMF** standpoint, the CBL consists of a few strong updraughts and a surrounding turbulent air with weaker updraughts and various downdraughts (Siebesma et al., 2007). While there are differences between various EDMF implementations, this explanation mostly focuses on the scheme used in the IFS. *Strong updraughts* are arbitrarily defined as updraughts in a small fractional area a_u containing the strongest upward vertical motions (IFS IV, 2013, pp.39–40). Strong updraughts at the bottom of the CBL are the basis of thermals that facilitate mass-transport of the warm moist air parcels higher up while smaller eddies are responsible for the diffusive transport of heat and moisture in horizontal and vertical gradients (Siebesma and Cuijpers, 1995).

The EDMF schemes are not concerned with each single updraught plume, but with their overall effect on the vertical transport (Witek et al., 2011). Denoting the vertical velocity w, the vertical flux of a scalar quantity φ in the kinematic form is expressed as

$$\overline{(w'\,\varphi')} = a_u\,\overline{(w'\,\varphi'_u)}^{(u)} \;+\; (1-a_u)\,\overline{(w'\,\varphi'_e)}^{(e)} \;+\; a_u\,w_u\,\big(\varphi_u-\varphi_e\big) \tag{1.3}$$

where $\overline{(\;)}^{(u)}$ denotes averaging over the area of strong updraughts, $\overline{(\;)}^{(e)}$ denotes averaging over the air surrounding updraughts, and φ_u and φ_e are values of the scalar quantity within the strong updraughts, respectively the air surrounding updraughts. The diffusion components are then estimated by first-order closure to obtain

$$\overline{(w'\,\varphi')} = -\,K_\varphi\,\frac{\partial\overline{\varphi}}{\partial z} \;+\; a_u\,w_u\,\big(\varphi_u-\varphi_e\big), \tag{1.4}$$

where K_φ denotes the *K-profile* that estimates the eddy diffusivity (O'Brien, 1970). The K-profile values are usually estimated by the method of Troen and Mahrt (1986).

The EDMF approach is usually applied between the surface layer and the top of the CBL. In the IFS, the EDMF is applied up to the inversion height above the CBL in the case it is clear or topped with stratocumuli clouds. In the case that cumulus clouds are present, the EDMF is applied up to the cloud base. The height of the inversion and the condition for cumulus clouds are determined diagnostically (Köhler et al., 2011). The

transport between the surface and the lowest model level is treated by a separate surface parametrization based on Monin-Obukhov theory (Beljaars, 1994).

The surface parametrization is also used to derive the vertical velocity variance σ_w at the lowest EDMF level and the difference between the values of φ_u and the horizontal mean $\overline{\varphi}$. Under the assumption that the distribution of vertical velocities follows a normal distribution, the vertical wind velocity an the lowest level is set to $\sigma_w \cdot \mathsf{z}_{1-a_u}$, where z_{1-a_u} is the $1 - a_u$ quantile of the normal distribution. The values of the kinetic energy $\frac{1}{2}\, w_u^2$ and the scalar quantity φ_u within the strong updraughts at other model levels are then obtained by integrating the mass flux equations

$$\begin{aligned} \frac{\partial \varphi_u}{\partial z} &= -\ \epsilon_e \left(\varphi_u - \overline{\varphi}\right) \\ \frac{1}{2}\,\frac{\partial w_u^2}{\partial z} &= -\ \epsilon_e \left(w_u^2 - \overline{w}^2\right) + \underbrace{g\,\frac{\theta_{v,u} - \overline{\theta_v}}{\overline{\theta_v}}}_{\text{(II)}}, \end{aligned} \tag{1.5}$$

where $\theta_{v,u}$ is the virtual potential temperature within updraughts, $\overline{\theta_v}$ is the horizontal mean of the virtual potential temperature and ϵ_e is fractional entrainment (Siebesma and Teixeira, 2000). The first term on each right-hand side of each equation represents the entrainment between the strong updraughts and the rest of the CBL air. The term (II) then accounts for the changes the vertical velocity of updraughts due to buoyancy.

The choice of the vertical velocity of updraught attracts further attention. Although the estimation of the vertical velocity variance in the vicinity of the surface is quite robust and supported by laboratory experiments (Holtslag and Moeng, 1991), we do not know much about the skew and further properties of the distribution of the vertical velocities. While some recent studies concerning EDMF schemes have taken into account variations in the distribution of strengths of updraughts (Sušelj et al., 2012), many other sources simply assume that the distribution of vertical velocity of updraughts and downdraughts follows normal distribution (IFS IV, 2013, pp.41-42).

The ABL parametrization in the operational version of the **MetUM** is dependent on the boundary layer type. The current version of MetUM (8.6 as of 2016) recognises seven different types of ABL. Out of that, five are concerned with the CBL (Lock and Edwards, 2013, p. 6). The computational scheme for vertical turbulent transport of heat and moisture differs between the types. Nevertheless, there are some main common points. Firstly, the ABL type is determined diagnostically. Secondly, the depth of the ABL and the heights of possible decoupling levels are estimated. In essence, these ABL properties are diagnosed by taking parcels of the air from the near-surface layer and the top cloud layer and evaluating their buoyancy at different altitudes. The prediction of

the vertical turbulent transport within the ABL is then based on the first-order closure of a *flux-gradient* relation (Lock et al., 2000).

In the flux-gradient approach, vertical fluxes of momentum and scalar quantities are replaced by a term for local gradient transport and an additional non-local term. The vertical kinematic flux of a scalar quantity φ is usually expressed as

$$\overline{\left(w'\,\varphi'\right)} = \underbrace{-\,K_h\,\frac{\partial \varphi}{\partial z}}_{\text{local}} + \underbrace{K_h^{(\text{surf})}\,\gamma_\varphi}_{\text{non-local}}, \tag{1.6}$$

where K_h is the K-profile that estimates the eddy diffusivity (O'Brien, 1970), $K_h^{(\text{surf})}$ is a term representing surface forcing and the variable γ_φ represents the effect of the entrainment at the top of the CBL (Lock and Edwards, 2013, pp. 21–22). The treatment of the vertical flux of momentum is analogous, although the coefficients differ.

The main idea behind the local gradient term is that smaller eddies facilitate the diffusion of the momentum and scalar quantities mostly in the down-gradient direction. The eddy diffusivity K-profile is determined based on the estimated Richardson number, indicated amount of wind shear and additional coefficients dependent on the model numerical set-up. The specific way of calculating these values differs between CBL types. Due to a rather complicated nature of these calculations, we point for the further details to the MetUM documentation (Lock and Edwards, 2013).

The non-local term accounts for additional forcings in the ABL. In the CBL cases, it consist of the impact of the surface-driven eddies and the impact of entrainment at the CBL top. The entrainment is parametrized by employing the direct scheme of Lock (2000) for well-mixed boundary layers and the mass-flux scheme of Gregory and Rowntree (1990) for cumulus-topped layers. The surface layer forcing term is computed with the help of the surface scheme based on Monin-Obukhov theory. This again alludes to some similarity to the EDMF scheme. For further details on the calculation, we again point to the MetUM documentation (Lock and Edwards, 2013).

1.1.2 Issues in Convective Boundary Layer Parametrization

A common feature of many ABL parametrization schemes is the assumption that the vertical wind velocity at the bottom of the ABL follows some specific distribution. Moreover, there is also the implicit assumption that the surface roughness, temperature and other properties are spatially homogeneous. The question whether the schemes work well for heterogeneous surfaces within the model grid cells is seldom addressed, let alone discussed. However, it is very likely that inhomogeneities contribute to the error in sub-

grid parametrization in atmospheric models (Love and Leslie, 1979).

The issue of the impact of a heterogeneous surface on CBL properties has gained more scientific attention in the recent decade. The impact of non-homogeneous surface forcing is slowly gaining attention in the development of NWP. This is also the case of both aforementioned examples of NWP systems. For example, the MetUM documentation offers a promise that future versions of the model will treat surface heterogeneity explicitly by a 'tiling' method (Lock and Edwards, 2013, p.55). In addition, a number of studies has proposed modifications of the surface drag coefficients over a heterogeneous surface (Lüpkes et al., 2012) or the modification of the entrainment estimation (Sühring et al., 2014). However, surface heterogeneity can affect the overall structure of the CBL (Desai et al., 2006), including the coherency of the larger convective eddies (Fesquet et al., 2009). Therefore, it is logical to ask whether ABL schemes require adjustments in a case of heterogeneous surface conditions.

1.2 Introduction to Stochastic Parametrization

The atmosphere is a complicated dynamical system that often exhibits a chaotic behaviour and a high sensitivity to initial conditions. Owing to various advances in NWP models, a deterministic simulation can approximate the effects of various processes on developing weather. However, one deterministic simulation does not take into account the variability in these processes. In this part of the chapter, we are going to explain the motivation for *stochastic parametrization* and introduce some of the issues related to it.

A recently popular approach to capturing the variability in the development of weather has been *ensemble forecasts*. The main idea behind them is that a large set of deterministic NWP runs is initialised with different perturbations in the parameters, and in some cases, also different parametrization schemes. The results of NWP runs are then statistically evaluated to estimate the most likely development of the dynamical system of the weather and estimate the likely variations in weather conditions (Weisheimer et al., 2011). Ensemble forecasts, though widely accepted as the state of art in NWP forecasts, have a tendency to under-represent the spread on the longer timescales and might often fail to predict serious weather events in advance (Palmer et al., 2005).

With a goal to counter these issues, another new approach based on stochastic treatment of uncertainty arises as well. The effect of various unresolved processes and variation in the initial conditions are represented by the deliberate introduction of uncertainty into models. Generally, there is no single main method for stochastic parametrization, but rather a growing selection of various, often very different approaches. Some of them are based on global parameter perturbations (Li et al., 2008), some others use stochastic

backscatter to retain the effect of high frequencies near cut-off length and scatter part of their effect onto lower frequencies (Buizza et al., 1999), and there are also a number of methods based on the application of cellular automata (Bengtsson et al., 2013). Specific stochastic parametrization schemes have been implemented within some established NWP models, including the ECMWF IFS (Weisheimer et al., 2014) and the Met Office Global and Regional Ensemble Prediction System (MOGREPS) (Tennant et al., 2011). It has been indicated that the skill of the forecasts have improved (Palmer, 2001, p. 290).

The approach to stochastic parametrization can be demonstrated in the modification of the existing decomposition of the system on resolved and unresolved scales. A number of conventional local-enclosure and bulk-parametrization schemes follows the premise behind the decomposition (defined in equation 1.2) by assuming that the contribution of unresolved processes at each N_d points is based only on a set of parameters and the local values of resolved variables, i.e.

$$\boldsymbol{X}_k = \mathbf{F}_k\big[\boldsymbol{X}\big] + \mathbf{P}\big[\boldsymbol{X}_k; \beta\big], \quad k = 1 \dots N_d, \tag{1.7}$$

However, resulting system of the ordinary differential equation would not cover the same variability as the original one, Palmer (2001, p. 283) argues. Although unresolved scales only hold a small portion of the total model variance, neglecting them in a non-linear system can easily lead to serious systematic errors (Bengtsson et al., 2011). To counter this issue, Buizza et al. (1999, p. 2889) suggest adding the stochastic perturbations that is schematically defined as

$$\boldsymbol{X}_k = \mathbf{F}_k\big[\boldsymbol{X}\big] + \nu\, \mathbf{P}\big[\boldsymbol{X}_k; \beta\big], \qquad \nu \sim \mathrm{U}(0.5, 1.5), \quad k = 1 \dots N_d, \tag{1.8}$$

where ν is the random number drawn from the uniform distribution on the interval $[0.5, 1.5]$. Orrell (1999) and Smith (2001) instead suggest various non-local parametrizations where the variance in the parametrized term is based on the estimated variance of the full system.

The aforementioned parametrization schemes usually employ random numbers drawn from the uniform distribution or Gaussian distribution. However Berner (2005) argues that that the underlying probability distribution should be non-Gaussian and presents few examples when this approach improves the skill of the forecast. Furthermore, it is important to consider some degree of auto-regression in the random variables. This possibility was already identified in the ECMWF stochastic schemes (Palmer et al., 2009).

Regarding different approaches in weather forecasting, one of the implicit questions is whether we can improve our knowledge of the underlying variability in some of the processes affecting the development of weather. A better insight into the variability

both on temporal and spatial scales can be beneficial for further improvement in the stochastic parametrization schemes. Moreover, there is also the question of which atmospheric phenomena can be determined accurately enough and which phenomena should be treated as a part of stochastic 'noise'.

1.3 Introduction to Cold-Air Outbreaks

One of the weather phenomena that leads to rapid changes in the extratropical ABL is known as *Cold-Air Outbreak* (CAO). CAOs strongly contribute to heat transfer in polar areas (Papritz et al., 2014). A number of studies indicate that they are very likely to influence the uncertainty in the extra-tropical weather conditions (Wacker et al., 2005) and affect the predictability of weather (Walsh et al., 2001). In this part of the thesis, we will characterise the phenomenon of CAO and explain its importance. Firstly, we start with a brief historical introduction. Secondly, we compactly characterise the main principle of CAO. Then we further describe the processes within CAO. As a next step, we show some differences between CAOs. Finally we focus on challenges faced in the previous model studies of CAO.

The phenomenon of cold-air outbreak was scientifically observed at least as early as mid-19th century, although the scientific name we use for it today was not yet adopted at those times. Researchers on the early Arctic expeditions described that CAO leads to rapid changes in the bottom part of the troposphere (Murphy, 1860, p.312). It was also recognised that high temperature differences together with the changing structure of Arctic sea-ice might affect wind patterns (Daly, 1877). Later expeditions then revealed a high variability in the weather patterns in the Arctic (Shaw, 1928).

The main principle of CAO can be described as follows: The mass of a cold stratified air originating over sea-ice or land is advected over a warmer surface of a marginal sea-ice zone (MIZ) or an open sea. A high surface temperature gradient over the surface then leads to a high flux of heat and moisture into the atmosphere (Moore et al., 2014). The originally stratified stable boundary layer (SBL) becomes unstable. This causes warm plumes to rise from the surface layer and form the CBL. Developing convective eddies than facilitate further vertical transport of heat and moisture from the surface (Skyllingstad and Edson, 2009). This allows deepening of the CBL and the formation of clouds. The main principle of CAO is illustrated in the figure 1.2. The processes present in a CAO are further described in the following paragraphs.

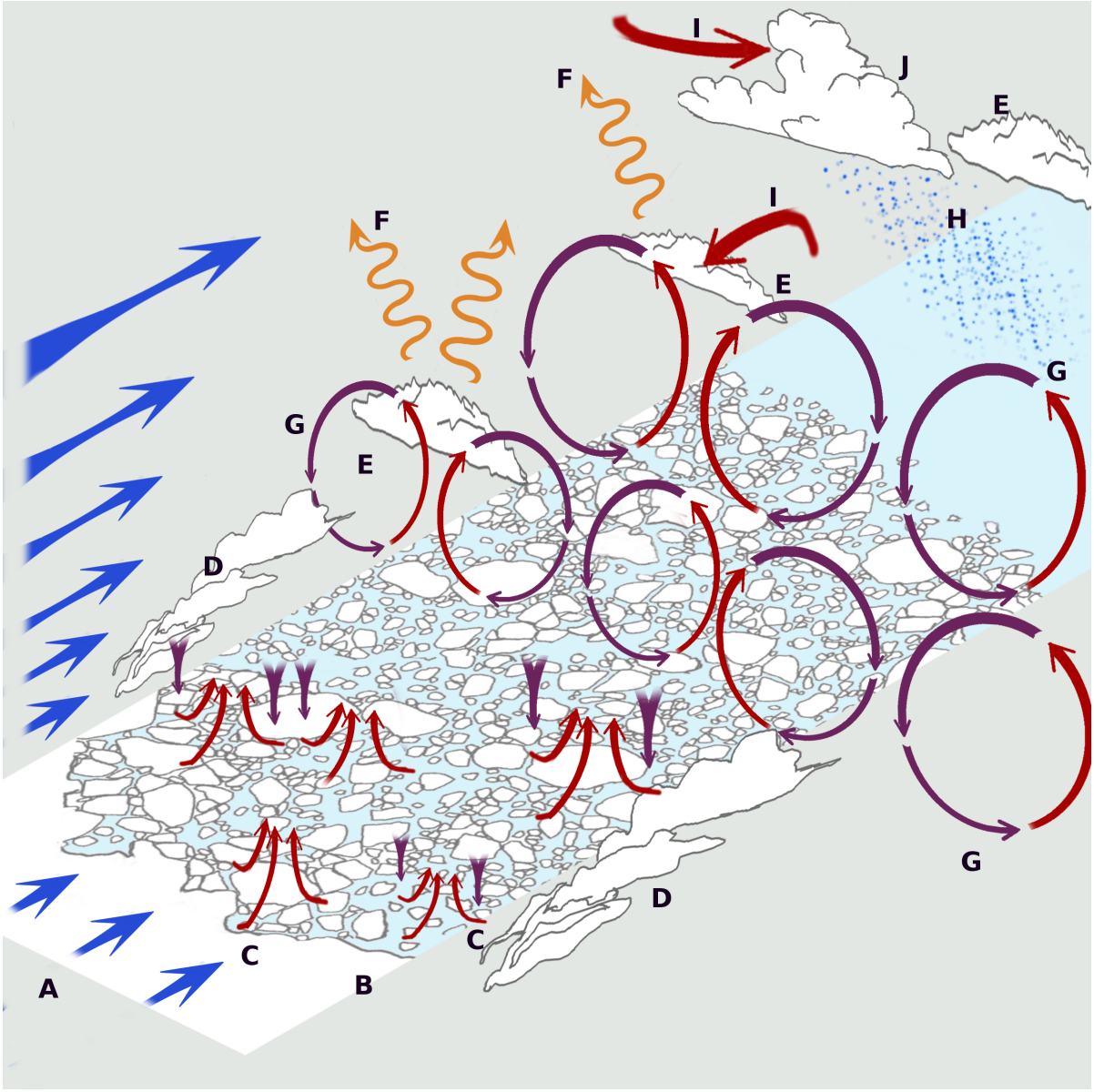

Figure 1.2: Illustration of a cold-air outbreak of a MIZ — The horizontal and vertical distances are not up to scale. The structure of the MIZ is based on figures from Rothrock and Thorndike (1984). Only the main processes are illustrated: **A**– the advection of cold air, **B**– the edge of ice, **C**– convective plumes, **D**– steam fog , **E**– clouds (stratocumulus type), **F**– outgoing longwave radiation, **G**– convective rolls (the mean wind component not displayed), **H**– precipitation, **I**– cloud entrainment, **J**– clouds (cumulus type)

1.3.1 Processes in Cold-Air Outbreak

With the warming of the near-surface air after the edge of ice, an internal boundary layer (IBL) is formed between the turbulent air and the remains of the original SBL. The IBL then grows due to heating from the surface and the entrainment of the air above the IBL (Renfrew and King, 2000). As the IBL rises, coherent convective structures are formed (Zurn-Birkhimer et al., 2005). Originally separate surface plumes blend with altitude into thermals (Couvreux, 2010). The inner portion of the CBL above the surface layer and bellow the IBL generally become well mixed (Ebner et al., 2011), leading to its

classification as *mixed layer* (ML) (Stull, 1988, p. 12)

The growth of the CBL is also associated with the formation of clouds. Clouds usually start forming soon after the air passes the edge of the ice. However, it is often difficult to distinguish between convective clouds and the steam fog (Brümmer, 2002). The steam fog and "steam devils" occur due to condensation in rising plumes (Zurn-Birkhimer et al., 2005). Clouds usually form atop larger thermals. Thermals are generally responsible for most of the vertical heat and moisture transport within the cloud layer (Klein et al., 2009). Due to the influx of heat and moisture, clouds continue growing and extend also into the inversion layer (Solomon et al., 2014). Due to longwave radiative cooling at cloud tops, droplets grow rapidly until subsaturation occurs (Jiang and Cotton, 2000).

While the upper part of the clouds mostly consist of growing supercooled water droplets, the situation in the lower portion of the clouds is significantly different. The bottom part of clouds experience glaciation, leading to the mixed-phase character of clouds (Klein et al., 2009). Despite a number of observational and model studies, the impact of the small-scale turbulence on the small droplets of supercooled water is still not properly understood (Forbes and Ahlgrimm, 2014). As a results, mixed-phase clouds are generally difficult to paremeterize, particularly in the representation of the supercooled liquid water. Therefore, NWP models face a number of difficulties reproducing Arctic clouds (Tjernström et al., 2008), leading to biases in Arctic radiative balance (Tsay et al., 2008). This bias is mostly indicated in the downwelling longwave radiation (Barton et al., 2014).

The formation of larger organised convective structures has been observed in many cases. The most common form are structures known as *convective rolls* where convection is organised into a quasi two-dimensional vortex circulation. These rolls generally have an opposite sense of rotation and are aligned parallel with the wind in the CBL (Etling and Brown, 1993). When cloud rolls form a repetitive horizontal pattern, their long axis are usually pointing 15° to 20° left from the direction of the geostrophic wind (Atkinson and Zhang, 1996). In the downwind direction, convective rolls grow in depth and sometimes merge (Liu et al., 2006). Due to clouds usually forming atop the convective updraught, convective rolls often lead to the formation of cloud streets (Gryschka et al., 2014). An example of a CAO with convective rolls is shown in the figure 1.1.

Convective rolls usually reach depth from 0.5 to 2 km and the horizontal wavelength of the pattern (i.e. the width of two counter-rotating rolls) is usually 2 to 5 km. The ratio between the wavelength and the depth is usually between 2 and 5. However, if we focus on cold outbreaks in the Arctic, shallower rolls and patterns with lower wavelength are also occasionally observed. During ARKTIS 1991 and ARKTIS 1993 field campaigns rolls of the depth 350 to 800 m were often observed. The pattern wavelengths were usu-

ally 1.2 to 4 km, with the aspect ratios between 3.5 and 6.5 (Brümmer, 1999).

Further downwind, the convection often undergoes a transition from the regime of convective rolls to a regime of cellular structures (Fedorovich and Conzemius, 2008). This transition is often associated with the decrease in the wind shear at the top of the CBL (Elperin et al., 2006). A CAO originating in the Arctic usually attains the form of *open cells* (Brümmer, 1997). These are dominated by large cells where the convective updraught is mostly contained on the edges and topped with clouds. The inner region of each cell consists of descending cold air. The centre of a cell usually stays nearly cloud-free (Atkinson and Zhang, 1996). Open cells then tend to grow further in size (Dörnbrack, 1997). Open cells usually attain the depth 1 to 2 km and the diameter 7 to 20 km (Brümmer, 1999).

1.3.2 Comparison of Cold-Air Outbreaks

Cold-air outbreaks are neither rare nor limited to a few areas. In the following paragraphs, we will compare general properties of CAO. Firstly, we look at the geographical variability. Secondly, we compare the vertical structure of the ABL in CAOs.

During the winter season in the northern hemisphere, CAOs are observed over a wide range of mid-latitude and high-latitude seas, for example:

- Arctic ocean near Svalbard (Brümmer, 1996),
- Laptev sea north off the coast of central Siberia (Ebner et al., 2011),
- Labrador Sea and neighbourhood areas of Northern Atlantic (Renfrew and Moore, 1999),
- Sea of Japan (Inoue et al., 2005a),
- East China sea (Yamamoto, 2012),
- Baltic Sea (Brümmer, 2002),
- Black Sea (Efimov and Yarovaya, 2014),

and also over some large lakes, for example

- Lake Erie (Gerbush et al., 2008).

CAOs also occur over seas in high-latitudes of the southern hemisphere (Papritz et al., 2014). In a number of mid-latitude cold-air outbreaks, the mass of cold air does not start over sea-ice, but over a cold land surface (Efimov and Yarovaya, 2014). In the CAOs over large lakes, the warming of the ABL is limited by the extent of the lake, as the heating from the surface ceases when the air passes over land (Gerbush et al., 2008).

Despite these differences, the main principles are same as in the Arctic CAO.

The cold air upwind from the warm water surface is often strongly stratified. The potential temperature lapse rate in the bottom few hundred meters can exceed 20 K km^{-1}. Such a strong stratification was observed for example in CAO on 20 March 1993 during the ARKTIS 1993 campaign (Brümmer, 1996). However in a number of other cases, the bottom part of the atmosphere was affected by warming from leads (Inoue et al., 2005b) or by previous cyclonic weather (Pagowski and Moore, 2001). This then generally caused a weaker stratification in the SBL. A high diversity in the vertical structure of lower troposphere during CAO is demonstrated in the comparison of previous CAO studies (see figure 1.3). Comparing the potential temperature between CAO studies is slightly complicated by the fact that measurements were taken at different stages of the CAO development.

The differences between the surface temperature and the potential of the forming CBL is often around 10 K (Brümmer, 1999), but it can also reach values up to 40 K (Ebner et al., 2011). There is a wide spread in the wind velocities between CAOs. The comparison of CAO studies by Brümmer (1999) concluded that wind velocities were in the range 3.8–14.4 $m\,s^{-1}$, although wind velocities over 15 $m\,s^{-1}$ are also seldom observed (Hartmann et al., 1999).

During CAO, cold air masses are often advected over a surface that is not strictly homogeneous. In the inner Arctic, the marginal sea-ice zone (MIZ) consist of large areas covered with broken sea-ice sheets and ice floes (Inoue et al., 2004). Similarly, coastal polynia of the Laptev Sea consist of patches of ice and open water (Ebner et al., 2011). MIZs can reach downwind extent from few kilometres (Kottmeier and Hartig, 1990) to few hundred kilometres (Streten, 1973). The sizes and shapes of ice floes can vary in scales from a few metres to a few kilometres (Esau, 2007) (Inoue et al., 2005b). There is high variability in this sea-ice mix. The distribution of sea-ice floes is often influenced by geographical region and the distance from coastal areas (Hudson, 1987) as well as by seasonal variability (Perovich and Jones, 2014).

Since the airborne lidar observations in mid-latitudes has shown the effect of surface heterogeneities on the organisation of coherent convective structures and the CBL entrainment (Grabon et al., 2010), the role of heterogeneities in MIZ should be considered. While a MIZ consists of a mix of sea water and patches of various kinds of ice (Gupta et al., 2014) of different temperatures, these surface heterogeneities are likely to influence the atmospheric conditions (Gryschka et al., 2008), including CAOs developing over the MIZ (Pagowski and Moore, 2001). Due to ongoing processes of freezing and melting as well as ice sheet dynamics, the structure of sea-ice is facing ongoing changes (Yang and Yuan, 2014).

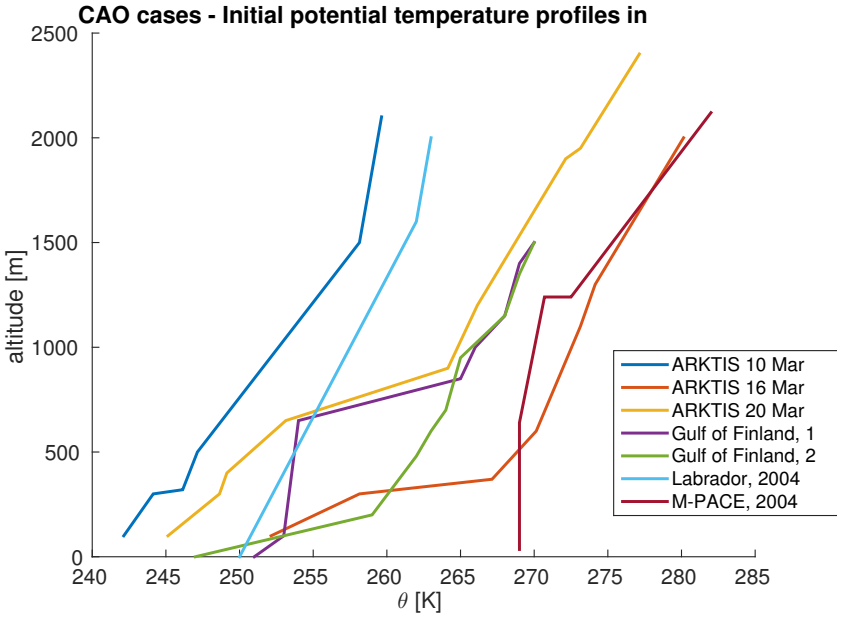

Figure 1.3: The vertical profiles of potential temperatures in previous studies of cold-air outbreak cases: *ARKTIS 1993* campaign took place in March 1993 in areas northwest and south of Svalbard (Brümmer, 1996); *Gulf of Finland* model study is based on observations from 6–8 December 1998 over the southern part of the Gulf of Finland (Savijärvi, 2012); *Labrador, 2004* model study is based on CAO case on 8 February 1997 over Labrador Sea (Liu et al., 2004); *M-PACE* model study (Klein et al., 2009) is based on the field observations of CAO on 9–10 October 2004 near Barrow on the north coast of Alaska (Verlinde et al., 2007)

To summarise, CAO occur in a wide range of high-latitude regions. There is a high diversity in the atmospheric conditions between different cases. The characteristic of the MIZ prompts questions as to whether surface heterogeneous forcing plays a significant role in the formation of the CBL and whether it affects the variability in the ABL. Therefore, in the next part of the thesis, we will focus on previous model studies that took into account the structure of the MIZ.

1.3.3 Previous Model Studies

Fine-scale model studies play an important role in the research of the CAO. In the following paragraphs, we will first provide a brief introduction to previous model studies. Then we will describe some of the common challenges in the implementation of heterogeneous surface forcing.

Various studies have tried to analyse the structure of CBL in CAO (Brümmer, 1996) and the developing cloud patterns (Clond, 1992). A number of studies have also focused on the convective rolls in CAO in various geographical locations, including Labrador Sea (Liu et al., 2004) and South China Sea (Alpers et al., 2012). Older studies almost al-

ways treated the surface as homogeneous, however this started changing in 21st century. Recent studies with cloud-resolving models have analysed the impact of sea-ice concentration on the formation of roll convection and clouds (Liu et al., 2006). Eddy-resolving model studies were usually employed to examine the impact of sea-ice inhomogeneities on the changes in the stratification of the ABL Lüpkes et al. (2008), and on the formation of cloud rolls (Gryschka et al., 2008). A relation between the relative scale of inhomogeneities and their impact on increasing convective forcing has been explored in Yates et al. (2003) and further modelled by Heerwarden et al. (2014).

Still, the question of the variability in the developing CBL induced by inhomogeneities in the surface has not yet been fully addressed. A common feature of many studies is that they define just one specific type of the heterogeneity. A common choice is a spatial heterogeneity in surface temperatures prescribed as a two-dimensional sinusoid wave (Kang and Lenschow, 2014) or a one dimensional wave oriented across the wind (Shen and Leclerc, 1995). The length of the wave and the amplitude of the temperature anomaly are then treated as model parameters. However the possibility that the effect of the heterogeneous surface forcing might differ for a heterogeneity of a different shape is usually not investigated.

Although there were also studies such as Courault et al. (2007) that investigated the impact of heterogeneous surface patches of different shapes, they were focused on heterogeneity in surface moisture. Furthermore, the study was concerned with the weak-wind scenario in mid-latitudes. Also, the often changing-structure of the sea-ice (Yang and Yuan, 2014) might present an issue in determining the heterogeneous forcing accurately.

1.3.4 Summary of Cold-Air Outbreaks

To summarise, CAOs are dominated by a rapid development of the CBL. The coherent convective structures that develop in the CBL then facilitate further transport of heat and moisture from the surface. CAO lead to significant changes in the structure of the ABL. CAOs in the Arctic region often occur over a MIZ with a high spatial variability in surface temperatures and roughness. The changing structure of sea ice (Yang and Yuan, 2014), together with high temperature gradients between the cold Arctic air and relatively warm sea water, can contribute to uncertainty in the prediction of extratropical weather. A number of previous studies therefore investigated the impact of heterogeneous surface forcing over MIZ on the developing CAO. However, it is not clear whether the models properly capture the variability in the surface conditions in the MIZ. This would logically lead to a question how to describe the resulting uncertainty in the ABL properties.

1.4 Thesis Aims

This part of the thesis first summarise the main problems regarding the parametrization of CAO and the variability within it. Secondly, it establishes the niche that this study intends to fill. Finally, it declares the thesis objectives.

The main motivation for this thesis is the uncertainty in the atmospheric processes over MIZ in Arctic. While the impact of heterogeneous surface conditions has been examined in various research studies there are still some unresolved questions. Generally speaking, previous studies were often focused on one specific aspect of cold-air outbreak, for example distribution of cloud sizes or the strength of entrainment (Sühring et al., 2014). Also, many model studies were limited by the specific definition of surface heterogeneous conditions. A common limitation was that only one shape of surface anomalies was defined, such as stripe or wave pattern oriented across the direction of the mean wind (Gryschka et al., 2014). Possibility of a different shape of surface anomalies or a different orientation was often not considered.

The main purpose of this study is therefore to improve our knowledge of the variability within CBL during the developing CAO. This study focuses on addressing the questions that were foreshadowed by previous studies, but not yet fully answered. We are therefore trying to examine the influence of different types of heterogeneous surface forcing in a developing cold-air outbreak. Although the heterogeneity in surface roughness is expected to be an important factor, the observational studies give quite a wide range for aerodynamic surface roughness (Gupta et al., 2014). Furthermore, observation are generally inconclusive about the additional drag provided by the edge of ice floes which can significantly alter the resulting aerodynamic properties of the ABL (Lüpkes et al., 2012). Therefore, in this study we focus exclusively on the impact of *spatial heterogeneity in surface temperatures*. The effect of the shape and the size of surface anomalies is examined. We are trying both to establish a better understanding of the variability within CBL in cold-air outbreak as well as to show implications for the parametrization schemes.

The first important question is *whether the local structure of the MIZ plays a significant role in the developing CBL during a CAO event*. This question requires exploring whether heterogeneity of the mix of sea-ice affects the structure of the developing CBL and whether the impact of this heterogeneity extends beyond the surface layer. The second important question is then *whether the heterogeneity introduces more variability in the behaviour of the CBL*. This point is concerned with the variability both in the temporal and the spatial scales. This also involves investigating the vertical transport of heat and moisture.

Since CAOs occur in a wider range of conditions, it is important to address whether

the impact of the local structure of the MIZ is not limited just to one specific setting of parameters. Therefore, we investigate the impact of modifying the properties of the heterogeneous surface:

- the **temperature scale** - difference between the anomalies and the mean values,
- the spatial **size** of the pattern;

and the impact of modification of the properties of the troposphere:

- wind forcing in the lower troposphere,
- initial stratification in the lower troposphere.

1.5 Introduction to Methodology

An indispensable part of each study is a suitable choice of research methodology. Generally speaking, *"The problem is not to find the best or most efficient method to proceed to a discovery, but to find any method at all"* (Feynman, 1965). This part of the thesis therefore introduces the methodology of our study. To thoroughly address the research questions (stated in 1.4), we perform an extended model study with the help of a *large eddy simulation* (LES). This powerful tool allows us to numerically model developing turbulence in a CAO scenario. Firstly, we will explain the choice of the modelling software. Secondly, we justify the choice of the initial conditions and the simulation framework. Finally we briefly introduce the methods for the analysis of model results.

From a selection of various LES software packages that are currently used in atmospheric research, we have selected the *Met Office Large Eddy Model* (LEM) that has been extensively used in improving MetUM boundary layer schemes (see 1.1). The LEM offers a number of features useful for modelling developing CBL, such as a well documented dynamic core, advanced treatment of dynamics and eddy viscosity, a full three-phase microphysics with a number of hydrometeor conversions, an interactive radiation code, and a well calibrated surface exchange model. Although the LEM is a powerful computational tool, it has also its shortcomings. The lateral boundary conditions are strictly periodic, and therefore the LEM does not allow us to model scenarios with a directly prescribed inflow and outflow from the model domain. Furthermore, a spatial domain that would include both the area over sea-ice as well as downwind over the MIZ would be extremely large. Therefore, we instead use the *Quasi-Lagrangian Approach* to simulate the downwind development of CAO.

This study applies the quasi-Lagrangian approach of Szoeke and Bretherton (2004). In their formulation, the entire column is *assumed to move at the mean ABL velocity*. While this approach was originally used for modelling boundary-layer transition in tropics, it has been successfully adjusted also for simulations of a large CAO over the Gulf Stream where the wind velocity is not constant with height (Skyllingstad and Edson, 2009).

An issue of this method is that it does not capture the effect of the different advection speeds due to shear within the ABL. However, this issue is of a minor importance when the ABL is mixed. The method is applied under the assumption that secondary mesoscale circulations generated near the front of the travelling air mass are relatively small in comparison with the direct response to the forcing at the surface. The resulting impact of neglecting the advection on the overall flow characteristics is relatively weak in comparison with the changes in surface temperature (Skyllingstad and Edson, 2009). To confront this assumption with real weather scenarios, we have investigated the CAOs observed during the ACCACIA field campaign. The specialised NWP forecast for this campaign predicted a few developing CAOs (see figure 1.4), however it did not generally indicate sharp fronts. Furthermore, the airborne observations from the flights in CAOs do not show signs of a front with a strong secondary circulations.

The initial conditions of the model runs were motivated by the examples of CAO cases from previous field studies (see figure 1.3) as well as cold outbreaks observed during the ACCACIA field campaign. It would be possible to base the control scenarios on some chosen CAO case, however there are some points to consider. On one hand, a scenario directly based on a previous case modelling study could provide a direct comparison for results. On the other hand, most of CAO cases exhibit quite complicated wind profiles and potential temperature profiles in the lower troposphere. While inserting these profiles into a model is simple, it would pose a serious issue in the evaluation of model result. Generally speaking it would be difficult to separate the effect of the surface forcing and the effect of jumps in the initial potential temperature and humidity. While the study is mostly concerned with investigating the impact of heterogeneous surface conditions, the main part of the study consists of idealised model runs. Additional case scenarios are performed with a goal to widen the scope of study on scenarios that are more similar to "real" weather conditions. These case study runs are based on CAO events observed during the ACCACIA field campaign, and their initial conditions are extracted from the regional NWP forecast for this campaign.

The declaration of the surface properties is motivated by surface conditions over MIZs. The spatial heterogeneity is introduced only into the surface temperature (see 1.4). We implement it as a repetitive pattern of both positive and negative anomalies in the surface skin temperature. Since there is not a single ultimate model of the distribution of water

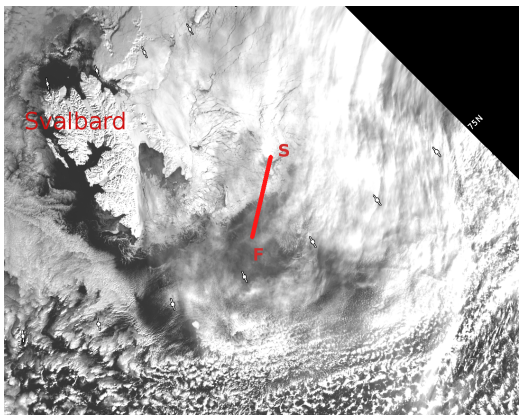

(a) The satellite image of the CAO interlaid with the location of vertical cross-section (b).

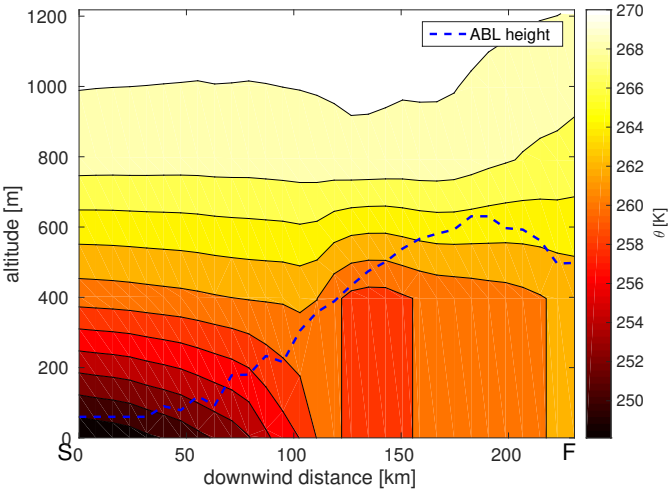

(b) Vertical cross-section of the CAO.

Figure 1.4: The CAO observed on 21 March 2013 during ACCACIA field campaign. The vertical cross-section starting approximately follows the direction of synoptic-scale wind. It starts over sea-ice at **S**– 26.93°E 77.50°N and finish over open sea at **F**– 23.6°E 75.60°N

and sea-ice within an MIZ, a wider variety of temperature anomalies and their spatial extent is considered. Three different types of patterns are considered - two different types representing segments aggregated in the direction along the mean wind, respectively across it, and one representing a chessboard-like pattern of ice segments. Two additional parameters then describe:

- the spatial extent of the anomalies — defined by the length of the pattern block including both positive and negative anomalies
- the temperature scale of the anomaly — defined by the maximum temperature difference between the anomaly and the mean surface potential temperature

The time duration is of the heterogeneity is again motivated by the MIZ properties. The heterogeneities grow abruptly when the air passes over the edge of ice (i.e. the mean surface temperature starts rising), then stay constant over the MIZ, and eventually decline at the end of the MIZ.

The other novel part of this study is the analysis of both the spatial and the temporal variability in the vertical transport of heat and moisture. For this purpose, additional model outputs are required. The time series of the horizontal mean of the sensible and the latent heat flux are recorded at prescribed altitudes. These altitudes are chosen with a goal to represent fluxes just above the surface layer, in the middle part of the mixed layer, an altitude in the cloud layer, and above the clouds.

In summary, the methodology of this study is concerned with both idealised simulations and case simulations of CAO. The novel approach includes the introduction of

different types of surface boundary conditions into LEM, as well as the evaluation of temporal variability in fluxes. Due to to limitations on the boundary conditions and the size of the computational grid, the model is performed in a Semi-Lagrangian framework.

1.6 Thesis Structure

The thesis structure generally follows the principle introduction – methods – results – discussion and conclusions. In this last part of the Introduction, we are going to explain the structure of this thesis. Stress is put both on the logical order of chapters as well as on the connections between them. The structure of the thesis is schematically shown in the figure 1.5. A further description follows.

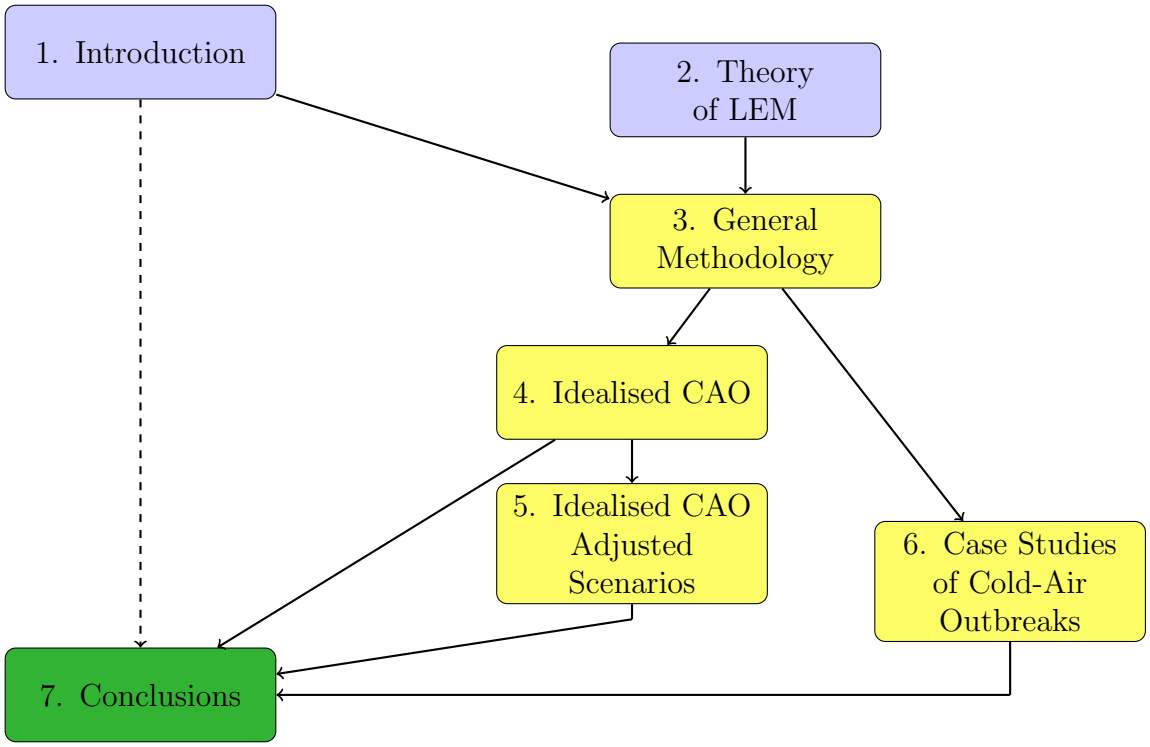

Figure 1.5: The structure of the thesis. A light blues background indicate chapters that are based solely on previous studies, a yellow background background inidicates chapters with new methods and new results, and a green background indicates conclusions. Lines indicate the connection between chapters.

Due to complexity of the modelling studies, Chapter 2 focuses exclusively on the theory behind the modelling software employed - The Met Office Large Eddy Model (LEM). If you are already familiar with the LEM, you may skip this chapter and move forward directly to the methodology presented in Chapter 3. First, it provides the overview of model setting. Second, it describes the main properties of the model scenario and introduces the spatially heterogeneous surface conditions. Then it presents the methods for

the analysis of the LEM results. The issue of model sensitivity is then further addressed. Finally, various possible shortcomings in model setting are discussed. The chapter is rather long, however the size is dictated by the complexity of the study and the necessity to justify the model settings.

Chapter 4 focuses on the impact of the heterogeneous surface forcing on the control scenario. Firstly, it presents the analysis of the control run with homogeneous surface conditions. Then it compares runs with three different types of surface heterogeneity against the control run. Finally, it investigates the impact of modifying the temperature scale and the spatial size of the heterogeneous pattern.

Since the model runs analysed in the Chapter 4 were so far limited just to one specific scenario, Chapter 5 extends the scope of this study to a wider set of idealised CAO scenarios. It investigates the impact of modifying the wind forcing in modifying the initial stratification in the lower troposphere. First, it defines the settings of new scenarios. Second, it presents a qualitative comparison of CBL development between scenarios. The chapter then presents specific results that are different from the results of control scenarios in Chapter 4 or otherwise expanding our knowledge with respect to previous studies.

While the idealised modelling studies might be limited by the simplification employed, Chapter 6 presents the example of a case study using the LEM and the observational data. Firstly, it introduces a CAO observed during the ACCACIA flight missions. Secondly, it shows an extension of the methodology from the Chapter 3. Then it provides the results of the case LEM runs. The results and the limitations of this study are further discussed.

Finally the last chapter, Chapter 7, summarises the progress of this study and draws the conclusions. Furthermore, it summarises the caveats and limitations. It also proposes possible questions for a future research.

Chapter 2

Theory for Large Eddy Model

The progress in atmospheric sciences since the 1960's has been greatly enhanced by advances in computational models. Amongst a wide palette of computational concepts used in atmospheric sciences, Large Eddy Simulation occupies one of the prominent places. A Large Eddy Simulation is a powerful tool for modelling turbulent motions in the atmosphere. It has been widely accepted as an instrumental part of methdology in the research of boundary layers (Stull, 1988, p.424-425). While our study is concerned with the boundary layer during cold air outbreaks, a Large Eddy Simulations is employed in our case as well.

The main idea behind Large Eddy Simulation (LES) concept is that the largest turbulent eddies are resolved (therefore the name) and the effect of smaller eddies is parametrized (Deardorff, 1974). This is also the main difference between LES and direct numerical simulations (DNS). While the DNS is constructed with the assumption of a constant eddy viscosity, it is required to resolve all eddy sizes down to scales where the effect of the dissipations becomes significant (Schaltter and Orlu, 2010). Specific implementation of DNS have been used in the studies of convective boundary layer, including the studies roll convections (Etling and Brown, 1993). DNSs were also extensively used for studies of turbulence affected by heterogeneous surface forcing (Heerwarden et al., 2014). Although DNS offers a deeper insight into the structure of turbulence than LES, it requires very high resolution and large grids just to capture a simple turbulent phenomenon (Salhi and Cambon, 1997). The advantage of LES is that does not resolve computationally expensive smaller scales. Since this study investigates a development of cold-air outbreaks over a pattern of heterogeneities, a LES is the preferred choice.

This chapter explain the theory behind the specific LES software chosen for our study, Met Office *Large Eddy Model* (LEM). A brief review of the background of LES (section 2.1) is followed by an introduction to the chosen LES software package, LEM version 2.4. Following sections further explore the theory of atmospheric modelling behind the LEM and its implementation. First we describe the dynamical core of the LEM (2.3).

Then we continue with describing the domain properties and the treatment of boundary conditions (2.3), the subgrid model for parametrizing unresolved phenomena (2.4) and the surface model (2.5). Finally we briefly review the topic of numerical methods in LEM and their stability (2.6).

The nature of this chapter is purely theoretical and it does not show any new information. However it is essential for establishing the methodologogy of this study. Therefore if you are already familiar with the LEM, you may skip this chapter and move forward directly to the methodology presented in the next chapter.

2.1 Brief Review of Large Eddy Simulations

Large Eddy Simulation (LES) is a powerful computational tool for modelling of various boundary layer phenomena. In this part of the chapter, we briefly describe the principles that LES built on and provide some examples of the capabilities of various LEM packages.

While the largest eddies are generated by convection or mechanically by wind shear, the grid resolution in horizontal and vertical direction must be chosen accordingly. This often requires a careful consideration, as the mechanically generated eddies are significantly smaller, especially in the case of strong stratification that suppress larger vertical motions (Arnal and Friedrich, 1992). Generally speaking, the LES resolution should be chosen in the way that unresolved scales are within the inertia subrange of the turbulence (Pope, 2004). Since LES does not resolve computationally expensive smaller scales, the effect of eddies on these scales then have to be parametrized. Various advanced subgrid models have been developed to fulfil this task (Love and Leslie, 1979). While describing the theory of turbulence closure is far beyond the scope of this study, we will rather look at one specific example of the subgrid model in the part 2.4.

Part of the boundary conditions in LES are not prescribed, but computed by separate routines. This usually applies to the surface layer, where the surface fluxes are modelled by surface parametrization that is mostly based on Monin-Obukhov theory (Monin and Obukhov, 1954). The top boundary of the model domain is usually rigid and supplemented with a damping layer that weakens motions propagating upwards, diminishing the effect of waves that would otherwise be reflected by the rigid lid boundary.

In recent decades, there have been a number of LES software packages (Siebesma et al., 2003, p.1217) (Beare et al., 2006, pp. 251-263) developed by various research institutions. A brief list follows in 2.1. The WRF, which has been increasingly popular since mid 2000's, also allows a LES setting with a fine grid, explicitly resolved convective

eddies and subfilter-scale stress model. (Kirkil et al., 2012). The nesting of the LES into the mesoscale models (Talbot et al., 2012) allowed to simulate various mesoscale phenomena, such as turbulence developing in the offshore winds (Muñoz-Esparza et al., 2014). More information about various LES models can be found in (Siebesma et al., 2003) and (Beare et al., 2006).

• CSU	Colorado State University
• IMUK	Univerisity of Hannover
• KNMI	Royal Netherlands Meteorological Institute
• LBNL/UW	Lawrence Berekely National Laboratory / University of Washington
• LEM	Met Office, UK
• LLNL	Lawrence Livermore National Laborator
• MPI	Max Planck Institute for Meteorology
• NCAR	National Centre for Atmospheric Research, US
• NERSC	National Energy Research Scientific Computing Center, US
• RAMS	Colorado State University
• UCLA	University of California, Los Angles
• UIB	Universitat de les Illes Bale
• UOK	University of Oklahoma
• WU	Wageningen university
• WVU	West Virginia University

Table 2.1: List of LES software packages from various institutions (not complete)

2.2 Large Eddy Model

From a selection of various LES that are currently used in atmospheric research, we have selected *Met Office Large Eddy Model* (LEM) due to its well documented scientific part (Gray et al., 2004), an advanced treatment of model dynamics and viscosity, full three-phase microphysics with a number of hydrometeor conversions and interactive radiation code (Gray and Petch, 2004, pp.5-9). The other advantage of LEM is a wide selection of diagnostic outputs.

2.2.1 The Background of LEM

LEM was originally designed to expand LES capabilities for very fine grids. The computational power in the middle of the 1980's did not allow successful LES of stable boundary layers (Stull, 1988, p.452), but became available around 1990 due to increase in the power of supercomputing clusters together with development of a better description of a stable boundary layer (Derbyshire, 1990) and subgrid models (Chasnov, 1991).

Since the beginning of its development at the end of 80's (Mason, 1989) the LEM has been used extensively for modelling of number of boundary-layer phenomena, ranging from simple simulations of a turbulence in a dry neutral boundary layer (Gray and Petch, 2004, p.46) to advanced simulations based on scenarios from number of field experiments, such as trade wind cumuli in BOMEX flight mission (Brown, 1999a). Further modifications of LEM allowed modelling of radiative fog and the effect of surface temperature anomalies in the stable boundary layer (Porson et al., 2011).

The LEM has been used in a development of new boundary layer schemes for The Met Office Unified Model (MetUM) (Lock and Edwards, 2013), where it was together with advanced cloud resolving models applied to modelling of various boundary layer types (Lock et al., 2000, pp.3190-3191). LEM has been thoroughly tested in a number of regimes. It has performed well against various other LES software packages in the intercomparison studies for neutrally stratified boundary layer (Andren et al., 1994), convective boundary layer (Siebesma et al., 2003, pp.1217–1218), and stably stratified boundary layer (Beare et al., 2006, pp.251–263).

The effect of the eddy cascade into unresolved scale was a motivation for the development of the LES backscatter (Brown et al., 1994) based on the improved stochastic backscatter of Mason and Thompson (Mason and Thompson, 1992). Recent research (Weinbrecht and Mason, 2008) has offered the modification of the backscatter for the CBL, including the setting with anelastic pressure approximation, however there are number of issues with the setting of the tuning coefficients and overall implementation (Weinbrecht and Mason, 2008, pp.137–138).

The current operational version of the LEM is *2.4*. The new development stage called *Met Office-NERC Cloud Model* (MONC) is scheduled to be released during the autumn 2015 (NERC, 2014). It is expected to further improve the cloud microphysics schemes as well as to offer easier modularisation and user extensions.

2.3 Dynamics in LEM

The central concept of the dynamical core of LEM is approximative solution of the primitive equations based on filtering the motions into resolved component and *"subfilter"* (subgrid) component (Mason, 1994, pp.2-3).
Denoting the Lagrangian derivative

$$\frac{D}{Dt} = \left(\frac{\partial}{\partial t}\right) + u_i \left(\frac{\partial}{\partial x_i}\right), \tag{2.1}$$

where u_i is the velocity of flow, the *basic equation* set of the LEM is in the tensor notation (Gray et al., 2004, pp.2–3):

$$\frac{\partial}{\partial x_i}(\rho_r\, u_i) = 0, \tag{2.2a}$$

$$\frac{Du_i}{Dt} = -\frac{\partial}{\partial x}\left(\frac{p'}{\rho_r}\right) + \delta_{i,3}\, B' + \frac{1}{\rho_r}\frac{\partial \tilde{\tau}_{i,j}}{\partial x_j} - 2\varepsilon_{i,j,k}\,\Omega_j\, u_k, \tag{2.2b}$$

$$\frac{D\theta'}{Dt} = \frac{1}{\rho_r}\frac{\partial h_i^{(\theta)}}{\partial x_i} + \left(\frac{\partial \theta}{\partial t}\right)_{(\text{mphys})} + \left(\frac{\partial \theta}{\partial t}\right)_{(\text{rad})}, \tag{2.2c}$$

$$\frac{Dq_n}{Dt} = \frac{1}{\rho_r}\frac{\partial h_i^{(q_n)}}{\partial x_i} - \left(\frac{\partial q_n}{\partial t}\right)_{(\text{mphys})}, \tag{2.2d}$$

where $\delta_{i,3}$ is Kronecker delta, $\varepsilon_{i,j,k}$ is Levi-Civita symbol and the other symbols represent:

ρ_r	reference state of the air density ρ
u_i	components of the vector of air velocity $\boldsymbol{u}$
p'	pressure perturbation (explained further)
B'	buoyancy
$\tilde{\tau}_{i,j}$	component of subgrid stress tensor (further explained in 2.4)
Ω_j	components of the angular velocity of the Earth (f-plane approximation for given latitude)
θ	potential temperature
$h_i^{(\theta)}$	components of subgrid flux of potential temperature (further explained in 2.4)
$\left(\frac{\partial \theta}{\partial t}\right)_{(\text{mphys})}$	the source term of potential temperature due to microphysical processes
$\left(\frac{\partial \theta}{\partial t}\right)_{(\text{rad})}$	the source term of potential temperature due to radiation
q_n	other scalar quantities
$h_i^{(q_n)}$	components of subgrid flux of the scalar quantity q_n
$\left(\frac{\partial q_n}{\partial t}\right)_{(\text{mphys})}$	the source term of the q_n due to microphysical processes

The LEM approximates the solution of these equation on the neighbourhood of the *reference state*. The definition of the reference state varies based on the scheme for pressure approximation. In the setting of the Boussinesq-type approximation, the reference state is characterised by scalar constants ρ_r, p_r and θ_r for the density, pressure and the potential temperature. While Boussinesq-type approximation is constructed under the assumption of a shallow model domain, such setting would be unsuitable for studies with deep stratified domain. The other option provided is *anelastic approximation for pressure* (Durran, 1989). In the anelastic approximation, the reference state is characterised by reference vertical profiles $\rho_r(z), p_r(z), \theta_r(z)$.

The main prognostic variables of LEM are three components u, v, w of the air flow velocity $\boldsymbol{u}$, potential temperature perturbation θ' and other scalar variables q_n such as water mixing ratio. Since $\theta = \theta_r + \theta'$, the equation (2.2c) is then rewritten as:

$$\frac{D\theta'}{Dt} = \underbrace{-w\,\frac{\mathrm{d}\theta_r}{\mathrm{d}x_3}}_{\text{I}} + \underbrace{\frac{1}{\rho_r}\,\frac{\partial h_3^{\theta_r}}{\partial x_3}}_{\text{II}} + \underbrace{\frac{1}{\rho_r}\,\frac{\partial h_i^{(\theta')}}{\partial x_i}}_{\text{III}} + \underbrace{\left(\frac{\partial \theta'}{\partial t}\right)_{(\text{mphys})}}_{\text{IV}} + \underbrace{\left(\frac{\partial \theta'}{\partial t}\right)_{(\text{rad})}}_{\text{V}}, \tag{2.3}$$

where the terms **I** and **II** account for the contribution to the resolved and subgrid fluxes due to differences in the vertical profile of the reference potential temperature. Term **III** then covers contribution of subgrid fluxes due to potential temperature perturbations. In the Boussinesq approximation, terms **I** and **II** disappear due to θ_r being constant.

The buoyancy term B' is defined as

$$B' = g\frac{\theta'_v}{\theta_r}, \tag{2.4}$$

where the perturbation θ'_v of the virtual potential temperature from its basis state is used purely as a measure of buoyancy. The virtual potential temperature here is defined as

$$\theta_v \equiv \frac{p}{R\,\rho\left(\frac{p}{p_0}^{R/c_p}\right)}. \tag{2.5}$$

While the density is not a prognostic variable in LEM (Gray et al., 2004, p.4), the perturbation in virtual potential temperature is instead computed as

$$\theta'_v = \theta' + \theta_r\, c_n\, q_n, \tag{2.6}$$

where c_n is a coefficient denoting the impact of the scalar quantity q_n on the virtual potential temperature.

The microphysics production-consumption terms in the equations (2.2c) and (2.2d)

are calculated by selected microphysics parametrization. There are number of options for warm rain, however they would not allow us to model mixed-phase clouds in CAO (Zuidema et al., 2005) (Morrison et al., 2009). The three-phase microphysics parametrization in LEM combines single-moment and double-moment schemes described by Lin et al. (1983) and Rutledge and Hobbs (1983). The parametrization schemes were further enhanced (Gray et al., 2004, pp.17–37). The treatment of the cloud ice was added based the parametrization scheme of Flatau (1989) for the RAMS model that was extensively used in number of fine-resolution studies (Hosannah and Jorge, 2014). The treatment of snow and graupel number concentrations is mostly based on the bulk ice schemes of Ferrier (1994) and Ferrier et al. (1995). In the current version 2.4 of the LEM, cloud and hydrometeor processes are represented by 36 different conversion terms (Gray et al., 2004, p.22) and the alternative settings of the microphysics constants are specified in (Gray et al., 2004, pp.48–49).

The radiation terms in the equation (2.2c) are computed by the Edwards-Slingo radiation code (Edwards and Slingo, 1996) , the same scheme is used in the MetUM (Cullen, 1993). The optical properties of the atmosphere above the model domain are calculated from supplemented Mcclatchey profiles of temperature, water vapour concentration and ozone concentration (McClatchey et al., 1971). However, the implementation of the Edward-Slingo radiation code in LEM differs from MetUM in the treatment of the snow and graupel impact on the scattering of radiation, since the LEM classifies hydrometeors into more categories than the MetUM does (Gray et al., 2004, p.38). The adjustment of calculations is based on the work Petch (1998). The treatment of the optical properties is based on studies Edwards and Slingo (1996) and Slingo and Schrecker (1982).

2.3.1 Model Domain and Boundary Conditions

The LEM allows both 2-dimensional (horizontal y-axis vertical z-axis) and 3-dimensional models. For the study of the turbulent boundary layer, the later is more suitable. The domain shape is the rectangular cuboid. The model grid is regular, with the horizontal grid spacing being constant, but permitting a different setting for grid spacing in the direction of x-axis and y-axis. The grid spacing in the vertical direction could vary with height, allowing more densely packed gridpoints at the altitudes where the main resolved features are expected (discretisation of the grid is described in 2.6).

The horizontal boundary conditions are periodic in all the main prognostic variables. The top and bottom of the domain are rigid lid boundaries, The treatment of the heat exchange and wind stress on the bottom boundary is further described in the section 2.5. While the top boundary should represent the effect of the other layers of the air

above, this is achieved by two techniques:

- Adding the *large scale subsidence*, i.e. directly setting the values w on the top model level, where the vertical wind velocity would be otherwise 0. (Gray and Petch, 2004, p.15)

- Adding a *Newtonian damping layer* in the upper part of the model domain to prevent the reflection of the gravity waves on the top rigid lid (Kanak et al., 2000).

The main principle of the Newtonian damping layer is relaxation of the values of the prognostic variables towards their horizontal mean values (Khairoutdinov et al., 2009) (Stevens et al., 2005). For the damping layer of the thickness $H_{(\mathrm{DL})}$ starting at the altitude $z_{(\mathrm{DL})}$, the damping term for each prognostic variable φ is given as (Gray et al., 2004, p.13)

$$\left(\frac{\partial \varphi}{\partial t}\right)_{(\mathrm{DL})} = \frac{-1}{\tau_{(\mathrm{DL})}} \left(\exp\left(\frac{z - z_{(\mathrm{DL})}}{H_{(\mathrm{DL})}}\right) - 1 \right) \left(\varphi - \bar{\varphi}\right), \tag{2.7}$$

where $\bar{\varphi}$ is a horizontal mean of the prognostic variable φ, and $\tau_{(\mathrm{DL})}$ is a damping timescale of the model. In the current version of LEM, the damping is applied in the source terms of all prognostic variables in the region of the damping layer. The main guidelines regarding the choice of parameters $\tau_{(\mathrm{DL})}$ and $H_{(\mathrm{DL})}$ are to set the $H_{(\mathrm{DL})}$ higher than the longest vertical wavelengths of observed gravity waves and to set $\tau_{(\mathrm{DL})}$ larger than the expected timestep of the dynamical core of the model.

While the type of boundary conditions described are well suited for modelling turbulence over a uniform surface, it brings also some limitation. It does not allow modelling scenarios with the prescribed properties of the air on the inflow and the outflow. However, it is still possible to supplement a large scale pressure forcing by defining the large scale geostrophic wind. Thermal wind can be supplemented by specifying the vertical geostrophic shear. (Gray et al., 2004, p.6)

2.4 Subgrid Model in LEM

One important concept of LES is the treatment of eddy spectra. While only the larger eddies are resolved, the effect of the turbulent transport on unresolved levels is parametrized (Lilly, 1967). A detailed explanation of the theory behind the treatment of sub-filter scales in LES would be far beyond the scope of this study. Therefore, in this part of the thesis, we focus just on the main concept of the subgrid parametrization in LEM.

The subgrid model of LEM is based on the work of Derbyshire (1994) and Brown et al. (2008), while the sensitivity of the turbulent shear flows to subgrid models in LES was further analysed by Brown (1999b). The effect of eddies on unresolved scales are modelled as subgrid stress $\tilde{\tau}_{i,j}$ and subgrid fluxes $h_i^{(\varphi)}$ of each scalar quantity φ from the set θ', θ_r, q_n. The subgrid stress is specified as

$$\tilde{\tau}_{i,j} = \rho_r \, \nu_m \, \mathbb{S}_{i,j}, \tag{2.8}$$

where ν_m is a subgrid eddy-viscosity and $\mathbb{S}$ is the rate of strain tensor, i.e.

$$\mathbb{S}_{i,j} = \frac{\partial u_i}{\partial x_j} + \frac{\partial u_j}{\partial x_i}. \tag{2.9}$$

Similarly, the scalar flux h_i^{φ} is specified as

$$h_i^{\varphi} = -\rho_r \, \nu_h \, \frac{\partial \varphi}{\partial x_i}, \tag{2.10}$$

where ν_h is a subgrid eddy-diffusivity for scalars and $\mathbb{S}$ is the rate of strain tensor. Based on the extension of Smagorinsky-Lilly approach (Gray et al., 2004, pp.6–7), ν_m and ν_h are prescribed as

$$\nu_m = \lambda^2 \, S \, f_m(Ri_p), \tag{2.11a}$$

$$\nu_h = \lambda^2 \, S \, f_h(Ri_p), \tag{2.11b}$$

where λ is the mixing length, f_m and f_h are functions of the *pointwise Richardson number* Ri_p, and S is the modulus of the tensor $\mathbb{S}$. The specification of f_m, f_h and λ is explained further.

With a goal to provide a smooth transition between the interior of the flow where the mixing length is constant $\lambda = \lambda_0$ and the levels near the ground where the impact of surface eddy mixing linearly depends on the distance from the surface, the λ is specified following Mason and Thompson (1992) as:

$$\frac{1}{\lambda^2} = \frac{1}{\lambda_0^2} + \frac{1}{\left(\kappa \, (z + z_0)\right)^2} \tag{2.12}$$

In this equation, κ is the von Kármán constant and z_0 is the aerodynamic mixing length. The classical Smaroginski-Lilly approach usually specifies λ_0 as

$$\lambda_0 = c_{(\mathrm{S-L})} \, \Delta_{(\mathrm{gh})} \tag{2.13}$$

where $\triangle_{(\mathrm{gh})}$ is the grid spacing in horizontal direction and $c_{(\mathrm{S-L})}$ is a constant (Canuto and Cheng, 1997). The resulting profile of λ is shown in the figure 2.1

The choice of the value of Smagorinsky-Lilly constant $c_{(\mathrm{S-L})}$ is often questioned. The

LEM documentation suggest that the value of *" 0.23 is usually considered desirable"* (Gray et al., 2004, p.7), which is in a good agreement with Lilly (1966). The proposed value of original coefficient for the subgrid eddy viscosity in the early numerical simulation of the primitive equations was 0.28 Smagorinsky (1963). The evaluation of the theory of eddy-viscosity lead to the approximation 0.23 (Lilly, 1966). However, Lilly later adjusted the approximation to 0.21, and subsequently to 0.2 (Deardorff, 1971).

Generally speaking, numerical simulations have mostly used value of $c_{(\mathrm{S-L})}$ in the range 0.2–0.22 (Canuto and Cheng, 1997). Later theoretical and model analysis showed that these values give a reasonable results in simulations where the turbulence is generated by surface driven thermal convection. However in case of the turbulence generated by large-scale wind shear, a significantly smaller values of 0.13 was deemed necessary (Deardorff, 1971). A number of other model studies suggested that the value 0.2-0.22 is significantly higher than required if the effect of the stratification and shear are taken into account (Hunt, 1988). Under the assumption of homogeneous shear and a local dynamic equilibrium, the value $c_{(\mathrm{S-L})}$ is approximated as 0.11 (Canuto and Cheng, 1997). However, even this value is not universal, and is expected to differ depending on the properties of the flow. Moreover, the approximation $c_{(\mathrm{S-L})}$ might be influenced by various other phenomena. It is very likely that that the effect of subgrid scales is also influenced by inhomogeneities in the forcings (Love and Leslie, 1979).

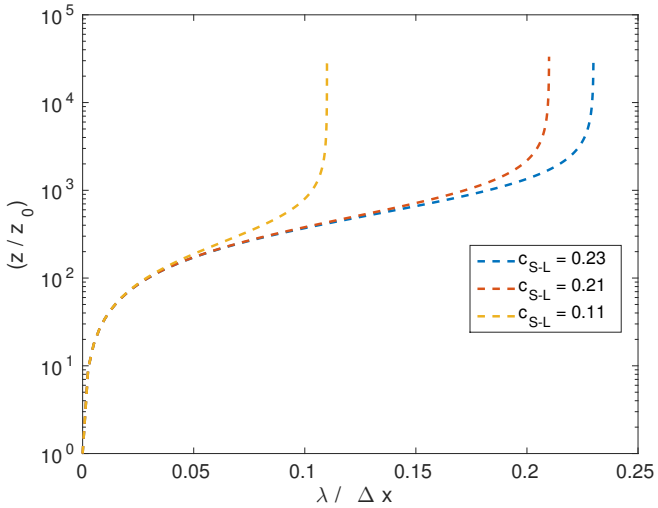

Figure 2.1: The vertical profile of the mixing length for different settings of the Smagorinsky-Lilly constant $c_{(\mathrm{S-L})}$

The pointwise Richardson number Ri_p is a non-dimensional number defined as

$$Ri_p = \frac{1}{S}\frac{\partial B}{\partial z}, \tag{2.14}$$

where B is the buoyancy and S is the modulus of the tensor $\mathbb{S}$. While turbulence persists for the lower values of the Richardson number and diminishes for the higher values of the Richardson number (Stull, 1988, pp.177-178), dependent function f_m and f_h are set to accordingly modify the subgrid eddy-viscosity and eddy-diffusivity. The exact definition (Gray et al., 2004, pp.7–8) goes as follows in table 2.2, where Ri_c is the critical Richardson number, conventionally set to 0.25 (Stull, 1988, pp.177-178). The constants $a_p, b_p, c_p, f_p, g_p, h_p$ and r_p are subgrid constants set accordingly to expected properties of the atmosphere (see figure 2.2). In this study, the default LEM settings defined in Gray et al. (2004, p.8) were employed.

function	interval		
	$Ri_p < 0$	$0 \leq Ri_p < Ri_c$	$Ri_p \geq Ri_c$
$f_m :=$	$\left(1 - c_p\, Ri_p\right)^{1/2}$	$\left(1 - \frac{Ri_p}{Ri_c}\right)^r \left(1 - h_p\, Ri_p\right)$	0
$f_h :=$	$a_p \left(1 - b_p\, Ri_p\right)^{1/2}$	$a_p \left(1 - \frac{Ri_p}{Ri_c}\right)^r \left(1 - g_p\, Ri_p\right)$	0

Table 2.2: Functions of the pointwise Richardson number

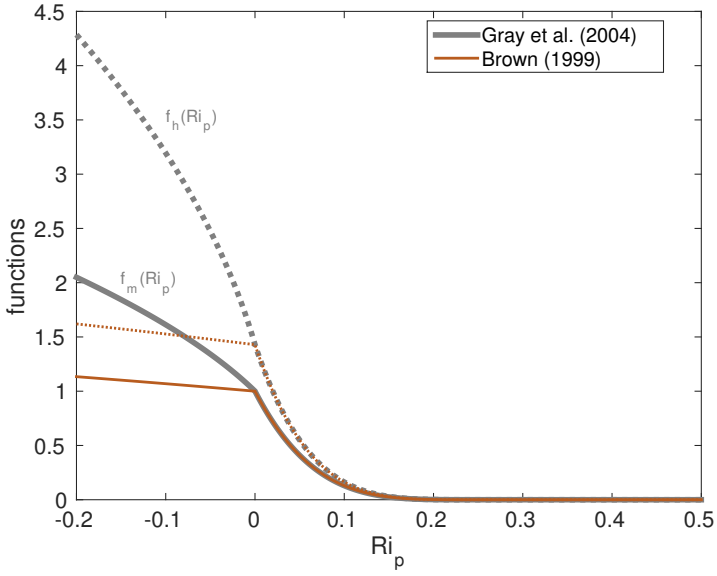

Figure 2.2: The graph of functions f_m and f_h that characterise the eddy-viscosity in the LEM subgrid model. Two common choices of the definition of these functions are shown: the default variant (Gray et al., 2004) and the alternative setting used in previous studies such as (Brown, 1999b)

2.5 Surface Model in LEM

An important component of a LES is the surface-air exchange. This part of the chapter explains the surface model used in LEM. Firstly, we briefly review the setting of the surface available in LEM. Secondly, we describe the case where the surface parametrization is applied. The subsequent paragraphs are then concerned with techniques for the evaluation of the surface model.

There are few options for the description of surface conditions, or to be precise, conditions on the lower model boundary. The first possibility are no additional boundary conditions apart from the $w = 0$. This option is used in model scenarios that do not start at the ground, such as simulations of decoupled stratocumulus (Gray and Petch, 2004, p.46). For other scenarios, it is more suitable to evaluate the aerodynamic drag based on Monin-Obukhov theory and directly prescribe the values of the surface sensible heat and latent heat flux. This approach was employed also in the previous study of CAO by Kershaw (1995). Finally, the LEM offers to parametrize the surface heat and moist exchange by Monin-Obukhov theory as well. Surface conditions are then set as the values of temperature and humidity of the surface microlayer together with the parameter of the aerodynamic roughness length for scalars. We are going to focus on this set up.

The surface scheme used in LEM is a modified version of the surface scheme proposed by Bull and Derbyshire (1990). This scheme is derived from Monin-Obukhov theory under the assumption that similarity functions and roughness lengths for temperature and water vapour mixing ratio are the same. The surface acts on the resolved wind fields through frictional wind stress and on the resolved potential temperature and water content fields through sensible and latent heat fluxes respectively. To link the surface model with the subgrid model, surface exchange phenomena are expressed in the viscous terms as

$$\nu_{m,s}\,\frac{\partial u_i}{\partial z},\quad \nu_{h,s}\,\frac{\partial \theta}{\partial z}\quad \text{and}\quad \nu_{h,s}\,\frac{\partial q_n}{\partial z}$$

The wind speed $U = \sqrt{u^2 + v^2}$ reaches zero at the height of $z = z_0$, the aerodynamic roughness length. Similarly, potential temperature θ reaches the temperature of the skin surface layer at the height $z = z_{0,\theta}$, the roughness length for scalars (Gray and Petch, 2004, p.9). While the surface stress is defined in the kinematic terms as $u_\star^2$, and upward temperature flux at the surface as $-u_\star\theta_\star$, surface-layer viscosity $\nu_{m,s}$ and diffusivity $\nu_{h,s}$ can be written in the form

$$\nu_{m,s} = \frac{u_\star^2 \, z_1}{U_1}, \tag{2.15a}$$

$$\nu_{h,s} = \frac{u_\star^2 \, \theta_\star \, z_1}{\theta_1 \, - \, \theta_{\text{surf}}}, \tag{2.15b}$$

where θ_1 and U_1 denote temperature and wind speed at z_1, the first grid level above the surface (which is `ZN(2)` in the LEM source code). Therefore the problem is reduced to approximating the values $u_\star$ and $\theta_\star$.

Recalling that the full surface exchange parametrization model is derived from the Monin-Obukhov similarity theory, $u_\star$ and $\theta_\star$ are present in the equations for local gradients

$$\frac{\partial U}{\partial z} = \frac{u_\star}{\kappa \, z} \, \phi_m \left(\frac{z}{L} \right), \tag{2.16a}$$

$$\frac{\partial \theta}{\partial z} = \frac{\theta_\star}{\kappa \, z} \, \phi_m \left(\frac{z}{L} \right), \tag{2.16b}$$

where κ is the von Karman constant, L is the Monin-Obukhov length, while $\phi_m(\frac{z}{L})$ and $\phi_h(\frac{z}{L})$ are Businger–Dyer functions (Stull, 1988, pp.383-384). Monin-Obukhov length is defined as:

$$L = \frac{u_\star^2}{g\kappa} \, \frac{\theta_r}{\theta_\star}, \tag{2.17}$$

while Businger-Dyer functions are in the empirical form (Dyer, 1974) defined as:

$$\phi_m = \begin{cases} 1 + \beta_m \, \dfrac{z}{L} & L \geq 0 \\ \left(1 - \gamma_m \, \dfrac{z}{L} \right)^{-1/4} & L < 0 \end{cases} \tag{2.18a}$$

$$\phi_h = \begin{cases} \alpha_h + \beta_h \, \dfrac{z}{L} & L \geq 0 \\ \alpha_h \left(1 - \gamma_h \, \dfrac{z}{L} \right)^{-1/2} & L < 0 \end{cases} \tag{2.18b}$$

where α_h, β_h, β_m, γ_h and γ_m are empirical constants. The standard setting of these constants is given in (Gray et al., 2004, p.13).

The gradient equations (2.16) are then integrated from z_0 to z_1 to obtain the expressions in the algebraic form. While stable and convective conditions require different treatment, a high priority is given to the classification of neutral, stable and convective areas of the surface layer (Gray et al., 2004, pp.16–18). In each timestep before the surface exchange computation, the buoyancy of the surface air is computed separately for each gridpoint and the surface column is classified accordingly.

- In the trivial case of neutral stratification in the column, the limit values of $\phi_m(\frac{z}{L})$ and $\phi_h(\frac{z}{L})$ reach 1. This the lead to simple relation for the $u_\star$ (Beljaars and Holtslag, 1991):

$$u_\star = \frac{\kappa\, U_1}{\log\left(\frac{z_1}{z_0}\right)} \tag{2.19}$$

  and the $\theta_\star$ is set to 0.

- For stable conditions, the integration of gradient equations is given by Monin and Yaglom (1971) and Holtslag and De Bruin (1988). Explicit relations for $u_\star$ and $\theta_\star$ then yield (Bull and Derbyshire, 1990) in the form

$$u_\star = \frac{\kappa\, U_1}{\log\left(\frac{z_1}{z_0}\right) + \beta_m \left(\frac{z_1 - z_0}{L}\right)} \tag{2.20a}$$

$$\theta_\star = \frac{\kappa \left(\theta_1 - \theta_{\text{surf}}\right)}{\alpha_h \log\left(\frac{z_1}{z_0}\right) + \beta_h \left(\frac{z_1 - z_0}{L}\right)} \tag{2.20b}$$

  Since L in (2.17) is a function of $u_\star$, the direct substitution into (2.20a) leads to a polynomial equation for $u_\star$. The higher root of this equation is then directly calculated.

- Corresponding relations for $u_\star$ and $\theta_\star$ in the convective case are slightly more complicated. The integration of gradient equations (2.16), leads to the expressions

$$u_\star = \frac{\kappa\, U_1}{\log\left(\frac{z_1}{z_0}\right) - \psi_m} \tag{2.21a}$$

$$\theta_\star = \frac{\kappa \left(\theta_1 - \theta_{\text{surf}}\right)}{\alpha_h \left(\log\left(\frac{z_1}{z_{0,\theta}}\right) - \psi_h\right)} \tag{2.21b}$$

  where ψ_m and ψ_h are functions of $\frac{z}{L}$; the function ψ_m is obtained by the integration

of ϕ_m following Panofsky (1963):

$$\psi_m\left(\frac{z}{L}\right) = \int_0^{-\frac{z}{L}} \frac{1 - \phi_m(\xi)}{\xi}\,\mathrm{d}\xi \tag{2.22}$$

and the approach for ψ_h is analogous.

Following the integration described by Paulson (1970), the functions ψ_m and ψ_h yield

$$\psi_m = 2\log\left(\frac{\tilde{x}_1+1}{\tilde{x}_0+1}\right) + \log\left(\frac{\tilde{x}_1^2+1}{\tilde{x}_0^2+1}\right) + 2\left(\tan^{-1}\tilde{x}_0 - \tan^{-1}\tilde{x}_1\right) \tag{2.23a}$$

where

$$\tilde{x}_1 = \left(1-\gamma_m\frac{z_0}{L}\right)^{1/4} \quad \text{and} \quad \tilde{x}_1 = \left(1-\gamma_m\frac{z_1}{L}\right)^{1/4} \tag{2.23b}$$

and

$$\psi_h = 2\log\left(\frac{\tilde{y}_1+1}{\tilde{y}_0+1}\right) \tag{2.24a}$$

where

$$\tilde{y}_0 = \left(1-\gamma_h\frac{z_{0,\theta}}{L}\right)^{1/2} \qquad \text{and} \qquad \tilde{y}_1 = \left(1-\gamma_h\frac{z_{1,\theta}}{L}\right)^{1/2} \tag{2.24b}$$

The solution for $\theta_\star$ and $u_\star$ in the convective case is approximated using the iterative procedure (Gray et al., 2004, p.74). Results are then stored in a look up table to be used as the initial value in for the iteration in the next timestep. This helps to reduce expensive calculations in each timestep (Gray et al., 2004, p.13).

2.6 Numerical Methods in LEM

An essential part of each numerical model is a suitable choice of the model grid and the computational schemes. In this part of the chapter, we briefly review numerical methods used in LEM. Firstly, we describe the model grid. Secondly, we describe the main rules for calculation and the conditions for stability. Finally, we briefly explain two advection schemes used in LEM.

The computational core of the LEM is designed to integrate the equations from the basic set (2.2a) along with computing the parametrizations for turbulence, radiation and microphysical processes. The model variables are discretised on a grid — in the horizontal layers is employed the *Arakawa C grid* (Arakawa and Lamb, 1977, pp.180–182) and in vertical is employed the *Lorenz grid* (Holdaway et al., 2013, pp.1075–1076). This results in a situation where each velocity component is staggered in its own direction while pressure p, potential temperature perturbation $\theta'$and scalars q_n are held on the centre point of the grid cell, as shown in the figure 2.3.

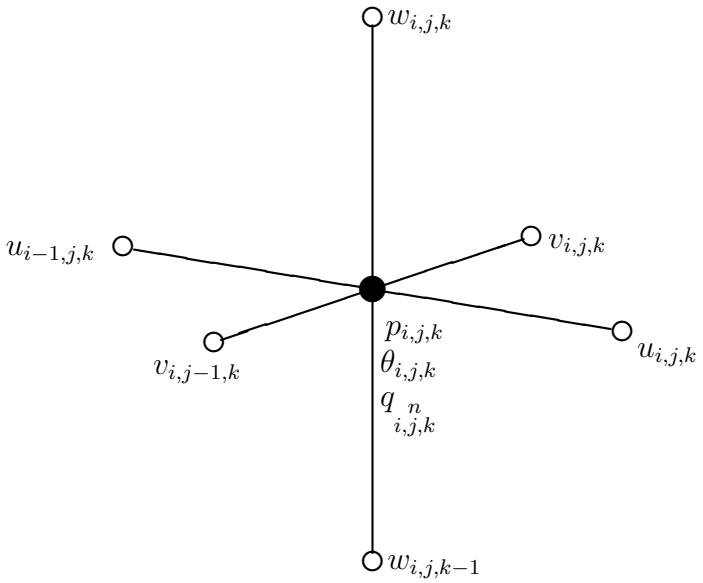

Figure 2.3: The scheme of the LEM discretisation, showing the relative position of main variables. Based on (Gray et al., 2004, p.39) and (Holdaway et al., 2013, p.1075)

Time integration in the LEM can be performed both with forward and centred time stepping. The majority of source terms on the right hand sides of equations (2.2a) are computed in parallel with the exception of the microphysics source terms that are calculated sequentially to other source terms (Gray et al., 2004, p.39). In order to maintain numerical stability, the length of the time step is constrained by the *Courant-Fridrichs-Lewy* (CFL) condition (Courant et al., 1967) for both the advection schemes and the viscosity. The numerical instabilities caused by the hydrometer fall velocities or the damping layer are not considered.

For the stability in advection schemes, all gridpoint velocities must remain in the numerically stable region. While the worst cases in each direction are considered, the resulting the largest advective Courant number (CVEL) is given as

$$\mathrm{CVEL} = \Delta t \left(\left(\frac{|u|}{\Delta x} \right)_{\substack{\max \\ \text{domain}}} + \left(\frac{|v|}{\Delta y} \right)_{\substack{\max \\ \text{domain}}} + \left(\frac{|w|}{\Delta z} \right)_{\substack{\max \\ \text{domain}}} \right) \tag{2.25}$$

In a similar manner, the worst cases in each direction are considered in determining the viscous stability parameter (CVIS), hence

$$\mathrm{CVIS} = \max_{\mathrm{domain}} \left(4\,\Delta t\ \max\left(\nu_m,\, \nu_h\right) \left(\frac{1}{\left(\Delta x\right)^2} + \frac{1}{\left(\Delta y\right)^2} + \frac{1}{\left(\Delta z\right)^2} \right) \right) \tag{2.26}$$

The maximum permitted values of the CVEL and CVIS are specified in the model setting as $\mathrm{CVEL}_{(\max)}$ and $\mathrm{CVIS}_{(\max)}$. The CFL number, defined as

$$\mathrm{CFL} = \frac{\mathrm{CVIS}}{\mathrm{CVIS}_{(\max)}} + \frac{\mathrm{CVEL}}{\mathrm{CVEL}_{(\max)}} \tag{2.27}$$

is calculated (Gray et al., 2004, p.38). To maintain the numerical stability, the value of $\mathrm{CVEL}_{(\max)}$ must be set to less than one, while the recommended value for $\mathrm{CVIS}_{(\max)}$ is 0.2 (Derbyshire, 1994).

2.6.1 Advection Schemes

For the calculation of the advection terms, the LEM offers the choice between two advection schemes, the centred difference *Piascek–Williams scheme* (P–W) and the total variation diminishing (TVD) scheme known as *ULTIMATE*. The standard approach in the LEM is to apply the P–W scheme in the prognostic equation for momentum and the ULTIMATE in the prognostic equations for thermodynamic variables (Shutts and Palmer, 2007). In the following paragraphs, we will briefly describe both schemes and their advantages.

The P–W is a centred difference scheme where the flux advection term for the gridbox with indices i, j, k is defined as

$$\left[\frac{\partial}{\partial x}\left(u\,\varphi\right)\right]_{i,j,k} = \frac{1}{\Delta x}\left(u_{i,j,k}\,\frac{\varphi_{i+1,j,k} - \varphi_{i,j,k}}{2} - u_{i-1,j,k}\,\frac{\varphi_{i,j,k} - \varphi_{i-1,j,k}}{2} \right) \tag{2.28}$$

The scheme was shown to conserve φ^2, but it is not positive definite (Piacsek and Williams, 1970). Despite relative simplicity, the scheme exhibits a number of advantages, including relatively good numerical stability (Schemm, 1974). It has been used in wide range of model studies, such as study of the flow around mountain ridges (Wells et al., 2005) and the study of impact of spatial variability on the marine bondary layer (Wai, 1988).

Before we step to the description of the ULTIMATE scheme, we briefly explain the TVD property. We recallthe definition of the total variance in the prognostic variable φ

(Harten, 1983)

$$TV(\varphi) = \sum_{j=-\infty}^{+\infty} \left| u_{j+1} - u_{j+1} \right|. \tag{2.29}$$

The numerical scheme is said to be TVD if there exist a time t_1 such that

$$TV(\varphi(t_2)) \leq TV(\varphi(t_1))) \qquad \forall t_2 \geq t_1 \tag{2.30}$$

The TVD schemes provide a number of advantages (Van Leer, 1974). Here we list the main ones:

- The schemes do not change near a boundary. Therefore, exact boundary conditions can be directly specified.
- For a given order of consistency, TVD schemes can be made more accurate than the ordinary upstream finite-difference schemes.
- Disturbance at some model levels does not propagate upstream.

Overall, TVD schemes tend to suppress oscillations in prognostic variables (Roe et al., 1985).

The ULTIMATE scheme, further described in Leonard (1991), was specifically developed to counter the issue of oscillation that appears in most of the higher–order finite difference schemes. The main principle of the scheme is that proposed advective fluxes are computed by a basic higher-order scheme, then taken by the postprocessor and limited to preserve positivity. In the LEM, the underlying scheme used is the QUICKEST scheme previously proposed by Leonard (1979). While the algorithm of the scheme is relatively complicated, we refer to the model documentation for the details on the implementation (Gray et al., 2004, p.42-43). Although the scheme is computationally expensive, it ensures preservation of positivity (Thuburn, 1997). It has been shown that the scheme performs well for resolving multidimensional advection (Leonard et al., 1993).

Chapter 3

Methodology for Idealised Model of Cold-Air Outbreak

The phenomenon of the cold air outbreak (CAO) was scientifically observed at least as early as mid-19th century. Already at this time, it was noted that CAO leads to rapid changes in the bottom part of the troposphere (Murphy, 1860, p.312). Later studies have revealed that CAOs are likely to influence the uncertainty in the prediction of extratropical weather (Wacker et al., 2005) (Papritz et al., 2014). With the advance of atmospheric models in recent decades, this phenomenon has been subject to a number of model studies. The data collected from field observation served to set up mesoscale model scenarios, such as the case of a CAO developing over a wide marginal sea-ice zone (MIZ), with a focus on the development of cloud streets (Liu et al., 2006). However, mesoscale models on their own do not allow accurate simulation of the structure of the convective boundary layer (CBL) developing over a MIZ and an open sea. For this purpose, we need to employ a *Large Eddy Simulation* (LES) that serves as a very powerful tool for numerical modelling of atmospheric boundary layer (ABL) processes and other small scale atmospheric phenomena.

This chapter focus on a methodology for the LES modelling of CAO over a heterogeneous surface. It explains how LES is employed for the analysis of a developing convective boundary layer in CAO in extra-tropical areas. The chapter starts with an overview of the model setting for the idealised CAO scenario. The overview covers both the control run and the set of model runs with modified surface conditions. All the defined properties are then further explained in the following parts of the chapter.

The novel part of this study - the introduction of the heterogeneity in the surface temperatures into the Met Office Large Eddy Model (LEM) is the subject of the next part (3.3). As the next step, the chapter moves to methods of the analysis of LEM model results (3.4). The main purpose of these methods is to evaluate the variability in the inner structure of a developing boundary layer and resulting properties of the

troposphere on the mesoscale. While numerical models often exhibit a sensitivity to the resolution and initial conditions, a summary of sensitivity study is the subject of the next part (3.5). The technical limitations of the LEM and possible sources of bias are then briefly discussed (3.6).

This chapter is solely concerned with the methodology, as the structure and processes in CAO have been described in 1.3 and the theory of LEM in the previous chapter. Results of the control run and the runs with heterogeneous surface temperatures are the main focus of the next chapter. The results of module runs are analysed, leading to drawing first conclusions about the impact of surface heterogeneities on the structure of the developing boundary layer. The scope of the study is widened by the Chapter 5 that examines CAO scenarios with a different structure of the lower troposphere. Chapter 6 then presents case studies from the ACCACIA flight mission. Since LEM is there set up and run with a non-idealised setting, further adjustment to the LEM code are described and explained in the section 6.2.

3.1 Overview of the Scenario Setting

The idealised model scenarios for CAO requires a cautious setting of the model runs. With an intention to maintain clarity and allow for reproducibility in future studies, all the scenario & model settings and assumptions are defined in the following tables. The first table summarises the simplifications under which we can model CAO. The second and third table define the entire setting of the control run. The following tables then just define the modification of the setting for the purpose of simulating the CAO over a heterogeneous surface.

property	constrain	details
CAO		
	• CAO is already in progress, there is no weather front in the modelled area	3.2.3
	• horizontally homogeneous air on the inflow	3.2.2
large-scale forcings		
	• large-scale wind is approximately in geostrophic balance	3.2.1
	• large-scale wind forcing constant in time	3.2.3
	• negligible subsidence	3.2.1
MIZ		
	• A gradual increase in surface temperature at the beginning of the MIZ without large-scale temperature discontinuities	3.2.3 3.3
	• No feedback loop for the surface — decrease of the surface temperature and freezing due to heat loss not modelled.	3.2.1 3.6

Table 3.1: Overview of the required assumptions

The following tables are designed in a way to provide a clear overview. The left column list a model properties and the central column defines its setting. The third column then provides a reference to the following parts of this chapter that offers a detailed description and the explanation of these settings. Finally the rightmost columns refers to the part of the software where is the setting implement. The names of LEM code segments start with the symbol * and the names of LEM namelists starts with the & symbol. Notwithstanding, the exact implementation in the idealised scenarios in LEM code is not included in this chapter. Due to its technical character and overall size, it is instead located in the Appendix.

property	setting	details	set in
initial conditions	altitude [m] / θ [K]: 12000 / 363; 5000 / 293; 1500 / 257; 0 / 253 altitude [m] / RH [%] / v [m s^{-1}]: 12000 / 0 / 10; 2000 / 60 / 10; 0 / 60 / 0	3.2.2	&INITPROF
dynamics	Coriolis parameter $1.4 \cdot 10^{-4}$	3.2.1	&DYNAMICS
forcing	large scale wind forcing in y-direction same velocities as in the initial conditions linearly decreasing to 0 m s^{-1} at the surface	3.2.1	*SET1D
run length	28 900 s	3.2.4	&TIMENML
boundary conditions			
• top	rigid boundary, no subsidence, stress-free for horizontal velocities with damping layer 2 km deep, located above 10 km	3.2.4	&DAMPNML
• lateral	periodic boundary	3.2.4	
• bottom	rigid boundary, with surface model, reference surface pressure 100 400 Pa	3.2.1	&INPUT
surface model	based Monin-Obukhov theory, prescribed surface roughness length and values for surface temperature and humidity	2.5	*PRAMETR
	$z_0 = 5.0 \cdot 10^{-3}$ $z_{0,\theta} = 5.0 \cdot 10^{-4}$	3.2.1	&INPUT
surface albedo	0.2		&RADCNTL
surface humidity	saturated surface	3.2.1	*PRAMETR
surface temperature	Time [s]: -10800, 0, 400, 1000, 1400, >1400 θ_{surf} [K]: 253, 253, 261, 265, 271, 271	3.2.3	&INPUT
reference profile	potential temperature reference profile at the beginning altitude [m] / θ [K]: 12000 / 363; 5000 / 293; 1500 / 257; 0 / 254	3.2.2	&THPROF

Table 3.2: Overview of model setting — control scenario

property		setting	details	set in
domain	width in x	16 km	3.2.4	runfile
	length in y	16 km	3.2.4	runfile
	height	12 km	3.2.1	&GRID
resolution				
	horizontal	160 m, in both directions x and y	3.2.4	runfile
	vertical	altitude [m] / spacing [m]: 7500–12000 / 100; 2500–7500 / 100; 100–2500 / 40; 0–100 / 10	3.2.4	&GRID
grid	type	Arakawa-C in horizontal, Lorenz in vertical	2.6	
	size	100 x 100 x 126		runfile
subgrid model		LEM subgrid model based on S-L theory	2.4	&SUBMODEL
microphysics		LEM 3-phase cloud microphysics precipitation: rain, snow, graupel	3.2.1	*PRAMETR
radiation				
	•solar	OFF	3.2.1	*PRAMETR
	•longwave	Edwards-Slingo radiation code	3.2.1	*PRAMETR
		radiation update every 5 timesteps		&INPUT
		sub-arctic winter profiles for upper atmosphere	3.2.1	*CALC_LEVS
numerics		• maximum advective CFL number 0.2	2.6	&NUMERICS
		• maximum viscous CFL number 0.2		
		• P–W advection scheme for momentum	2.6	*PRAMETR
		• ULTIMATE advection scheme for scalars	2.6	*PRAMETR
		• initialisation by perturbations in wind velocity	3.2.5	*START

Table 3.3: Overview of model setting — computational setting of control scenario

'40 m' horizontal resolution				
property		setting	details	set in
resolution				
	horizontal	40 m, in both directions x and y	3.2.4	runfile
domain	width in x	4800 m	3.2.4	runfile
	length in y	4800 m	3.2.4	runfile
	height	12 km	3.2.1	&GRID
grid	size	120 x 120 x 126		runfile

Table 3.4: Overview of model setting — model runs with increased horizontal resolution

heterogeneity in surface temperatures

property	setting	details	set in
types		3.3	update code

type	pattern
along	stripes along wind
across	stripes across wind
chessboard	chessboard pattern

spatial scales	size of the square block of the pattern ($d_{(\mathrm{h})}$)	3.3.2	update code

options	used horizontal resolution [m]
400 m	40 m
1600 m	40 m and 160 m
3200 m	160 m

temperature scales	maximum scale of a positive anomaly ($\delta_{(\mathrm{h})}T$)	3.3.2	&INPUT

options
1 K
3 K
7 K

time development		3.3	&INPUT

Time [s]	0	400	1000	1400	>1400
persistent	0	1	1	1	1
diminishing	0	1	1	0	0

Table 3.5: Overview of model setting — model runs with surface heterogeneity

The model runs were performed in LES software package *Met Office Large Eddy Model, version 2.4* (the most recent version available during the project). All runs were performed on the UEA supercomputing cluster Grace. Each run was performed as a computational job on a single computational core, no parallelisation was employed (see 3.6).

3.2 Control Scenario

While CAO events occur in a wide range of geographical locations, from the Arctic Ocean north of Svalbard (Brümmer, 1996) to the East China Sea (Yamamoto, 2012), there is not a single correct generic setting of the properties of the lower troposphere. The setting of this control scenario is motivated by examples of CAO cases from previous field studies (see 1.3.2) as well as cold outbreaks observed during the ACCACIA field campaign. However, it is not a reproduction of any of the previous studies. Although it would be possible to base the control scenarios on some chosen CAO case, there are some issues to consider. On one hand, a scenario directly based on a previous case study could provide a direct comparison for results. On the other hand, most of CAO cases exhibit quite complicated wind profiles and potential temperature profiles in the lower

troposphere (see figure 1.3). That would pose a serious issue in the evaluation of model result — it would be difficult to separate the effect of the surface forcing and the effect of jumps in the initial potential temperature and humidity. Furthermore, we would need to consider the cross-interaction between the heterogeneous surface forcing and variations in the mean surface temperature with time. Therefore, with a goal to avoid these aforementioned issues, the control scenario is rather prescribed as an idealised scenario, inspired by previous case studies.

Previous LES studies of similar idealised CAO cases have usually started with a stratified troposphere that follows a piecewise linear profile (Kershaw, 1995) (Gryschka et al., 2014) — the bottom few hundred metres are almost neutrally stratified, followed by a stronger stratification above. The large scale wind forcing followed a linear profile in the lower troposphere and was constant above in Kershaw (1995). The idealised control scenario in this study follows the same principles. With a goal to model the conditions in CAO observed over coastal polynia and marginal sea-ice zone (MIZ), the control scenario starts with a stratified troposphere over a cold surface. Large scale wind forcing is supplemented. Air masses are first advected over a cold surface during the spin-up. Later, they are advected over warming surface (specified in 3.2) which results into the development of a CBL. The time of the transition is set to represent the time for which an air parcel at the upper part of the boundary layer travels over the MIZ .

While the specification of the control scenario also requires an explanation of the setting, following text is logically divided into few parts. It starts with describing the general physical setting (3.2.1), description of the initial conditions (3.2.2), explanation of the quasi-Lagrangian moving domain (3.2.3) and the setting for the other domain properties (3.2.4). In continues with initialising of the turbulence by random perturbations (3.2.5) and briefly explains adding the model outputs (3.2.6, 3.2.7). It is important to stress out that this methodology is focused just on one chosen idealised scenario that does not represent all CAOs. Therefore separate scenarios are created by adjustment of the initial potential temperature profile in the mid-troposphere and the large scale wind forcing, as further described in the chapter 5.

3.2.1 General Physical Setting

To represent conditions at higher latitudes during winter months, the outgoing long-wave radiation should be taken into account. Therefore, the code for long-wave radiation is switched on with the updates in the values of radiation computed after every 5 steps of numerical integration. In the calculations of radiative budget, the radiative properties of the upper atmosphere have to be taken into account as well. Since the Mcclatchey profile supplemented with the LEM applies to the atmosphere in tropics, an adjustment

is required. The *profile for subarctic winter* is implemented based on the revisited Mcclatchey measurements (McClatchey et al., 1971, pp.7-8).

Similarly, the choice of cloud microphysics should reflect the climate conditions of the scenario. While mixed-phase clouds are very common in Arctic conditions (Zuidema et al., 2005) (Klein et al., 2009), a full three-phase microphysics is required. Therefore, we switch on the main three-phase microphysics scheme provided with the model. This allows us to simulate the glaciation of supercooled water in clouds as well as the collections of cloud water and ice by falling hydrometeors.

The other issue is the surface roughness. Here we need to set two values of the aerodynamic roughness lengths — one for momentum and one for scalars, as explained in (Gray et al., 2004, pp.11-13). Considering the lack of suitable reanalysis data for setting these properties, we rather use the values from observational studies. The aerodynamic roughness length for scalars is set to $z_0 = 5.0 \cdot 10^{-3}$, which is value commonly measured in Arctic (Mäkiranta et al., 2011). The aerodynamic roughness length for scalars is by order lower than the roughness length for momentum, following the suggestion from studies of surface properties in extratropical areas (Andreas, 1987). This means that the value of surface roughness for scalars is set to $z_{0,\theta} = 5.0 \cdot 10^{-4}$.

Subsidence is another factor that should be considered. The large scale subsidence plays an important role in balancing the cooling effect of the cold surface in Arctic (Vihma at al., 2005). The subsidence was also indicated in some observed cases of cold outbreaks such ARKTIS 1991 and ARKTIS 1993, (Brümmer, 1999), however there were not enough data to determine its character. The climatology study of observed cold outbreaks (Walsh et al., 2001) has also admitted that subsidence is often present, yet difficult to estimate. Faced with the difficulty of determining the subsidence, a number of modelling studies on cold outbreaks discussed it and then set its value to zero in the absence of suitable data (Muller et al., 1999) (Vihma at al., 2005). Fortunately, satellite studies of cold outbreak suggest that vertical transport of heat and moisture is not sensitive to subsidence (Chou and Atlas, 1982). However, a strong subsidence (in order $10^{-2}\mathrm{ms}^{-1}$) can lead to a weak decrease in liquid water content in clouds. Nevertheless, the effect is too weak to significantly alter the development of CBL (Weinbrecht and Raasch, 2001). Therefore, we assume that subsidence is not a significant factor in our study. Considering the implications of previous studies, the subsidence at the top boundary is set to zero for simplicity.

Other physical properties of the scenario are set accordingly:

- Coriolis parameter $0.00014\,\mathrm{s}^{-1}$ — Set based on Coriolis parameter for high latitudes $70 - 80°\mathrm{N}$.

- surface pressure 100 400 Pa — This value of pressure is on a lower boundary of long-term pressure trends in Arctic around Greenland and Svalbard (Polyakov et al., 2003).
- saturated surface — Since the surface consists of water and sea-ice, it is expected that the skin surface is saturated.

3.2.2 Initial Conditions

The main motivation for the choice of the control scenario is modelling rapidly developing CBL under the influence of a relatively weak wind shear. While the impact of strong stratification and different strength of wind shear is later explored in chapter 5, this part of the chapter is concerned with the description of the control scenario only. In the following paragraphs, we are going to explain the reason for the specific choice of the idealised profiles of potential temperature, humidity and the mean wind velocity.

Although most of the troposphere is strongly stratified, a weaker stratification is achieved in the bottom few hundred metres due to effects of orography (Kilpeläinen et al., 2012) and evaporation from leads (Esau, 2007). This property of the lower troposphere has been observed in a number of CAO cases, including CAO over Labrador Sea (Renfrew and Moore, 1999, p.2383) and some CAOs observed during March 2013 on the ACCACIA flight campaign (see chapter 6). Detailed description of the setting of the initial conditions follows.

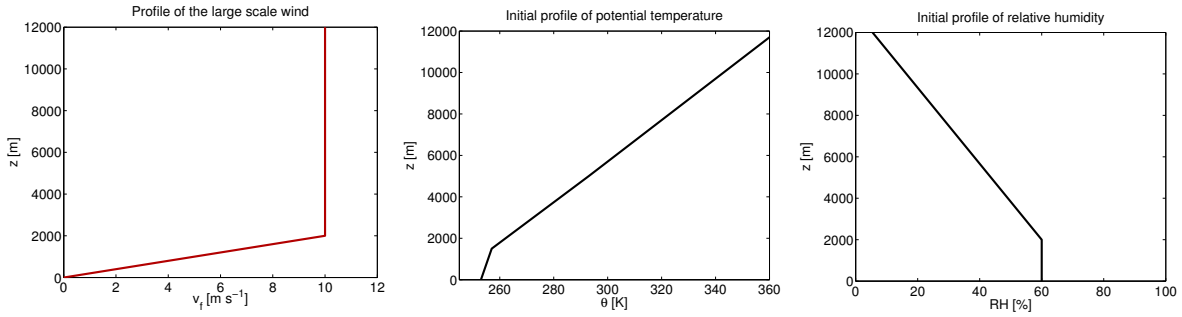

(a) (b) (c)

Figure 3.1: The setting of the vertical structure of the control scenario - the profile of the large scale wind forcing in the direction of y-axis, the initial profile of the potential temperature and the initial profile of the relative humidity.

The initial potential temperature profile (shown in figure 3.1) is stable, with the surface layer temperature of 253 K and stratification

$$\frac{\partial\theta}{\partial z} = 2.6 \quad \mathrm{K\,km^{-1}} \quad \text{in the bottom 1.5 km}$$
$$\frac{\partial\theta}{\partial z} = 10.2 \quad \mathrm{K\,km^{-1}} \quad \text{in the rest of domain}$$

The initial profile of relative humidity is constant at the value 60 % up to altitude of 2000 m and then linearly decreasing to 5.5 % at the top of the domain.

Large scale forcing is supplemented in the form of a large scale wind in the y-axis direction. It increases linearly from $0\,\mathrm{m\,s^{-1}}$ at the surface up to $10\,\mathrm{m\,s^{-1}}$ at the altitude of 2000 m, and further up in the atmosphere it remains constant (see figure 3.1a).

3.2.3 Quasi-Lagrangian Approach

One of the serious concerns in the idealised model is capturing the downwind spatial extent of CAO. In the following paragraphs, we first explain the limitation of the boundary conditions in LEM, and then we propose the approach that allows us to solve this issue. We show the previous applications of this approach as well as indicated shortcomings. Finally, we define the surface conditions used in out control model run.

Setting the surface and boundary conditions for a developing CAO brings some challenges. Since the LEM is limited by a periodic boundary condition in horizontal directions 3.2.4, we cannot set different conditions of air on the inflow and the outflow. An air parcel that leaves the model domain downwind immediately appears upwind. Furthermore, a spatial domain that would include both the area over sea-ice as well as downwind over the MIZ would be extremely large. Therefore, we instead use a *Quasi-Lagrangian Approach* to simulate the downwind development of the CAO.

The main idea behind this approach can is to simulate an 'air parcel' that is advected from over a cold surface (e.g. sea ice) to over a relatively warm surface (e.g. MIZ or open water), the spatial changes in the surface condition along the trajectory of the moving air parcel are replaced by temporal changes in surface conditions with time. There have been various examples of "small domain simulations in a frame of reference moving with the mean wind have been used to explore some aspects of the evolution of roll convection" (Liu et al., 2004). Despite some degree of simplification, model scenarios with periodic boundary conditions and a moving frame of reference are very useful in the studies of convective systems (Richardson et al., 2007).

In this study, we specifically implement a quasi-Lagrangian approach similar to the method used in the model study of the campaign EPIC 2001 by Szoeke and Bretherton (2004). In their formulation, the entire column is *assumed to move at the mean ABL velocity*. An issue of this method is that it does not capture the effect of the different advection speeds due to shear within the ABL. However, this issue is of minor importance when the ABL is mixed. Generally speaking, their results compare well with observations from EPIC 2001 (Caldwell and Bretherton, 2009) as well as with the mesoscale

models with directly prescribed boundary conditions based on the same field campaign (Small et al., 2005).

Although the aforementioned approach of Szoeke and Bretherton (2004) was originally used for the boundary-layer transition in tropics, it has been successfully adjusted also for simulations of a large CAO over the Gulf Stream where the wind velocity is not constant with height (Skyllingstad and Edson, 2009). It is applied under the assumption that secondary mesoscale circulations generated near the front of the travelling air mass are relatively small, in comparison with the direct response to the forcing at the surface. The resulting impact of neglecting the advection on the overall flow characteristics is relatively weak in comparison with the changes in surface temperature (Skyllingstad and Edson, 2009, p.1278). This model study compares well with the field observations over the Gulf Stream (Marshall et al., 2009).

It is a common computational approach in LES with a Quasi-Lagrangian parcel is to apply a Galilean transformation for horizontal velocities (Wyant et al., 1997). This is defined as

$$\left(\boldsymbol{x}, t, \boldsymbol{u}\right) \longmapsto \left(\boldsymbol{x}', t', \boldsymbol{u}'\right) = \left(\boldsymbol{x}' - t\,\boldsymbol{u}_{\mathrm{Gal}},\, t,\, \boldsymbol{u}' - \boldsymbol{u}_{\mathrm{Gal}}\right) \tag{3.1}$$

where $\boldsymbol{x}$ is the vector of position, t is the time, $\boldsymbol{u}$ is the vector of velocity and $\boldsymbol{u}_{\mathrm{Gal}}$ is the chosen Galilean velocity. Setting $\boldsymbol{u}_{\mathrm{Gal}}$ to the mean advection clearly leads to weaker velocities $\boldsymbol{u}'$ within the simulation. This provides a significant advantage in calculations, since smaller velocities allow longer timesteps that still fulfils the CFL condition (see 2.6). While LEM allows the setting of Galilean transformation within the simulation (Gray et al., 2004, p.5), it is not suitable for simulations with surface heterogeneity. To maintain the consistency of the model would require the surface heterogeneities to move in the simulation with the velocity $-\boldsymbol{u}_{\mathrm{Gal}}$. Since the model grid consist of discrete points, this transition of the surface heterogeneitities would not be smooth. Furthermore, it would pose a number of possible computational issues to implement such conditions. Therefore, we do not use Galilean transformations in this model study.

Bearing in mind the aforementioned limitations, we replace the spatial development in surface temperatures with the domain-wise mean surface temperature that changes with time. While the trial model runs (see Appendix) showed that the model spin-up is reached during the second hour of the run, the surface conditions and outer forcing are kept constant until the end of the second hour, and subsequently altered. The surface temperature stays at the value of 253 K for the first 3 hours of the model run. Then the surface warms over a period of 1400 s (as described in the table 3.2), until it reaches the temperature 271 K. The surface temperature than further remains constant. The time at which the heating starts is referred to as t_0. This point serves as a reference point for the time coordinate. The apparent location of the domain is then estimated

based on modelled wind velocity in the boundary layer. The estimation of the position is explained in 3.4.1.

The surface conditions have been prescribed in the table 3.2 in the model overview. While this part of the chapter provided the explanation and likely issues identified in previous studies, the model setting should simulate the developing CAO reasonably well. Possible limitations of this approach are further discussed in 3.6.

3.2.4 Domain and Computational Setting

however the specific choice of the computational domain and computational properties should be carefully considered as well. A number of studies have shown the importance of a model resolution and the choice of subgrid parametrization (Arnal and Friedrich, 1992) (Maryon, 1989) (Pope, 2004). In the following paragraphs, focus is given to the choice of subgrid model, model domain and the model resolution.

One of the main motivations for the choice of the domain depth is to model the propagation of waves in the upper troposphere. Previous studies have shown that the domain depth of 8 km or more should allow modelling of propagating waves (Young et al., 2002). In this study, the model domain should include a large part of a stratified troposphere without venturing into stratospheric air (McClatchey et al., 1971, pp.7-8). However, additional requirement have to be considered as well. While convection generated waves may propagate in the stratified atmosphere up to the top model boundary, there is danger of a reflection of waves from a rigid top boundary. To prevent this, the damping layer is switched on. The properties of the damping layer (Gray et al., 2004, p.13) are set to the thickness of 2 km. Considering both these issues, the depth of the model domain was set to 12 km with the damping layer starting at the height of 10 km. Due to the large vertical extent of the domain, the pressure is computed by anelastic equations (Gray et al., 2004, pp.4-5). For the explanation of these calculation, please see 2.3.

The horizontal extent of the domain is a peculiar question. The domain should be relatively small to limit possible errors due to differential advection (Szoeke and Bretherton, 2004) in quasi-Lagrangian approach (as explained in 3.2.3). At the same time, the domain should be large enough to capture the formation of larger convective structures. A number of previous studies has investigated what domain size is required to properly capture developing atmospheric phenomena. For modelling CBL capped with a shallow cumulus, a domain of a size of 6.4 km x 6.4 km is sufficiently large, and increase in the domain size did not have a significant impact on model results (Brown et al., 2002). However, we cannot just assume that the cloud layer in a developing CAO in

Arctic is simplified as shallow cumulus. An extended study of LES sensitivity instead concluded that the horizontal domain size should be at least 2.5 times larger than the characteristic horizontal length scale of the atmospheric structure that is modelled (Agee and Gluhovsky, 1999). Since the developing cloud rolls reach widths from 1 km to 4 km (Brümmer, 1999) (Atkinson and Zhang, 1996), the domain size of 10 km would seem reasonable.

Although the model is large enough to capture roll convection, this might not be enough to properly capture the propagation of gravity waves. While gravity waves reach sizes over 4 km (Gossard and Munk, 1954), a larger domain should be employed. Based on an extended study of roll convection and waves, Young et al. (2002) arrived at the conclusion that domain of the size 18 km x 18 km is already considered relatively large.

The previous chapter on model theory has already explained that LES resolves just the large turbulent eddies and the rest of the turbulent cascade is parametrized. For this purpose, LEM employs an advanced subgrid model based on the extension of Smagorinsky-Lilly theory (for explanations, see 2.4). The setting of the subgrid model representing viscosity is directly taken from LEM test case 5 (Gray and Petch, 2004, p.47) that is based on an extended study on modelling cold outbreaks by Kershaw (1995).

Notwithstanding, the choice of the model resolution still remains an important question (Zacharias et al., 2012). Higher grid resolution allows us to resolve a wider palette of turbulent processes, however the computational expenses grow significantly. Generally speaking, the spacing of the grid should be within the inertia subrange (Pope, 2004). Although a well calibrated subgrid parametrization should correctly model the inertia cascade (Arnal and Friedrich, 1992), there might be occasional errors due to inhomogeneities in a developing CBL (Love and Leslie, 1979).

altitude $[m]$	spacing $[m]$	
	vres0	**vres1**
7500–12000	100	240
2500–7500	100	130
100–2500	40	40
0–100	10	20

Table 3.2: The general setting of vertical layers in the simulations

Previous modelling studies of CAO has applied resolutions from few hundred of metres to tens of metres. A horizontal grid spacing lower than 250 m was usually described as "fine resolution", however there is not a clear consensus on this term. And extended study of a roll convection by Muller et al. (1999) used a horizontal spacing of 200 m and a vertical spacing of 32 m. On the other hand, Schröter et al. (2005) set the horizontal spacing to 100 m, however the vertical resolution 50 m. Roode et al. (2004) also applied the horizontal spacing 100 m, but the vertical spacing was as low as 20 m. Still, the model domain in the majority of these studies included only the lower troposphere. While the

model in this study spans up to 12 km, we also found that memory and computational expenses were becoming an issue as well.

For the purpose of this study, a sensitivity testing was performed (see 3.5) for reasonable settings of horizontal and vertical grid resolution. Still, any computationally available choice of the resolution leads to the situation when the horizontal grid spacing is larger than the height of plumes (Gibert et al., 2007) in the shallow CBL. Therefore, the convectively generated turbulence is not resolved at this stage. To address this issue, we have performed separate model runs with a very high resolution for the first hour of the CBL development. A comparison between the control run and the very-high resolution runs then showed that LEM subgrid scheme covers the early development of CBL reasonably well (see 3.5.3). Notwithstanding, this part of the CBL is not fully in the inertia part of the spectrum (Couvreux, 2010) and therefore is deemed not representative enough for the further analysis. Therefore, the later-described methods for the analysis of model runs (3.4) *are applied only for the model outputs after 0.75 hour when the IBL is high enough and the larger CBL eddies are fully in the LES-resolved regime.* The resulting choice of the vertical and horizontal resolution for the control run is described in the next two paragraphs.

The vertical resolution is generally highest by the surface and then decreases with altitude. The highest resolution was utilised in the bottom 100 m to resolve the surface layer properly, followed by high resolution up to 2500 m to contain the whole ABL and part of the free atmosphere above. From a few different settings tested, two settings of the vertical resolution were employed (described in table 3.2). The setting **'vres0'** is used for majority of runs with a goal to properly resolve shallow boundary layers. However, model runs were usually quite time-consuming. Due to these performance issues, the setting **'vres1'** is used for scenarios where a shallow ABL is not an issue.

Horizontal grid resolution is set to 160 m in both x-axis and y-axis direction. The sensitivity testing showed that a further increase in resolution did not produce results that were significantly different (see 3.5.2), but were computationally more expensive (see Appendix). However, this resolution might not be sufficient in the model runs with a fine heterogeneity pattern surface temperatures. The increased horizontal resolution of 40 m in both directions was utilised in these cases with a goal to properly resolve the secondary circulation forced by surface heterogeneities (see 3.3.2). The size of model domain is in this case decreased to 6 km in both horizontal dimensions to avoid memory issues. This would unfortunately mean that the domain size might not be large enough for larger convective rolls, as further discussed in 3.6.

3.2.5 Initial Perturbations

Generally, a LES requires some sort of the initial perturbation to disrupt the homogeneous flow and start an eddy motion. In the initially unstable conditions, the common approach is a small perturbation in the potential temperature (Walko et al., 1992) on the second vertical level that causes differences in the buoyancy of parcels, resulting in the development of convective eddies. In the initially stable conditions, the situation is slightly different. Perturbations in the temperature on the second layer of the model domain tend to quickly dissipate with time. Therefore, perturbations in some other model variable, such as velocity (Boris et al., 1992) or turbulent kinetic energy (Beare et al., 2006), should be used to initiate the model runs (Mason and Derbyshire, 1990).

The reasoning goes as follows: while perturbations in the vertical component of velocity would most likely just dissipate while propagating upwards, inserting a perturbation in the horizontal components of wind velocity has the goal of introducing more vorticity into the model. However, adding an independent perturbation to each horizontal component of wind velocity might violate the continuity equation. Instead, a random streamfunction is generated and values of wind perturbation are calculated from that.

In the LEM example simulation for the unstable conditions, perturbations between -0.1 and +0.1 K were initially added to potential temperature on each grid point on layers from the second layer up to 250 m, i.e.

$$\begin{aligned} \theta_{i,j,k}(t_{\mathrm{INI}}) &= \bar{\theta}_k^{(\mathrm{INI})} + 0.1 \cdot \epsilon_{i,j} && \big\{\forall\, k \,:\, (k \geq 2) \wedge (z_k \leq 250)\big\}, \\ \epsilon_{i,j} &\sim \mathrm{U}(-0.5, 0.5) && \forall\, i,j = 1 \ldots N, \end{aligned} \tag{3.2}$$

where $\theta_{i,j,k}(t_{\mathrm{INI}})$ is the potential temperature at the grid point with coordinates i, j, k at the time t_{INI}, i.e. at the beginning of the simulation, $\bar{\theta_k}^{INI}$ is value on the k-th layer in the initial temperature profile, z_k is the height of this layer and $\epsilon_{i,j}$ are random numbers drawn from $\mathrm{U}(-0.5, 0.5)$, the uniform distribution on the interval $[-0.5, +0.5]$.

Based on this example, we prepared an initialisation of simulations based on the perturbation in the horizontal components of wind velocity. First, a random 2D array of streamfunction values is generated as

$$\begin{aligned} \tilde{\psi} &= \Delta y\, \alpha_{(\mathrm{s})}\, \eta_{i,j}, \\ \eta_{i,j} &\sim \mathrm{U}(-0.5, 0.5) && \forall\, i,j = \ 1 \ldots (N-1), \\ \eta_{N,j} &= \eta_{1,j} && \forall\, j = \ 1 \ldots (N-1), \\ \eta_{i,N} &= \eta_{1,j} && \forall\, i = \ 1 \ldots N, \end{aligned} \tag{3.3}$$

where Δy is the grid resolution in the horizontal direction, constant $\alpha_{(\mathrm{s})}$ sets the spread in streamfunction perturbations, and $\eta_{i,j}$ are again random numbers drawn from the uniform distribution on the interval $[-0.5, +0.5]$, . The initial values of horizontal com-

ponents of wind velocity are then calculated as follows:

$$u_{i,j,k}(t_{\mathrm{INI}}) = \begin{cases} \bar{u}_k^{(\mathrm{INI})} - \dfrac{\tilde{\psi}_{i,j+1} - \tilde{\psi}_{i,j}}{\Delta y}, & \{\forall k : (k \geq 2) \wedge (z_k \leq z_{\mathrm{s},1})\} \\ \bar{u}_k^{(\mathrm{INI})} - \dfrac{z_{(\mathrm{s}),2} - z_k}{z_{(\mathrm{s}),2} - z_{(\mathrm{s}),1}} \cdot \dfrac{\tilde{\psi}_{i,j+1} - \tilde{\psi}_{i,j}}{\Delta y}, & \{\forall k : (z_k \geq z_{\mathrm{s},1}) \wedge (z_k \leq z_{\mathrm{s},2})\} \end{cases} \tag{3.4a}$$

$$v_{i,j,k}(t_{\mathrm{INI}}) = \begin{cases} \bar{v}_k^{(\mathrm{INI})} + \dfrac{\tilde{\psi}_{i+1,j} - \tilde{\psi}_{i,j}}{\Delta x}, & \{\forall k : (k \geq 2) \wedge (z_k \leq z_{\mathrm{s},1})\} \\ \bar{v}_k^{(\mathrm{INI})} + \dfrac{z_{(\mathrm{s}),2} - z_k}{z_{(\mathrm{s}),2} - z_{(\mathrm{s}),1}} \cdot \dfrac{\tilde{\psi}_{i+1,j} - \tilde{\psi}_{i,j}}{\Delta x}, & \{\forall k : (z_k \geq z_{\mathrm{s},1}) \wedge (z_k \leq z_{\mathrm{s},2})\} \end{cases} \tag{3.4b}$$

where $z_{(\mathrm{s}),1}$ and $z_{(\mathrm{s}),2}$ give an interval of the altitudes up to which the stable boundary is likely affected by surface orography (Kilpeläinen et al., 2012, p.237). These two parameters are in the control run set to values $z_{(\mathrm{s}),1} = 250\,\mathrm{m}$ and $z_{(\mathrm{s}),2} = 500\,\mathrm{m}$ based on indicated stable boundary layer 100–300 m in (Brümmer, 1996) and 500 m in (Bian et al., 2013). The spread in streamfunction values is set to $\alpha_{(\mathrm{s})} = 2.0$. Since the initial perturbations in the wind velocity are calculated as differences of two random numbers drawn from uniform distribution, their resulting distribution on the horizontally equidistant grid follows symmetrical triangular distribution (Johnson, 1997) with the mode 0 and the maximum

$$\frac{z_{(\mathrm{s}),2} - z_k}{z_{(\mathrm{s}),2} - z_{(\mathrm{s}),1}}\ \alpha_{(\mathrm{s})}$$

(i.e. in the bottom part of the model domain, the initial wind perturbations reach values between from the symmetrical triangular distribution between -2 and +2).

3.2.6 Model Output

We have so far explained the simulation inputs, however the model outputs are essential as well. Without a suitable model outputs, we would not know how is the CBL developing. Therefore, this part of the chapter explains the setting of model outputs that are suitable for the further analysis of idealised CAO development. Due to a technical nature of some output settings, we focus just on the main points.

The LEM routinely saves a number of timeseries, direct outputs of fields and time averaged vertical profiles, with the first output file being generated after the set-up job and other output files during the 'chain run' (Gray and Petch, 2004, pp.11–13).
A time output is generated at the time t_0. Other outputs then follow in intervals of the quarter of hour (900 s). This time interval has been chosen
as a balanced pay-off, offering both enough time for time-averaged statistics and frequent snapshots of fields for the observation of the boundary layer and cloud layer develop-

ment. After the end of the second hour, the changes in a thickened CBL are slower. Therefore, further outputs follow in the pace of one outputs per hour.

There are number of tools to gain a deeper insight into turbulent transport within the ABL. One of those tools is adding a passive aerosols tracer at chosen altitudes within the troposphere and then observing the development of its concentration (Dosio et al., 2003). This approach was also employed in number of boundary layer studies, including the study of the effect of the surface temperature anomalies on the ABL (Huang et al., 2010).

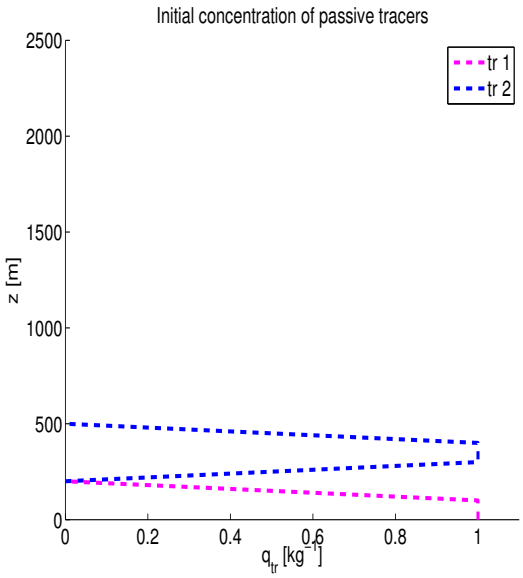

Figure 3.3: Initial profiles of tracers content for two passive tracers.

In this study, two passive tracers were added (see figure 3.3) into the lower part of the domain:

1. the tracer in the bottom of the domain, with initial extent up to 200 m
2. the tracer at altitudes above the expected stable boundary layer turbulence, with initial extent from 200 m to 500 m

Both tracers were implemented as passive scalars (Gray and Petch, 2004, p.9). The initial vertical profiles were prescribed. No sinks or sources were defined. For the details on technical implementation, please see the Appendix.

3.2.7 Adding Flux Timeseries

A short code update for the computation of timeseries of horizontally averaged sensible heat flux and latent heat flux at fixed heights was constructed based on the example of the code lines for respective fluxes at the surface. For the convenience of comparing fluxes at different heights, values of fluxes are recorded both in the kinematic form, $\overline{(u'w')}$, $\overline{(v'w')}$, $\overline{(\theta'w')}$ and $\overline{(q_v'w')}$, as well as full dynamic form of the sensible heat flux Q_{SH} and the latent heat flux Q_{LH} and the wind stress τ.

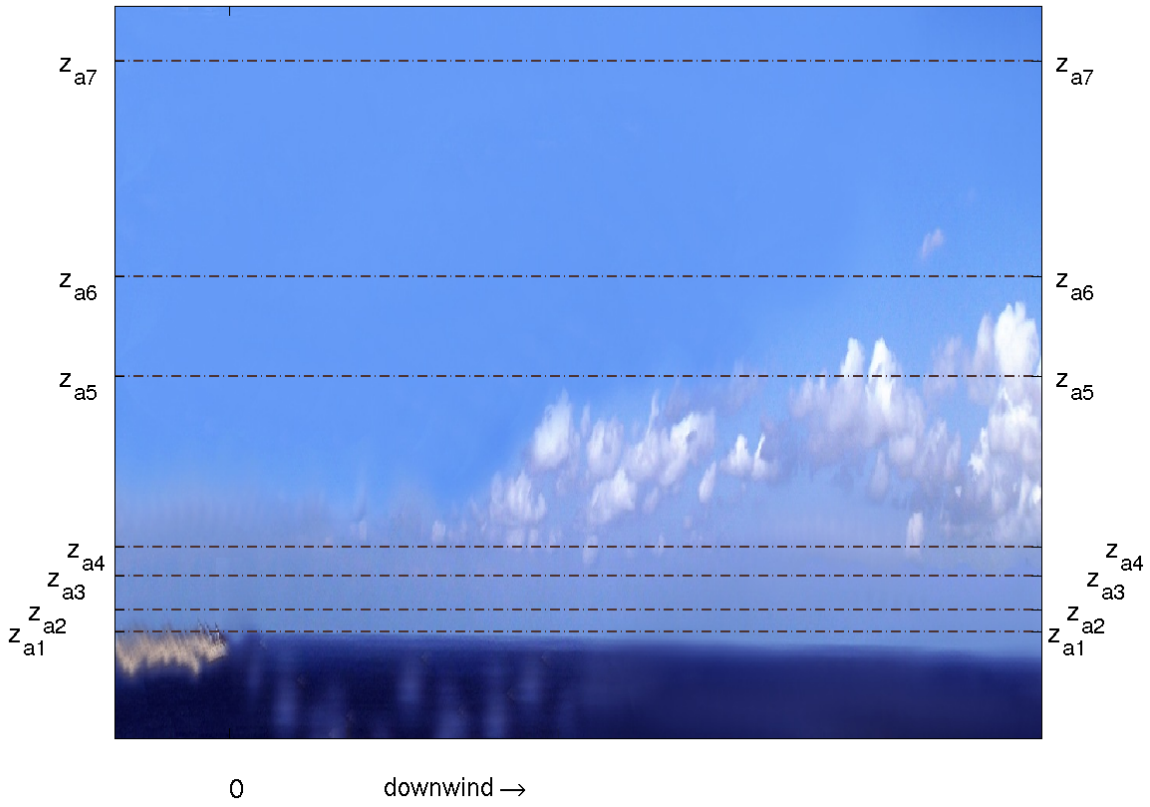

Figure 3.4: Illustrative picture of clouds downwind of MIZ showing the altitudes at which are the timeseries of fluxes recorded. The upper part of the model domain is not shown in the picture.

The calculation in the LEM at the vertical layer k_a could be symbolically expressed as

$$\begin{aligned} Q_{\mathrm{SH}}(k_a) &= C_p\,\rho(k_a)\,\frac{1}{N_x\,N_y}\sum_{\substack{i=1\ldots N_x\\ j=1\ldots N_y}}\big((\theta' w')_{\mathrm{RE}}(i,j,k_a)+(\theta' w')_{\mathrm{SG}}(i,j,k_a)\big),\\ Q_{\mathrm{LH}}(k_a) &= L_v\,\rho(k_a)\,\frac{1}{N_x\,N_y}\sum_{\substack{i=1\ldots N_x\\ j=1\ldots N_y}}\big((q_v' w')_{\mathrm{RE}}(i,j,k_a)+(q_v' w')_{\mathrm{SG}}(i,j,k_a)\big), \end{aligned} \tag{3.5}$$

where N_x and N_y are numbers of grid points in the directions x and y, and subscripts RE and SG indicate the resolved and subgrid contribution respectively.

Based on the trial runs of simulations, the following seven vertical levels were chosen based on an expected physical character of the atmosphere (see figure 3.4) at these altitudes:

1. Within the convective surface layer (altitude $z_{a_1} = 45$ m), where plumes of warm air are rising from the surface.

2. Above the surface layer (altitude $z_{a_2} = 170$ m), where strong fluxes over the surface are expected. At the same time separate small plumes are supposed to connect below that height.

3. Lower part of the ABL (altitude $z_{a_3} = 360$ m), where a strong fluxes over the surface are expected. At the same time separate small plumes are supposed to connect below that height.

4. Bottoms of clouds or clear air below the cloud layer (altitude $z_{a_4} = 520$ m), where both strong updraughts and downdraughts are likely to occur.

5. The upper part of the cloud layer (altitude $z_{a_5} = 1480$ m), which contains descending outer part of clouds, warm updraughts within clouds, and areas of clear air between the cloud streets.

6. Above the cloud tops (altitude $z_{a_6} = 2040$ m). At this height, the fluxes are mostly driven by the effects of cloud layer below.

7. In the mid-troposphere (altitude $z_{a_7} = 3250$ m), where the effect of the shallow convection is supposed to diminish.

The setting of the altitudes for recording fluxes could be easily manually adjusted based on specifics of new scenarios. This approach is later applied in the case simulations in Chapter 6 where altitudes are chosen to reflect the mean altitude of horizontal flight legs of the research aircraft.

3.3 Heterogeneity in Surface Conditions

During cold air outbreaks in Arctic, the cold air is often advected from a contiguous sea-ice surface over a warmer marginal sea-ice zone and later to the open sea. The control scenario shows a CAO developing over a homogeneous warming surface (see 3.2), however this is often not very realistic. The surface of marginal sea-ice zone (MIZ) generally consists of a very heterogeneous mix of sea-water and various types of ice (Gupta et al., 2014). There are areas of packed ice interrupted by long leads (Elvidge et al., 2016) as well as areas of floating ice of different sizes (Inoue et al., 2004).

Studies modelling CAO over the MIZ found that inhomogeneities in MIZ affect surface fluxes (Claussen, 1991) and provide favourable conditions for roll convection and a development of secondary circulation (Gryschka et al., 2008). Therefore, this study has considered the importance of the heterogeneous surface and investigated its influence on a developing CBL in CAO. In the following paragraphs, we show the current state of

knowledge of MIZ and explain the reasons for an idealisation of surface heterogeneities. The declaration of idealised surface conditions is the subject of the 3.3.1. A brief description of the implementation of heterogeneous surface conditions to LEM then follows in the 3.3.2.

The first issue is determining a realistic heterogeneous surface in MIZ. There have been a number of observational studies of sea-ice morphology based on satellite products (Kwok, 2014), and observations from buoys, boats and aircraft (Barry et al., 1989) (Kottmeier and Hartig, 1990). A progress in image processing and recognition also offered methods for a faster processing of observational data and an automatise identification of sizes of ice segments (Zhang et al., 2015). Studies generally show a wide spectrum of sizes of ice floes (Rothrock and Thorndike, 1984). Statistically speaking, the sizes of ice floes mostly follow a power law distribution (Hudson, 1987). Some studies further specify that this distribution is followed for large floes. Small floes of the sizes below 40 m often follow a slightly different distribution (Toyota et al., 2006). Nevertheless, there is a wide variability in the parameters of these distribution. This variability is often influenced by geographical region and the distance from coastal areas (Hudson, 1987). Furthermore, there is also a high degree of seasonal variability (Perovich and Jones, 2014) (Wang et al., 2016). Generally speaking, there is no clear way how to prescribe a common MIZ.

One of the possible solutions would be to directly choose an example of some observed MIZ. Still, the knowledge of the size distribution of floes alone does not necessary define the spatial structure. MIZs often exhibit a grouping of floes (Toyota et al., 2006) that leads to a complicated spatial pattern of smaller and larger ice floes (Savage, 1995). Moreover, the spatial grouping can often lead to an aggregation of floes (Inoue et al., 2004) and refreezing in some of the gaps between them. Furthermore, a high degree variability in physical properties was observed within an observed MIZ. The floes and the new ice within MIZ often exhibit different physical behaviour due to height of the packed segment, snow cover and occasional melting or flooding of the elements. This particularly apply surface roughness (Gupta et al., 2014) and surface reflectance (Liu et al., 2016) (Barry et al., 1989).

Considering the difficulties in inserting "realistic" sea-ice mixture, we will instead prescribe an idealised heterogeneity in surface conditions. Due to difficulties in determining the variability in surface roughness (Schröder et al., 2003) (Mäkiranta et al., 2011) and reflectance, the study is going to focus just on spatial heterogeneities in surface temperatures. 3.6.

3.3.1 Idealised Heterogeneity in Surface Temperature

In this proposal of an idealised heterogeneity in surface temperatures, we seemingly follow examples of previous studies of a developing CBL over a heterogenous surface. A common feature of previous studies, such as Gryschka et al. (2014) and Esau (2007) and, is that they usually defined a strip-like anomaly in surface temperatures. Although this approach is valid, it ignores the possible effect of changing the shape of an anomaly. While the previous study of the impact of patches of anomalies in surface humidity (Courault et al., 2007) have an impact dependent on the shape of patches, we consider this parameter worth investigating. Therefore, we are going to introduce few different idealised shape types of the anomaly in surface temperatures for the purpose of further investigation. First, this part of the chapter defines three different types of the pattern representing the shape parameter. Then it is going to define other parameters related to the time duration of the temperature heterogeneity, its spatial extent and the difference against the mean temperature.

With a goal to explore variability in a CBL over a mix of the sea water and sea-ice in the MIZ, three different patterns types are introduced. Heterogeneity is modelled as one of the following repetitive patterns of positive and negative anomalies:

- stripes of anomalies *along* the direction of the synoptic scale wind,
- stripes of anomalies *across* the direction of the synoptic scale wind,
- a *chessboard* pattern, with sides of squares aligned with the direction of the synoptic scale wind

The positive temperature anomalies are higher and their spatial extent is smaller. This follows the example of MIZ in Okhotsk sea during a CAO event (Inoue et al., 2004). Negative anomalies are larger and their values are set to maintain a zero mean over all anomalies, i.e. so the mean domain temperature is the same as the case of homogeneous surface temperature (schematics are shown in figure 3.5). Anomalies appear at the beginning of the transition, $t_0 = 0$, and the temperature difference between the anomaly and its surrounding grows linearly during the warming of the surface. In the basic setting of heterogeneity, anomalies then stay constant for the rest of the run. This set up represents conditions over a large area of scattered ice floats in the MIZ. (Claussen, 1991)

However the possibility of a relatively short MIZ (Williams et al., 2013) that is followed by an open sea surface with almost homogeneous surface temperatures should to be taken into account as well. The effect of this shorter MIZ is modelled in the set of runs where heterogeneity declines in a given number of hours after the transition into warm region (see figure 3.6).

Since there is not a single ultimate model of the distribution of water and sea-ice within MIZ, a wider variety of temperature anomalies and their spatial extent should be considered. In this idealised version of the surface heterogeneity, they are for simplicity represented by two defining parameters:

- the spatial extent of the anomaly, defined by the length $d_{(\mathrm{h})}$ of a side of building block of the chessboard pattern
- the temperature scale of the anomaly $\delta_{(\mathrm{h})}T$, which is the maximum temperature difference between the anomaly and the mean surface potential temperature.

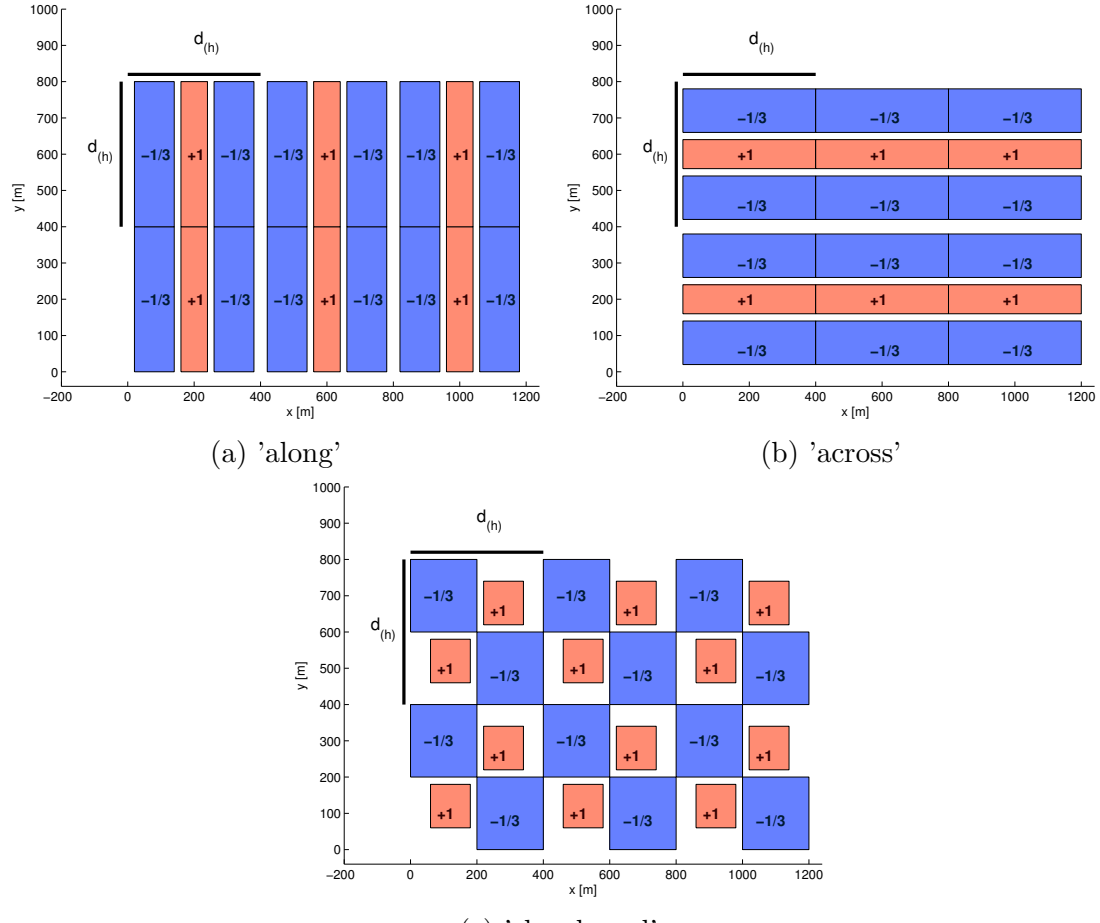

(a) 'along' (b) 'across'

(c) 'chessboard'

Figure 3.5: Illustrative schemes are showing three different patterns of anomalies in surface temperature. The size of the building block of the pattern is clearly marked as $d_{(\mathrm{h})}$. In each case, the direction of the large scale wind is in the positive direction of y-axis

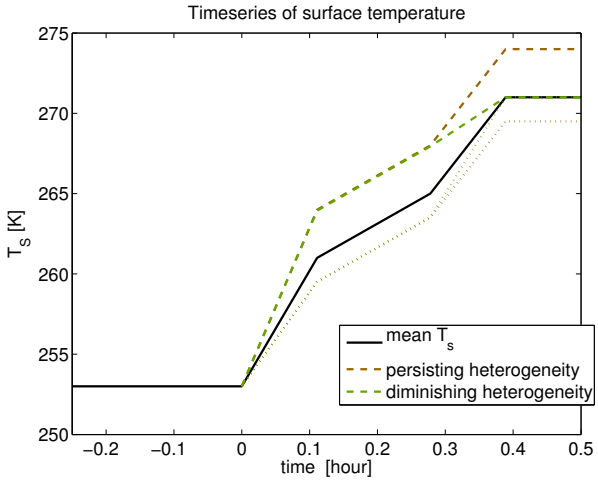

Figure 3.6: The example of the setting of surface temperature. The detail of the transition is shown. Dashed lines (−−) marks positive anomalies while dotted lines (· · ·) mark negative anomalies.

3.3.2 Implementation of Heterogeneous Surface Conditions

We have so far proposed the idealised heterogeneities in surface temperatures. However, there are still issues in implementing these heterogeneous surface conditions in the chosen model. The LEM did not offer a setting for spatially heterogeneous surface conditions, a substantial updates to the LEM code was required. First, the LEM source code was thoroughly investigated by tracking the variables for surface temperature in the code. This was followed by planning of code updates, adding them and performing extensive testing. Due to a strongly technical nature of these steps, they are not discussed here (instead, please see the Appendix). This part of the chapter is concerned solely with a brief description of the implementation of code updates.

The heterogeneous surface conditions are introduced intothe LEM by adding perturbations to the original scalar value assigned to the surface. For the surface temperature values, the array of perturbations is created by setting a mask with a repetitive pattern. The pattern is then multiplied by the temperature scale $d_{(\mathrm{h})}$ and added to the mean surface temperature. Basic building blocks of the pattern consist of a few well defined anomalies of a rectangular shape (for illustration, see figure 3.5). The first size of the building block was 10x10 gridpoints, which in the basic horizontal resolution represents the square of the size 1600 m by 1600 m. The building blocks of the size 10x10, 20x20 and 40x40 gridpoints are set in the way that the relative area of the positive anomalies is approximately same for all three types of masks (along stripes, across stripes and chessboard).

The mask of anomalies is taken in each timestep and multiplied by the scaling factor before adding it to the scalar value of the original surface temperature. The scaling value

allows for easier manipulation. It consists of temperature scale $\delta_{(\mathrm{h})}T$, which is a constant value, and time dependent factor from the interval $[0, 1]$, representing the development of anomalies with time. A maximum value of anomaly allows an easy adjustment of the heterogeneity scale between different model runs that use the same pattern of anomalies but a different temperature scale $\delta_{(\mathrm{h})}T$. A number of model runs were set with temperature scales 1 K, 3 K and 7 K. An example of fluxes over heterogeneous surface is shown in figure 3.7, where surface fluxes clearly respond to the underlying surface temperature pattern.

The mask in the simulations represents a sea-ice mix with the areas of packed ice and water of different sizes. It is stressed that the masks of perturbations are always balanced in the way that the mean value of the surface temperature over the whole domain is the same as the original value of this scalar variable.

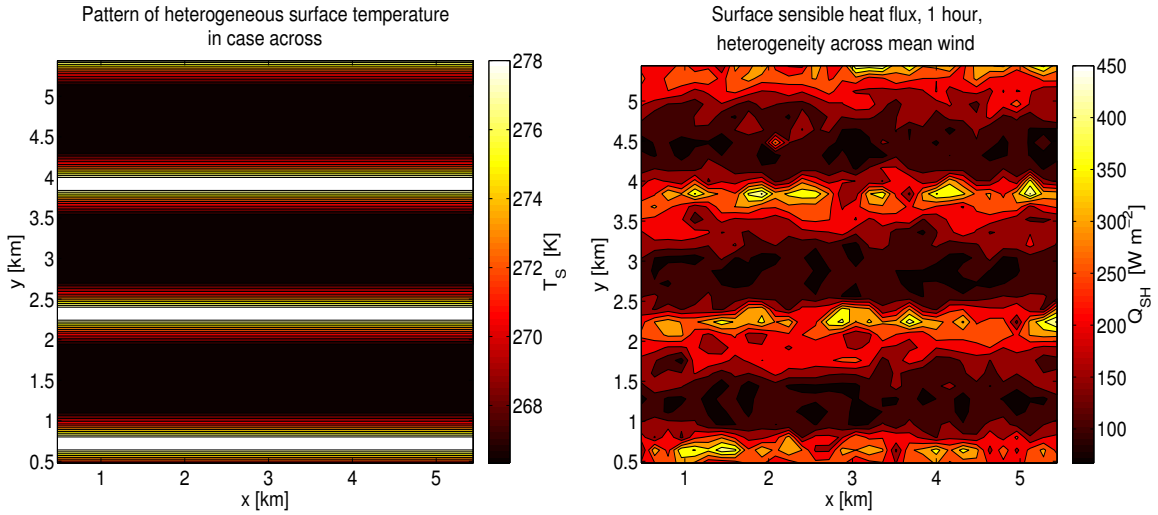

(a) (b)

Figure 3.7: Example of the heterogeneous pattern 'across' in surface temperature with the setting $\delta_{(\mathrm{h})}T = 7\,\mathrm{K}, d_{(\mathrm{h})} = 1600\,\mathrm{m}$ and surface sensible heat flux at 1 hour after t_0. The contourplots show just a part of the domain. Note that the atmospheric flow is in the direction of y-axis (e.g. up the page).

3.4 Methods of Evaluation

With a goal to closely investigate a developing convective boundary layer (CBL) in cold air outbreaks (CAO), a number of model runs are perforemed for the idealisced CAO scenario. While the previous two parts of this chapter (3.2 and 3.3) described the input into LEM software, this part of the methodology focuses on the evaluation of large

quantities of data from LEM outputs.

Horizontally averaged vertical profiles of wind velocity and scalar quantities provide a basic insight into the vertical structure of the developing CBL. Although the LEM provides a wide palette of timeseries and averaged vertical profiles of model variables, a further postprocessing is required for the proper assessment of the variability in the CAO and the impact of modified surface forcing. From the model output, the distribution of updraughts and downdraughts is evaluated at different stages of the development of the mixed boundary layer, followed by further analysis of resulting vertical fluxes of heat, moisture and momentum. The following sections focus on some specific parts of the evaluation of model results.

3.4.1 Boundary Layer Height

Since the LEM does not directly output boundary layer height(s) (Brooks and Fowler, 2012, pp.249-250), a careful treatment must be given to the determination of this quantity (Denmead et al., 1996). While there are number of alternative formulations for the height of the boundary layer (Vogelezang and Holtstag, 1996), a clarification is required. In the following paragraphs, we are going to explain the detection of z_{bl}, the total height of ABL, and z_i, the height of the mixed layer. These two quantities are then further used for the approximation of the distance travelled by the Quasi-Lagrangian parcels during the CAO.

The boundary layer height in this study follows the formulation *"highest levels reached by thermals and the lowest levels attained by free atmospheric air"* of Grabon et al. (2010). Instead of estimating the boundary layer height z_{bl} from the vertical fluxes or the velocity variance, we apply a simplification of the approach of Brooks and Fowler (2007) of tracking a passive tracer within the CBL. This approach is also well justified by lidar observational studies (Morille et al., 2007). Since passive tracers were added into the bottom part of the LES domain the extent of ABL is bounded by the tracer concentration. However, due to effects of diffusion and the cloud detrainment (Taylor and Baker, 1991), it is likely that some amount of tracer escapes above ABL. While the convection facilitates a transport of the tracer up to the top of the CBL and the cloud top entrainment is dominated by a downward transport, a rapid drop in the tracer concentration is expected at these altitudes.

However, estimating the height of deep ABL by the steepest slope would put the top of the ABL at the altitude of majority of cloud tops and would cut off higher clouds. Therefore, the height of the ABL is estimated as the first altitude where the concentration

normalised by its maximum value falls bellow a threshold, i.e.

$$z_{\mathrm{bl}} \approx \min \left\{ z \; : \; \frac{q_{tr}(z)}{(\max q_{tr})} < C_{tr} \right\}, \tag{3.6}$$

where C_{tr} is the threshold and $\max q_{tr}$ is the maximum of tracer concentrations over all the vertical levels.

Even more peculiar is estimating z_i, the height of the well-mixed layer (ML) (Stull, 1988, p.12) (Brooks and Fowler, 2012, pp.251-2) , which is usually defined (IFS IV, 2013, p.38) as

- The altitude of the capping inversion jump or discontinuity in the case of clear ML or stratocumulus topped ML
- The altitude of the cloud base in the case of cumulus topped ML.

In the second case, the z_i is set to be the level of lowest cloud base of the cumulus layer (CuL). In the first case, we can either apply threshold for gradient in temperature or search for a change in the gradient. In this study, the second option is preferred. The height of the ML is estimated as the lowest altitude with a positive gradient where the second derivation is negative. This avoids problems with an arbitrary setting of thresholds that might be exceeded in a case of rapid entrainment at the top of the ML. The question of estimating the ML height is further addressed in the discussion (3.6). To reflect the variation of the height of ML within the domain, the estimated z_i can be calculated for a part of the domain. However, z_i should not be estimated from a single column only (Brooks and Fowler, 2012, p.461).

This estimation of z_i might at first seem unnecessarily complicated in comparison with applying the threshold on the difference in potential temperature between two levels. However, in a case of a relatively weak inversion over CBL, rapid entrainment might cause an increase in potential temperature at the top of ML. This would then require repeated adjustment of the threshold value to fit conditions. Other problems would arise in the case of a strong stratification that is often present in the Arctic troposphere. Due to a strong stratification, the threshold would be exceeded in the strongly stratified layers even before the formation of a ML. Another apparent solution is to estimate the ML height by the minimum in the second derivative. However, this method is sensitive to changes in the stratification of the free atmosphere above. If there is a decrease in stratification somewhere higher up in the troposphere, the second derivation there could be lower than at the top of the ML and the height of the ML would be misclassified.

The other issue related to the boundary layer height is how far have air parcels travelled with wind during the CAO. Estimating this distance is a vital in our setup of

the Quasi-Lagrangian domain (see 3.2.3) Although the large scale forcing v_f is linearly increasing with height in the lower troposphere, the developing CBL alters the wind profile. While the horizontal mean of wind velocity in the ML is approximately constant within the ML (Stull, 1988, p.450) it serves as a good estimation of the velocity with which the CBL is travelling downwind. The distance travelled since the reference point t_0 is then approximated as

$$s(t) = \int_{t_0}^{t} v(\tilde{t}, z_i)\, \mathrm{d}\tilde{t} \;\approx \sum_{\{j\,:\,t_0<t_j\leq t\}} \bar{v}(t_j, z_i) \cdot (t_j - t_{j-1}), \tag{3.7}$$

where $\bar{v}(t_j, z)$ is the velocity at given altitude averaged horizontally (over the whole domain) and in time (over the interval $(t_{j-1}, t_j]$).

3.4.2 Updraught Distribution

Parametrisation schemes for CBL make various assumptions about the inner structure of the convection, proposing different distributions of updraughts and downdraughts. Schemes are usually based on the application of Monin-Obukhov similarity theory, Most of these assumptions were based on studies in tropics and mid-latitudes (Berg and Stull, 2004) (Raupach, 1993). While these assumptions might not necessary hold for higher latitudes, it would be reasonable to investigate further. Firstly, we briefly remind parametrization schemes (1.1.1) and explain why we are focusing on eddy-diffusivity mass-flux. Then we process with methods for the analysis of the distribution of updraughts and downdraughts in the boundary layer. The conditional distribution of scalar quantities in updraughts is then the subject of the next part of the chapter.

The main idea behind *eddy-diffusivity mass-flux* (EDMF) schemes is that the CBL consists of a few strong updraughts and surrounding turbulent air with weaker updraughts and various downdraughts (Siebesma et al., 2007). *Strong updraughts* are arbitrarily defined as updraughts in a small fractional area a_u containing the strongest upward vertical motions (Siebesma and Cuijpers, 1995). (IFS IV, 2013, pp.39–40) . Strong updraughts at the bottom of the CBL are the basis of thermals that facilitate mass-transport of the warm moist air parcels higher up, while smaller eddies are responsible for the diffusive transport of heat and moisture in horizontal and vertical gradients. Some models of CBL also introduce terms for small-eddy counter-gradient transport. Although some recent articles on EDMF schemes have taken into account variation in the distribution of strengths of updraughts (Sušelj et al., 2012), many other sources simply assume that the distribution of vertical velocity of updraughts and downdraughts follows a normal distribution (IFS IV, 2013, pp.41-42) .

Under the assumption that the distribution of vertical velocities w at a given level follows a normal distribution $\mathcal{N}(0, \sigma_w^2)$, the values of vertical velocities in strong updraughts must fulfil $w_u \geq \sigma_w \cdot \mathsf{z}_{1-a_u}$, where z_{1-a_u} is the $1 - a_u$ quantile of the normal distribution. The kinetic energy $\tilde{E}_w$ of strong updraughts is then calculated using the pdf of the normal distribution (Casell and Berger, 2002, pp.102-103) as

$$\tilde{E}_w = \frac{1}{2} \int_{w \geq \sigma_w \mathsf{z}_{1-a_u}} w^2 \, \frac{1}{\sqrt{2\,\pi}\,\sigma_w} \, \exp\left(\frac{-w^2}{2\sigma_w^2}\right) \mathrm{d}w, \tag{3.8}$$

which could be analytically evaluated (for details, see appendix A) as

$$\tilde{E}_w \;=\; \frac{1}{2}\sigma_w^2 \int_{s \geq \mathsf{z}_{1-a_u}} \frac{s^2}{\sqrt{2\,\pi}} \exp\left(\frac{-s^2}{2}\right) \mathrm{d}s \;=\; \frac{1}{2}\,\sigma_w^2 \left(\frac{\mathsf{z}_{1-a_u}}{\sqrt{2\,\pi}} \Big(\exp \frac{\mathsf{z}_{1-a_u}^2}{2} \Big) + a_u \right), \tag{3.9}$$

In the case of different, non-symmetrical distributions, results might be different. For a direct comparison, we perform a numerical estimation of the kinetic energy as

$$\hat{E}_w = \frac{1}{2\,N} \sum_{w \geq S_{w,\,1-a_u}} w^2, \tag{3.10}$$

where N is the total number of recorded values at a given level and $S_{w,\,1-a_u}$ is the sample quantile of the recorded vertical velocities for the probability $1 - a_u$.

3.4.3 Conditional Statistics for Updraughts

The EDMF schemes are not concerned with each single updraught plume, but with their overall effect on the transport of heat, moisture and momentum in the areas of convection (Witek et al., 2011). The important property is the transport within the strong updraughts. Some EDMF schemes further distinguish between updraughts with condensation and dry updraughts (Sušelj et al., 2012). If the potential temperature or some other scalar quantity denoted φ is higher by $\triangle_u \varphi$ than the surrounding environmental air, then the transport of the said quantity by strong updraughts (in a kinematic form) yields

$$\overline{(w'\varphi')}_u = a_u \;\cdot\; w_u \triangle_u \varphi + a_u \, \overline{(w'\varphi')}_u^{(u)}, \tag{3.11}$$

where $\overline{(\;)}^{(u)}$ is averaging over the area of updraughts only. Some of the implementations of EDMF schemes assume that the second term is relatively negligible in comparison with the first term (IFS IV, 2013, pp.42). Although single updraughts and downdraughts can attain various values of potential temperature and humidity, the essential part is evaluating their overall distribution.

The evaluation of updraughts as described in the previous subsection is further extended by processing the values of the potential temperature and other scalar quantities.

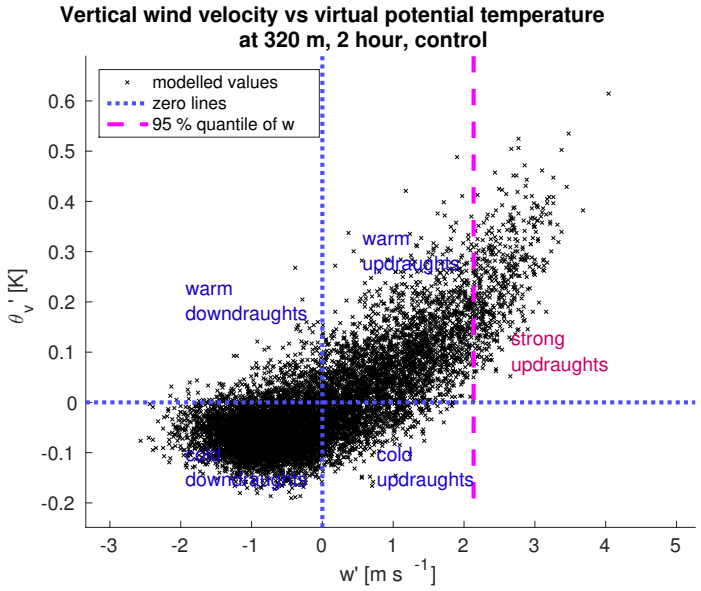

Figure 3.8: The example of a scatterplot of updraughts and downdraughts in the CBL, using vertical velocity and virtual potential temperature perturbations from the mean. This figure is generated from the values on the vertical level 320, approximately in the middle of the ML that reaches the depth $z_i = 630$ m at 2 hour.

To further investigate this topic, we perform a *quadrant analysis* (Mahrt and Paumier, 1984). The main idea behind this method is that plotting a 2D statistical distribution of $[\varphi' \text{ vs } w']$ offers a good insight into differences between updraughts and downdraughts (see figure 3.8 for example of cold and warm updraughts). This method of visualisation has been used with various adjustments in a number of research publications (Stull, 1988, p.463). It can be applied both for model and observational data. The common choices of evaluated scalar quantities include potential temperature (Sullivan, 1998), liquid water potential temperature (Sušelj et al., 2012), virtual potential temperature (Mahrt and Paumier, 1984) and liquid water content (Kang et al., 2007).

To better assess the joint probability distribution of the vertical velocity and perturbations in the scalar quantity (Berg and Stull, 2004), we can apply one of the following two methods:

- *Thresholding* - setting intervals for both φ' and w', then counting number of datapoints that falls into each interval.
- *Gaussian Blur* (Shapiro and Stockman, 2001, pp. 137–150) by the expected trust region for the values. Each datapoint is replaced by a joint pdf of φ vs w representing values that are expected in the grid cell. Variances in φ and w are taken from the modelled subgrid variances

$$\overline{(\varphi'\,\varphi')}_{SG}(z_c) \quad \text{and} \quad \overline{(w'\,w')}_{SG}(z_c),$$

multiplied by a tuning parameter α_a, so the kernel of resulting pdf of updraughts and downdraughts yields

$$f(\varphi, w) \propto \sum_{i,j} \exp\left(\frac{-1}{2}\left(\frac{(\varphi-\varphi_{i,j})^2}{\sigma_\varphi^2}+\frac{(w-w_{i,j})^2}{\sigma_w^2}\right)\right), \tag{3.12}$$

$$\text{where} \qquad \sigma_w^2 = \alpha_a \overline{(w\,w)}_{SG}(z_c), \qquad \sigma_{\varphi'}^2 = \alpha_a \overline{(\varphi'\,\varphi')}_{SG}(z_c),$$

and the multiplicative constant is evaluated afterwards (see example in figure 3.9). The joint distribution $P(w\varphi)$, (as shown in the figure 3.9) then serves for further analysis of the properties of the ABL. The marginal distribution of the scalar quantity in strong updraughts is approximated by integration over all $w \geq S_{w,1-a_u}$.

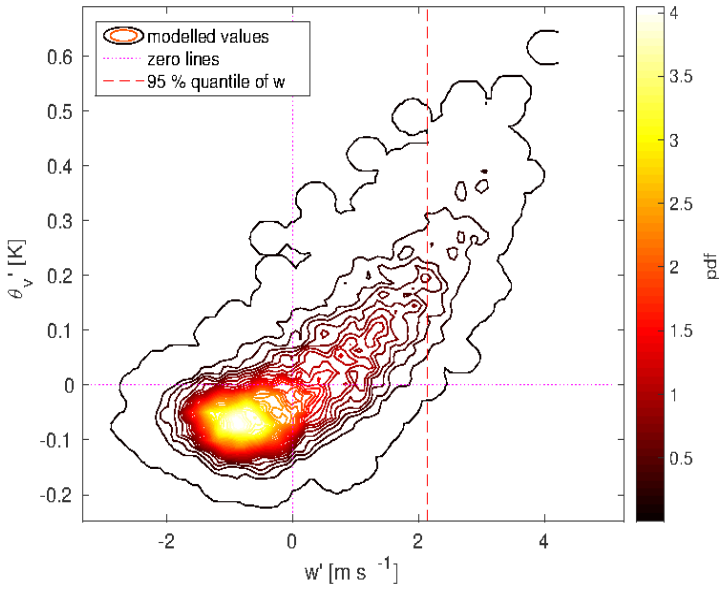

Figure 3.9: The example of the joint pdf of perturbations in vertical velocity w and virtual potential temperature θ_v that was computed from gridpoint values shown in figure 3.8.

3.4.4 Sub-mesoscale Variability

The evaluation of the overall vertical structure of CBL in CAO and the resulting vertical transport of the heat and momentum within the CBL are of a great importance (Song and Yu, 2012) (Papritz et al., 2014). While there could be a significant variation in structural parameters on both large and local scales (Cheinet and Siebesma, 2009), observed variability in structure of CBL could be divided into mesocale and sub-mesoscale fluctuations (Strunin and Hiyama, 2005). The sub-mesoscale variability could be modified by inhomogeneity in surface conditions (Shen and Leclerc, 1995) (Górska et al., 2008). Furthermore, it can have a significant effect on results of airborne field studies and their

comparison with numerical models (LeMone et al., 2003). Therefore, this part of the chapter intends to provide tools for the analysis of sub-mesoscale variability.

While the distribution of updraughts and downdraught is approximated over the whole model domain, it does not reflect local differences. To address the spatial variability in resulting boundary layer fluxes, we apply coarse sampling inspired by coarse-grained study in a cloud resolving model (Shutts and Palmer, 2007). The model domain is horizontally divided into a number of square shaped column subdomains (as shown in figure 3.10). The vertical extent of each subdomain is over the whole vertical extent of the domain. Vertical fluxes of sensible heat, latent heat and momentum are separately evaluated in each subdomain. The length of the side of each subdomain should be set higher than the horizontal extent of the observed convective structures.

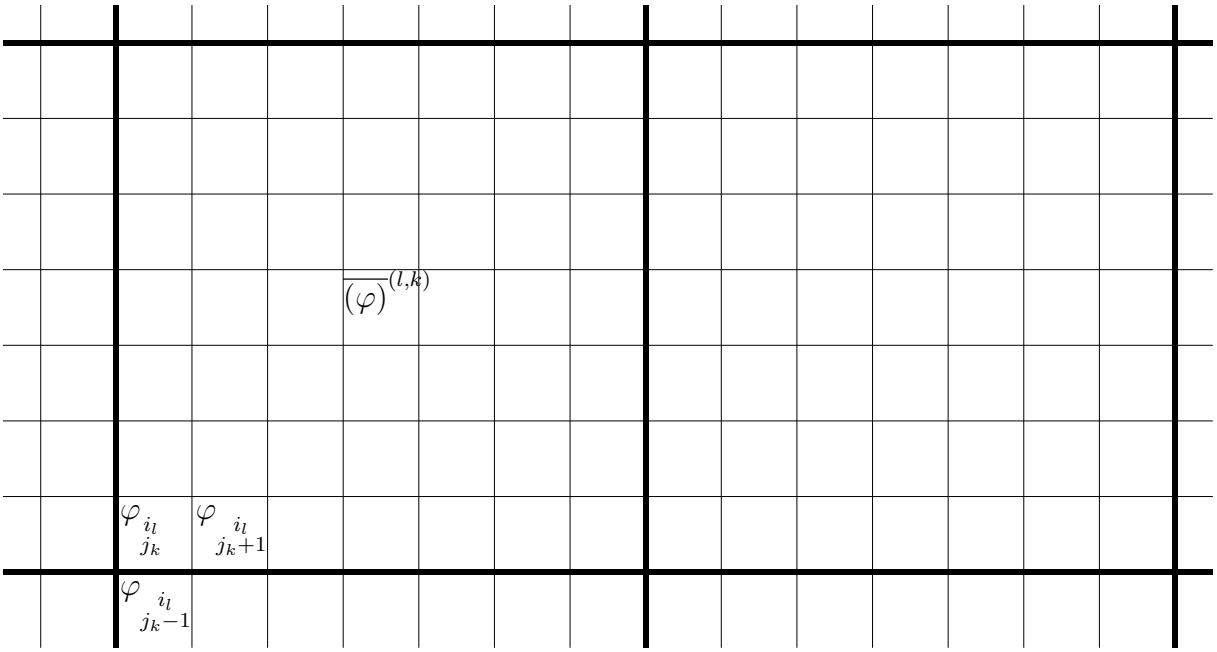

Figure 3.10: The illustrative example of a horizontal grid and the subdomains, and subdomain mean values.

At each output time, the LEM records instantaneous values of three dimensional fields of vertical velocity w and each observed scalar quantity φ. The vertical flux of a scalar quantity φ at in each subdomain marked l, k then yields:

$$\overline{w'\varphi'}^{(l,k)}(z) = \frac{1}{(i_{l+1} - i_l) \cdot (j_{k+1} - j_k)} \sum_{\substack{i \in [i_l, i_{l+1}) \\ j \in [j_k, j_{k+1})}} \Big(w(x_i, y_j, z) - \bar{w}^{(l,k)}(z)\Big) \cdot \Big(\varphi(x_i, y_j, z) - \overline{\varphi}^{(l,k)}(z)\Big), \tag{3.13}$$

where i_l and j_k are indices of LES gridpoints in the South–East corner of each subdomain, and $\overline{\varphi}^{(l,k)}$ is a horizontal mean value of the scalar quantity φ within the subdomain. Estimated values of vertical fluxes from each subdomain are then compared against the

domain–wide horizontal mean at a given timestep $\overline{w'\varphi'}(z,t)$. For a better assessment of the variability, minimum, maximum, 0.25 and 0.75 quantiles of resulting values over subdomains are calculated. This allows the construction of a min–max envelope of the subdomain set showing the likely extent of possible values. Steps of the evaluation are depicted in figure 3.11.

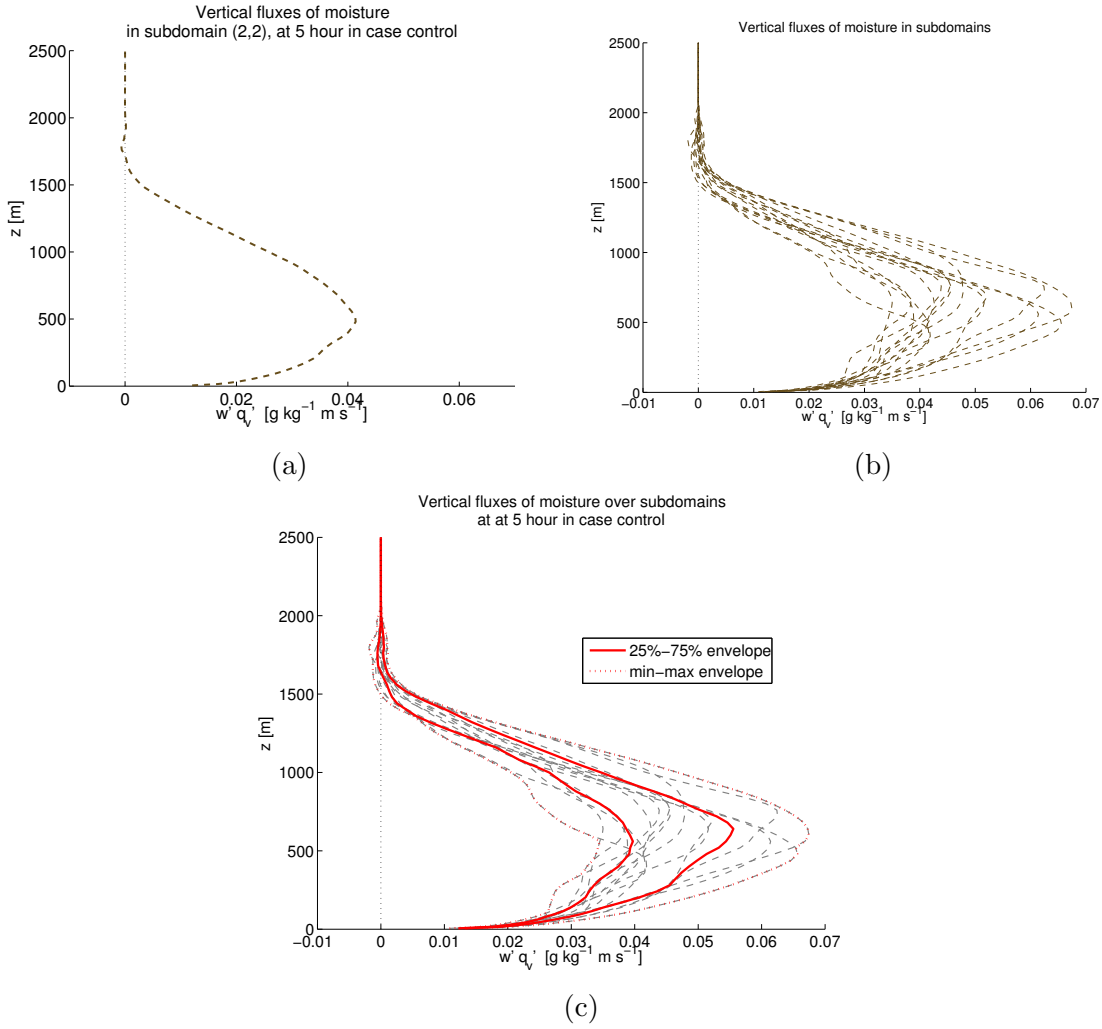

Figure 3.11: Illustration of steps in subdomain evaluation for kinematic moisture flux in one timestep of the model run. The profile values of $\overline{w'\varphi'}^{(l,k)}$ are computed in each **(a)** subdomain separately. **(b)** From the set of all these profiles is then calculated **(c)** the min-max envelope that encloses the whole set and $[0.25, 0.75]$ quantile envelope.

Subdomains obtained from the runs with the same forcing and initial conditions can be viewed not only as a separate representations of subdomain variability, but also as a sample of a larger size. This larger set of all subdomains can be further statistically processed. Box-and-whisker diagram (Tukey, 1977) with the standard setting of whiskers as 1.5 of the interquartile range (IQR) provides a measure of the spread (Weisstein, 2015) in the values of fluxes. Constructing box-and-whisker at each model level in the lower troposphere allows to a visualisation of the spread of flux values within CBL. Further-

more, it provides a measure for the spread of subdomain fluxes (see 3.12) in the runs with surface heterogeneity.

The IQR and whiskers of the control run provides an expected spread in the values of vertical fluxes. When the mean vertical fluxes differ between the model runs, the box-and-whiskers plots allow to demonstrate whether the differences between the CBL are larger than the variations within the CBL itself. Furthermore, the whiskers spread suggest whether two different surface conditions lead to a similar variability within the developing CBL.

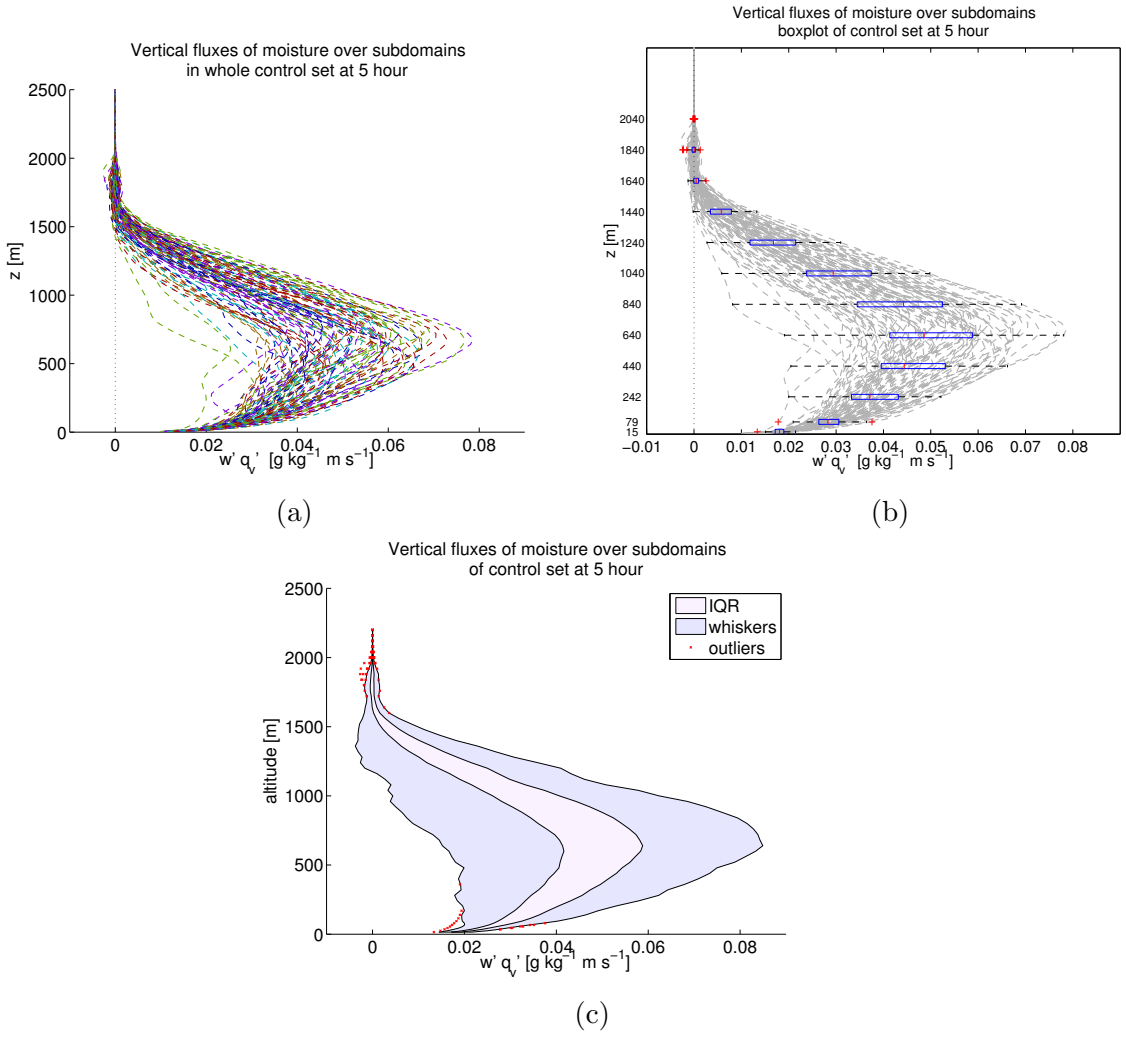

Figure 3.12: Illustration of steps in subdomain evaluation for kinematic moisture flux in the control set. The set of all subdomain profiles $\overline{w'\varphi'}^{(l,k)}$ in the same timestep of all runs of control set **(a)** is collected. The IQR and whiskers are calculated at each model level. The box-and-whisker illustrates that at a few chosen levels **(b)**. In the figures that compare some modified model runs, control set box-and-whiskers are visualised in the form of a colour shading **(c)**.

A higher amount of subdomains would allow us to perform further statistical test. One possibility would be the comparison of the subdomains that are approximately at the same distance downwind (i.e., line of subdomains in the x-direction). This would then allow to further investigate the spatial variability in CBL. Other option would be to estimate the statistical distribution of the values of subdomain fluxes. However, the size of the domain in this study is limited to single-core runs. Therefore, it was not possible to utilise runs with larger domain that would allow division into a high number of subdomains that would be still representative enough.

Still, it is important to stress that this analysis provides a measure of the spatial variability in instantaneous values of vertical fluxes, not a measure of the spatial variability in their time-averaged values. Therefore, it does not show whether subdomain values further from the mean are a longer lasting phenomenon or just a product of temporal oscillation in the CBL (Letzel and Raasch, 2003). Nevertheless, the statistical evaluation of the subdomain values provide an insight into a local sub-mesocale variability in CAO. It might also contribute to explanations of the variability in estimated fluxes from airborne observations (see Chapter 6).

3.4.5 Vertical Fluxes

A growing CBL is likely to trigger temporal oscillations (Kang, 2009) in vertical fluxes of heat and momentum. Temporal oscillations have been studied both in field observations (LeMone et al., 2003) and LES studies (Letzel and Raasch, 2003). While the effect on large surface heterogeneities was studied in mesoscale models (Kang and Davis, 2008), this study tries to provide an evaluation of the effect of convective scale heterogeneities on oscillation within CBL fluxes. Therefore, this part of the chapter provides a methodology for the analysis of variability in vertical fluxes within the CBL.

To offer greater insight into the time variation of the vertical transport in the troposphere, timeseries of vertical fluxes of sensible heat, latent heat and momentum flux, as well as their related fluxes in kinematic form, are recorded at chosen altitudes inside the ABL and in the free atmosphere above. Specific setting of these altitudes representing different part of troposphere (see 3.2.7 for details) are left the same within a batch of model runs .

Turbulence parametrization schemes usually evaluate the general tendency in the vertical flux $\overline{(w'\varphi')}$ of the scalar quantity φ, however the spatial and temporal variability in the value of the flux (Letzel and Raasch, 2003) is often ignored. While the spatial variability was the subject of the previous section, now we focus on the variability in

time. The timeseries of the horizontally averaged values of vertical flux at the altitude z is denoted $\overline{(w'\varphi')}(t;z)$. This timeseries can decomposed as

$$\overline{(w'\varphi')}(t) = \overline{(w'\varphi')}_{(\mathrm{gen})}(t) + \triangle_{w'\varphi'}(t), \tag{3.14}$$

where $\overline{(w'\varphi')}_{(\mathrm{gen})}(t)$ represents the mean and tendency. The temporal perturbation in source terms $\triangle_{w'\varphi'}(t)$, is then modelled as a Markov Chain

$$\triangle_{w'\varphi'}(t) \Big| \triangle_{w'\varphi'}(t-\delta t) \;\sim\; P_{\triangle,w'\varphi'}, \tag{3.15}$$

where δt is the time step.

Each flux timeseries defined in 3.2.7 is first divided into three segments:

1. the stable regime
2. the propagation of the internal boundary layer (Renfrew and King, 2000, pp.336–337) through the altitude of recording
3. the convective boundary regime

If there are visual signs of a repetitive pattern and the length of the segment allows it, the power spectra are estimated. The segment of the series is first detrended and periodogram estimators $\widetilde{PW}(f_k)$ for frequencies f_k are constructed in each segment of detrended values $\overline{(w'\varphi')}(t)$ marked as $(c_j)_{j=1,\dots N}$. The periodogram estimator for the sample $(c_j)_{j=1,\dots N}$ is defined (Press et al., 2007, pp.653–654) as

$$C_k = \sum_{j=1}^{N-1} c_j \exp\left(2\pi jk/N\right), \quad k = 0,\dots,N-1 \tag{3.16a}$$

$$\widetilde{PW}(f_k) = \frac{1}{N^2}\left(|C_k|^2 + |C_{N-l}|^2\right), \qquad f_k = \frac{k}{(N\delta t)} \quad k = 1,2,\dots(N/2-1),, \tag{3.16b}$$

where δt is the length of the timestep. Under the assumption that the length of the timestep does not significantly change in the observed segment, this method is a relatively good estimator of the signal frequencies (Oppenheim et al., 1999).

With a goal to estimate the $\triangle_{w'\varphi'}$, a decomposition of the timeseries is performed. Applying smoothing by the moving average (Press et al., 2007, p.767) of the length λ_t in the time domain, we can divide the timeseries into a smoothed part associated with the general trend and a series of residua

$$r_{w'\varphi'}(t_i) = \overline{(w'\varphi')}(t_i) - \overline{(w'\varphi')}_{(\mathrm{sm}),\lambda_t}(t_i), \tag{3.17}$$

where $\overline{(w'\varphi')}_{(\mathrm{sm}),\lambda_t}(t_i)$ is the smoothed part of the series.

The series of residua then allow an estimation of the conditional distribution of perturbations from the simple Markov Model. An empirical pdf is obtained by bracketing of the values of residua. For a smooth estimation, we then apply the Gaussian Blur in a similar way to 3.4.3

$$f_{w'\varphi'}(r_{+\delta t}, r) \propto \sum_j \exp\left(\frac{-1}{2}\left(\frac{(r_{+\delta t} - r(t_j + \delta t)^2}{\widetilde{\sigma_r}^2} + \frac{(r - r(t_j))^2}{\widetilde{\sigma_r}^2}\right)\right), \quad \text{where} \quad \sigma_r^2 = \alpha_r \, \overline{(w'\, w')}_{SG}(z_c), \tag{3.18}$$

An approximation of the joint pdf $f_{w'\varphi'}(r_{+\delta t}, r)$ of the residual part of fluxes is then calculated, followed by the evaluation of the conditional pdf $P_{w'\varphi'}$

$$P_{w'\varphi'}(r_{+\delta t}|r) = \begin{cases} \dfrac{f_{w'\varphi'}(r_{+\delta t}, r)}{\sum\limits_{\forall \tilde{r}} f_{w'\varphi'}(\tilde{r}, r)} & \text{for } \sum\limits_{\forall \tilde{r}} f_{w'\varphi'}(\tilde{r}, r) > \epsilon_0, \\ 0 & \text{for } \sum\limits_{\forall \tilde{r}} f_{w'\varphi'}(\tilde{r}, r) < \epsilon_0, \end{cases} \tag{3.19}$$

where ϵ_0 is a very small numerical threshold set to avoid problems with numerical artefacts. The conditional pdf shows the dependence of the values of residua in the current step on values of residua in a previous timestep. In case the oscillations behave like a white noise, the residua are uncorrelated and the contours would approximately attain a shape of a one large square without any peaks inside. However if oscillations are conditionally dependent, the residua are correlated and the shape will be different.

If the conditional pdf indicates a correlation in between some adjacent residua, the next step consists of estimating the autocorrelation $R_{\mathrm{A}}(\tau)$ in the timeseries of residua. Under the assumption that the length of timestep does not significantly vary in the observed segment, the sample autocorrelation (Wichern, 1973, p.236) is calculated as

$$R_{\mathrm{A}}(k \cdot \delta t) = \frac{1}{\sum_{j=1}^{N-k}(r(t_j) - \bar{r})^2} \sum_{j=1}^{N-k}(r(t_j) - \bar{r})^2 (r(t_{j+k}) - \bar{r})^2, \tag{3.20}$$

where N is the number of timesteps in the segment and $\bar{r}$ is the mean value of residua. Due to a short length of the segment 2 (the propagation of the IBL) at majority of recording altitudes, the sample autocorrelation is calculated only for segment 3 (the CBL regime) of each flux timeseries. The values of autocorrelation are then visualised by *Autocorrelation Plot* (Box and Jenkins, 1976, pp.28-32). The whole process is illustrated in the figure 3.13.

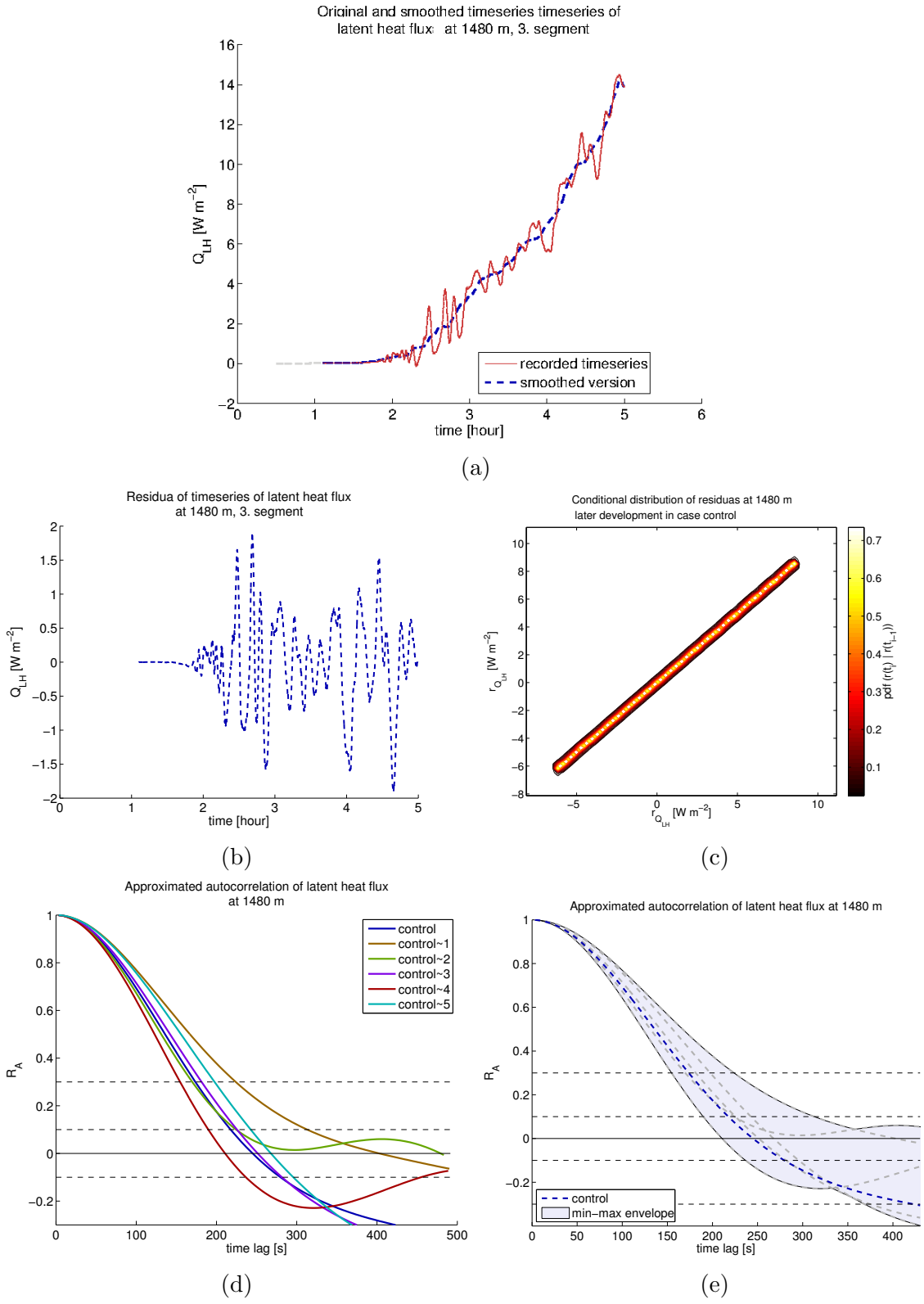

Figure 3.13: Illustration of steps in the evaluation of vertical fluxes. The timeseries of the latent heat flux at chosen altitude is smoothed **(a)** and the residua in segment 3 are separated **(b)**. Conditional pdf is calculated from residua **(c)**. Autocorrelation of residua is calculated for each run in the control set **(d)** and the control set min-max evelope is prepared **(e)** for further comparisons.

3.5 Sensitivity Testing

The presented methodology for the LEM model runs and their comparison with a caontrol set is inevitably going to raise questions on how sensitive the results are to the choice of model parameters. To address the question of sensitivity to the setting of the grid and the initial conditions, a set of model runs with adjusted setting was prepared. The construction of sensitivity tests was inspired by a sensitivity testing describe by Muller and Chlond (1996) and by Agee and Gluhovsky (1999). The focus is given both to the questions of vertical and horizontal resolution as well as to the issue of setting of some initial conditions.

In the part of the chapter on the computational setting of the model (3.2.4), it was stated that the choice of the domain size and the resolution of the grid were subject to careful consideration. Therefore, this part of the chapter will first focus on the sensitivity of the model results to the size of the domain 3.5.1 and resolution both in vertical and horizontal directions (3.5.2). Then we address the issue of the formation of a shallow CBL and its early development. For this purpose, we utilise a very-high resolution LEM runs (3.5.3).

The development of a CBL might also be affected by an increase in humidity. A higher humidity is likely to lead to an earlier formation of clouds and their swift growth. With a goal to check whether an increased humidity would lead to a qualitative changes in CAO development, runs were performed with humidity increased to Rh 80 % and 85 %. The results showed that changes in the initial humidity do not lead to any qualitative changes in the developing CBL. In this part of the thesis, we present just the main results. Other figures on sensitivity testing are in the Appendix.

3.5.1 Sensitivity to Domain Size

While grid size and resolution are often considered a source of possible errors (Cheng et al., 2010), we are going to evaluate how sensitive are model results to these parameters, firstly the domain size. It is preferable to to analyse this model parameter first, since many of the later test runs were executed with a smaller domain due to memory limitations. To briefly remind, the requirement of the domain size is that it is sufficiently large to capture cloud rolls and possibly also gravity waves (see 3.2.4) for details.

For the purpose of testing sensitivity to the domain size, we performed a set of runs that differed from the control run (see tables 3.2 and 3.3) in the setting of the domain size:

- Control; **16 km** ×16 km.

- Horizontal extent of the domain extended to **19.2 km** ×19.2 km.
- Horizontal extent of the domain extended to **25.6 km** ×25.6 km.
- Horizontal extent of the domain decreased to **12.8 km** × 12.8 km.
- Horizontal extent of the domain decreased to **4.8 km** × 4.8 km.
- Vertical depth of the domain decreased to **5 km**. Due to changed in the depth of the domain, damping layer of the depth 2 km is starting at the altitude 3 km.
- Vertical depth of the domain decreased to **5 km** and the horizontal extent of the domain decreased to **12.8 km** × 12.8 km. Damping layer of the depth 2 km is starting at the altitude 3 km.

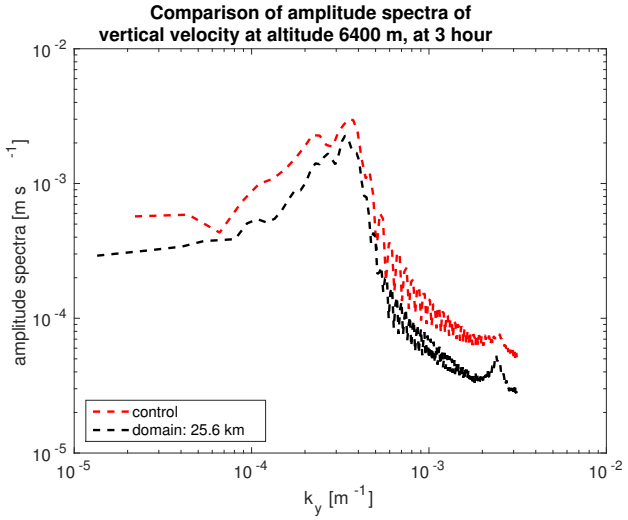

Figure 3.14: The sensitivity of the spectra of the upper atmosphere to increased domain size

The analysis of the results of this test set did not reveal any specific changes in the development of the CBL. The surface fluxes of heat and moisture exhibited virtually no difference. The differences in the other CBL properties were as similar between runs as with the control setting. The evaluation of the frequency spectra in the upper atmosphere showed a minor difference between the control run and the run with the domain size '25.6 km'. The amplitude spectra were slightly lower in '25.6 km' case (see figure 3.14), however the peak in the spectra was located at the same wavenumber. The slope towards higher wavenumbers was also similar in both cases. Since the increase in the domain size yielded no qualitative changes in results, we conclude that the domain size in the control run (16 km × 16 km) is large enough to capture waves generated by convection.

We conclude that the simulation of CBL in CAO is not sensitive to a reasonable decrease in the model domain size. Therefore, it is possible to execute tests with increased model resolution on a smaller domain. However, it is important to stress that this applies to CBL only. The model runs with a smaller domain will not be included in the evaluation of the spectral properties of the upper atmosphere.

3.5.2 Sensitivity to Resolution

With an aim to evaluate the sensitivity, we performed a number of runs with modified horizontal and vertical resolution. These runs were then compared against the control run. While the surface conditions were the same as in the control run (ie. spatially homogeneous), a question arises as to whether the results are applicable also on the runs with heterogeneous surface conditions. The heterogeneity in surface temperature present a forcing that generates a secondary circulation (Gryschka et al., 2008). It might possibly exhibit a different sensitivity to model resolution. Therefore, we have also performed additional model runs with different horizontal resolution for the same heterogeneity setting. The description of model runs follows.

The setting of vertical resolution is defined in the table 3.7. The control run (with 'vres0' setting) and the run with 'vres1' resolution (see 2.3.1 for explanation) are compared against the runs with the decreased vertical resolution **'vres01'** and the increased vertical resolution **'vres01'**. Again, the remaining settings were kept same as in the control case.

height [m]	spacing [m]			
	vres01	**vres0**	vres1	vres2
7500–12000	100	100	240	240
2500–7500	100	100	130	14
100–2500	20	40	40	60
0–100	10	10	20	20

Table 3.7: The setting of vertical layers in the simulations for sensitivity testing

In a similar way, the impact of the horizontal resolution in the lower troposphere was examined. The horizontal spacing Δx was always kept the same for both horizontal directions. The runs were performed on a grid with the horizontal extent 120×120 points. Setting of other model properties remained the same as in control run unless stated otherwise:

- $\Delta x = \mathbf{480\ m}$
- $\Delta x = \mathbf{320\ m}$

- $\Delta x = \mathbf{160\ m}$
- $\Delta x = \mathbf{80\ m}$
- $\Delta x = \mathbf{40\ m}$

The additional set consisted of model runs with heterogeneous surface conditions. For simplicity, we present the result only for the set of the model runs with the type 'along', of the pattern block of the size $d_{(\mathrm{h})} = 1600\mathrm{m}$, temperature scale $\delta_{(\mathrm{h})}T = 3\,\mathrm{m}$ diminishing over time (see 3.3.2). The setting of the horizontal resolution were following:

- $\Delta x = \mathbf{160\ m}$ (Standard setting)
- $\Delta x = \mathbf{80\ m}$, performed on a grid with the horizontal extent 120×120 points.
- $\Delta x = \mathbf{40\ m}$, performed on a grid with the horizontal extent 120×120 points.

Again, the rest of the LEM setting is maintained the same as in the control run.

The runs with coarse resolution exhibited significant differences in the formation of clouds and vertical fluxes of heat and moisture. Surface fluxes were more than 30 % lower at 1 hour than in the control run. Although this difference vanished by 2 hour, the amount of cloud water was still more than 3 times underestimated. We conclude that coarse resolution is not suitable for this CAO scenario and continue with other test runs.

On the other hand, none of these test model runs with increased resolution indicate a qualitatively different development of the boundary layer, however there are significant quantitative variations that should be further taken into account. The increase in the horizontal resolution altered the distribution of convective clouds, which is consistent with previous research on shallow cumulus clouds (Brown, 1999b). Although an increase of horizontal resolution to 20 m was suggested (Matheou et al., 2011), it would require further decreasing in the model domain size to avoid computational issues.

Further investigation of wind velocity fields revealed that there are changes in the structure of eddies inside clouds. The increased resolution lead to changes in resolving the secondary circulation, as described in a study on convectively induced secondary circulation (Ching et al., 2014). The model runs with increased finer resolution showed an increased liquid water mixing ratio in clouds, however altitudes of the cloud base and the cloud tops do not differ between runs (see figure 3.15).

The impact of increasing the resolution was similar also in the model runs with heterogeneous surface conditions. The model runs with increased finer resolution again

show an increased liquid water mixing ratio in clouds, however this effect is similar to the runs with homogeneous surface conditions. There were also changes in the secondary circulation by the surface, yet relatively minor in scale. Although the variance in the vertical velocity differed between the runs during 1-2 hour, the differences in the vertical flux of moisture in ML did not exceed 7%.

Perhaps surprisingly, the increase in the vertical grid resolution does not lead to significant changes in the amount of cloud liquid water, indicating that both setting of vertical resolution are sufficient for resolution of cloud motions. We have indicated a slightly increased spread in the vertical momentum flux during the second hour between the model runs. However, there is not a clear trend in this spread. While further result of the model sensitivity to horizontal and vertical resolution are not essential to this chapter, they are instead shown in the Appendix.

In summary, model results are influenced by the horizontal and vertical resolution of the simulation. However, further increase in the model resolution leads only to a minor quantitative changes in the amount of cloud liquid water. Although the higher horizontal resolution allows us to resolve more of the secondary circulation within clouds, the effect on the overall transport within CBL is relatively small. The impact of the increased resolution in runs with spatial heterogeneities in surface temperature is similar as the runs with homogeneous surface conditions. We conclude that the resolution of the control run is suitable for this study of CBL.

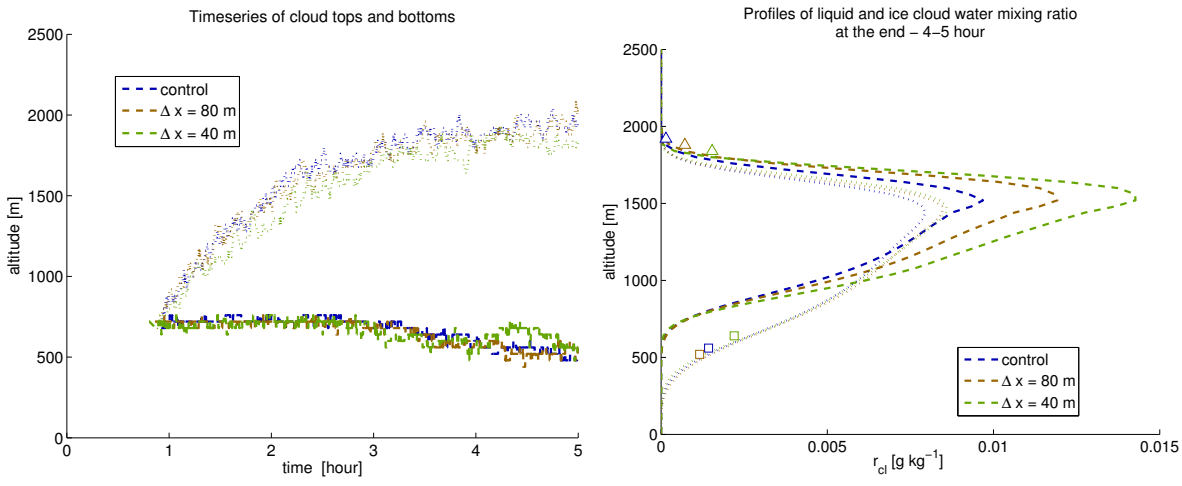

(a) (b)

Figure 3.15: The sensitivity in the formation of clouds to the horizontal resolution Dashed line (−−) marks liquid cloud water, dotted line (· · ·) ice cloud water.
The symbol □ marks the altitude of cloud base, the symbol △ the altitude of cloud tops.

3.5.3 Early CBL Development

One of the main issues regarding the setting of a LES is that any computationally available choice of the resolution leads to the situation where the horizontal grid spacing is larger than the height of plumes in the shallow CBL (see 3.2.4). Therefore, during the formation of a shallow boundary layer, most of the heat and moisture transport is parametrized, rather than resolved (Couvreux, 2010). While the model runs in this study start with stratified surface conditions, we have to address the question whether the early development of the CBL is estimated correctly.

With an aim to investigate the impact of possible errors in the early CAO development, we set up two additional model runs with a very fine resolution and compare them with the control run. The setting is defined in table 3.9 Due to very high resolution, the size of the model domain is reduced. This further implies that these model runs can properly capture convective eddies only in a shallow CBL. The size of the convective eddies was checked from the horizontal cross-sections of velocity fields.

property		setting	
		'fine'	**'extrafine'**
domain	width in x	1.2 km	0.48 km
	length in y	1.2 km	0.48 km
	height	5 km	5 km
horizontal resolution		10 m	6 m
vertical resolution			
	height [m]	spacing [m]	
	2500–5000	125	125
	500–2500	40	37
	100–500	6	6
	0–100	5	4
damping layer		2 km deep, located above 10 km	

Table 3.9: The setting of 'fine' and 'extra-fine' model runs

The comparison of the control run with the runs with fine resolutions shows that there are some qualitative differences. The model runs 'fine' and 'extrafine' capture the formation of condensation in plumes over the surface layer. Although this phenomena is supported by observations (Renfrew et al., 1999), here it is just of a minor importance. On the other hand, there are no significant differences in the surface fluxes of the sensible and the latent heat. For a better demonstration of the quality of subgrid estimation, we focus on the vertical flux of moisture in the early CBL. The comparison

of the control run with the 'extrafine' run shows that during the first half hour, only a small portion of the moisture flux is resolved by the model (see 3.16a). In addition to that, LEM parametrization of the subgrid flux underestimates the flux of moisture. However, this quickly changes with the deepening of the CBL. During 0.5–0.75 hour, more than 75 % of the model moisture flux is resolved in the control run. Furthermore, the subgrid parametrization estimates most of the remaining portion of the flux.

In summary, the subgrid model in LEM allows to estimate the formation of the shallow CBL reasonable well. With the deepening of the shallow CBL during 0.5–0.75 hour, most of the kinetic energy and flux become resolved. Although the flux of moisture is slightly underestimated during 0–0.5 hour, it seems that this issue disappears during the later growth of the CBL.

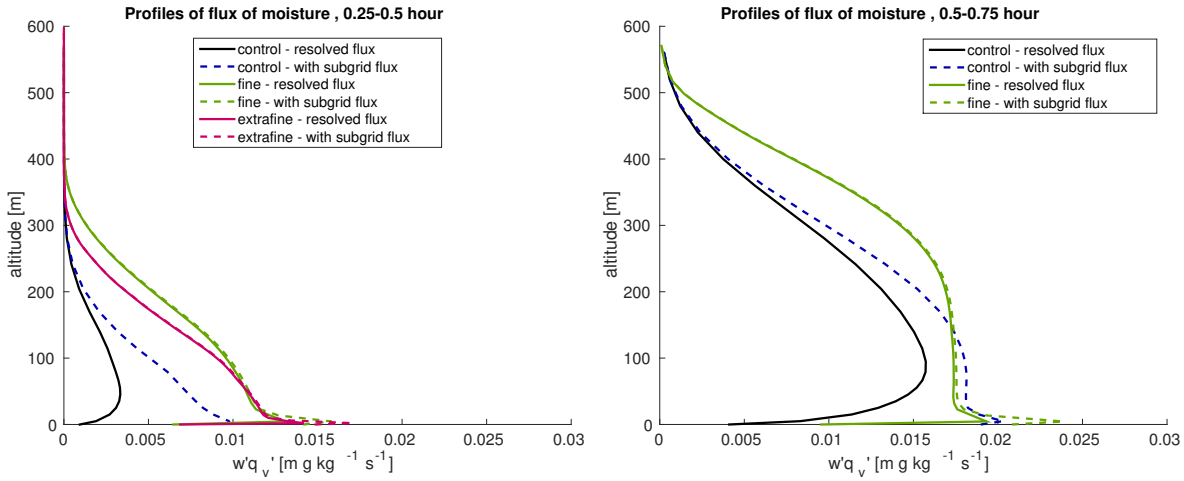

(a) (b)

Figure 3.16: The comparison of the control with the 'fine' and 'extrafine' resolution during the early development of the CBL.
Note: The 'extrafine' run is not shown in **(b)** since the larger eddies were not properly captured by the model anymore at 0.75 hour.

3.6 Discussion

Although the LEM is a powerful modelling tool, there are number of issues and open questions related to the software and its setting. In this discussion, we are going to address the main issues that might be invoked by the idealised setting, as well as various possible shortcomings generally attributed to LES. Firstly, we will cover the model resolution. Secondly, we will look upon the Quasi-Lagrangian domain. And then we will cover other setup issues that are specific to LEM.

The common argument against the results of LES studies usually involves paraphrasing the fact that LES resolves just a part of the eddy cascade and therefore the results does not fully capture the effect of processes on smaller scales. This issue has been partially examined in the sensitivity study (see 3.5). In the current setting, a further increase in resolution led just to small changes in results , while computational expenses were growing much faster. Generally speaking, halving the grid spacing in all directions increases the computational cost by about the factor of 2^4 (Pope, 2004). However there are also other issues connected to increasing the resolution. On one hand, it is preferable to increase both the vertical resolution in the lower troposphere and the horizontal resolution to better resolve eddies in the early CBL development. On the other hand, it can result in disproportionate grid cells in the upper atmosphere – grid cells that are very narrow yet relatively high.

In addition, increasing the domain resolution soon encountered limits of processing on a single core of the supercomputer employed (UEA HPC Grace). Due to the original purpose of the LEM, its multicore processing scripts are optimised for a specific type of Met Office computers (Gray and Petch, 2004, p.7) and therefore relatively complicated to adjust for other machines. However, the successors of the LEM, which is currently under development (NERC, 2014), is supposed to be better adjusted for multicore computations. Therefore we expect that chosen batches of model runs might be rerun in the future with adjusted setting of the vertical and horizontal resolution.

One of the related issues is the question how representative are models during the different stages of the model development. A LES with a small horizontal extent of the domain and a high resolution allows us to resolve the small eddies in forming CBL, but the domain would not be large enough to model large eddies in cellular convection. On the other hand, a LES with a large domain that allows us to capture open or closed cells would pose and excessive requirements on memory unless the resolution was decreased. Notwithstanding, the large convective cells would not have developed due to length of the run (3.1). The model generally covers just the development of convective rolls. Previous observations have shown that open and closed cells does not appear until 100 km downwind (Brümmer, 1997) Furthermore, the early cells reach sizes 3–7 km (Brümmer, 1999) and therefore it would be possible to capture them in the model.

An alternative approach that allows us to properly capture various stages of CBL development is the adaptive resizing of the model domain by Muller and Chlond (1996). In their framework, the simulation starts with a small high resolution domain. CBL starts deepening and the strongest convective eddies are increasing in size. After a certain amount of time, the simulation is stopped and all the fields of prognostic variables are interpolated onto a coarse grid. The interpolated fields are then repeated to cover a larger domain, and used as the initial conditions for the new simulations. This process

is then repeatedly applied to cover the transition of cloud rolls and broadening of convective cells. Although this model suffers from a number of issues related to interpolation, it provides a good model representation for the developing CAO until late stages over open ocean (Schröter et al., 2005) (Gryschka and Raasch, 2005). Notwithstanding, this approach is not applicable in the LEM. Although it would be possible to modify LEM to allow directly inserting initial values of all prognostic fields, there is still an issue of the subgrid model. The subgrid part of the fluxes and the subgrid part of the energy are calculated by LEM subgrid model and cannot be separately inserted. This means that there is no way to add the contribution of resolved scales averaged through interpolation and the contribution of subgrid scales. The model would be therefore losing a portion of the kinetic energy and fluxes with respect to the previous step of the last run.

We have instead employed The Quasi-Lagrangian framework (see 3.2.3) that allows us to replace the horizontal extent of MIZ with a temporal change in surface conditions. While the periodic lateral boundary conditions in LEM 3.2.4 might be considered a serious limitation, they are suitable in case of this approach. This model property does not allow us to set different conditions upwind of the domain and downwind of the domain, since air leaving the domain downwind flows in on the other side. Therefore this approach is not suitable for modelling the development of a CBL on a sharp ice edge. However a long marginal sea-ice zone is reasonable approximated by a temporal increase in the surface temperature. A gradual increase in surface temperatures also allows us to fulfil the conditions that the secondary circulation related to the front of the travelling air is relatively small (Skyllingstad and Edson, 2009).

The Quasi-Lagrangian approach introduces a significant amount of simplification into the model. It does not allow us to capture the differential advection speeds caused by the wind shear (Szoeke and Bretherton, 2004). While the advection of the environmental air above the ABL can be easily added to model forcings (Gal-Chen, 1982, pp.2282-2285), the advection within the ABL remains an issue. However, the effect of the differential advection in a CBL is relatively weak in comparison with other simplifications used in LES studies of CBL. A thorough analysis of the Quasi-Lagrangian approach implied that the effect of surface temperature on variations in pressure exhibit a more significant influence (Putrasahan et al., 2013). Therefore, the Quasi-Lagrangian frame of reference is, despite various shortcomings an acceptable simplification in studies of convection (Richardson et al., 2007).

While the Quasi-Lagrangian framework exhibits aforementioned shortcomings, it also offers some advantages. Since the model time spent over a certain portion of the surface is in order of tens of minutes, we do not have to take into account the CBL feedback on the surface. If the timescale were larger, we would need to take into account that heat loss from the sea surface leads to the decrease in surface temperatures and the growth

of sea-ice. For example in CAOs with mean wind velocity similar to our model setup, the ice edge can expand 20 km offshore within less 12 hours (Inoue et al., 2004). Adding a surface feedback to the model would require a significant adjustment of the surface model. Therefore in this aspect, Quasi-Lagrangian domain helps avoiding issues that are present in static domain with prescribed inflow conditions.

Perhaps a more limiting factor in the current set-up of LEM is a treatment of aerosols and cloud microphysics. The model of cloud microphysics in LEM has undergone very little changes since 1998. Although the distributions of hydrometeors are treated by double-moment schemes, some other parts of microphysics are quite simple. The distribution of cloud water droplets follows single-moment scheme, described solely by the water mixing ratio (Gray and Petch, 2004, p.17-18). Furthermore, aerosols are treated as passive aerosols only and therefore their concentrations do not interact with cloud formation. However, an advanced model for microphysics and aerosols is expected in MONC, the successor software package to LEM (NERC, 2014).

There have been a number of questions surrounding the setting of the surface humidity. On the one hand, direct setting of surface microlayer that is not saturated usually resulted in a very weak convection. On the other hand, setting a slightly oversaturated surface microlayer with a goal to simulate conditions over a sea surface with a foam resulted in a formation of dense near-surface clouds. In the end, the simple solution was to switch on the model parameter for the saturated surface.

3.7 Summary of the Applicability of Methods

The main purpose of this chapter was to provide tools for extending our knowledge of the cold-air outbreak by means of Large Eddy Simulations. The chapter introduces the idealised CAO scenario, its setting in Met Office LEM and the methods for the analysis of model outputs. While the setting of initial profiles of prognostic variables is similar to previous studies of cold outbreaks performed in LEM, the novelty of the approach lies in the introduction of heterogeneous surface boundary conditions to LEM. The methodology presented in this chapter allows us to perform the extended study of idealised CAO scenarios that are presented in chapter 4 and chapter 5. These chapters also discuss the adequacy of the choice of model parameters as well as some possible shortcomings of the implemented model. Although the methodology in this chapter focuses on idealised large eddy simulations, it can be also applied in case studies of CAOs observed during field campaigns. However, in requires some further adjustment of surface conditions as well as direct input of the initial condition. The modification of the methodology for the purpose of CAO case studies is explained in 6.2.

Chapter 4

Idealised Large Eddy Model of Cold-Air Outbreaks with Surface Heterogeneity

The changing structure of sea ice (Yang and Yuan, 2014), together with high temperature gradients between the cold Arctic air and relatively warm sea water, contribute to uncertainty in the prediction of extratropical weather (Wacker et al., 2005) (Chapman et al., 1994). Since cold-air outbreaks contribute strongly to heat transfer in the polar areas (Papritz et al., 2014), a proper assessment of variability in them can help both in improving numerical weather prediction (NWP) as well as in planning future field campaigns. While the observations of the atmospheric boundary layer (ABL) in the Arctic are relatively sparse (Alexeev et al., 2012, pp.219-236) the purpose of this study is to enhance our knowledge by other means.

One promising possibility is to employ Large Eddy Simulations to numerically model a development of the convective boundary layer (CBL) in a cold air outbreak (CAO). Idealised model scenarios provide an opportunity to analyse the variability in the ABL over a heterogeneous surface in the marginal sea-ice zone (MIZ). Previous studies of a similar problem include mesoscale 2D studies such as (Chechin, 2013) and 3d studies of the impact of leads on CAO, for example (Gryschka et al., 2008). While some studies such as (Heerwarden et al., 2014) focused on the impact of scaling of heterogeneous pattern of surface fluxes in CBL, their results were limited by the choice of the fixed heterogeneous surface pattern. Two main questions addressed by this study are: whether the local structure of the MIZ plays a significant role in the developing CBL during a CAO; and whether it introduces more variability in its behaviour.

This chapter presents the results of idealised CAO scenarios simulated by the Met Office Large Eddy Model (LEM) following the methodology that was the subject of the previous chapter. First, it describes basic qualitative properties of the modelled

transition from stable boundary layer (SBL) to CBL capped with developing boundary layer clouds. The chapter further investigates variability in the developing CBL. The distribution of updraughts and downdraughts is described in section 4.1.2, while larger variations in the fluxes inside the domain are analysed in the section 4.1.3. With a goal to address the variability in vertical subgrid fluxes in NWP, modelled timeseries of fluxes of heat and momentum at chosen altitudes are evaluated and results are presented in the section 4.1.4.

To assess the impact of a spatial heterogeneity in surface temperatures, model runs with idealised heterogeneity in the surface temperature are compared against a control run in 4.2.1. The ensemble of model runs with control setting then allows us to estimate the inner variability in convection. Then, it is possible to evaluate how significant the impact of surface heterogeneities and surface roughness are against the background noise.

Limitations of this study and other related issues are discussed (4.3). The scope of the study is further expanded on a wider palette of CAO scenarios in Chapter 5. While the this chapter is concerned with an idealised model, the impact of heterogeneous surface forcing in an CAO case study is presented in Chapter 6. Although this study is mostly concerned with the ABL, the effects of the convection the troposphere above is also taken into account. Waves generated by convection and propagating into stratified layers above (Lane and Moncrieff, 2010). While the analysis of the gravity waves goes beyond the scope of this study, it is instead presented in the Appendix D.

4.1 Cold-air Outbreak over a Homogeneous Surface

The *control run* is an idealised example of a CAO over a spatially homogeneous surface. A cold air mass is advected over a cold homogeneous surface that starts warming up at time t_0 leading to a development of a CBL with convective clouds. The exact setting of large scale forcing as well as initial profiles of potential temperature and humidity follows 3.2. This part of the chapter first offers a brief qualitative comparison of CAO development that is followed by the evaluation of the internal structure of the CBL and the impact on fluxes averaged over the whole domain. The time coordinate is always given with respect to the reference point t_0, i.e. the time when the surface started warming.

4.1.1 Basic Qualitative Results

A rapid development of the convective boundary layer is observed after the increase of the surface temperature. Very shallow mixed layer (ML) starts developing during the first hour, with thermals forming over 900 – 1800 s and growing upwards in the following hours (see figure 4.1). Due to shallow depth of the early CBL the convectively

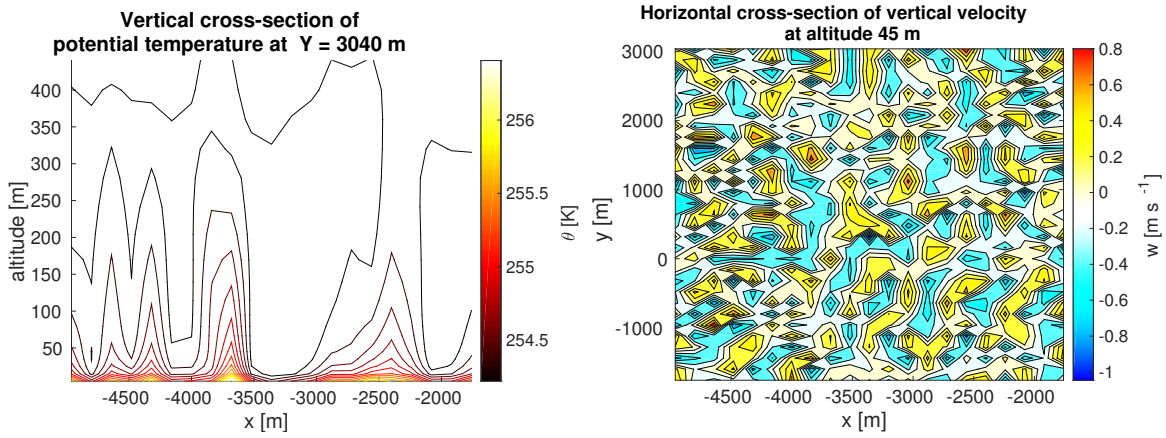

(a) (b)

Figure 4.1: The potential temperature and the vertical velocity at the bottom of a shallow CBL, 0.5 hour after t_0.

generated turbulence is not resolved at this stage (see for details 3.2.4). The sensitivity study showed that the subgrid model covers this early development relatively well (see for details 3.5.3), however CBL is not fully in the inertia part of the spectrum. Therefore is not considered representative enough. The further analysis is applied for model model result after 0.75 hour when the larger CBL eddies are fully in the LES-resolved regime.

While the bottom part of the atmosphere is swiftly warming after 0.75 hour, mild cooling is observed at altitudes above 500 m (see figure 4.2a). This phenomena is caused by penetrative updraughts and resulting displacement of the potentially warmer air from above. A contribution of the convection inside clouds should be also taken into account. Scattered clouds appear already at the end of the first hour, and the cloud layer then develops during the second hour. The radiative cooling at the top of the clouds then lead to a rapid growth of water droplets (Jiang and Cotton, 2000, p. 587). Developing clouds exhibit a shape prolonged in the direction of a large scale wind forcing. The location of clouds indicate a random pattern (see figure 4.3) without larger organised structures such as cloud streets.

Apart from large convective eddies of the size 2 km and larger, described also in number of observational studies (Atkinson and Zhang, 1996, p. 406–407), there are number of smaller structures. A cross-section of larger clouds reveals a secondary circulation as well as pockets of ambient air descending around them. A representative example of the developing cloud (see figure 4.4) exhibits both large convective eddies with strong updraught in the middle of the cloud as well as the secondary circulation. The indicated structure of clouds would classify them as cumulus clouds (Stull, 1988, pp.562–564) which is further supported by the potential temperature profiles (see figure 4.2a) showing an increase in the mean potential temperature inside the cloud layer.

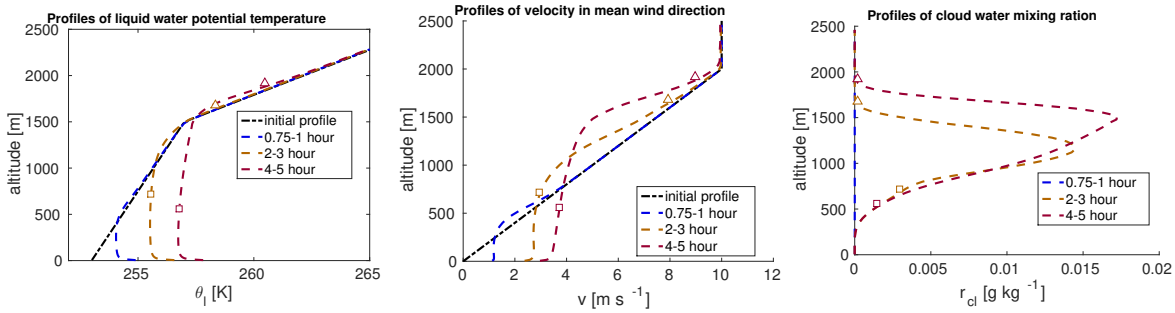

(a) (b) (c)

Figure 4.2: The development of the potential temperature and the wind velocity in the mean wind direction in the lower troposphere with the growing ABL. The symbol □ marks the altitude of cloud base, the symbol △ the altitude of cloud tops.

The structure of the cloud further shows that the centre of the strong updraught continues nearly up to the top of the cloud (see figure 4.4a). The centre is further surrounded by weaker updraughts and circulating patterns (see figure 4.4b). These organised circulating patterns were identified in other model studies of cumulus clouds (Klaassen and Clark, 1985). The circulating pattern are involves both the air within the cumulus cloud as well as around it. They indicate that the entrainment to the cumulus occurs not just at the top, but at all levels of the cloud (Blyth, 1993). The model results further shows that the descending air is mostly on the edges of clouds. The model results did not show any downdraughts that would be penetrating through the centre of the cloud. That agrees well with the study of Blyth et al. (1988) and their concept of the undiluted cloud core that drives the entrainment into the rest of the cumulus clouds. However, their observational study was concerned with cumuli in mid-latitudes. Therefore, our results differ both in the vertical extent of the clouds and the extent of the turbulent wake generated by the cloud core.

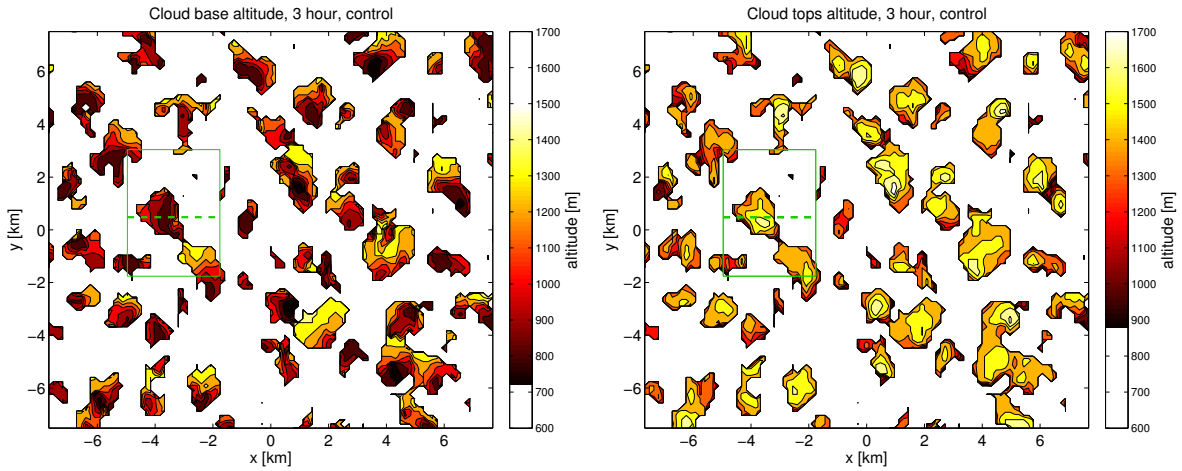

(a) (b)

Figure 4.3: Indicated altitude of cloud bottoms and cloud tops at the end of the third hour. Note that some parts of clouds are displaced against the lowest cloud basis. The light green frame marks the area of horizontal and vertical cross-section in figure 4.4

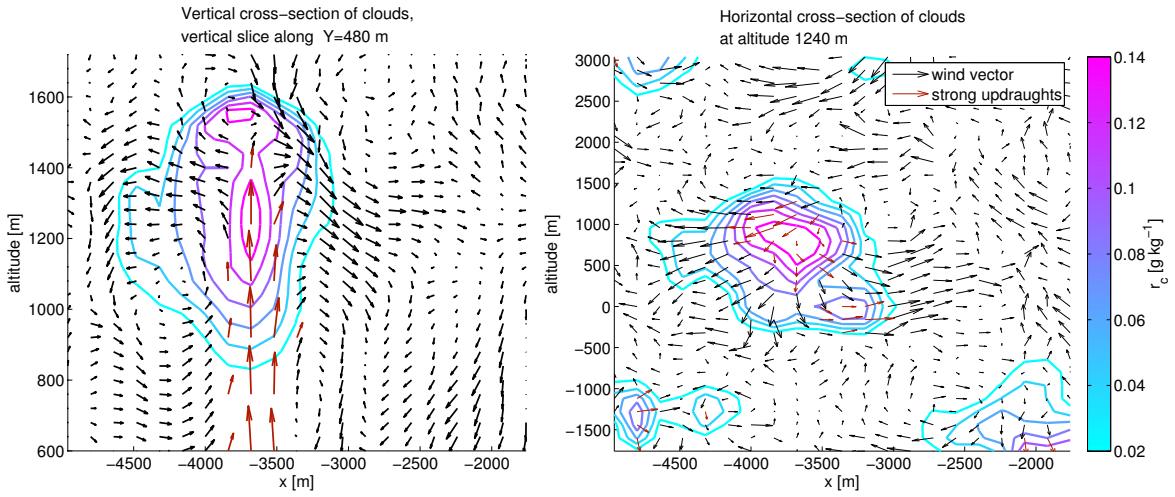

(a) (b)

Figure 4.4: The structure of a cloud in a developing convective boundary layer at the time 3 hour. The value of large scale wind forcing $v_f(z)$ was subtracted from wind velocity to provide a clear representation of circulation.

Moreover, the vertical profile of variance in specific humidity (see figure 4.5a) attains maxima at altitudes 600–900 m in the lower part of clouds, indicating a clear change in the character of the air surrounding clouds. Therefore, it is safe to deduce that the cloud layer is not a part of ML and should be classified as separate cumulus layer (CuL) (Betts, 1976, pp.2367-68) (Johnson, 1978, pp.1496, 1501). That further implies that z_i, the height of ML, is set to the height of the cloud base (IFS IV, 2013, p.38).

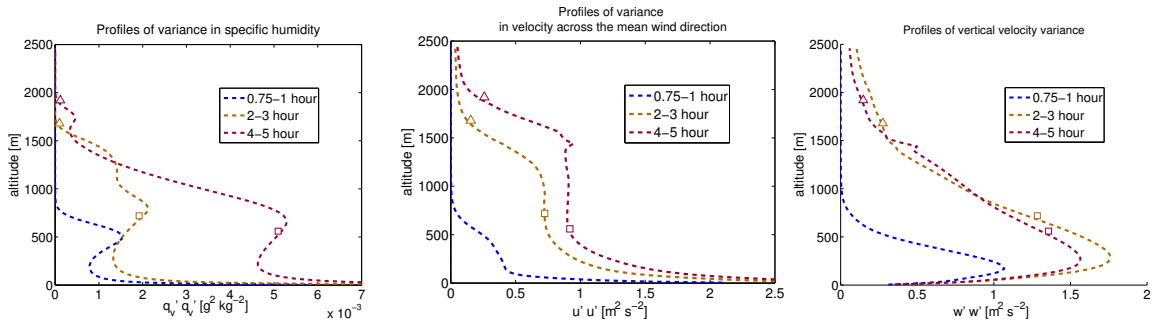

(a) (b) (c)

Figure 4.5: Domain averaged potential temperature profile and variance in specific humidity.
The symbol □ marks the altitude of cloud base, the symbol △ the altitude of cloud tops.

The development of CuL is connected to a sharp increase in the vertical flux of kinetic energy during the second hour. As the ML continues warming, the CuL further grows in thickness both upwards and downwards (see figure 4.6a). Between the beginning of the second hour and the end of the fifth hour, the altitude of the top of cloud grows at a decreasing rate from 900 m to 1900 m. These altitudes compare well with results of observational studies that measured the total boundary layer depth as 900–2200 m over

sea during wintertime CAO events (Brümmer, 1996).

Although the cloud base slowly descends to 500 m by the end of the hour 4, the maxima of the cloud water mixing ratio shifts upwards (see figure 4.6a). This might indicate a development of cores of active cumuli clouds, i.e. cumuli clouds where the latent heat release is effectively driving further increase in the convection, venting out additional air from the ML (Stull, 1985, pp.50–51). Further investigation of the vertical velocity and vertical fluxes of moisture (see figure 4.7a) supports this hypothesis. Results imply that cumuli clouds in the CAO scenario differ from shallow marine cumulus not only in the thickness, but also in the internal structure, since maxima in the amount of cloud water are located in the middle part of clouds instead of at bottoms (Jiang and Cotton, 2000, pp.589-591).

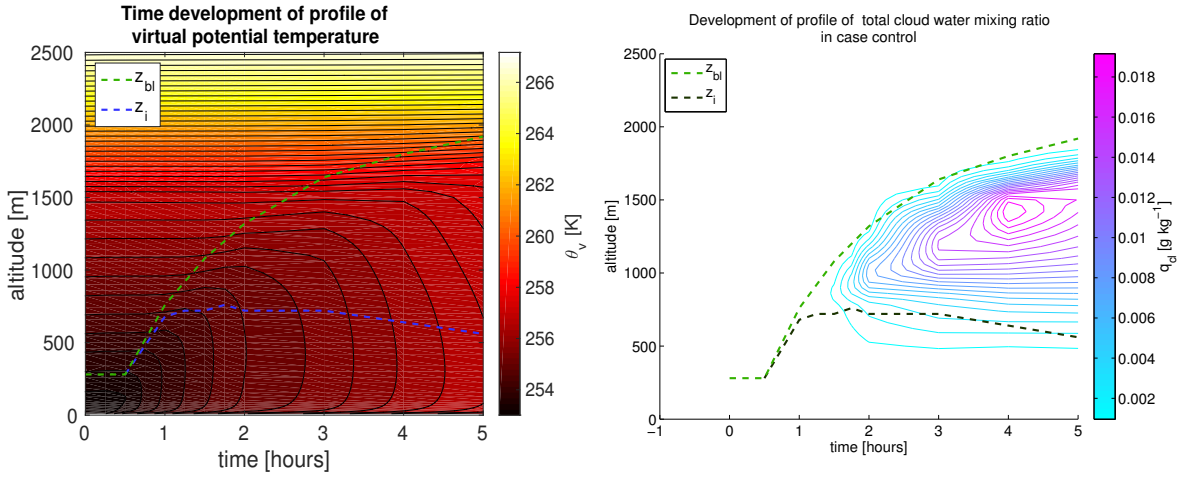

(a)

Figure 4.6: The development of potential temperature and cloud water mixing ration in the lower troposphere with the growing CBL.

While the turbulent kinetic energy (TKE) initially reaches high values in the middle of ML (at 250–300 m), an increase is observed at altitudes in the cloud layer during the second and third hour (see 4.8b). The kinematic moisture flux in the vertical direction increases strongly during the third hour, with values in the cloud layer exceeding values at the surface by 60 % at 4–5 hour (see again figure 4.7a). Moreover, peaks in vertical fluxes of both passive tracers shift in 2-3 hour towards the upper part of the CuL (see figure 4.7b). These effects of the forcing by active cumuli cloud cores need to be taken into account in the later analysis of the impact of variations in surface forcing (part 4.2).

While the wind velocity is nearly constant in the most of the ML and the bottom part of CuL, the top parts of clouds are located in the area of increased wind shear (see figure 4.2b). This agrees well with the previous LES studies claiming that the shear is confined mostly to the cloud tops (Skyllingstad and Edson, 2009, p.1283). Moreover, most of the

shear TKE production occurs by the tops of clouds (see figure 4.8a), contributing to the total TKE budget (see 4.8b).

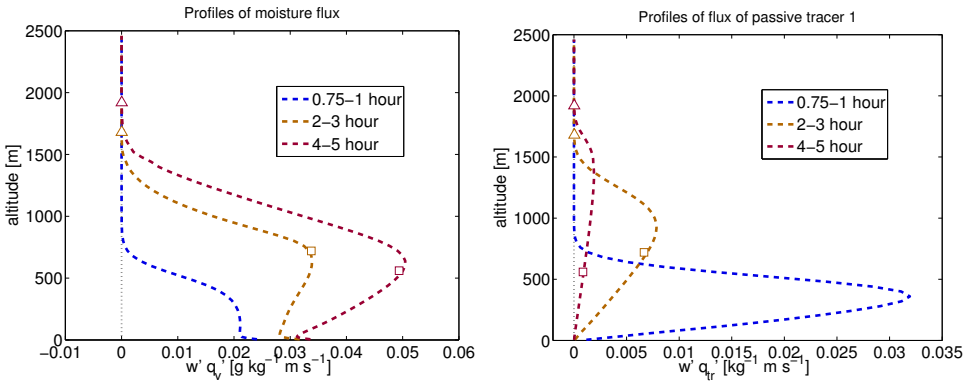

(a) (b)

Figure 4.7: Vertical profiles of moisture flux and passive tracer flux in the control run compared with the mean amount of cloud water content.

At the top of the CuL, vertical fluxes of passive tracers exhibit a sharp decline showing that there is just a negligible amount of tracers escaping from clouds. Vertical profiles of variance in potential temperature peak at this altitude and decline higher up. The decline in the variance of the wind component across the mean flow is similar (see figure 4.5b), indicating a turbulent mixing at these altitudes. These findings suggests that there is an ongoing cloud entrainment and a relatively negligible cloud-top detrainment.

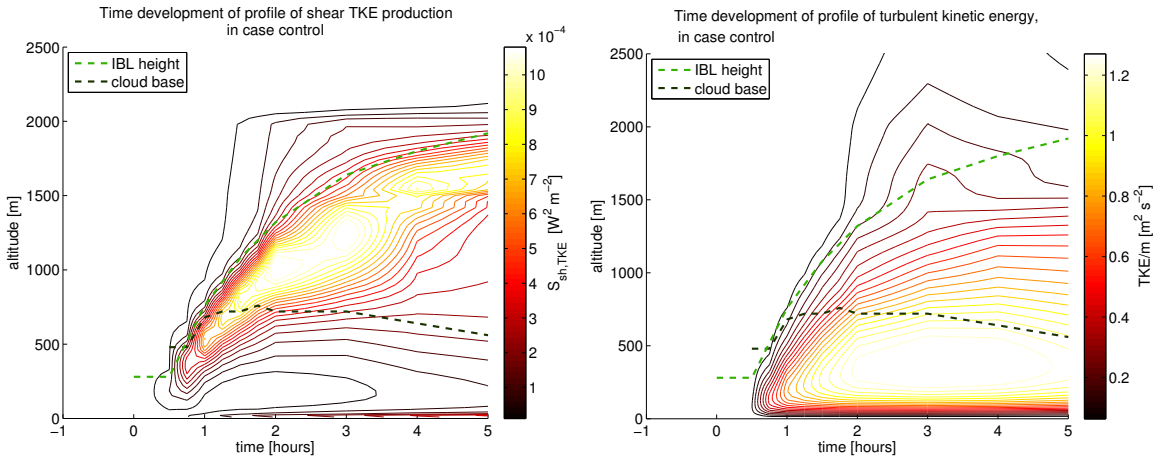

(a) (b)

Figure 4.8: Shear produced TKE and total TKE

The changes in the structure of the CBL can be also expressed in the terms of similarity theory (see figure 4.9). At the end of the first hour, there is a steep increase in w_*, the convective velocity scale (also known as Deardorff velocity). The increase continues during the second hour together with the increase in u_*, the friction velocity. The increase in u_* from 0.12 0.2 $\mathrm{m\,s^{-1}}$ and in w_* from 1.3 1,7 $\mathrm{m\,s^{-1}}$ agree with the result of previous field campaigns. Similar result from observation of growing convective rolls during the ARKTIS project (Brümmer, 1996). The u_* continues slowly increasing during 3–5 hour, while w_* slightly declines during 3–5 hour. This is mostly due to lower temperature gradient between the surface and the ML.

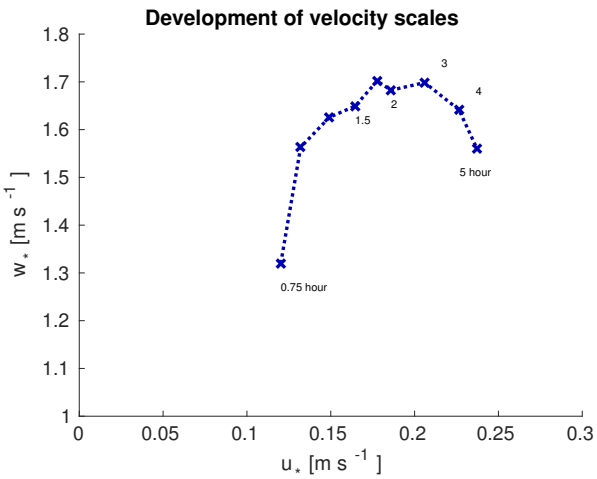

Figure 4.9: The development of the friction velocity and the convective velocity scale in the control run. The numbers next to points indicate times of model outputs in hours.

4.1.2 Updraught Distribution

The study of the distribution of updraughts and downdraughts is motivated by the use of eddy-diffusivity mass-flux (EDMF) schemes (Huang et al., 2013) implemented in a number of meteorological models including ECMWF (Watson et al., 2015). The main idea behind EDMF schemes is that the CBL consist of a few strong updraughts and surrounding turbulent air with weaker updraughts and various downdraughts. The transport of mass and energy within CBL is then modelled as a combination of upward transport inside the strong updraught and a diffusion into the rest of CBL. While these schemes make some restrictive assumptions about the distribution of updraughts and properties of the air inside them (Sušelj et al., 2012), the question remains whether these assumptions fit on the CBL in a developing CAO. This section present the distribution of updraught evaluated by the methodology from 3.4.2 and 3.4.3.

A basic evaluation at model levels chosen (see figure 3.4) to represent distinctive parts of the CBL (45 m, 170 m, 360 m, 520 m, 1480 m, 3250 m) reveals high spatial variability in the vertical velocity w, potential temperature θ and humidity q_v. Contourplots of these variables show a high spread in the values of respective variables. Generally speaking, their character is slightly more complicated than just a basic classification into updraughts and downdraughts. This is well shown in the figure 4.10 –

while majority of columns are in a cluster of weak downdraughts, there are also number of warm updraughts forming, though without any specific gap from the downdraught cluster. With the deepening of CBL and the formation of large convective eddies, there is further differentiation in downdraughts and updraughts. The spread in vertical velocities of downdraughts increases. Updraughts also exhibit increased spread in vertical wind velocities, together with an increase in the amount of weak cold updraughts.

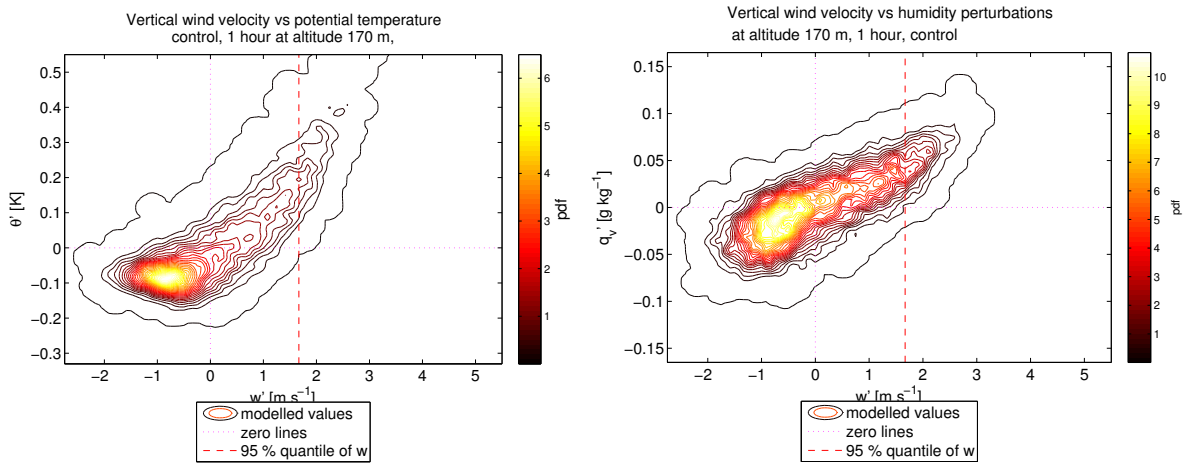

Figure 4.10: The joint distribution of $[\theta \quad w]$ and $[q_v \quad w]$ in the lower part of the boundary layer in the early development of the CBL.

Although values of $\overline{w'\,\theta'}$ and $\bar{q_v}$ at constant levels approximately follow the normal distribution in the SBL before the transition and at levels above the convection, the assumption of normality does not hold for the developing CBL. The distribution of w at altitudes just above the surface layer shows a peak in negative vertical velocities, with a slow decline into negative velocities (see figure 4.11a). The distribution of w at altitudes 170 m and 360 m then shows distribution skewed towards negative values, however with a long tail into positive numbers (see 4.11b), indicating a number of forming strong updraughts at a bottom of thermals.

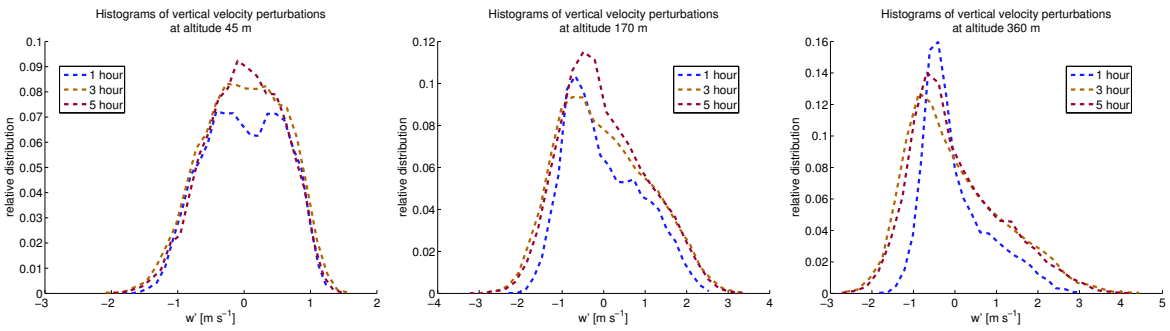

(a) (b) (c)

Figure 4.11: The comparison of histograms of vertical velocities at the bottom part of ML and in the middle of ML

An important quantity used in the EDMF schemes is E_w, the kinetic energy of strong updraughts. Values of E_w at different altitudes are estimated from wind velocity variance (IFS IV, 2013, p.41) under the assumption of normality (using the 0.05 fraction definition for the equation 3.9) and compared against values directly calculated from wind velocity fields by formula 3.10. The results show that E_w is slightly overestimated at the top of the surface layer (45 m) and underestimated at majority of other recording levels. In the middle of the ML and in the sub-cloud layer, E_w is usually underestimated by 20-25 % (see figure 4.12). These results pose some concerns for currently used EDMF schemes. Even if the surface parametrization in a forecast model is well calibrated, E_w in EDMF scheme would be underestimated or overestimated based on the altitude of the model level where EDMF algorithm is initiated. The numerical results in this study suggest that the lowest bias would be achieved for EDMF scheme initiated over the top of surface layer at 135–170 m.

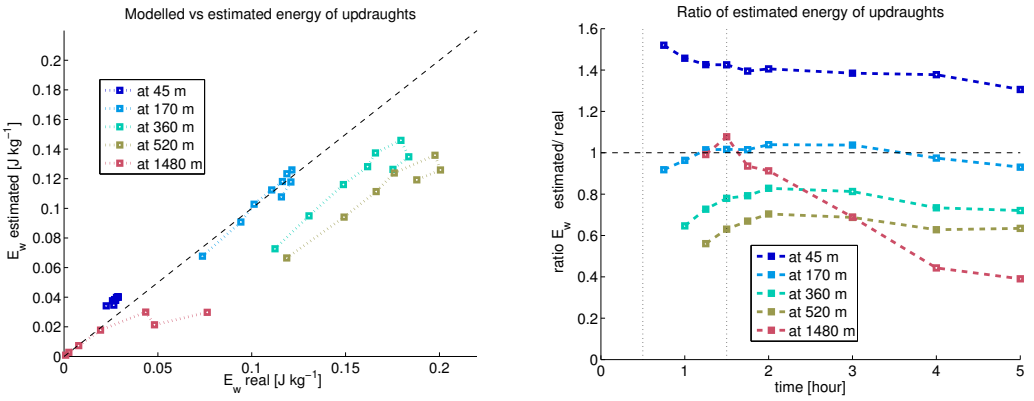

(a) (b)

Figure 4.12: The time development of the ratio of estimated value of kinetic energy of updraughts to its modelled value.

Although the distribution of the potential temperature is not normal, the distribution of the potential temperature inside the strong updraughts at the bottom of thermals (135 m) approximately follows normal distribution. The vast majority of strong updraughts are warmer than the horizontal mean value. Moreover, all the warmest gridpoints are inside strong updraughts (see figure 4.13). This finding agrees with lidar observations of convective plumes that found a correlation between temperature and vertical velocity (Gibert et al., 2007).

The joint distribution of $[\theta \quad w]$ and $[q_v \quad w]$ in the figure 4.10 clearly shows that there is a majority of weaker updraughts and downdraughts followed by the a into more prevalent updraughts that are usually warmer and more moist than the surrounding air. The situation at the bottom of CuL is similar, however it changes inside the CuL. In the upper part of CuL (altitude 1480 m), a significant portion of strong updraughts are

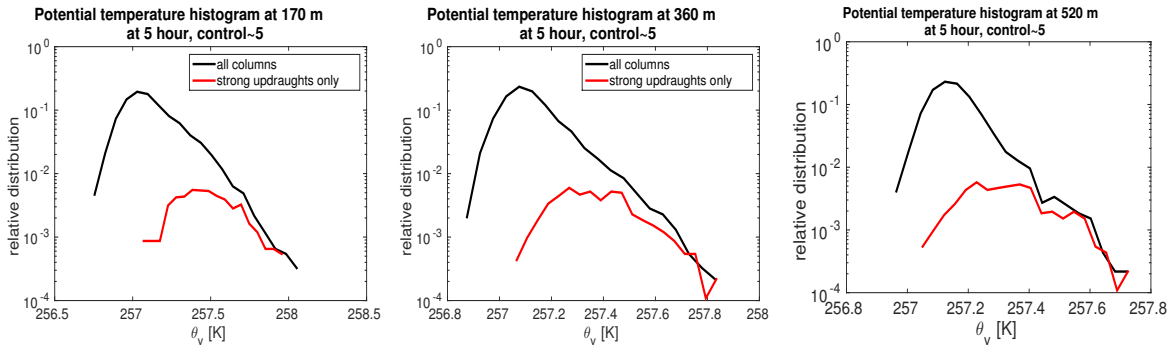

Figure 4.13: The distribution of potential temperature in strong updraughts compared to the distribution in all columns. Displayed as logarithmic histograms for an easier reading. The red line — marks the distribution within strong updraughts while the black line — marks the distribution for all point in the horizontal layer.

cold, indicating convective overshoots. Furthermore, the joint distribution $[q_v \quad w]$ inside CuL clearly shows the difference between clouds and the surrounding air. There are two distant clusters of higher probability density that account for ambient air (lower cluster) and clouds (upper cluster). In the ambient air, humidity is generally lower and both weak updraughts and downdraughts are present. In comparison with that, clouds show less variability in humidity, however there is a higher spread of vertical velocities and a long tail into high vertical velocities that indicates penetrative updraughts. Furthermore, it agrees with a previous LES studied of convection (Schröter et al., 2005) that found updraughts mostly in areas with high liquid water content.

Strong updraughts facilitate a significant portion of the transport of heat, moisture and momentum. At the time 1 hour, strong updraughts account for more than 50% of the kinematic heat flux budget at altitude 360 m and more than 100 % at 520 m (i.e. remaining columns are dominated by downward transport of heat). These results compare well with the studies on resolved plumes in the boundary layer (Couvreux, 2010) that estimated that resolved thermals account for 50–60% of heat transport bellow $0.6\, z_i$. The portion of kinematic moisture flux facilitated by strong updraughts is slightly smaller, 20–40 % . After second hour, this decreases to 20–60 % of the kinematic heat flux budget and 20–30 % of the kinematic moisture flux (see figure 4.14). However, the contribution to the kinematic heat flux later increases with a the development of larger convective eddies forced by active cumuli clouds.

The evaluation of the distribution of updraughts and downdraughts in the modelled CBL has shown that the assumption of normal distribution of velocities used in EDMF leads to an underestimation of the kinetic energy of strong updraught in the middle of the ML and in the sub-cloud layer. While strong updraught are always associated with higher values of both potential temperature and specific humidity in the ML, the situation changes within CuL. Strong updraughts still show increased values of specific

humidity, however they do not exhibit any clear trend for the potential temperature. Overall, strong updraught facilitate a very significant portion of the transport of heat and moisture.

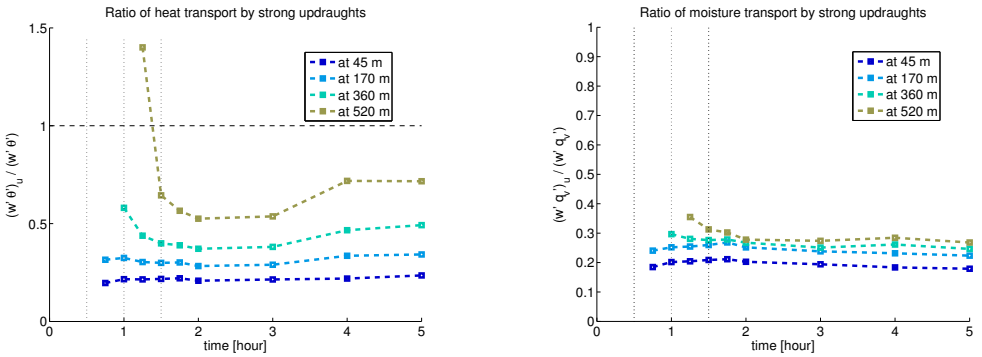

Figure 4.14: The portion of vertical kinematic heat flux and kinematic moisture flux facilitated by strong updraughts.

4.1.3 Variability on Domain and Subdomain level

This section focuses on a comparison of the control run with the other model runs with the same setting that differed only in the random seed used in the model initialisation. The evaluation of the control set allows to account for the inner variability of the model, providing a vital reference scale for the assessment of the impact of heterogeneous surface forcing.

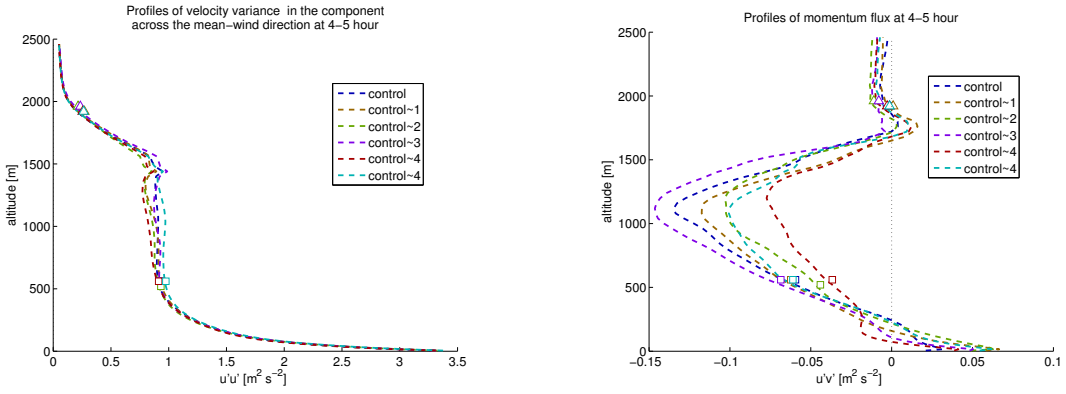

(a) (b)

Figure 4.15: The comparison of profiles of variance in wind velocity and horizontal flux of momentum at time 5 hour.
The symbol □ marks the altitude of cloud base, the symbol △ the altitude of cloud tops.

The comparison of updraughts and domain averaged profiles shows that there are generally very small differences in resulting development of the boundary layer between the runs of the control set (see Appendix). There are slight differences in the modulus of vertical wind velocity distributions, however they are relatively small and generally diminish by the beginning of hour 2.

Although domain averaged profiles virtually do not differ for any model variable, there are significant differences in the variance of wind velocity across the mean wind direction at altitudes 1000–1500 m (see figure 4.15a). This phenomena is most likely connected to the turbulent mixing of the ascending thermals with the air inside cumulus clouds. While horizontal fluxes of momentum (see figure 4.15b) show a high spread in the lower part of clouds, differences in vertical fluxes of the heat and moisture do not vary by more than 5 %. While domain-averaged values of vertical kinematic fluxes show relatively few differences, the question of variability on smaller scales needs to be investigated for the purpose of variability in subgrid fluxes in NWP models. Following the methodology described in 3.4.5, instantaneous values of fluxes through subdomains of the side size 4000 m are estimated.

Although the majority of subdomain profiles of the kinematic heat flux do not significantly differ in the ML, there are strong variations in the CuL above, as figure 4.16 shows. There is a wide extent of min-max envelopes, however the 0.25–0.75 quantile envelopes are relatively narrow for each run in the control set. Profiles of the kinematic moisture flux show higher variability, both for min-max envelope and for 0.25–0.75 quantile envelope. In the control run, the min-max envelope extends from 75 % to 120 % of the values of the mean profile. control∼3, reaching from 50 % to 125 % of the values of its mean profile. This increase in the variability is most likely linked to the cumulus convection and gives some further implications for the variation in parametrization in NWP on the 4 km grid. (see chapter 7).

Since subdomains in all runs from the ABL have developed from the same forcing and initial conditions, the set of all subdomains provides a larger sample size for the estimation of the variability in fluxes of heat and moisture. Box-and-whisker diagram with standard setting of the whiskers as 1.5 of the interquartile range (IQR) then displays the spread in fluxes. The control set IQR and the whiskers allows to later asses the spread in the subdomain values for cases with surface heterogeneity (see figure 3.12).

In summary, there are relatively few differences in the developing CBL on the scale of the model domain. On a smaller scale, there are significant variations in the vertical fluxes of heat and moisture. The variations in the kinematic moisture flux increase with the height in the ML and slowly decrease within the CuL. On the other hand, variations in kinematic heat flux are relatively low in the ML and reach higher values in the CuL.

These sub-mesoscale variation in CBL properties should be taken into account in field observations as well as in NWP models with a fine grid.

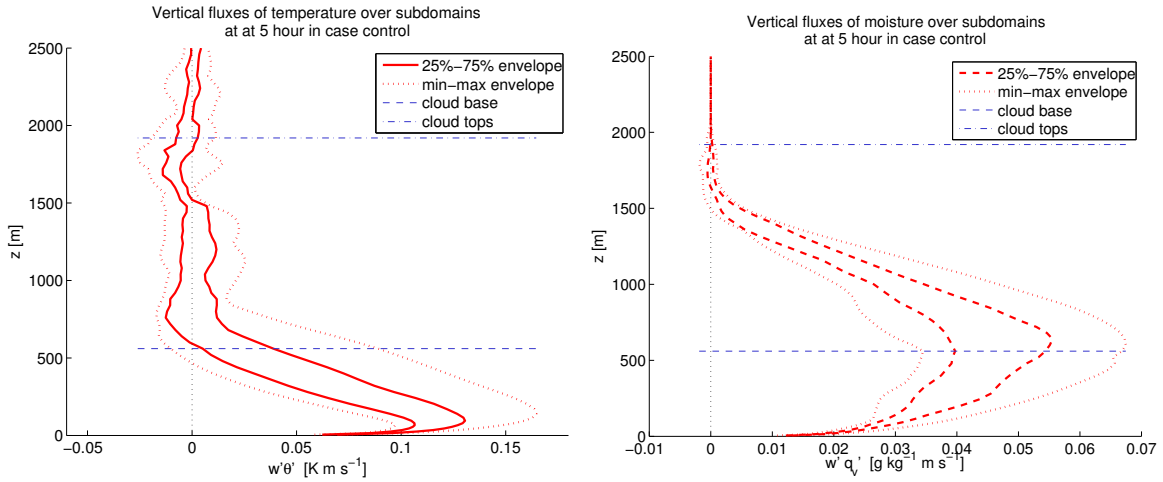

Figure 4.16: The comparison of the kinematic fluxes in subdomains showing the min-max envelope and the $[0.25, 0.75]$ quantile envelope at 5 hour.

4.1.4 Variability in Flux Timeseries

In the nowcasting and customised forecast for some field missions, there are number of NWP models run on relatively fine resolution and with relatively short time steps. While the previous section has addressed the spatial variability in the CBL, the other question is whether the vertical fluxes of heat, moisture and momentum exhibit variability on a short time scales, as indicated in (Kang, 2009) and (LeMone et al., 2003).

While the time averaged model statistics and instantaneous outputs provide a valuable information about the vertical and horizontal structure of the developing CAO, they do not allow us to fully assess the variability in fluxes with time. For this purpose, a set of fine timeseries of vertical fluxes is recorded in the model. In addition to already existing timeseries of the sensible and the latent heat flux at the surface, recordings at other altitudes are added into the model, as described in 3.2.7. In this section, the recorded timeseries are closely examined for the control set, with focus both on general trends and a variability in values.

The kinematic heat flux and kinematic moisture flux close above the surface rise steeply in the first hour after t_0, followed by a stagnation later (see figure 4.17). Timeseries of the kinematic heat flux at the chosen altitudes in lower troposphere exhibit rapid increase, followed by a stagnation after and a slight decrease. The exception are the altitudes atop the Cul (1480 m) and above it (2080 m), where the displacement of colder air from below and the entrainment of air into clouds lead to negative values

of fluxes (for details, see 4.1.1). Although the kinematic moisture flux by the surface stagnates during the hour 3, fluxes at other altitudes continue to rise due to venting by active cumuli clouds and the entrainment of dry air from free troposphere above.

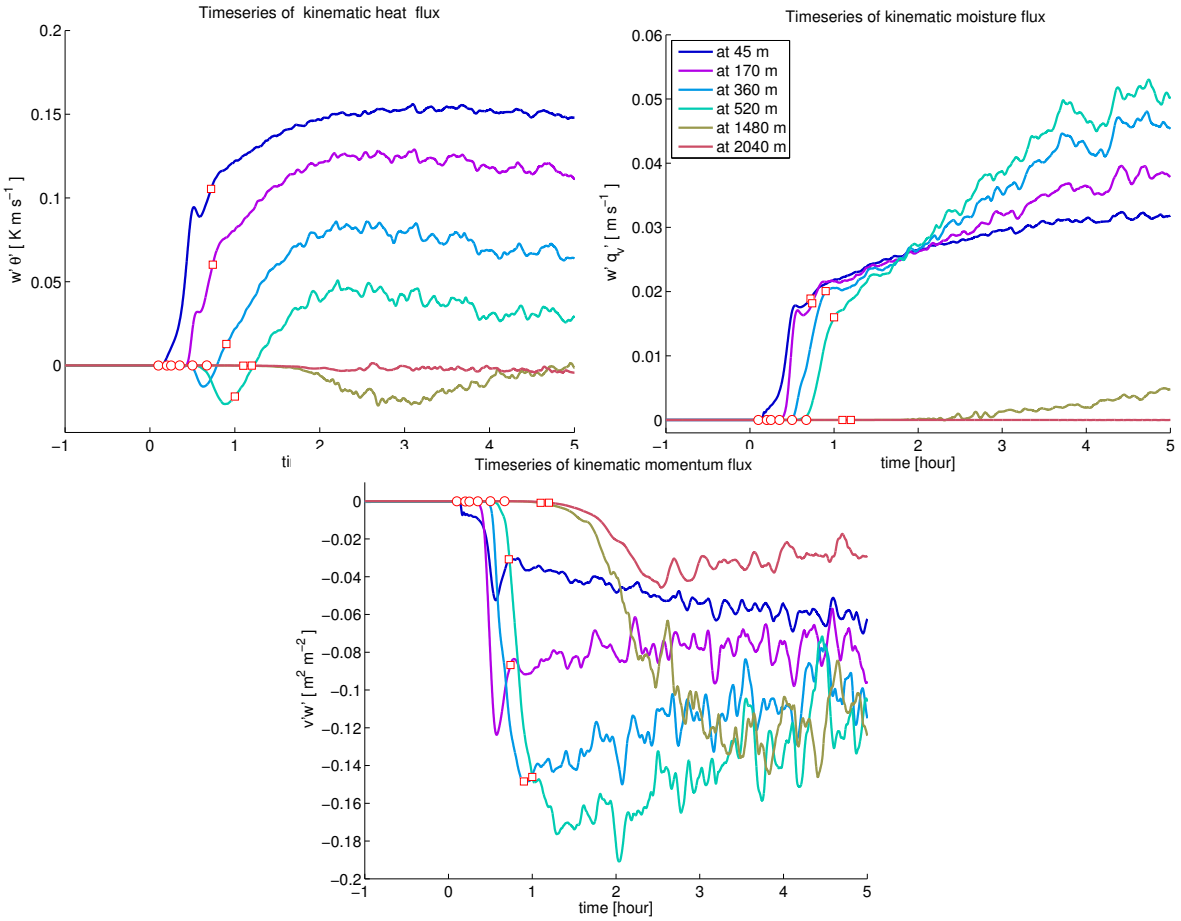

Figure 4.17: Timeseries of the kinematic heat flux and the momentum flux at different recording altitudes with the marks separating the segments.
Circles mark the passing of the internal boundary layer through each recording altitude and squares mark the peak of the early abrupt growth in vertical fluxes.

All model runs in the control set follow the same trends at each chosen altitude, however they differ in oscillations. Figure 4.17 clearly shows an abrupt rise in the kinematic flux of potential temperature during the propagation of IBL through the recording altitude, followed by a weaker growth with oscillations. The same phenomena is demonstrated by the kinematic momentum flux in the direction along. An abrupt growth in downward flux is then followed by a later development with nearly-linear trend at majority of altitudes.

Dividing the timeseries onto disjunct segments – the 'stable', 'IBL-propagation' and the 'CBL-regime' (described in 3.4.5) marked in the figure 4.17, allows to evaluate mean trends and oscillations. The 'IBL-propagation' segment is mostly concerned with the propagation of the rising IBL through the recording altitude. Mild oscillations at the

beginning indicate propagation of waves from below, followed by an increase in oscillations indicating the turbulent entrainment and penetrative updraughts, and finally an abrupt growth in flux values marks that the internal boundary layer has passed through the altitude. The 'CBL-regime' segment exhibits approximately constant or linear trends with significant oscillations in values.

Due to the relatively short length of the 'IBL-propagation' segment at some recording altitudes, the further analysis applies just for the 'CBL-regime' segment. *Note: For the convenience, values of the latent heat flux and sensible heat flux are used in the later analysis instead of their kinematic forms.*

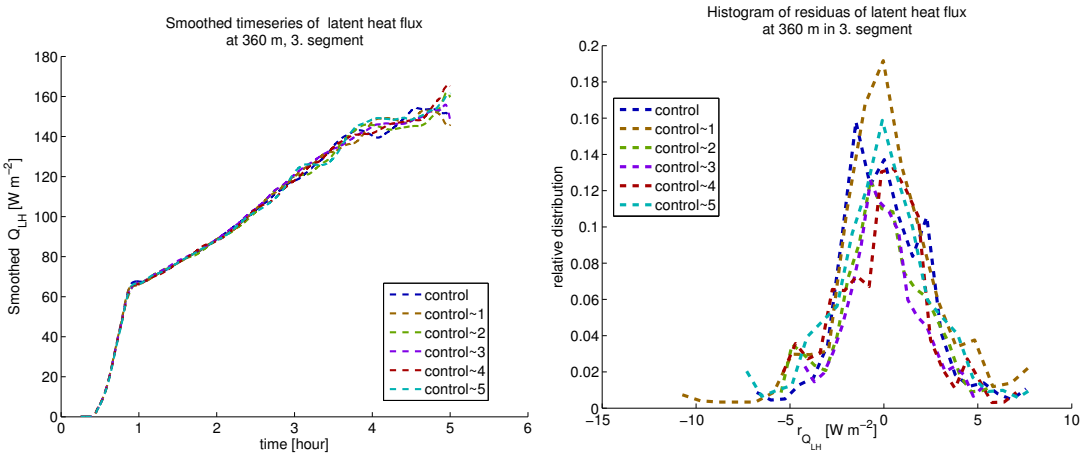

(a) (b)

Figure 4.18: The comparison of smoothed flux timeseries and remaining residua

The trial of the smoothing of flux timeseries at all three recording altitudes inside CBL for the segment 3 has revealed that the optimal results in the terms of sum of residua and simple long-term trend is obtained for the smoothing lengths 400–600 s (for details, see Appendix). Based on the trial of smoothing, later segments of flux timeseries were smoothed by the moving average of the length 500 s. The figure 4.18 shows negligible differences between smoothed timeseries of LH flux of runs in the control set as well as histograms of residua. The vast majority of residua (97.5 % probability) of the latent heat flux falls into the interval $[-5W, +6W]$. The figure 4.19 of the conditional distribution $p\big(r_{Q_{LH}}(t)|r_{Q_{LH}}(t-\triangle t)\big)$, shows that a new residuum is always likely to attain values in a relative proximity of the value in the previous timestep, indicating a high degree of autocorrelation.

The evaluation of the autocorrelation in residua of latent heat fluxes at different altitudes (figure 4.20a) shows that autocorrelation of residua decline gradually within few hundred seconds. The values of autocorrelation decrease bellow the threshold 0.3 for time lag 200–300 s and below the threshold 0.1 for time lag 280-380 s. These values com-

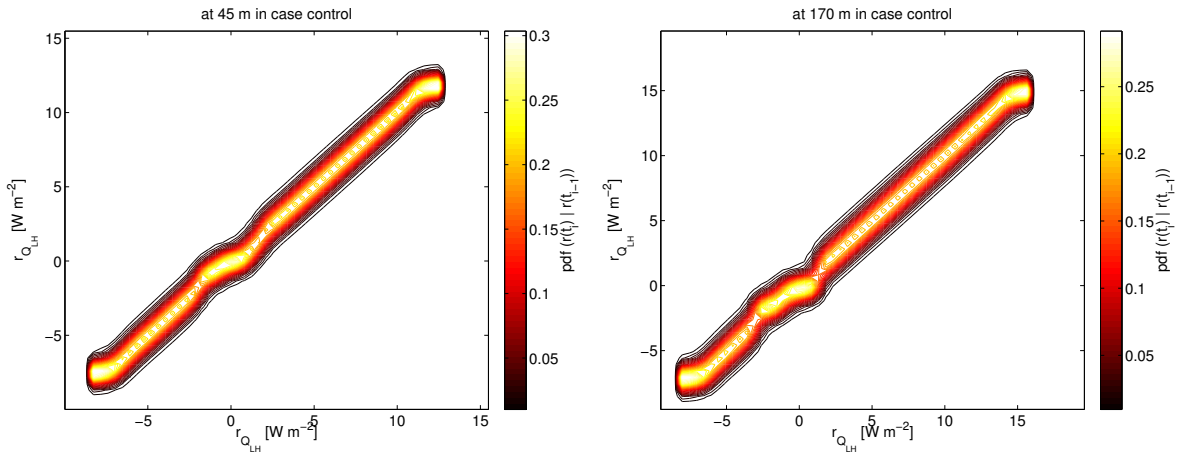

Figure 4.19: Conditional distribution of residua in time series of the latent heat flux. Dashed lines mark 0.3 and 0.1 thresholds for autocorrelation values.

pare well with values of ML timescale $t_\star^{(\mathrm{ML})} = 360\,\mathrm{s}$ during 3–5 hour. A slightly stronger autocorrelation is attained at the upper part of the ML (520 m) and upper part of the CuL (1480 m) in the majority of control runs. The decline in autocorrelation values is steeper at the altitudes above ABL (2040 m). The situation for the SH flux is equivalent, with values of autocorrelation declining to values bellow the threshold 0.3 for the time lag 200–260 s for residua at altitudes within ABL and for the time lag 140-180 s for residua at altitude 2040 m. The situation differs for the fluxes of momentum. There are no obvious differences between the autocorrelation of residua at chosen altitudes. Autocorrelation values decline below the threshold 0.3 for time lags between 200 s and 300 s.

Runs in the control set slightly differ in the autocorrelation in flux residua. The highest spread in autocorrelation values is reached for residua of the LH flux at the altitude 520 m. This is consistent with the previous results for spectra of flux timeseries and most likely influenced by the variation in cumulus cloud base.

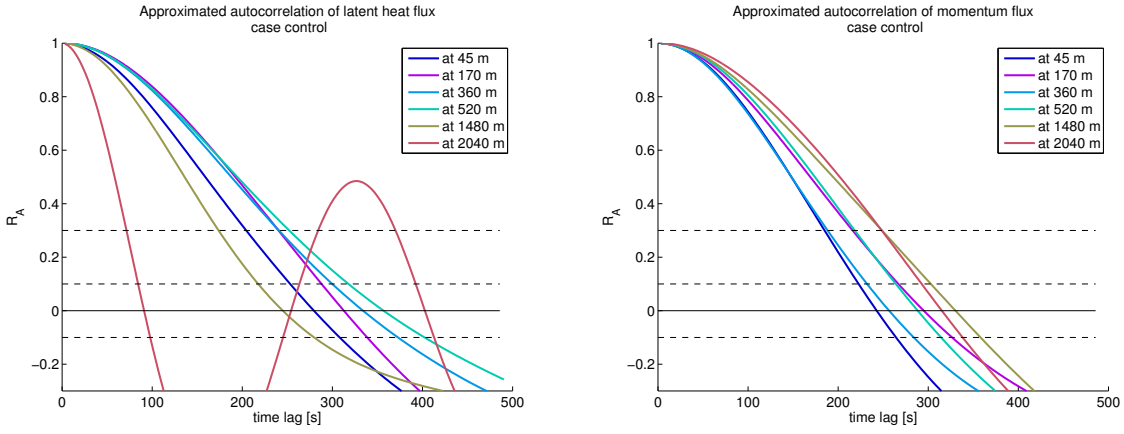

(a) (b)

Figure 4.20: The estimated autocorrelation in the residua of flux timeseries at different recording altitudes. Dashed lines mark 0.3 and 0.1 thresholds for autocorrelation values.

To summarize – The evaluation of flux timeseries indicates oscillations in the values in the vertical fluxes of SH, LH and momentum. These oscillation should be taken into account when explaining the spread in measured values in observational studies. Although some newcasting models might approximate them as a white noise, the high degree of autocorrelation in residua suggests that autoregressive models should be applied in models with timesteps shorter than the ML timescale. The min-max envelope of the control set is later employed as a reference frame for evaluating the impact of surface heterogeneity on the flux development.

4.2 The Impact of the Surface Temperature Heterogeneity

While a MIZ consists of a mix of sea water and patches of various kinds of ice (Gupta et al., 2014) of different temperatures, these surface heterogeneities are likely to influence the atmospheric conditions (Gryschka et al., 2008, p.5), including CAOs developing over the MIZ (Pagowski and Moore, 2001). The presence of the MIZ prompts questions whether surface heterogeneous forcing plays a significant role in the formation of the CBL and whether its effects persist with time. Therefore, this part of the chapter deals with an investigation of the impact of a heterogeneous modification of the surface on the developing convection in CAO.

For the purpose of this study, the heterogeneity is modelled as positive and negative spatial anomalies in the surface temperature. To represent different shapes of ice floats and shapes of leads in the ice, three distinctive patterns of the surface temperature heterogeneities were considered for simplicity (see figure 3.7):

- stripes of anomalies **along** the direction of the synoptic scale wind,
- stripes of anomalies **across** the direction of the synoptic scale wind,
- anomalies following a **chessboard** pattern.

These surface conditions were implemented in LEM as further described in the methodology in 3.3.2 and number of model runs were set for each type with a different setting of the temperature scale of the positive anomaly ($\delta_{(\mathrm{h})}T$) and the size of the building block ($d_{(\mathrm{h})}$) in the pattern. Results of model runs with different setting of heterogeneous surface temperature are compared against each other and against the control set.

Although the majority of the model runs used the same setting of the grid as the control set, a few runs with a smaller scale heterogeneity required the increased horizontal resolution (see model setting in 3.1). The increased resolution also allows to better

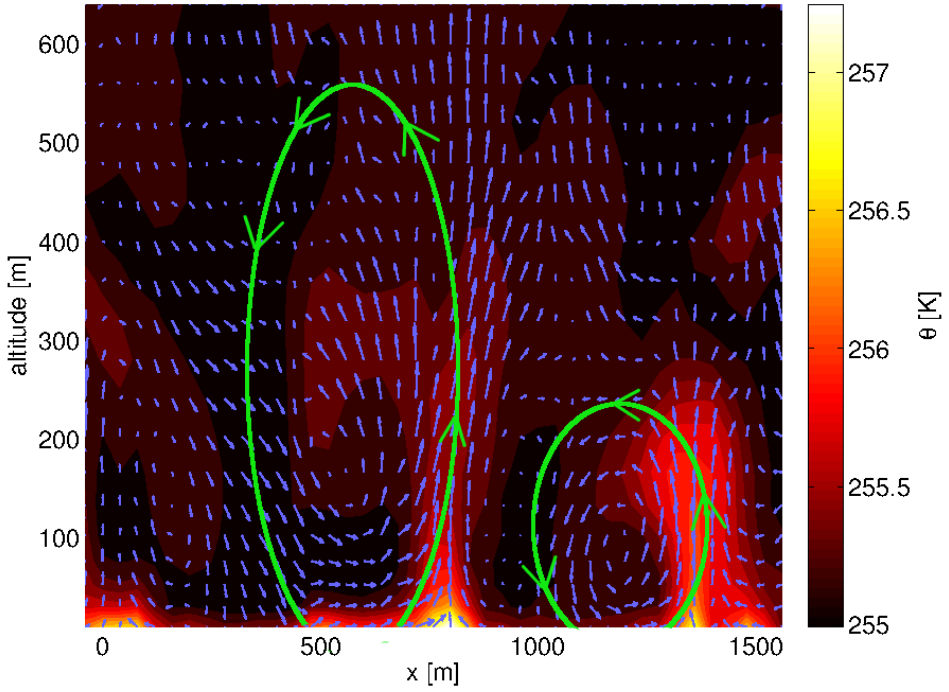

Figure 4.21: An example of the secondary circulation induced by heterogeneity 'along', of the pattern size $d_{(\mathrm{h})} = 800\,\mathrm{m}$ and the temperature scale $\delta_{(\mathrm{h})}T = 3\,\mathrm{K}$.
Green circles mark examples of forced eddies that are part of the secondary circulation.

demonstrate the secondary circulation pattern inside the ML, which is caused by the surface heterogeneous forcing (Gryschka et al., 2008) in the early stages of the growth of CBL (Liu et al., 2011). Figure 4.21 displays an example of the secondary circulation with forced eddies up to size 400 m.

4.2.1 Comparison of Types of Heterogeneity

This section provides a comparison of 4 runs with a different surface conditions — the control run and runs with repeating heterogeneous surface patterns of types along, across and chessboard. In each run with heterogeneity, the block size was set $d_{(\mathrm{h})} = 1600\,\mathrm{m}$ and the temperature scale to relatively high $\delta_{(\mathrm{h})}T = 7\,\mathrm{K}$.

In the model runs with a spatial heterogeneity in the surface temperature, a clear impact on the structure of near surface eddies and spatial distribution of the surface fluxes of the sensible heat and latent heat is observed. The spatial distribution of fluxes clearly follows the pattern of underlying surface temperature (see figure 4.22). The surface pattern is generally more prevalent in the spatial distribution of the surface LH flux than the surface SH flux.

Although the differences in surface fluxes remain high during the further development of the ML, the direct influence of the surface heterogeneity on the structure of ML mostly

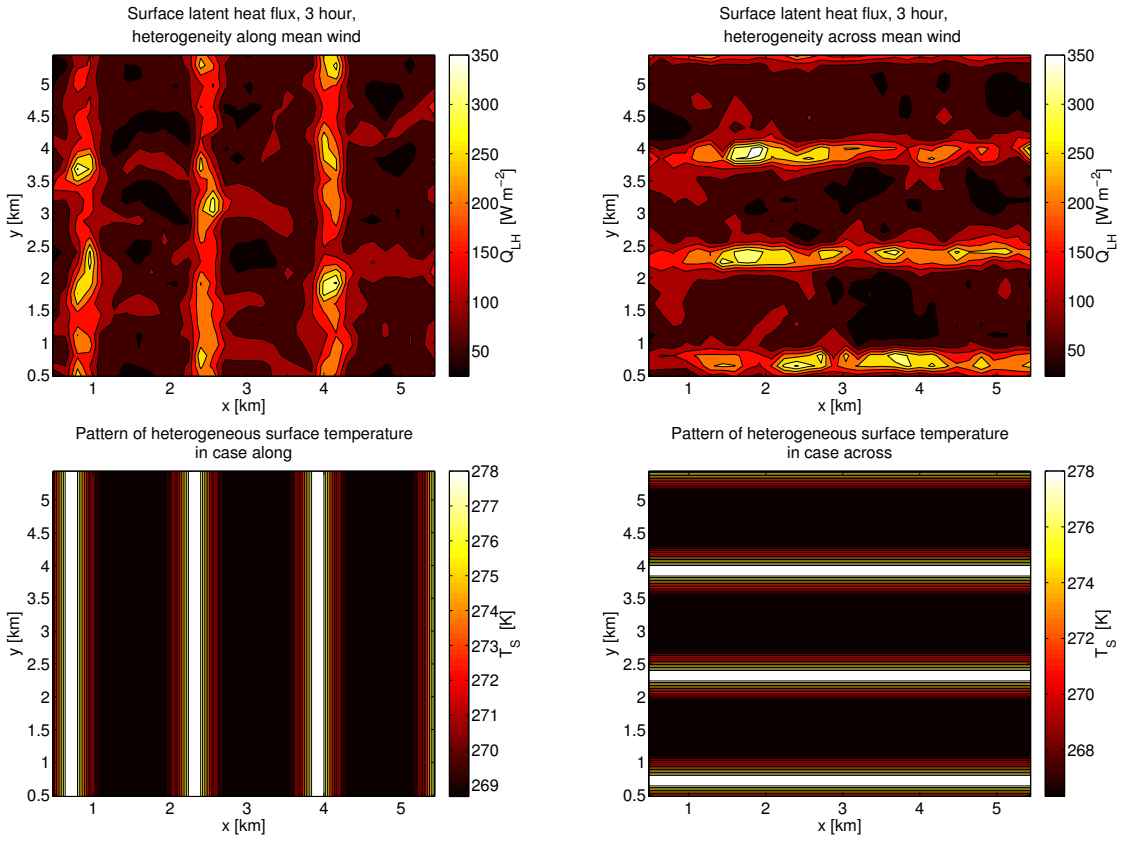

Figure 4.22: The latent heat flux over the heterogeneous surface - a comparison of values of fluxes in the model runs with temperature anomalies in directions along the large scale wind and across it. The underlying patter of the surface heterogeneity shown bellow.

disappears. The differences in the spatial structure of convective eddies and the variations in air temperature diminish during the first three hours after t_0 (figure 4.23). This result stands in a contrast with the previous study of the convection over heterogeneous surface (Maronga et al., 2014) that found a persistent heterogeneity-forced pattern up to altitude 100–200 m. This would however agree with the concept of blending height – i.e. that the IBL above the temperature anomaly at some altitude blends with the surrounding air (Sühring and Raasch, 2013). However, study of Mahrt (2000) suggested that the IBL often does not develop. However, our data are not sufficient for the evaluation of this hypothesis.

Furthermore, while the vertical concentration of passive tracer flux in the first three hours varies strongly between the model runs, by the fourth hour the passive tracer profiles reach nearly same values (see figure 4.25a) in all four runs. The vertical profiles of variance in the velocity component across the mean wind and vertical velocity attain similar values earlier, at the end of the second hour (see figure 4.25b) during the increase in cloud turbulence and the deepening of clouds. This would imply that the turbulent mixing and the effect of latent heat release in developing clouds are more deciding factors

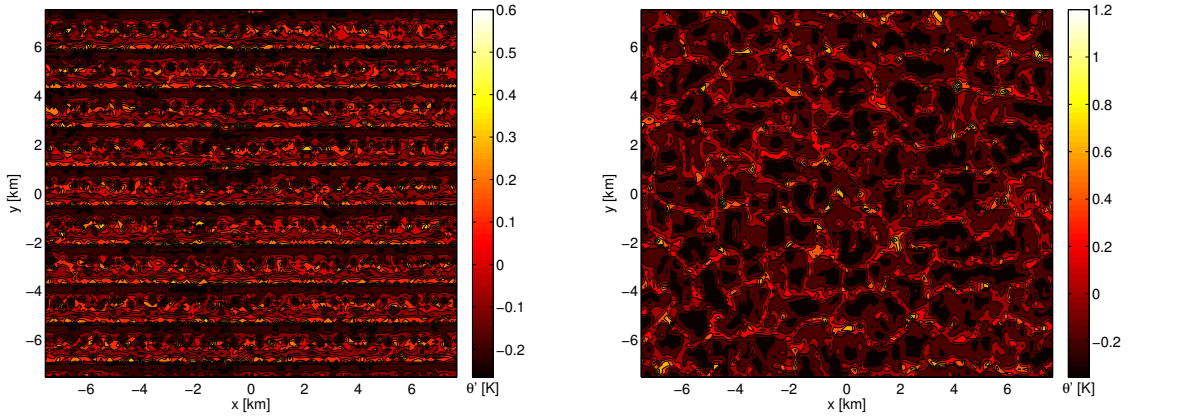

Figure 4.23: The contours of potential temperature over the heterogeneous surface 'across' at altitude 45 m - comparison of the horizontal structure at times 0.75 hour and 3 hour

for the structure of maturing ML than the distribution of surface temperature forcing. Similar results were reached in other studies. Mahrt (2000) suggested that the effect of heterogeneity is decreased with increasing CBL depth. However this hypothesis is not fully suggested by our results, since there was only minor increase in the CBL depth between 2 hour and 3 hour (from 1400 to 1550 m, see figure 4.6).

The analysis of the updraughts and downdraughts finds clear differences between the model runs in the early development of the CBL. The quadrant analysis in figure 4.24 demonstrate the differences in updraughts and downdraughts over a heterogeneous surface. While the control run and the run with 'chessboard' heterogeneity are dominated by warm updraught and cold updraughts, there are also some warm downdraught and cold updraughts. Run 'along' and 'across' differ, as the exhibit a significant amount of warm downdraughts. As the study of Sullivan (1998) shows, these downdraught are mostly caused by the entrainment of the air towards the ground. This suggest that might caused an increased entrainment at the top of CBL and therefore faster CBL growth. However, a further comparison with the results of Sullivan (1998) is not possible since they did not take into account moist process. Nevertheless, these differences are relatively short-lived. They virtually disappear by the third hour after t_0 (compare the left and right column in figure 4.24). Results show that the differences between model runs diminish with the thickening of the CuL.

Each type of heterogeneity affects the forming ML in a slightly different way. Generally speaking, the orientation of the temperature anomalies along the mean wind direction facilitate a formation of moist updraughts, while the anomalies oriented across the wind allow an increased flow of the drier air towards the surface. These differences diminish with time as the ML is deepens.

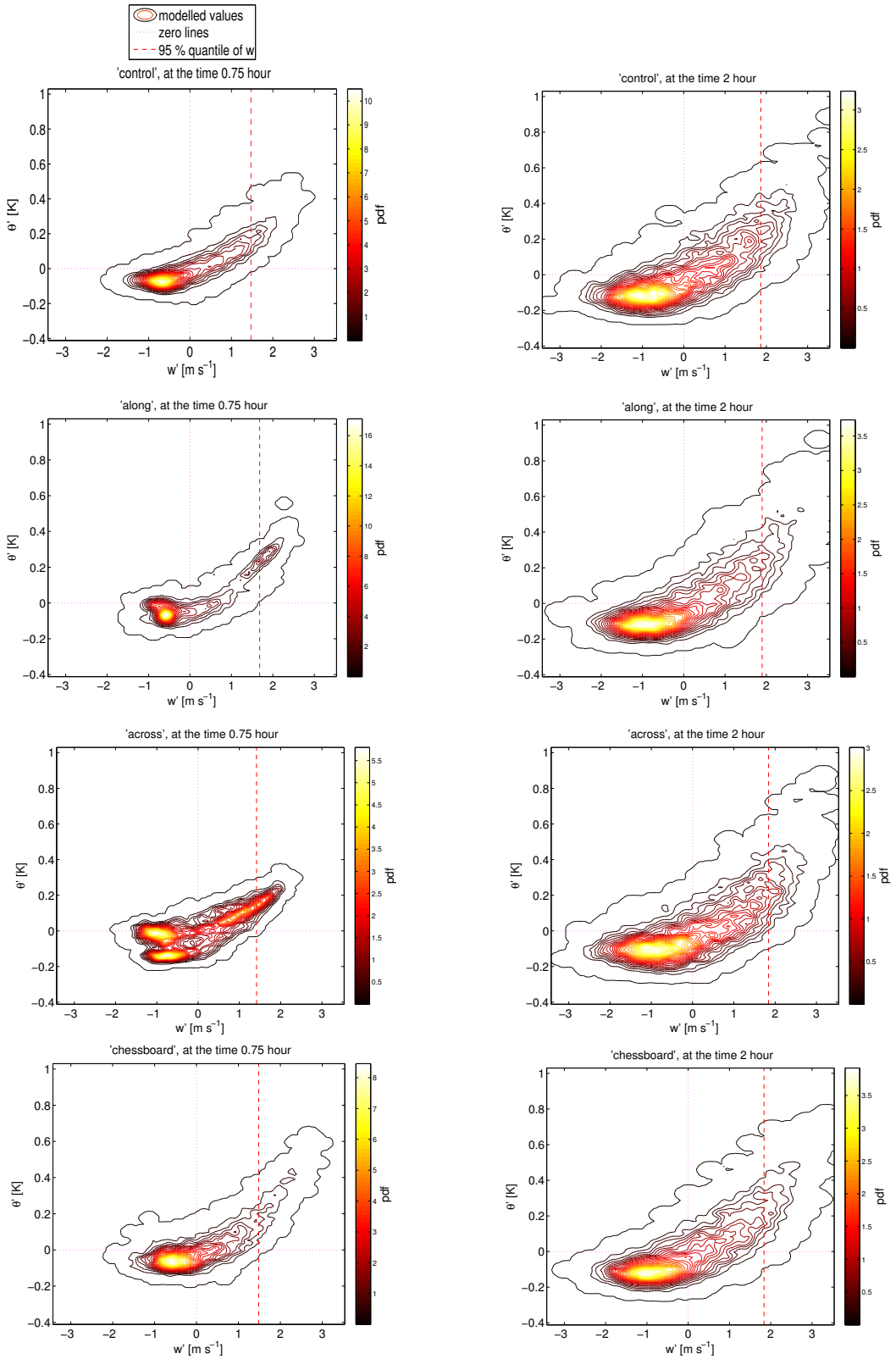

Figure 4.24: Joint distribution of vertical wind velocity and potential temperature perturbation at altitude 170 m over different types of heterogeneous surface at 0.75 hour (left column) and at 2 hour (right column)

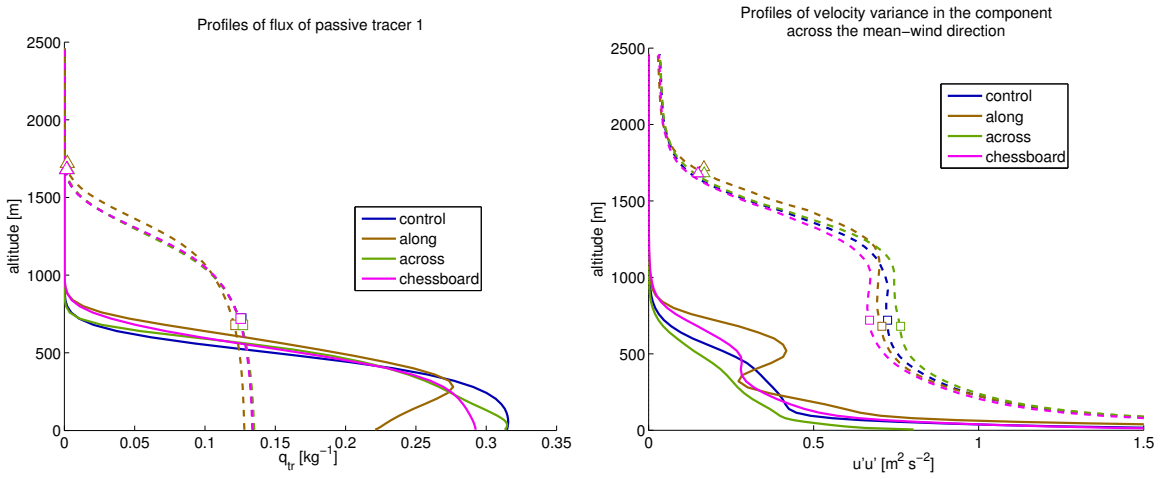

(a) (b)

Figure 4.25: The comparison of profiles of mean vertical concentration of the passive tracer 1 at different times and the comparison of profiles of wind velocity along the mean wind direction at different times. Full lines (–) show averaged profiles for 0.75-1 hour and dashed lines (- -) show averaged profiles for 2-3 hours.

While there are clear differences in spatial distribution of surface fluxes, domain averaged values follows the same development for all three types of heterogeneous pattern (see figure 4.26). For the model runs with the same setting of $d_{(\mathrm{h})}$ and $\delta_{(\mathrm{h})}\theta$, initial abrupt growth of the surface fluxes peaks between 2 hour and 3 hour, followed by a stagnation and even a slight decrease in the SH flux in later hours. Values of the SH flux for the case 'along' are by up to 15 % higher than in other cases until 3 hour. The LH flux is also higher in the case 'along' until the time 3 hour. Differences in fluxes later slightly decrease — they do not exceed 7 % after 3 hour. Fluxes in case 'chessboard' later reach lower values than in the control run.

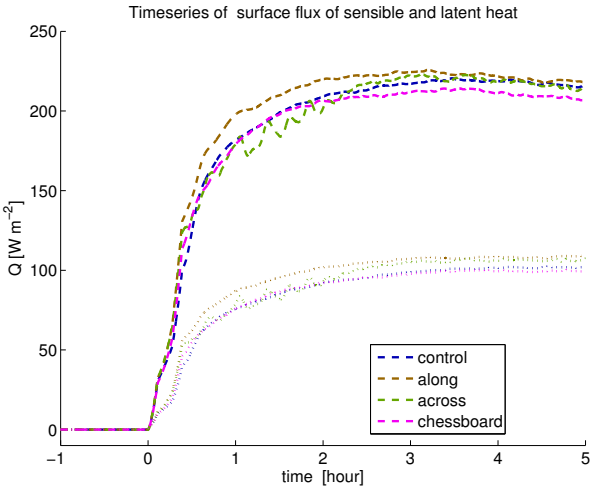

Figure 4.26: The timeseries of the sensible hat flux (——) and the latent heat flux (· · ·) at the surface for runs with different type of heterogeneity.

There are noticeable differences in the early formation of clouds, as figure 4.27 shows. In the 'chessboard' case, scattered glaciated clouds appear at altitudes of 200–600 m in the first half hour. This phenomenon is to lesser extend observed in the case of 'along' anomalies but is virtually non-existent in the 'across' case, most likely owning to the increased mixing of warmer and colder air due to the direction of the anomalies.

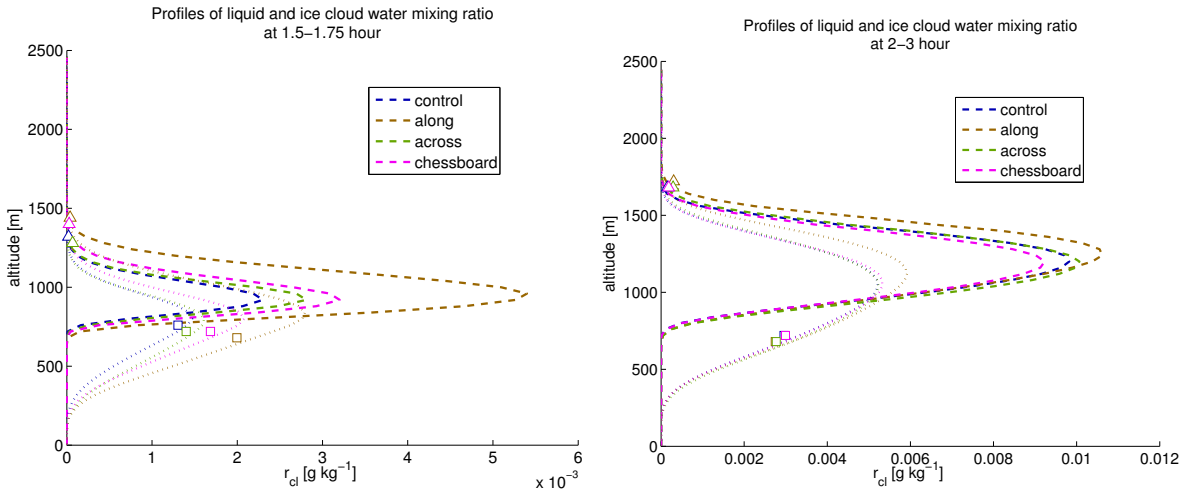

(a) (b)

Figure 4.27: The comparison of vertical profiles of the mean value of cloud water content at 1.5–1.75 hour and 2–3 hour. Dashed line (−−) marks liquid cloud water, dotted line (· · ·) ice cloud water.
The symbol □ marks the altitude of cloud base, the symbol △ the altitude of cloud tops.

In the early development of clouds, the anomalies in the direction of the mean wind pose a direct influence on a pattern in cloud formation, as demonstrated by figure 4.28. This clear pattern of cloud streets disappears during the third hour as clouds grow larger and more latent heat is released inside them (see figure 4.29). At the end of the fifth hour, only the case 'along' shows cloud structures with a pattern different from other runs.

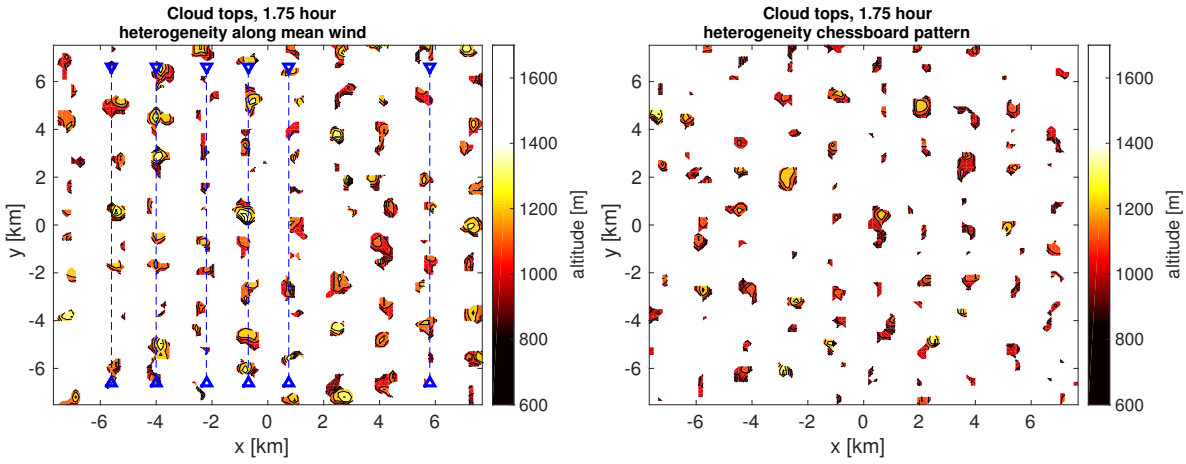

(a) (b)

Figure 4.28: Cloud patterns over heterogeneous surface at 1.75 hour. The blue lines highlight the organisation of cloud streets that develop in the case of heterogeneity 'along'.

Although the direct influence of surface heterogeneities on the ML structure vanishes in the later hours of the development of the convection, there are still significant differ-

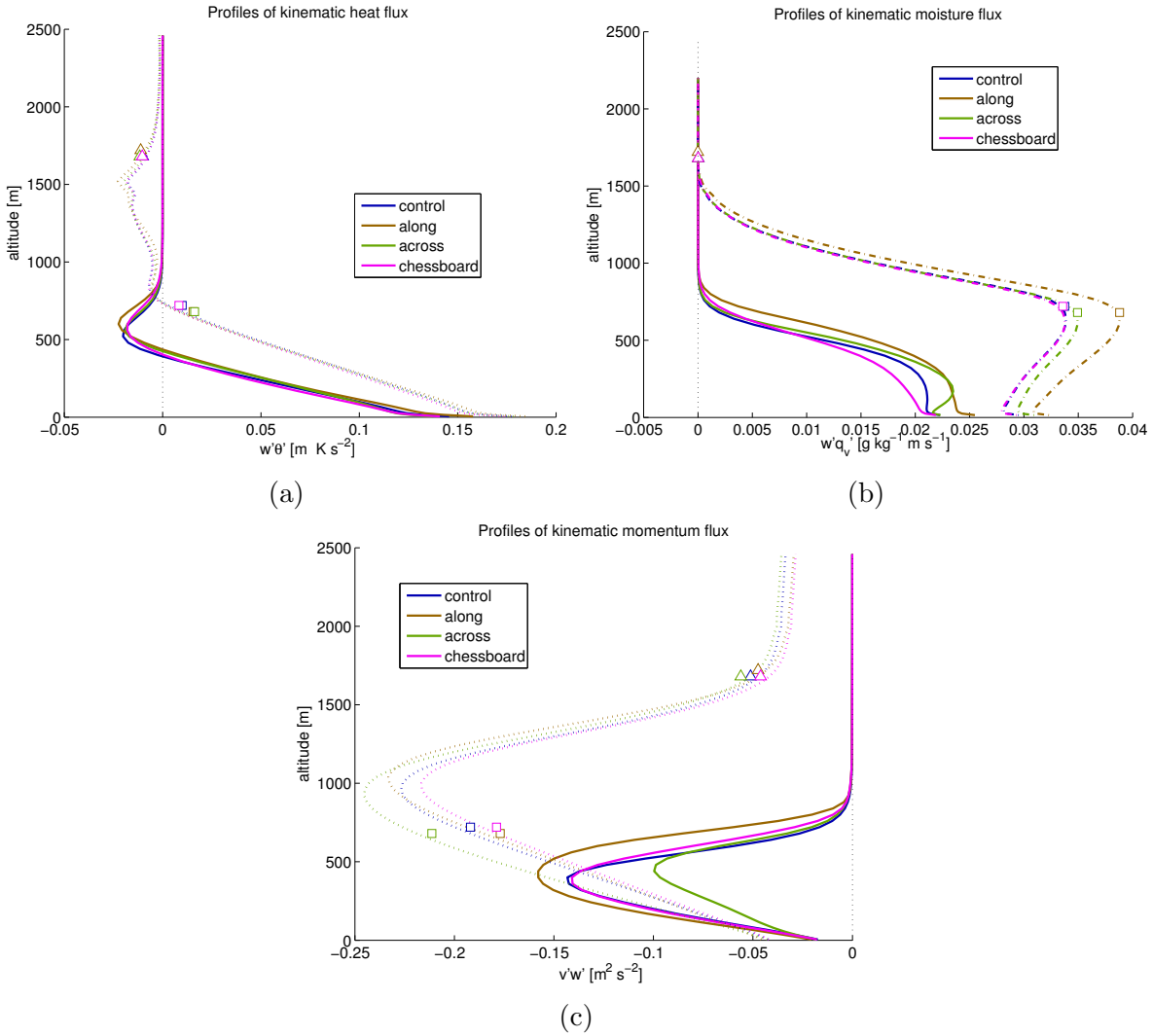

Figure 4.29: Profiles of the kinematic heat flux, the kinematic moisture flux and the kinematic mometnum flux for runs with different type of heterogeneity.
Full lines (–) show averaged profiles for 0.75-1 hour, whiled dashed and dotted lines show averaged profiles for 2-3 hours. The symbol □ marks the altitude of cloud base, the symbol △ the altitude of cloud tops.

ences in the kinematic heat flux in the CuL. Figure 4.29 further shows that there are moderate differences in the moisture flux both in the ML and the CuL, with relative differences between the 'along' and 'control' up to 10 % in the lower part of clouds. This likely indicates that venting of the ML by active cumuli clouds differs between the cases. At the same time, differences in the potential temperature flux are much smaller, practically negligible.

The development of momentum fluxes is slightly more complicated. In the middle of the first hour, momentum fluxes are generally stronger in both cases with stripe-like heterogeneities. As the ML deepens and larger convective eddies appear, momentum fluxes in the 'across' case are exceeded by both 'chessboard' and 'control'. The differences between the momentum fluxes tend to decrease. During the fifth hour, momentum fluxes in each of three heterogeneous cases vary from the control by less than 10 %.

The comparison of the subdomains shows relatively small differences between the model runs in terms of the kinematic heat flux. In the early development of the CBL, all three model runs show a wide extent of the min-max envelopes. By the 3rd hour, the differences in the ML diminish (see figure 4.30a), and all three cases show an increased variability in the CuL, mostly at altitudes of 820 m.

However there are number of differences in the kinematic flux of moisture. The 'along' case shows higher values of maxima of subdomains than the other cases. Despite that, the full width of the min-max envelope is higher in the 'across' case. However, it does not significantly exceeds the width of the whisker span of the control set, apart for the case 'along' (see figure 4.30b). Furthermore, the [0.25, 0.75] quantile envelopes remain similar for all three cases. These results indicate that stripes in the direction 'along' allow the formation of large eddies that can locally result in a higher transport of the moisture, while the stripes in the direction 'across' generally lead to a higher variability in moisture transport.

In summary, heterogeneous surface patterns play a significant role in the CBL development. Each type of the surface pattern leads to a slightly different structure of eddies during the formation of the ML and the first hour of its thickening. The distribution of updraughts and forming clouds also show a clear influence of the surface pattern. These differences later diminish, most likely due to the effect of the forcing by active cloud cores and the entrainment in the CuL.

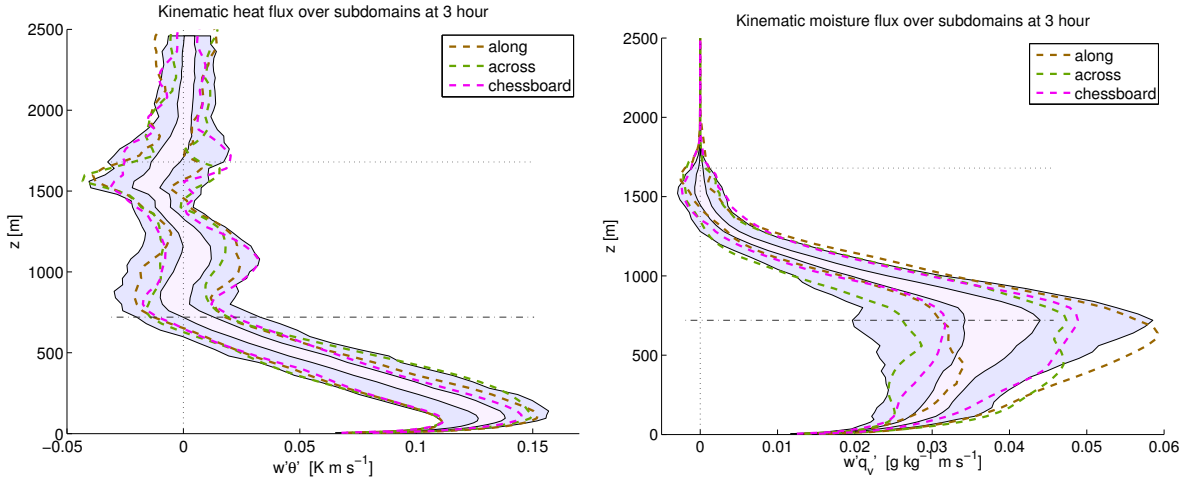

(a) (b)

Figure 4.30: Comparison of min-max envelops of the kinematic heat flux and the kinematic moisture flux for runs with different type of heterogeneity at 3 hour. The shaded areas mark the IQR (light purple) and span (light blue) of the control set.

4.2.2 Impact of Scaling of Heterogeneity

Due to a number of ongoing processes in sea-ice (Meylan et al., 1997), it would be too simplifying to model temperature anomalies in MIZ just as one chosen difference in the surface temperature. Therefore, this section shows how adjustment of the temperature scale $\delta_{(\mathrm{h})}T$ of anomalies modify the development of ABL in a specific way for each heterogeneity type.

The effect of $\delta_{(\mathrm{h})}T = 3\,\mathrm{K}$ heterogeneities **'along'** is significantly less profound than for $\delta_{(\mathrm{h})}T = 7\,\mathrm{K}$. The higher temperature scale leads to an earlier formation of clouds (see figure 4.31b), however further growth of clouds is slower than in the control case. All three model runs reach same amounts of cloud liquid water content as the control run by the 4th hour. Similarly, the variance in the wind velocity attains higher values for stronger surface temperature heterogeneities, however these differences mostly vanish by the end of 3 hour with the thickening of CuL. Figures for other wind variance components are shown in the Appendix.

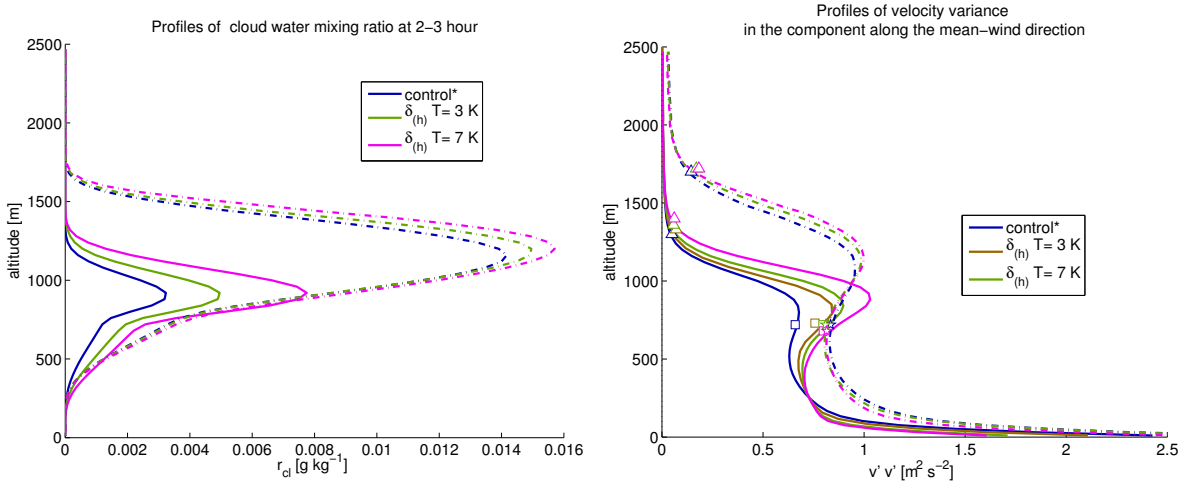

(a) (b)

Figure 4.31: The comparison of averaged profiles of cloud water mixing ratios for 'along' heterogeneity with different temperature scales and the velocity variance at same times. Full lines (–) show averaged profiles for 0.75-1 hour and dashed-dotted lines ($- \cdot -\cdot$) show averaged profiles for 2-3 hour. The symbol □ marks the altitude of cloud base, the symbol △ the altitude of cloud tops.

In contrast, increasing the $\delta_{(\mathrm{h})}T$ of stripes **'across'** the mean wind direction weakens the turbulence in growing ML. The variance in both horizontal components of wind velocity is weaker then in the control run. While the runs with lower heterogeneities converge to the control at the beginning of the second hour, the run with $\delta_{(\mathrm{h})}T = 7\,\mathrm{K}$ maintains lower values until the third hour of model runs. The effect of the scaling of the heterogeneity 'across' on updraught distribution is also significant in the estimation of kinetic energy of strong updraught. During the rapid growth of ML and development of

CuL, the E_w in $\delta_{(\mathrm{h})}T = 7\,\mathrm{K}$ is less underestimated than in other cases (see figure 4.32). This

Altering the temperature scale of the **'chessboard'** heterogeneous pattern leads mainly to differences in the early growth of the ML. Profiles of the vertical flux of passive tracers indicate that the IBL in model runs with $\delta_{(\mathrm{h})}T = 7\,\mathrm{K}$ grows up to 750 m during the second half of the first hour, exceeding the runs with weaker heterogeneities by more than 40 %. However, this difference in the IBL height is relatively short-lived. As the depth of ML increases, large temperature differences generally act against the formation of larger eddies. This is demonstrated by profiles of wind variances – model runs with strong surface heterogeneity maintain slightly higher velocity variances in the component along the mean wind direction but a lower kinematic moisture flux at the end of the first hour. The differences between the runs with different temperature scales of chessboard heterogeneity and the control run decrease below 5 % during the second hour.

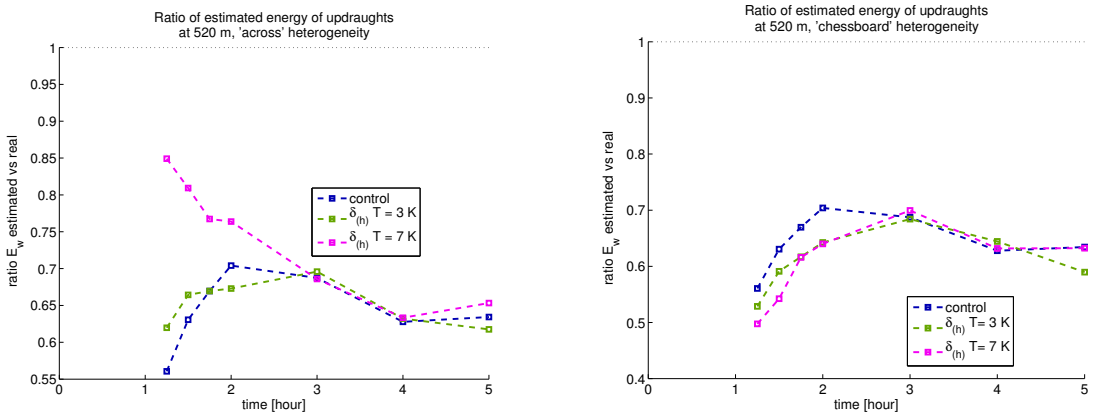

(a) (b)

Figure 4.32: The time development of the ratio of estimated values of kinetic energy of updraughts to its modelled values at altitude 520 in runs with heterogeneity

The coarse study of vertical fluxes reveals an increased spread in kinematic fluxes in subdomains. Although estimated kinematic fluxes of potential temperature are after the hour 1 found within the control set span, estimated fluxes of moisture often exceed the control set span even during the 3–4 hour. The effect is strongest for 'along'. While all estimated subdomain fluxes for case $\delta_{(\mathrm{h})}T = 3\,\mathrm{K}$ are within the control range, the situation in the case $\delta_{(\mathrm{h})}T = 7\,\mathrm{K}$ strongly differs. More than 25 % of the subdomain fluxes between the 1 hour and 3 hour exceed the control range in ML (see figure 4.33).

Generally speaking, the adjustment of the temperature scale of the heterogeneity $\delta_{(\mathrm{h})}T$ does not change the structure of eddies, but rather modifies how strong is the effect of the forcing. Higher temperature scale of the heterogeneity **'along'** leads to a faster growth of the CBL in the early hours after transition, while the heterogeneity **'chessboard'** leads to relatively negligible differences from the control run.

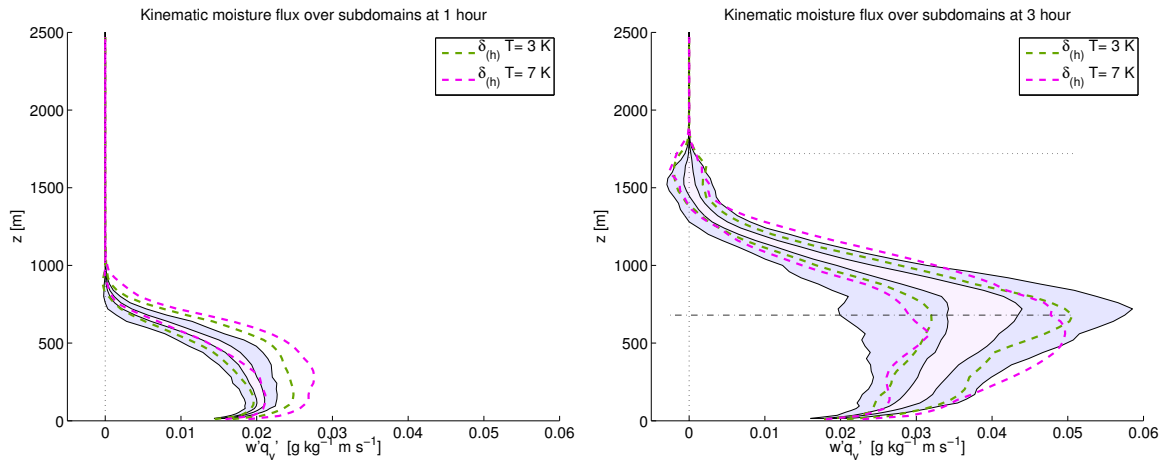

(a) (b)

Figure 4.33: The comparison of estimated kinematic moisture fluxes in subdomains for scaled heterogeneity 'along' against the control set at 1.5 hour and 3 hours.

4.2.3 Impact of the Size of Heterogeneity

The size of ice floats and leads in sea-ice sheet can vary in scales from few metres to few kilometres (Esau, 2007) (Inoue et al., 2005b). Due to ongoing processes of freezing and melting as well as dynamics of ice sheet, these properties can often change. Therefore it was reasonable to model runs with a different spatial extent of surface temperature anomalies. While the previous section has addressed the impact of adjustments in the temperature scale, this section is going to show how is the developing CBL affected by adjusting $d_{(\mathrm{h})}$, the size of the blocks of the heterogeneous pattern.

Increasing $d_{(\mathrm{h})}$ for the **'chessboard'** type heterogeneity to 3200 m allows a formation of clear cloud streets during 2-3 hour. The larger size of anomalies enables the formation of forced circulation. However, the clear pattern in clouds disappears at the end of the 3rd hour (see figure 4.34). This generally agrees with the findings of Gryschka et al. (2008) that forced rolls and free rolls might coexist. There are also significant differences in horizontal velocity variance that continue to grow until 2–3 hour (see figure 4.35). Later decrease in these differences follows. By the time 5 hour, vertical variance in the run with a large 'chessboard' heterogeneity does not differ from the control by more than 5 %.

Decreasing the $d_{(\mathrm{h})}$ in the case **'along'**, i.e. decreasing the width of stripes of positive and negative anomalies, generally leads to an increased mixing near the surface and a quick formation of a shallow ML. Although the mass flux and the flux of passive tracer are in the first half hour after t_0 highest in the case with the fine heterogeneity pattern,

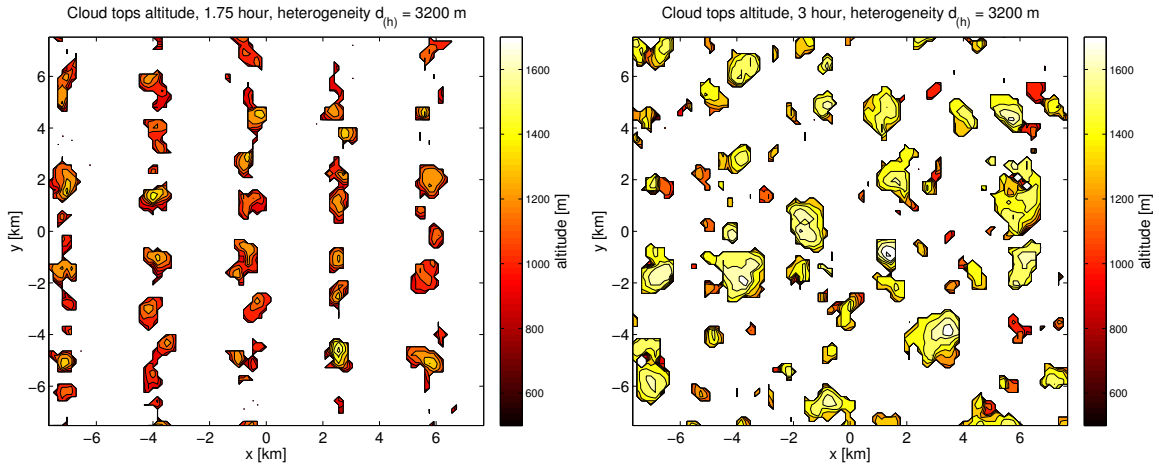

Figure 4.34: The comparison of cloud top altitudes at time 1.75 hour and 3 hour over the heterogeneous surface 'chessboard', $d_{(\mathrm{h})} = 3200\,\mathrm{m}$

$d_{(\mathrm{h})} = 400\,\mathrm{m}$, they are surpassed by respective fluxes in the run with $d_{(\mathrm{h})} = 1600\,\mathrm{m}$. The effect on the vertical fluxes of moisture is negligible from 1 hour onwards (see 4.36). With the deepening of the ML, the size of large convective eddies soon exceeds the block size of the fine heterogeneus pattern. As a consequence, runs with fine heterogeneity do not exhibit any clear impact on cloud patterns.

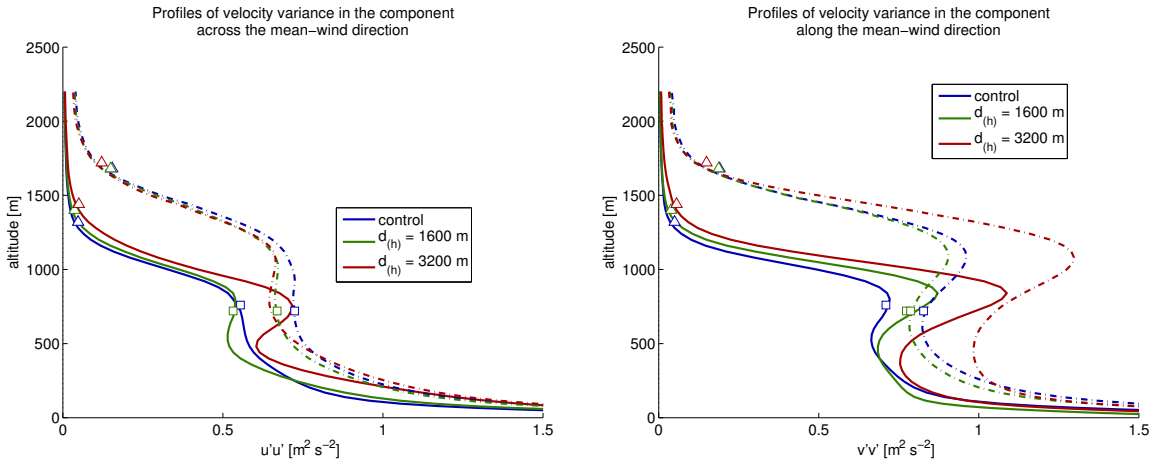

Figure 4.35: Profiles of variance in horizontal components of wind velocity for different sizes of 'chessboard' heterogeneity at the time 2 hour.
Full lines (–) show averaged profiles for 0.75-1 hour and dashed lines (- -) show averaged profiles for 2-3 hours. The symbol □ marks the altitude of cloud base, the symbol △ the altitude of cloud tops.

Increasing the $d_{(\mathrm{h})}$ for heterogeneity 'along' leads to even more distinct impact. The first obvious difference is an earlier formation of clouds, with some of them appearing close to surface, effectively within the surface layer. Although majority of cloud bases are located at altitudes 580 m or higher, some scattered glaciated clouds form as low as 50–200 m over the surface. This phenomena is clearly driven by near-surface plumes, since it was not indicated for any of the control set runs. Forming clouds follow a street-like pattern forced by positive surface anomalies. With the growth of the CuL and the increased cloud-top forcing, lines of clouds in the case $d_{(\mathrm{h})} = 1600\,\mathrm{m}$ veer off the original direction and start connecting into wider cloud streets (see figure 4.37). It is likely that these wider cloud streets would later transform into open cells, which are commonly found downwind in CAO cases (Atkinson and Zhang, 1996, pp.404,410).

For a lower values of $d_{(\mathrm{h})}$, street-like patterns effectively disappear once the height of IBL exceeds the size of heterogeneity. Furthermore, single active clouds grow to extend of 2–4 x size of heterogeneity. On contrary, a larger size of the heterogeneity allows to maintain patterns aligned with the mean wind. The model run with $d_{(h)} = 3200\,\mathrm{m}$ demonstrates this phenomena (see figure 4.38). Nevertheless, it is clearly shown that the cloud streets do not follow all the pattern of the surface heterogenity anymore. This is mostly due to fact that the growing width of convective rolls (Atkinson and Zhang, 1996) has exceeded the width of the heterogeneous pattern.

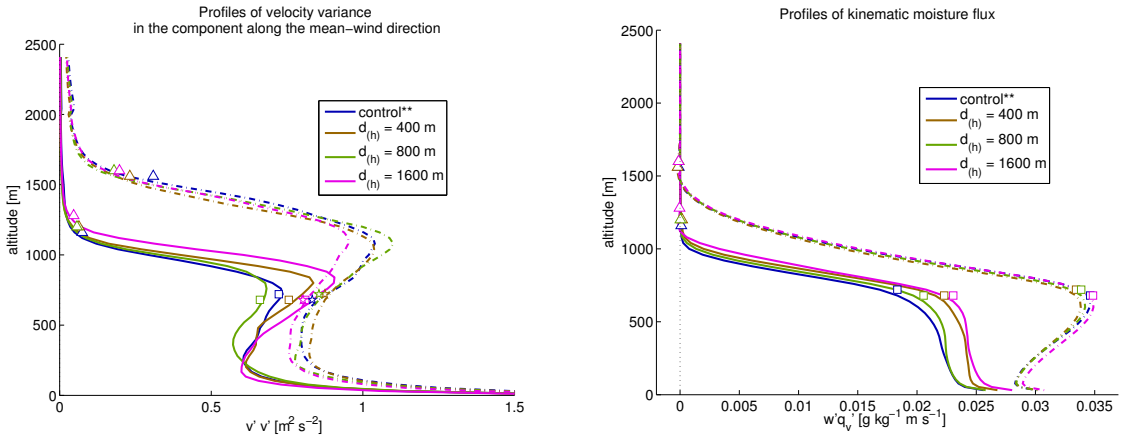

(a) (b)

Figure 4.36: The impact of fine heterogeneous forcing of the type 'along' on the profiles of wind variances and the kinematic moisture flux averaged over 1–1.25 hour.
Full lines (–) show averaged profiles for 0.75-1 hour and dotted lines (···) show averaged profiles for 2-3 hours. The symbol □ marks the altitude of cloud base, the symbol △ the altitude of cloud tops.

While the estimated depth of ML is $z_i = 600 - 700$ m during 3–5 hour, the total ABL height is calculated to be $z_{\mathrm{bl}} = 1600 - 1800$ m in the same time period. Relative ratios of surface heterogeneities to ML depth and total ABL height are then

$$4 < \frac{d_{(\mathrm{h})}}{z_i} < 6, \qquad 1.5 < \frac{d_{(\mathrm{h})}}{z_{\mathrm{bl}}} < 2,$$

which according to the previous study (Patton et al., 2005, pp.2088-89) is the case when the effect of surface heterogeneous forcing is the strongest.

Larger size of anomalies also affect the organisation of updraughts. Although the updraughts with velocities over 1 ms^{-1} occupy smaller fraction of the area in the middle of ML, updraughts are generally warmer and more moist, leading to higher SH and LH flux. Despite the different spatial organisation of updraughts, there are (surprisingly) no clear differences in the overall statistical distribution of vertical wind velocities in the surface layer.

Generally speaking, an increase in $d_{(\mathrm{h})}$, the size of the blocks of the heterogeneous pattern, leads not only to a stronger impact of temperature anomalies but also to a modification of the structure of the CBL. In case of heterogeneous surface temperature pattern 'along' of the large size (3200m), the pattern of cloud streets is maintained without significant changes in the direction or the width of these streets. Decreasing the $d_{(\mathrm{h})}$ generally leads to an increased mixing during the early development of CBL and a quick formation of a shallow ML.

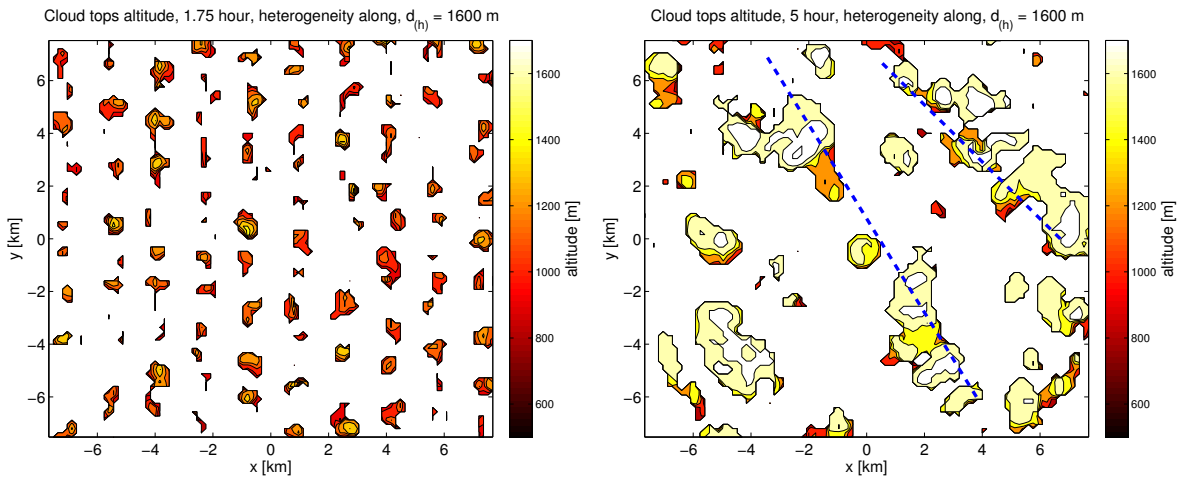

Figure 4.37: The comparison of cloud top altitudes at times 1.75 hour and 5 hour over the heterogeneous surface 'along', $d_{(\mathrm{h})} = 3200$ m

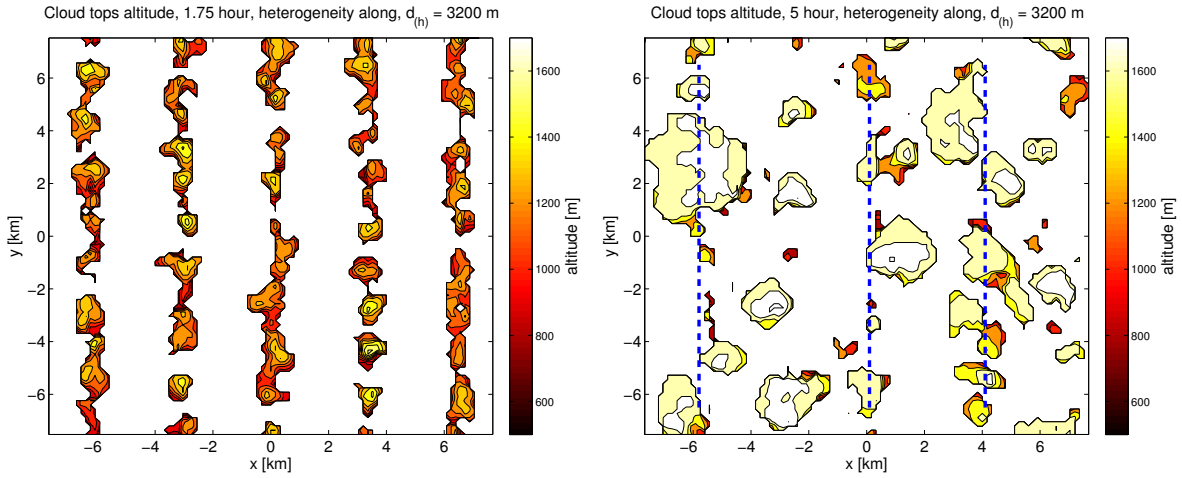

Figure 4.38: The comparison of cloud top altitudes at times 1.75 hour and 5 hour over the heterogeneous surface 'along', $d_{(\mathrm{h})} = 1600\,\mathrm{m}$

4.2.4 Diminishing Surface Heterogeneities

Since the main motivation for the introduction of spatial heterogeneity in surface temperatures is to model conditions over a MIZ, it is realistic to assume that some short MIZs (Brümmer, 2002, p.111) are followed by open sea with small spatial differences in surface temperatures. This case is pragmatically modelled as a heterogeneous pattern that diminishes with time (see figure 3.6). The scale of anomalies starts to decrease after 0.5 hour and reaches zero by 1 hour instead of staying constant like in previous cases (for details, see the LEM setting in 3.3.2 and the Appendix). To investigate the impact of these relatively short-lived heterogeneities, model runs runs with the diminishing heterogeneity ('diminish') setting are compared against the model runs where the surface heterogeneity persisted ('per').

The impact of heterogeneities 'across' and 'chessboard' is relatively minor. Both cases lead to an increased mixing in comparison with the control during the first hour, however their effects disappear together with the forcing.

The ABL modified by a temperature heterogeneity 'along' the direction of the mean wind maintains its character significantly longer, for at least one hour after the surface heterogeneity diminishes The velocity variance and the kinematic moisture flux in the model run with the diminishing heterogeneity (**'diminish:along'**) differs strongly from the control run even at the end of 2nd hour. Figure 4.39 shows that the values are actually closer to values of the run with the persistent heterogeneity (**per:along**). However, 'diminish:along' values are closer to the control* run after 3 hour.

In essence, a short-lived heterogeneity in surface temperature during the formation of CBL can have impact on the properties of CBL downstream. The effect of the diminishing heterogeneity of the type 'along' is maintained for at least one hour after the heterogeneity disappears.

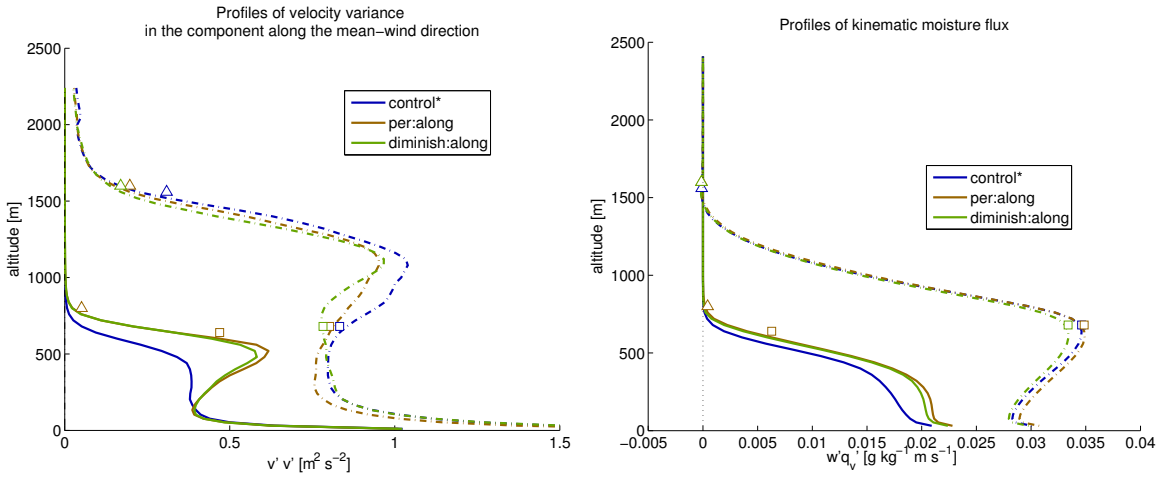

(a) (b)

Figure 4.39: The impact of the diminishing heterogeneus forcing on the profiles of wind variances and the kinematic moisture flux. Full lines (–) show averaged profiles for 0.75-1 hour and dash-dotted lines (– · –·) show averaged profiles for 2-3 hours. The symbol □ marks the altitude of cloud base, the symbol △ the altitude of cloud tops.

4.2.5 Timeseries of Fluxes

It has been stressed in the introduction that one of the main goals of this study is to estimate the impact of uncertainty in conditions on the distribution of vertical fluxes of the momentum, the latent heat and the sensible heat different altitudes in the boundary layer and the free troposphere above. The evaluation of flux timeseries follows the same path as in 4.1.4.

While the recorded timeseries (see figure 4.40) do not vary in the general tendency of the development, there are differences in oscillations. Apparently, the 'across' case shows slightly larger oscillations in flux values. However, normalised power spectra follow the same slope as in other cases (for details, see Appendix) Larger fluctuations clearly appear in histograms of residua — the 'across' case exhibits a higher spread in residua, particularly at altitudes 520 m and 1480 m (see figure 4.41). In all three cases, the distributions of residua are mostly symmetrical around 0, with the exception of residua of the LH flux at the altitude 800 m in 'along' and 'chessboard' cases that shows a longer tail into negative values.

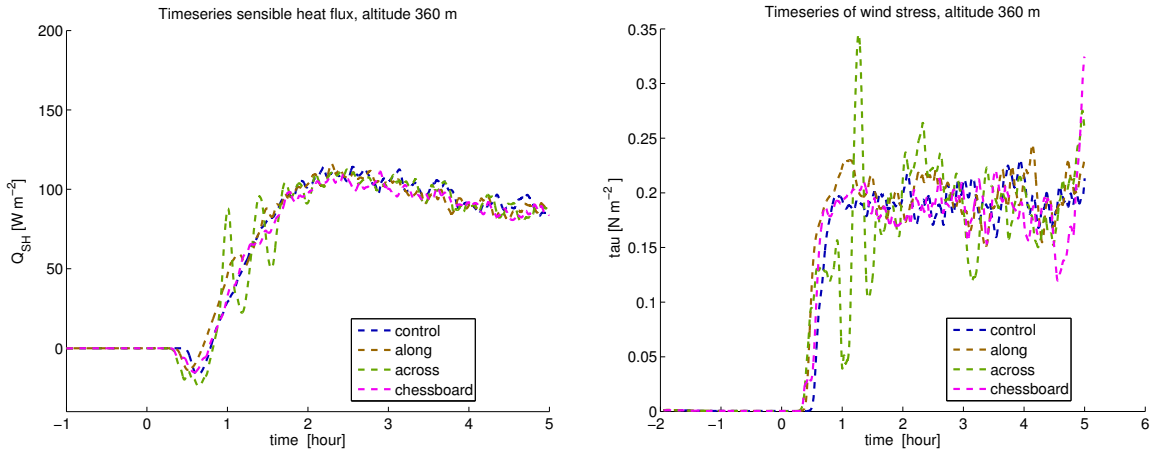

(a) (b)

Figure 4.40: The comparison of the timeseries of the SH flux and wind stress at the altitude 360 m between the runs with different type of heterogeneity.

While results indicate that the oscillation in fluxes of the latent heat, the sensible heat and the wind stress depends on the type of the heterogeneity, the character of the conditional distribution of fluxes is similar to the control. New values of residua are located with a high probability close to values from the previous step.

Autocorrelation in the timeseries of LH and SH fluxes at altitudes inside the ABL are generally stronger in the 'across' case. The autocorrelation values decrease below the threshold 0.3 for the time lags between 280 s and 300 s. This stands in the contrast to 'along' case where autocorrelation values decrease below the threshold 0.3 for time lags of 150–200 s (see 4.43).

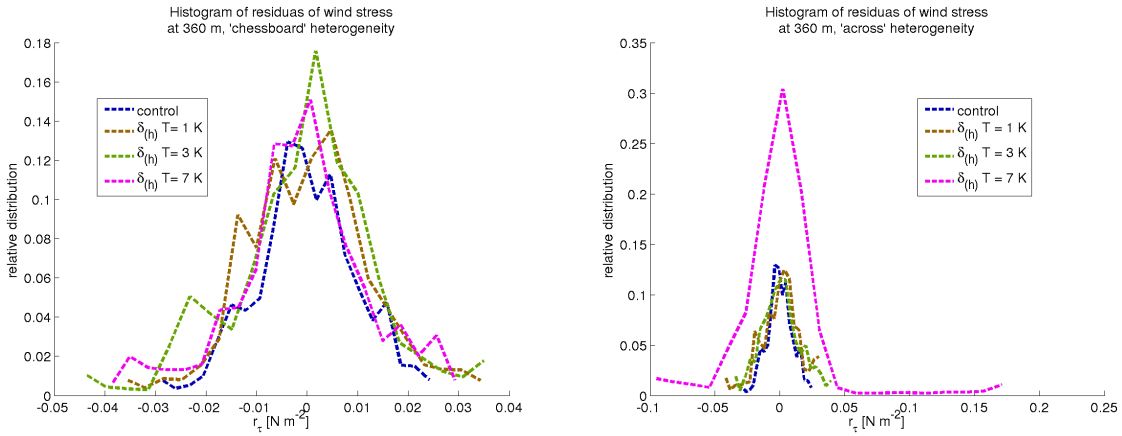

(a) (b)

Figure 4.41: The comparison histograms of residua of wind stress at altitude 360 m.

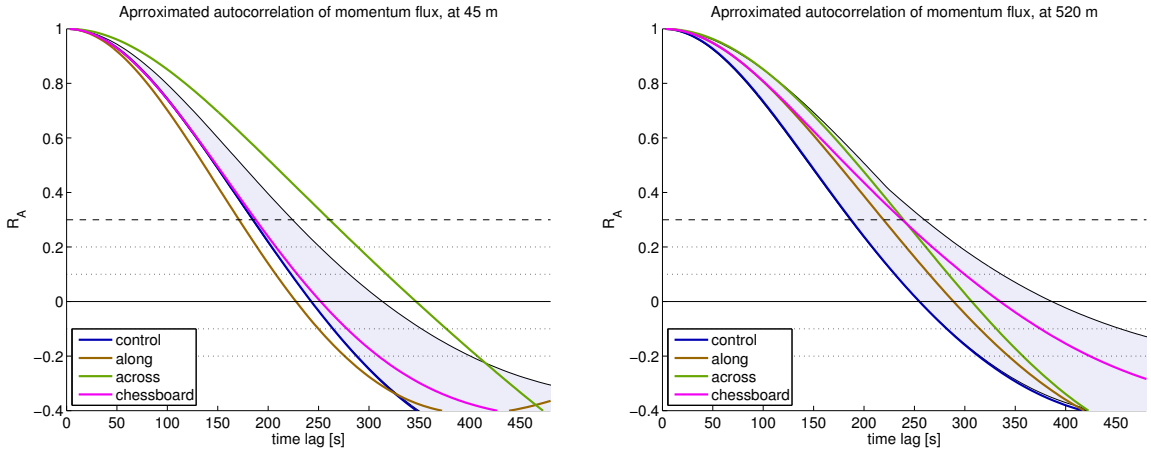

(a) (b)

Figure 4.42: The comparison of the autocorrelation of wind stress residua at altitudes 45 m and 520 m for runs with different heterogeneity.

The autocorrelation in the timeseries of wind stress by the surface is also stronger for 'across' case. At higher altitudes in the ABL, autocorrelation is enclosed within the control set min-max envelope (see figure 4.42). In the free atmosphere, autocorrelation values reached for both 'across' and 'chessboard' case are similar as for the control run, however the autocorrelation in the 'along' case is generally weaker.

The temperature and the size scaling of heterogeneities further modify the nature of oscillations in vertical fluxes. Increasing the $d_{(\mathrm{h})}$ usually affects the spread in residua of momentum fluxes. In the case 'chessboard', it also leads to a stronger autocorrelation in momentum flux residua at altitudes within the ML.

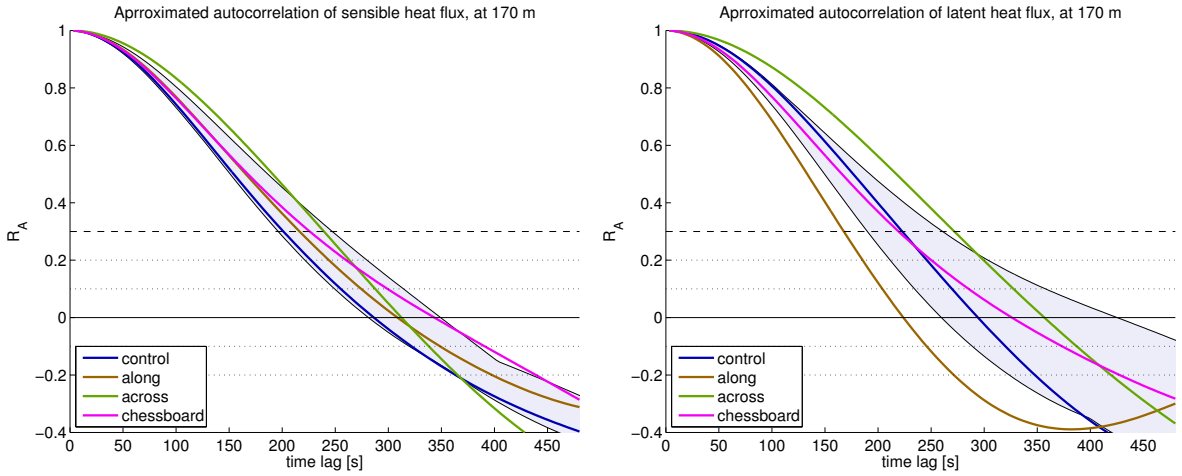

(a) (b)

Figure 4.43: The comparison of the autocorrelation in the segment 3 of SH and LH flux residua at altitude 170 m for runs with different heterogeneity.
The blue shading indicates the min-max envelope of the control set.

Increasing the $d_{(h)}$ for heterogeneity 'along' leads to generally weaker autocorrelation in the sensible and latent heat flux. On the other hand, stronger autocorrelation is calculated for the wind stress at 520 m and 1480 m (see figure 4.44). These are the altitudes corresponding to the sub-cloud layer and cloud tops, respectively. Since most of the wind shear is confined to the top part of clouds (see 4.1.1), the stronger autocorrelation in the wind stress at this altitude most likely indicates that larger heterogeneities lead to slower fluctuation in the shear-generated momentum flux.

Overall, the heterogeneity in surface temperatures effects the oscillation in vertical fluxes of LH, SH and momentum in the CBL and above it. Similarly to other studies, there was no significant gap in the spectra of flux timeseries (Kang, 2009, pp.77-78). Model runs with the heterogeneity 'across' exhibit stronger autocorrelation in flux timeseries residua. Increasing the size of heterogeneity 'along' can lead to a slower fluctuation in shear and cloud convection generated momentum flux. This impact of surface heterogeneity on oscillation in fluxes should be taken into account both in field measurements as well as in NWP with short timesteps.

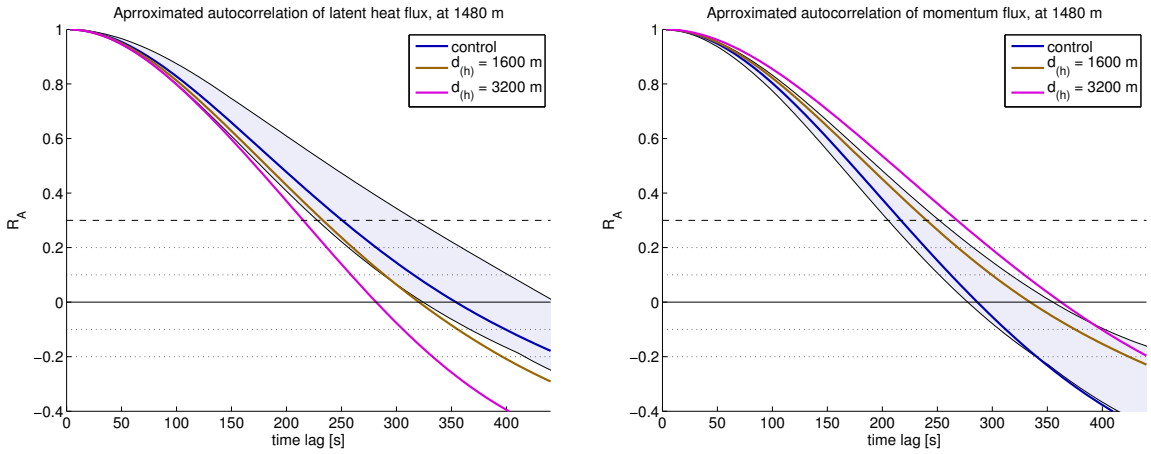

(a) (b)

Figure 4.44: A comparison of autocorrelation in the later segment of LH flux and wind stress residua at altitude 1480 m for different sizes of the heterogeneity 'along'.

4.3 Discussion

While the sensitivity testing shows that increasing the horizontal resolution does not lead to significant changes in model results apart from shapes of clouds 3.5, majority of cases used the control setting of the horizontal resolution. However, there was a serious concern about modelling the heterogeneous surface pattern of the size $d_{(h)}$ smaller than 1600 m. In the control setting of the resolution, positive anomalies in each block were represented just by a few gridpoints. While it was not clear whether the impact

of heterogeneous surface heating would be properly resolved, additional runs with the increased horizontal resolution (40 m) were set as well (see description in 3.1) Due to memory constrains, the domain size in these runs was necessary smaller With the width of the domain set in that case to 6 km, which is 3-5 times the width of a developed cumulus cloud (Craig and Cho, 1988) (Jiang and Cotton, 2000), it was deemed unreasonable to use these runs for the analysis of gravity waves and the analysis of subdomain variability. Dividing the domain into subdomains would result in a cut-off issues as in some subdomains would be just a part of cumulus cloud while in some other would be a few cumuli clouds.

The background reading for this study has also revealed some noticeable limitations in the previous studies of the ABL over a heterogeneous surface. Despite wide variety of scenarios and model setting, previous studies usually focused just on one specific regular shape of heterogeneity (Kang and Lenschow, 2014) or employed some randomly generated patters of surface patches (Maronga et al., 2014). Furthermore, the majority of studies have usually focused on the transport in stable or near-neutral layer (Esau, 2007). Although there have been also studies of the heterogeneous surface during CAO, they have modelled surface heterogeneity in a slightly different way. Often, the prescribed property of the surface was not temperature but surface SH and LH fluxes. This kind of setting used in (Avissar and Schmidt, 1998), is likely to rise some specific issues.

1. Heterogeneous heating cause significant differences in buoyancy of air parcels, generating secondary circulation within CBL.
2. Secondary circulation alters the spatial distribution of wind velocities by the surface.
3. Different wind velocity leads to different conditions for the heat and moisture transport from the surface to the ABL

If the surface SH and LH fluxes are already prescribed in the model surface conditions, then the feedback of the secondary circulations is not properly represented. On the other hand, if the surface conditions are characterised by surface temperature and humidity, the model evaluates the fluxes based on relations for the surface transport. Therefore, this study uses model setting where the surface heterogeneity is prescribed as a difference in the surface temperature.

The regular pattern of surface anomalies in number of previous studies usually consisted of stripes in the direction of the wind or across it. The other common choice was a regular wave pattern in anomalies. In some studies it was two-dimensional wave pattern (Kang and Davis, 2008), in others it was a wave in one dimension only (Kang and Lenschow, 2014), either in the direction along the mean wind or across it. Values of

anomalies followed the sinus function in one direction and remained constant in the other direction. The main advantage of this set-up was that it allowed to propose a simple analytical formula for the circulation forced by fluxes. However, it was generally used in the cases where the scale of anomaly was same as the size of convective eddies. The conflict between the size of convective rolls and the size of surface forcing was usually not addressed. Furthermore, in scenarios that started with initially unstable boundary layer, the model essentialy represented the semi-stationary CBL. This presents two moderate shortcomings:

- The ratio of the wavelength of surface anomalies to ABL height is nearly constant.
- The effect of the heterogenous heating on the formation of shallow CBL and its subsequent growth is not explored. The possibility that heterogeneous pattern determines the shape of the early convective eddied is practically omitted.

While some studies noted that surface fluxes decrease with increased number of heterogeneous patches (Courault et al., 2007), our study shows that it happens in case of stripes 'across' and 'chessboard'. On the other hand, in case of stripes 'along', the fluxes are generally higher.

Although the regular chessboard-like or stripe-like patterns of the temperature anomalies might not represent the real shapes and distribution of sea ice and areas of open water in the MIZ (Meylan et al., 1997) , they serve as a basic approximation of heterogeneous structures. Although there have been various observational studies of the distribution of sizes of ice floats (Inoue et al., 2004) and (Gupta et al., 2014), they have unfortunately not provided guidelines for the respective shapes and widths of areas of water between the floats. There has been also an argument that the boundary layer fluxes are much more dependent on the amount of open water (Inoue et al., 2005b), however other case study (Cooper et al., 2000) showed that surface fluxes over partially ice-covered sea are not negligible. Nevertheless, the pattern can be easily modified in the upcoming years when comprehensive observations of MIZ morphology and variation in surface temperatures become available.

The other factor that might have an impact on the development of the CBL is the setting of microphysical properties used by the model. The intercomparison of various LES of the Arctic mixed-phase clouds (Ovchinnikov et al., 2014) showed that the ice particle size can play a significant role. While the setting of microphysics in the current version of the LEM is limited, there is a strong incentive for improved aerosol modelling in MONC, the successor software package to LEM. (NERC, 2014)

While some studies of cold-air outbreak show that cloud street tilt sideways in a similar way as in observations (Kristovich, 1993), this phenomena is in this study indicated

only in the case 'along'. The fact that LEM uses periodic boundaries is likely to be the culprit. Once the direction of the streets slightly tilts from the direction parallel to axis y, the clouds leaving the domain downwind appears at the upwind side of the domain at different place than the previous beginning of the street, possibly causing subsequent merging of cloud streets.

4.4 Conclusion and Outputs

The study based on idealised Large Eddy Simulation of a simple cold air outbreak scenarios assessed the variability in the development of the convective boundary layer. While number of previous studies of heterogeneous surface forcing, for example (Avissar and Schmidt, 1998) and (Heerwarden et al., 2014), addressed the impact of a chosen type of heterogeneity on the growth of convective boundary layer, this study has taken a different path.

The main novel part of this study is that it focused on the comparison of different patterns of the surface heterogeneity. The other novel part of this study is the analysis of the variability in the fluxes of heat and moisture at different altitudes above the surface. With these study aims (1.4), we introduced three distinctive *types of heterogeneous pattern* in surface temperatures and executed scenarios starting with *initially stable stratified* atmospheric boundary layer. The impact of the chosen patterns of surface heterogeneity in surface temperatures was then analysed and compared with the variability in the ensemble of model runs with homogeneous conditions.

In the agreement with many other studies such as (Kang et al., 2007), (Maronga et al., 2014) or (Beyrich and Mengelkamp, 2006), the heterogeneous surface conditions modify the properties of the atmospheric boundary layer. The results are consistent with the findings of studies on surface inhomogeneity in the MIZ. The surface inhomogeneities affect the vertical structure of the ABL (Lüpkes et al., 2008) and contribute to the formation of convective rolls (Gryschka and Raasch, 2005). The most significant is the impact on the structure of the growing convective boundary layer in the first two hours over the warm surface. During the formation of the mixed boundary layer and the first hour of its thickening, each type of surface heterogeneity leads to a slightly different structure of eddies and a different distribution of updraughts and clouds.

Surface temperature heterogeneities play an important role in the formation of convective rolls and cloud streets. Model runs with a different setting of the heterogeneous forcing vary from the control run, however domain averaged statistics show relatively small differences in vertical profiles of potential temperature and vertical fluxes. This

stand in a good agreement with other studies (Cheinet and Siebesma, 2009), which concluded that vertical profiles behave accordingly to mixed layer similarity theory (Stull, 1988, pp.450-456).

In the later development of the convection, differences between the model runs with surface heterogeneities tend to diminish. The thickening of the mixed-phase cloud layer leads to positive cloud forcing, recognised also in other studies (Zuidema et al., 2005). The formation of active cumuli cores leads to an increase in the turbulent kinetic energy. This *top-driven forcing contributes to the decline* in the impact of the surface forcing. In less than 4 hour after t_0, there are no significant qualitative differences between the behaviour of model runs with different setting of heterogeneity. From the quantitative point of view, the differences between the model runs are relatively small yet not negligible. Values of fluxes and horizontally averaged prognostic variables do not differ by more than 7 % between the model runs.

The question of the scaling of the heterogeneity was investigated. On one hand, adjusting the temperature scale of the heterogeneity results in a weaker or a stronger effect of the heterogeneous pattern. On the other hand, adjusting the spatial extent of heterogeneity may lead to qualitative differences. While some studies claimed that larger size of surface anomalies lead to stronger surface fluxes (Kang and Davis, 2008), and increasing number of surface patches lead to lower surface fluxes (Courault et al., 2007), findings of our study indicates that *the effect depends on the type of heterogeneity.* In case of the heterogeneity type with the stripes along the mean wind direction, pattern of the size $d_{(\mathrm{h})} = 3200\,\mathrm{m}$ not only influences the formation of cloud streets, but also allows to maintain the organisation of cloud streets along the mean wind.

The study has also taken into account different widths of marginal ice zones (Claussen, 1991). The role of short-lived surface heterogeneities in a sea-ice marginal zone is not negligible. Heterogeneous surface forcing that was applied in the first hour of the CBL development affects the structure of the CBL for the following 1–2 hours. This represents the distance of 18–30 km downwind of the edge of ice. Although this distance might seem relatively short, it is likely the area where field observations of the boundary layer over marginal sea-ice zone are taking place.

The evaluation of updraughts showed that strong updraughts facilitate a significant portion of the heat and moisture transport. Other conclusions about the structure of updraughts and downdraughts in a developing convective boundary layer follows:

- The distribution of the vertical velocities in a developing ML shows a heavier tail into positive values (4.1.2).
- The vertical wind velocity distribution in the ML is generally not symmetric,

skewed towards positive numbers near the surface and towards negative in the upper part of the ML. This indicates a number of forming strong updraughts at a bottom of thermals (4.1.2).

- Although the distribution of potential temperature perturbations does not follow normal distribution, the distribution of potential temperature inside strong updraughts is approximately normal (see figure 4.13).
- While the distribution of vertical velocities in ML is not normal, the approximation by normal distribution results mostly in an underestimation of the kinetic energy of updraughts (see figure 4.12).
- The initial development of the convective boundary layer over surface anomalies might influence the structure of the developing clouds. This effect might persist despite the fact that mean properties of the developed ML do not differ (4.2.4).

The coarse study of fluxes has revealed that although the domain-averaged values of kinematic fluxes are similar, there might be a large spread in the values estimated in limited subdomains (here set 4 km x 4 km for the purpose of the evaluation). This result is important both for computing fluxes in fine-resolution NWP and for the evaluation of field measurements. It is very likely that there might be high differences in the estimated fluxes along short flight trajectories.

The timeseries of fluxes of the sensible heat, latent heat and momentum show a number of oscillations. The oscillation is usually strongest in model runs with surface temperature anomalies oriented in the direction across the mean wind. A high degree of autocorrelation is found in the oscillation of flux timeseries. Significant time lags are generally shorter than the ML timescales. Nevertheless, the autocorrelation in flux oscillations should be taken into account in NWP with short timesteps.

Findings of this study extend our knowledge of the convective boundary layer in cold air outbreaks. The impact of the different shapes of surface temperature heterogeneities is shown, as well as the importance of the surface heterogeneity for the formation of cloud streets. The results of the study give further implications for the explanation of the variability in aircraft measurements, presented in the chapter 5, and the adjustment of the parametrization schemes, presented in the chapter 7. However, first I must address the question whether the surface heterogeneities play similar role also in cold outbreaks with stronger wind forcing or different initial conditions. Therefore, adjusted cold outbreak scenarios are the subject of the next chapter.

Chapter 5

Adjusted Scenarios of Cold-Air Outbreak with Surface Heterogeneity

Cold-air outbreaks occur in a wide range of geographical locations (Papritz et al., 2014). During the winter season in the northern hemisphere, cold outbreaks are observed both in high latitudes of Arctic (Brümmer, 1996) (Ebner et al., 2011), areas over Labrador Sea (Liu et al., 2004) as well as in mid-latitudes (Inoue et al., 2005a) (Yamamoto, 2012). In CAO events at all these geographical locations (see 1.3.2), it is reasonable to assume that the cold air masses are advected over a surface that is not strictly homogeneous — in the inner Arctic, marginal sea-ice zone consist of large areas covered with a broken sea-ice sheet and ice floes (Inoue et al., 2004). Similarly, coastal polynyas of the Laptev Sea consist of patches of ice and open water (Ebner et al., 2011). Regions around Labrador and Greenland are dominated by areas of ocean convection where patches of colder water sink and are replaced with warmer water from below (Renfrew et al., 2002).

While the vertical structure of the troposphere varies between different locations and seasons, it is logical to ask how does the heterogeneity in surface temperatures influence a developing CAO. Chapter 4 has demonstrated how the different types of heterogeneous surface temperature modify the developing CAO in one chosen idealised scenario. However, the question remains whether these results are applicable on other CAO cases as well. This chapter therefore logically aims to address this question by extending the model study on a wider palette of CAOs. It introduces new idealised CAO scenarios and explores the impact of heterogeneous surface conditions on the development of convective boundary layer (CBL) in each scenario. The numerically modelling is again performed in the Met Office Large Eddy Model (LEM). The setting of different scenarios is explained in the part 5.2. Each scenario is prepared with a set of model runs with a different setting of the surface heterogeneity.

Before the chapter investigates the impact of heterogeneity, it first presents a qualitative comparison of CBL development between scenarios (5.3). While increased stratification or increased wind forcing might modify the vertical structure of the CBL (Liu et al., 2011) (Fedorovich and Conzemius, 2008), it is reasonable to discuss specific properties of each scenarios first. The chapter then moves to the analysis of the impact of surface heterogeneity on a developing CBL, first in the scenarios with increased wind forcing (5.4), followed by scenarios with increased stratification (5.5) and scenarios where both increased stratification and adjusted wind forcing were present. However, these parts of the chapter do not provide a catalogue description of the results of simulations with heterogeneities in each model setting. Since the purpose of this study is to extend our understanding of the role that heterogeneous surface temperatures play in CAO, this chapter instead presents specific results that are different from the results of control scenarios or otherwise expanding our knowledge with respect to previous studies. The results are then compared, further discussed and possible limitations of this study are addressed (5.6).

5.1 Brief Review of Previous Studies

Due to a wide range of wind conditions observed in the Arctic (Kilpeläinen and Sjöblom, 2010) (Mäkiranta et al., 2011) a variety of wind velocities are considered in the studies of turbulent fluxes over wide Arctic leads (Esau, 2007). A number of observational and modelling studies have shown that a decrease in wind shear can result in a stronger impact of the anomalies in the surface temperature (Gryschka et al., 2008). These result were similar to a number of other studies of the impact of inhomogeneities in surface temperatures (Sühring et al., 2014) and inhomogeneities in surface fluxes (Avissar and Schmidt, 1998) where stronger winds lead to a diminishing impact of surface inhomogeneities.

Furthermore, an extensive study of the impact of heterogeneities on the vertical structure of the ABL (Mahrt, 2000) concluded that the effect of surface heterogeneities generally increase with the scale of heterogeneity and decreased with the wind speed, boundary layer depth and stability. Idealised studies of the atmospheric boundary layer with heterogeneous surface conditions (Heerwarden et al., 2014) often indicated a ratio between the depth of the boundary layer and the wavelength of the heterogeneous pattern when the effect of the heterogeneous forcing is the strongest (Patton et al., 2005). However, it was not generally addressed whether the results are not directly dependent on the stratification in the troposphere.

Although previous studies provided interesting insight into the impact of heteroge-

neous surface conditions, they were often limited on one chosen shape of heterogeneity. Therefore, the main hypothesis investigated in this chapter is that:

- *stronger wind forcing leads to a weaker effect of the heterogeneity in surface temperatures*
- *increased stratification alters the effect of the heterogeneity in surface temperatures.*

5.2 Settings of Adjusted Scenarios

Previous idealised studies of CAO, for example (Kershaw, 1995) and (Gryschka et al., 2014), have usually started with a stratified troposphere that follows a piecewise linear profile - the bottom few hundred metres are almost neutrally stratified, followed by a stronger stratification above. Relative humidity was usually highest by the surface and then continued decreasing with height. The large scale wind forcing generally consisted of a linear profile in the lower troposphere and was constant above. This study generally follows this approach to setting of the properties of the troposphere, however model runs always start with a stable boundary layer (SBL). The main reason for this setting is that it allows us to record early stages of a developing CBL. A description of specific cases follows.

A case of a moderate wind shear and a weaker stratification in the bottom troposphere was chosen as a control scenario and explored in the previous chapter. While the sensitivity testing has already addressed the case of troposphere with increased humidity, cases of other changes in the vertical structure of the troposphere are examined in this chapter. The scenarios setting adjusted in LEM are:

- increased stratification in the lower troposphere
- increased large scale wind forcing
- weaker wind shear

In the setting assumes a multilayer structure with the possible temperature inversion in the lower troposphere (Bian et al., 2013). All model runs start without clouds, since most of observed CAO cases are cloud-free over the ice-edge (Brümmer, 2002).

Initial profiles of potential temperature are adjusted to represent cases of stronger and weaker stratification (see figure 5.1). They generally followed the conditions over the Arctic Ocean where the troposphere exhibits a multi-layer structure with a strong stratification the stable boundary layer (SBL) (Bian et al., 2013). The profile **strat2** was set to represent the influence of strongly stratified boundary layer on developing convection. The potential temperature lapse rate in the bottom 1500 m reached 13.2 K km^{-1}. Profile

strat3 exhibit stratification 9.5 K km^{-1} above 1500 m and slightly weaker (8.7 K km^{-1}) bellow. The profile **strat4** then implements basic McClatchey profile for winter subarctic conditions (McClatchey et al., 1971), which represents standard observed stratification in the outer Arctic areas during the winter months. Finally the profile **'strat5'** with the potential temperature lapse rate 5.3 K km^{-1} covered the gap between the stratified scenarios and a relatively weak potential temperature lapse rate 2.6 K km^{-1} in the control scenario (see figure 3.1b). All profiles with the exception of 'strat4' started with a temperature 253.0 K at the bottom of the boundary layer, following the setting of the study on modelling the convective internal boundary layer (IBL) in the off-ice flow (Renfrew and King, 2000). The exact numerical values of the initial potential temperature profiles are displayed in the Appendix.

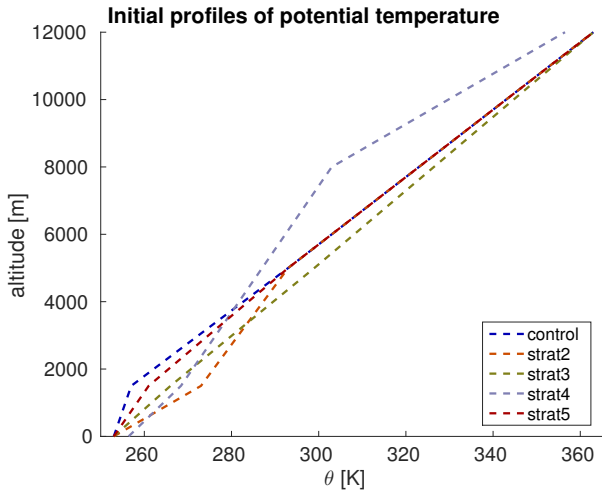

Figure 5.1: The setting of initial potential temperature profiles for adjusted cases

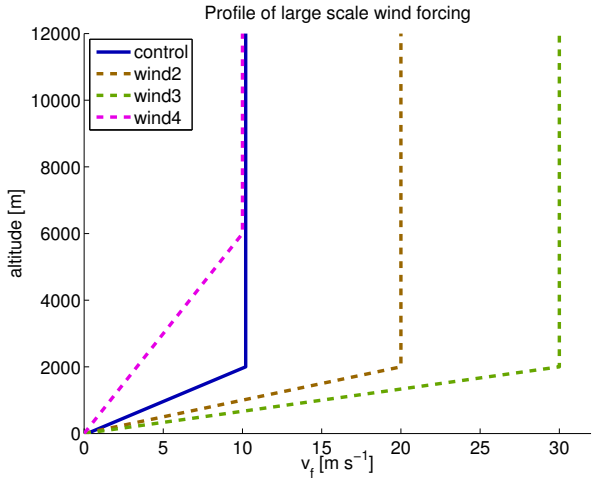

Figure 5.2: The setting of large scale wind forcing for adjusted cases

Adjustment of the large scale wind forcing (see figure 5.2) represents idealised cases with stronger quasi-geostrophic wind, which reach in the scenario **wind2** value of 20 m s^{-1} and in the scenario **wind3** value of 30 m s^{-1}. Evaluation of scenarios with stronger wind is important because cases where convection occurs in subarctic areas often coincide with regions of stronger winds (Moore et al., 2014). The possibility of a weak wind shear is represented by case **wind4** where the wind speed does not reach 10 m s^{-1} bellow 6000 m.

The possibility of CAO with a high wind shear in a strongly stratified troposphere is covered by the combination of large scale scale wind forcing from 'wind2' and the initial temperature profile 'strat2'. This scenario is further referred as **wind2-strat2**. In a similar manner, the model scenario **wind4-strat2** represents a CAO with a weak wind conditions and a strongly stratified lower troposphere.

A batch of model runs is prepared for each model scenario with a goal to investigate the impact of heterogeneous surface forcing. One run is always set with a surface temperature that is constant over whole model domain. These runs are marked as 'homogeneous'. Other runs are set with a pattern of anomalies in the surface temperature (introduced in 3.3). There are three distinctive patterns - 'along', 'across' and 'chessboard' (see figure 3.5) The heterogeneity is modified by two parameters:

- the spatial extent of the anomaly, defined by the length $d_{(\mathrm{h})}$ of a side of building block of the chessboard pattern
- the temperature scale of the anomaly $\delta_{(\mathrm{h})}T$, which is the maximum temperature difference between the anomaly and the mean surface potential temperature.

The full list of model runs is located in the Appendix.

The setting of the growth of surface temperature with time remains the same as in the control case (see figure 3.6). The setting of other ambient parameters, as well as the setting of the grid and other parameters in LEM remain the same as described in the general setting in 3.2.1. The mechanical turbulence in the SBL is again initialised by random perturbations in the potential vorticity (see 3.2.5). It should be stressed that in the rest of the chapter, the time coordinate is always given with respect to the reference point t_0, i.e. the time when the mean surface temperature starts rising.

5.3 CAO under Various Wind and Stratification

The main purpose of this chapter is to assess the impact of a heterogeneous surface in a wide range of CAO scenarios, however each of these scenarios have its specifics. CAO scenarios vary both in the temperature gradient at the surface that drives the convection as well as in wind shear and stratification in the lower troposphere that modifies the growth of the CBL (Fedorovich and Conzemius, 2008). Although a direct description of model runs in each scenario would manifest an impact of the surface forcing, it might overlook some of the distinctive features of each model run. Therefore, this part of the chapter provides a comparison of the development of CBL between the scenarios. Runs with homogeneous surface are analysed and the qualitative differences between the scenarios discussed.

The chosen set of model scenarios cover a wide range of CBL regimes. This is demonstrated on the comparison of friction of friction velocity scales and convective velocity scales in figure 5.3).The modelled values of u_* and w_* agree with observed cases of roll convection in Arctic (Brümmer, 1996). All of the scenarios show a quick development of a shallow CBL. The IBL between the CBL and remains of the SBL continues to grow and exceed the original SBL height within 0.3–1 hour. During 2–5 hour, the estimated CBL height reaches values between 700 m and 2400 m (see figure 5.4). This is consistent with previous observations of atmosphere over sea in Arctic that recorded the thickness of the boundary layer over open sea between 900 m and 2200 m (Brümmer, 1996). Clouds start forming between 1.25 hour in the scenarios 'wind3' and 3 hour in the scenario 'strat2'. The scenario 'strat4' remain nearly cloud free. Though unusual, examples of cloud-free CBL were also observed in some CAO field studies (Chou and Fergusson, 1991). In scenarios 'wind2', 'wind3', 'wind4' and 'strat5' the cloud layer quickly deepens.

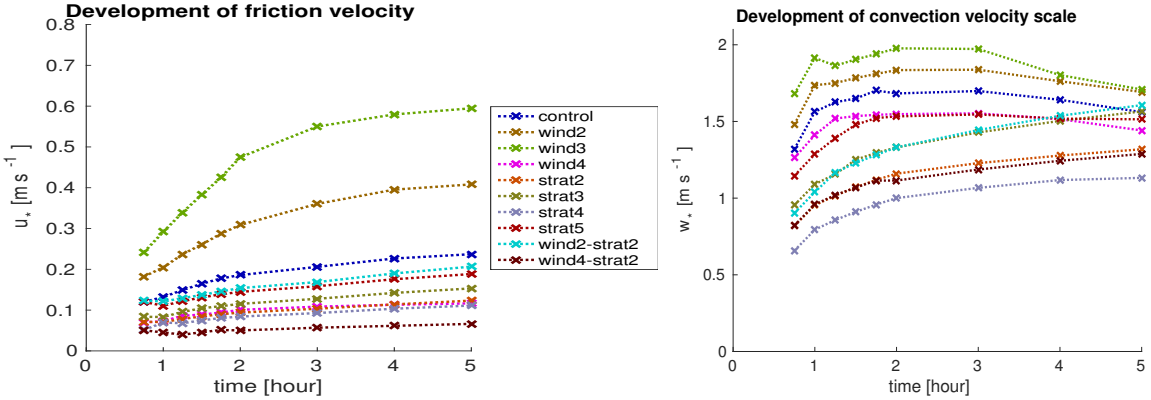

(a) (b)

Figure 5.3: The development of the friction velocity scale and the convective velocity scale for ML. The comparison of show all control runs of each scenario.

Growing clouds exhibit a vertical structure (see example of 'wind2' in the figure 5.5a) where the highest cloud water mixing ratio is reached around the middle part of the cloud layer and the potential temperature is increasing nearly linearly with height (see again figure 5.4). Similarly to the clouds in the control scenario (see figure 4.4), they show signs of a developing secondary circulation as well as pockets of ambient air around them (not shown here). Furthermore, kinematic heat flux in the middle of cloud again reach positive values 5.5b).

Due to describe properties, the cloud layer in scenarios 'wind2', 'wind3', 'wind4' and 'strat5' is classified (Stull, 1985) as a separate cumulus layer (CuL). On the other hand, in scenarios 'strat2' and 'strat3', clouds remain relatively shallow with cloud water concentration increasing towards the top (see 5.5a) The bottom part of the cloud remains the same. However, the potential temperature higher up in the clouds increases rapidly due

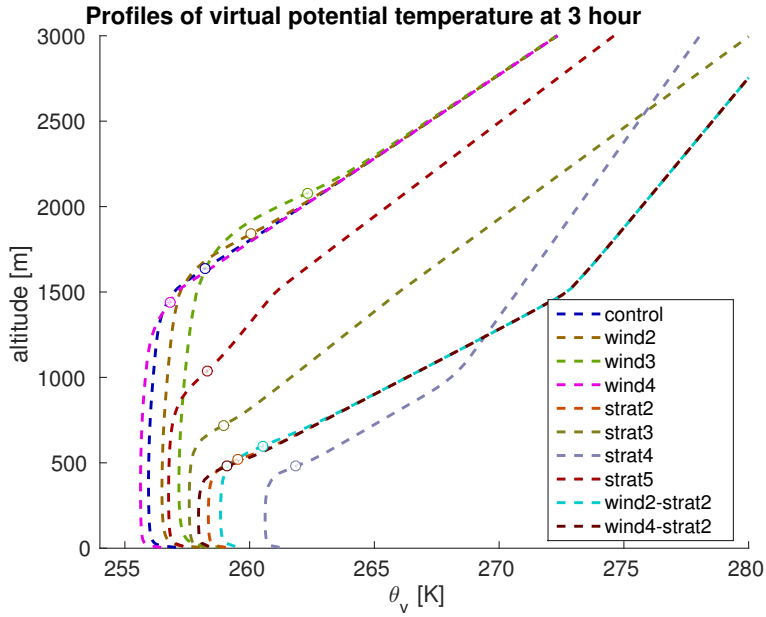

Figure 5.4: The comparison of virtual potential temperature profiles in runs with homogeneous surface. All lines show horizontally-averaged values of virtual potential temperature at 3 hour. Symbol ∘ marks the estimated height of CBL in each scenario.

to entrainment. Due to clear qualitative differences in the vertical structure of the CBL, the further description of cases is split on scenarios with the weaker and the stronger stratification in the lower troposphere.

Note: due to a different depth of the CBL, vertical profiles are displayed up to 3000 m in scenarios with a weaker stratification and up to 1200 m in scenarios with a stronger stratification.

5.3.1 Scenarios with Weaker Stratification

The general development of the CBL with a cumuli cloud has been overly described in the previous chapter (see 4.1.1 and 4.1.2). However, scenarios exhibit some differences in the vertical transport of heat, moisture and momentum. Since these properties might play a role in the response to heterogeneous surface forcing, we briefly investigate them here.

The scenario 'strat5' exhibit slightly slower growth of the CBL than the control scenario and the development of CuL is delayed until the 4 hour. The scenarios with the higher wind forcing exhibit an increased upward transport of heat and moisture. As a consequence, clouds generally appear earlier and grow faster. Strong winds forcing in scenarios **'wind2'** and **'wind3'** lead to situations that that wind shear in CBL is not exclusively confined to the cloud tops, but partially spread across whole CuL and ML

(see figure 5.6a). As a consequence, upper parts of clouds are often horizontally displaced along the direction of wind with respect to their cloud base. Although the difference between the height of the cloud bases and cloud tops is lowest in the scenario with low wind shear (**'wind4'**), the cloud layer achieves higher vertical maxima in the amount of total cloud water than the control run. This is due to the fact that lower horizontal winds do not inhibit formation of organised convective eddies (Maronga, 2014).

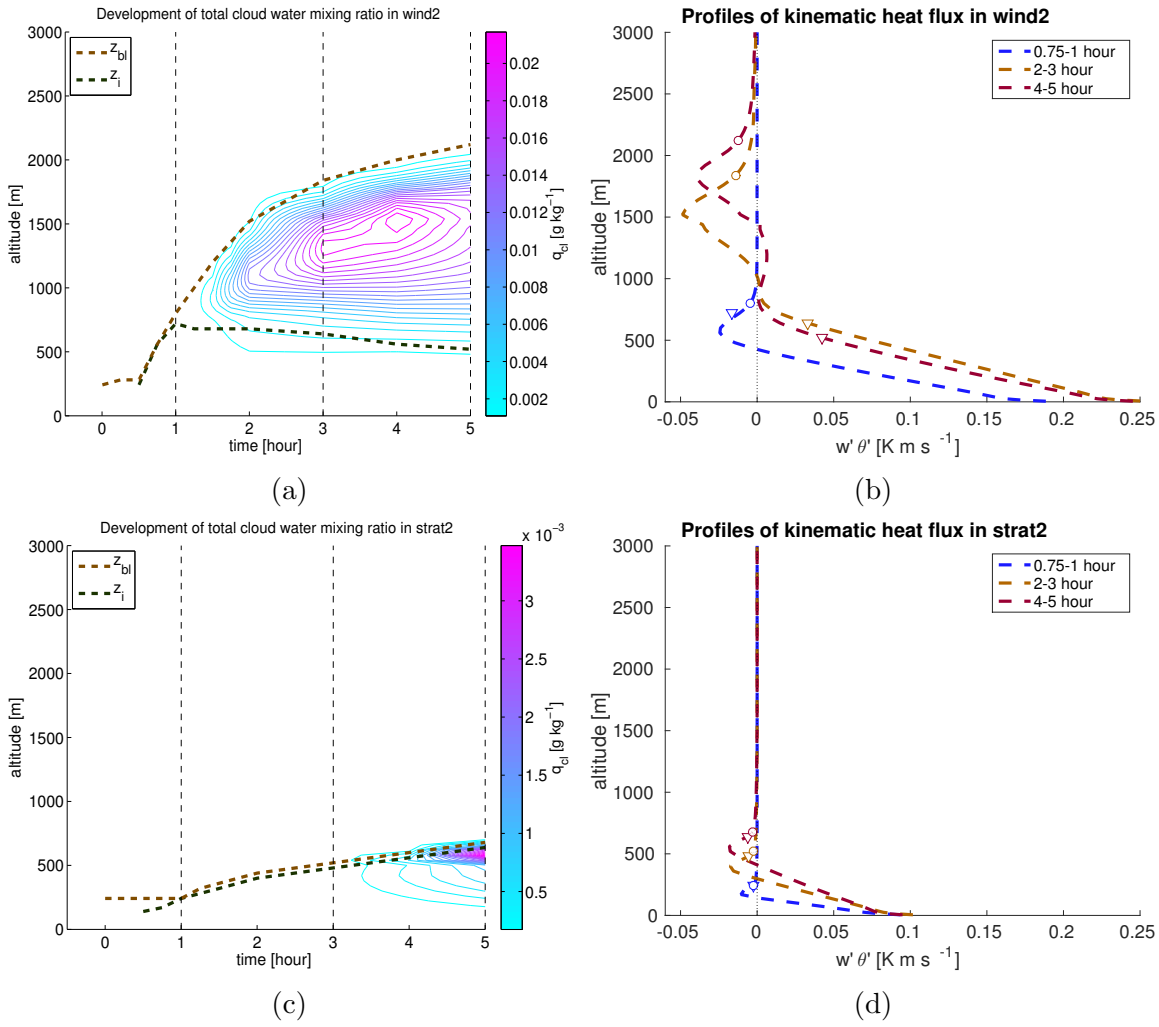

Figure 5.5: The comparison of a different development of the CBL in scenarios with a weaker stratification and in scenarios with a stronger stratification. Thin vertical lines over the countour-plots of total liquid water mixing ratio (a) and (c) mark the times of outputting the averaged flux profiles shown on the right side of the page. Note that colourbars of total water mixing ratio are not up to scale. Symbols ▽ and ○ indicate the approximated top of the ML and the top of the CBL respectively.

The statistical distribution of updraught and downdraughts does not qualitatively vary between the scenarios. Although the stronger wind forcing leads to faster growth of the CBL, by the end of the second hour, all observed levels between the 45 m and 1480 m (upper part of clouds) exhibit relatively minor differences between the model scenarios in the spread of potential temperature perturbations and humidity perturbations. The distribution of the vertical wind velocity is in all five scenarios slightly skewed

towards negative numbers. With a strong wind forcing, the spread in values increases and the strong updraughts also reach higher values. Strong updraught in ML generally attain values above 2.1 m s^{-1} in the control scenario, while in scenarios 'wind3', strong updraught in ML are almost always above 2.5 m s^{-1}.

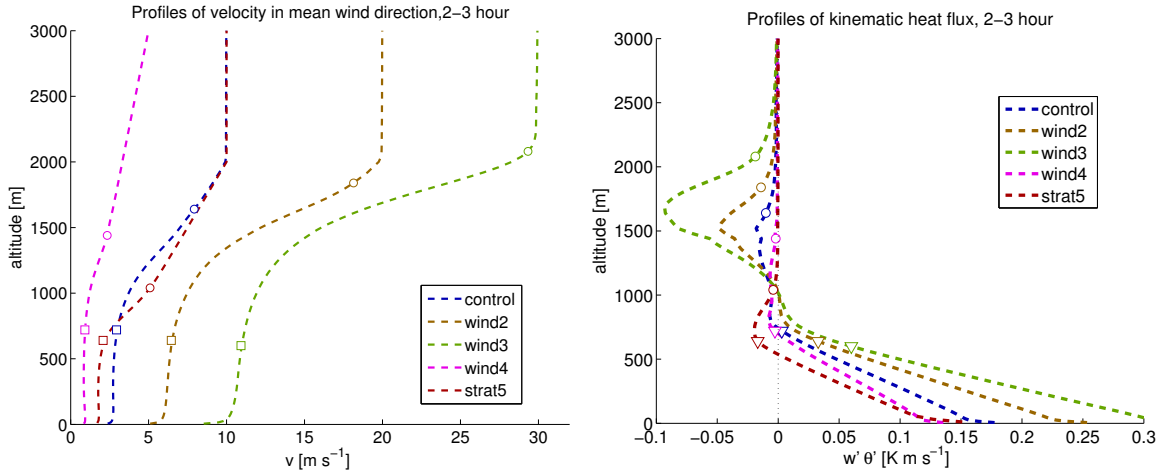

(a) (b)

Figure 5.6: The comparison of mean wind profiles and the profiles of kinematic heat during 2–3 hour. The symbol □ marks the altitude of cloud base and the symbol ○ indicate the top of the CBL.

The kinematic moisture flux in the MBl is higher in scenarios with higher wind shear. Figure 5.7a shows that during the 2–3 hour, maxima are reached at the bottom of CuL. By the fifth hour, moisture fluxes exceed the surface fluxes in all four scenarios (see figure 5.7a), indicating venting of the air from the ML by active cumuli cores. The differences in each scenario are approximately 40 %. The kinematic heat flux in ML follow a linear profile, followed by a negative heat flux in the bottom part of CuL. In the middle of cloud layer, values are close to 0, falling deep into negative number bellow the cloud tops (see figure 5.6b). The negative heat flux below the top of clouds is approximately proportional to wind shear.

This phenomenon is caused by the increased entrainment of the warm air into the CuL due to stronger wind shear and stronger turbulence inside clouds. Increased turbulence in the scenarios with increased wind shear is clearly demonstrated by comparison of vertical profiles of the variance in the vertical velocity (see figure 5.8a). Unlike in the control case, the variance in the vertical velocity in both horizontal wind components grow with altitude in cases 'wind2' and 'wind3', reaching maxima in the upper part of clouds. The variance in the wind component across the main wind exhibit even stronger impact of the increased wind forcing. There, the values for 'wind3' scenario are approximately four times higher than for 'control'. Overall, turbulent kinetic eddy energy (TKE) in-

creases with the wind-shear. This finding agrees with comprehensive study on transport on the grey-zone area (Shin and Hong, 2013). The increase in fluxes of momentum (not shown, see Appendix) is also disproportionally higher than the increase in the wind shear.

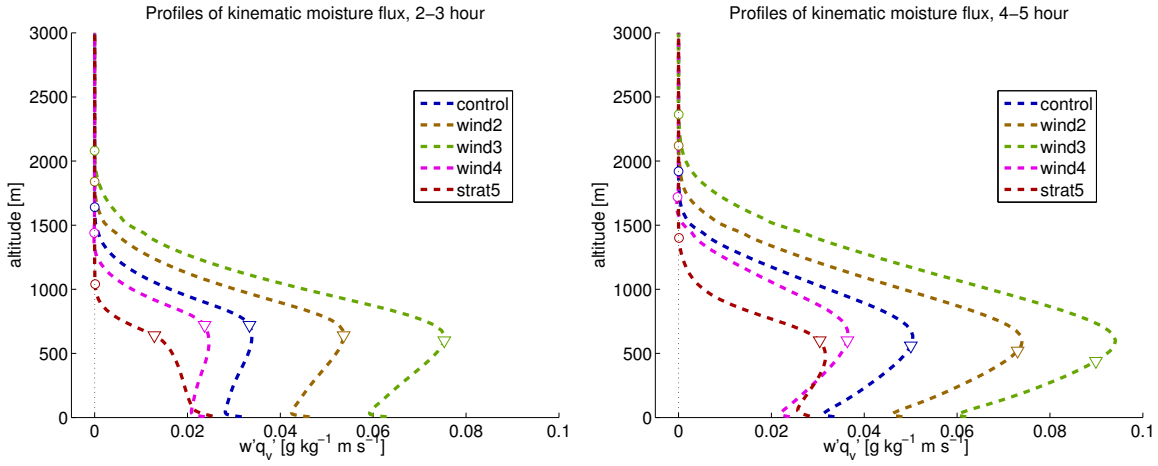

(a) (b)

Figure 5.7: Profiles of the kinematic moisture flux in scenarios with a weaker stratification. The symbol ▽ indicates the top of the ML and the symbol ∘ indicates the top of the CBL.

In summary, the scenarios with weaker stratification generally experience a rapid growth of the CBL and development of CUL after 2 hours. The scenarios with the increased wind forcing differs form the control scenario mostly in the amount of shear generated TKE.

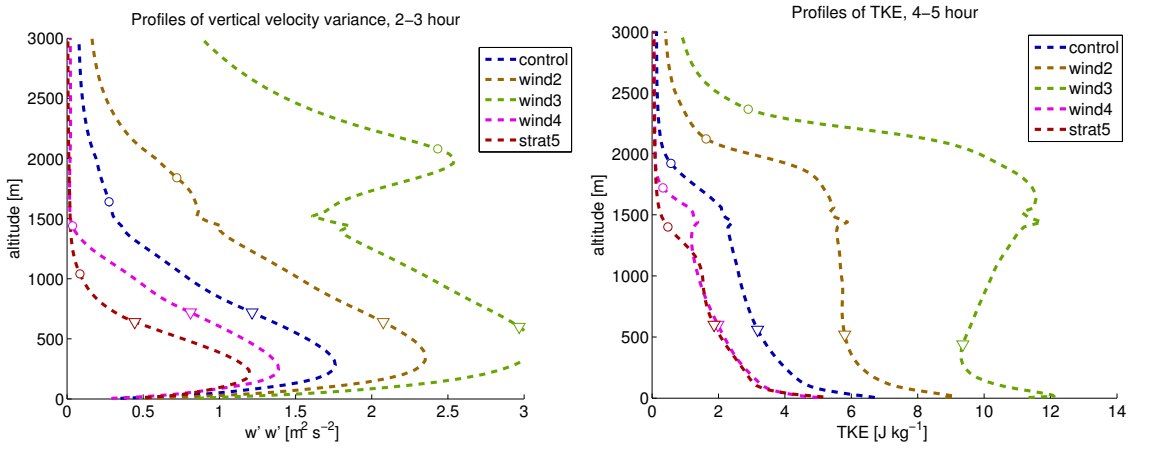

(a) (b)

Figure 5.8: The comparison of vertical wind velocity and turbulent kinetic energy in scenarios with weaker stratification. The symbol ▽ indicates the top of the ML and the symbol ∘ indicates the top of the CBL.

5.4 Heterogeneity under Wind Shear

One of the main research questions of this chapter is whether an increased wind forcing decreases the effect of heterogeneous surface forcing. Studies of convection over terrain with patches of different temperature have showed that the wind reduces the effect of heterogeneous heating. Near-surface wind of 2.5 m s^{-1} were enough to reduce the effect of the surface forcing and winds exceeding 5 m s^{-1} eliminated all impact (Avissar and Schmidt, 1998). Moreover, there are indications that the fluxes from the surface layer exhibit qualitatively different properties for wind regimes below 4 m s^{-1} and above 8 m s^{-1} (Grossman et al., 2005).

However, these studies were mostly performed in mid-latitudes. While the CAO are generally dominated by high temperature gradients and strongly stratified troposphere above, the impact of higher wind speed might differ. Furthermore, weak vertical wind shear over inhomogeneous MIZ can increases the chance of formation of cloud rolls (Gryschka et al., 2008). Although the aforementioned studies provided some vital findings, they focused mostly on the convective-scale structures and have not sufficiently discussed the impact on heat and moisture transport. With a goal to extend findings of previous studies, this part of the chapter investigates the impact of heterogeneities in surface temperatures under different wind shear conditions.

5.4.1 The Impact of Weak Wind Shear

The near-surface winds in the control scenario reached mean values 3.5 m s^{-1} by 4 hour, which is above the aforementioned threshold 2.5 m s^{-1} sufficient for reducing the effect of surface forcing (Avissar and Schmidt, 1998). Since the effect of the surface heterogeneity might have been already diminished, it would be reasonable to ask whether the surface heterogeneity plays a more important role in case of a weaker forcing. Therefore, this section investigates the impact of different types of surface patterns on a developing CBL in a scenario 'wind4' where the near-surface wind speed reached values between 0 and 2 m s^{-1} (see figure 5.6a).

Three runs with a different setting of the type surface heterogeneity ('along', 'across', chessboard') of the temperature scale $\Delta_{(\mathrm{h})}T = 7\,\mathrm{K}$ and the size $d_{(\mathrm{h})} = 1600\,\mathrm{m}$ are added to the 'homogeneous' run (see again figure 3.5). The investigation starts with the comparison of basic properties of the CBL. After the rapid formation of the CBL, strongest vertical flux of passive tracer is indicated in the run 'chessboard', followed by the run 'across'. During 0.5–0.75 hour, the IBL propagates highest in the run 'chessboard'. The height of the IBL reaches generally 100–200 m higher than in other runs. This stands in

the contrast with the control scenario, where the case 'across' lead to increased mixing and the growth of the IBL was fastest in case 'along' (see figure 4.25). However, due to weaker mean wind by the surface in 's4' scenario, 'chessboard' pattern drives the formation of eddies by the surface. Nevertheless, as CBL continues in deepening, large forced rolls starts forming in 'along'. As a results, the IBL height in 'along' exceeds the IBL in 'chessboard' at the end of the first hour.

However, organised convective structures are indicated in all three runs with surface heterogeneity. This is clearly demonstrated in spatial distribution of vertical wind velocity in the slice at the top of the mixed layer (see figure 5.10c and 5.10e). Both figures show well-defined thermals that facilitate the transport of heat and moisture further into the CuL. These results stand in a stark contrast to the results of the effect of surface heterogeneities in the control scenario (see 4.2.1). While the effect of surface heterogeneity 'across' on the structure of the CBL in the control scenario was limited to the surface layer, figure 5.10e shows a clear pattern even at the top of the ML. A clear structure of the pattern of surface heterogeneity propagating up to 600 m greatly exceeds the altitudes of 100-200 m indicated by previous studies (Maronga et al., 2014). This indicates that in case of a weak mean wind, heterogeneities in surface temperatures drive formation of large convective structures that can span across the whole ML.

Although the cloud layer starts forming at the end of the first hour, it is not until the end of the second hour that the active cumuli cloud cores start developing. After the development of the active cumuli cores, the turbulent mixing at the top of the CBL increases and the organised convective structures in the ML disappear during the time period 2–3 hour. A CBL later undergoes formation of larger convective structures that exhibit wide areas of weak downdraughts surrounded by weaker updraughts. This is clearly demonstrated by the spatial distribution of the vertical velocities at the top of ML at 5 hour (see figure 5.10d and 5.10f). Modelled structures bear the characteristic open cells — convective updraught is mostly contained on the edges while the inner consists of descending cold air. This generally agree with observations of open cells are downwind of the edge of ice in CAO cases (Atkinson and Zhang, 1996).

Despite the formation of large organised convective structures in all three runs with the surface heterogeneity, there are no significant differences in domain-averaged values of surface fluxes between the runs 'across' and 'along' and the runs with homogeneous surface temperature. The timeseries of the surface SH and LH flux (see figure 5.9) show that only the run with the heterogeneity 'along' exhibits significantly higher values. During the abrupt growth of the CBL in the period 0.5–1.5 hour, the SH flux in 'along' exceeds the SH flux in the 'homogeneous' case by more than 13 %. It has been already established that during the same time period, the case 'along' exhibited much faster propagation of the IBL and exceed the indicated CBL height in other runs

with heterogeneities by 100–200 m. This indicates that the convective structures oriented along the mean wind direction drive the formation of convective structures that improves further growth of the CBL. On the other hand, convective structures driven by heterogeneities 'across' and 'chessboard' generally slows down further growth of the CBL.

While the difference between the 'along' and 'homogeneous' run disappears during the second hour, there is a persisting difference in the surface LH flux. This effect of the surface heterogeneity is maintained even after the suppression of organised convective structures by cloud-top forcing in the CuL. The likely explanation is that the orientation of the stripes of positive and negative temperature anomalies in the pattern 'along' allow a secondary circulation close to the surface without disturbing larger convective structures that has formed around. These results also support the findings of the previous study of the heat budget in CAO in Arctic that on the edge of the ice the SH flux is the most important, while the LH flux starts playing more dominant role downwind (Brümmer, 1997).

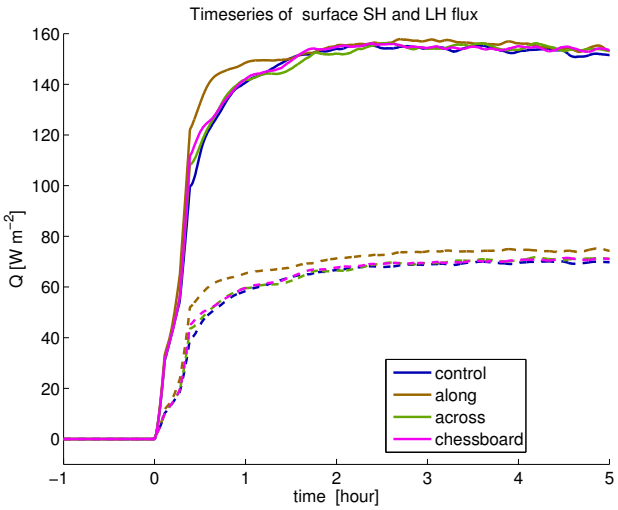

Figure 5.9: Timeseries of the surface SH and LH flux for the runs with heterogenous surface forcing in the scenario with a weak wind shear.

In summary, weaker wind conditions allow the formation of larger convective structures for all three types of heterogeneous patterns. However, structures oriented by anomalies across and chessboard generally do not lead to increase in surface SH and LH flux. On the other hand, convective structures driven by heterogeneities of the type along improves the surface LH and SH flux. In the absence of a wind shear, a larger convective structures tend to develop and suppress smaller organised convection within ML.

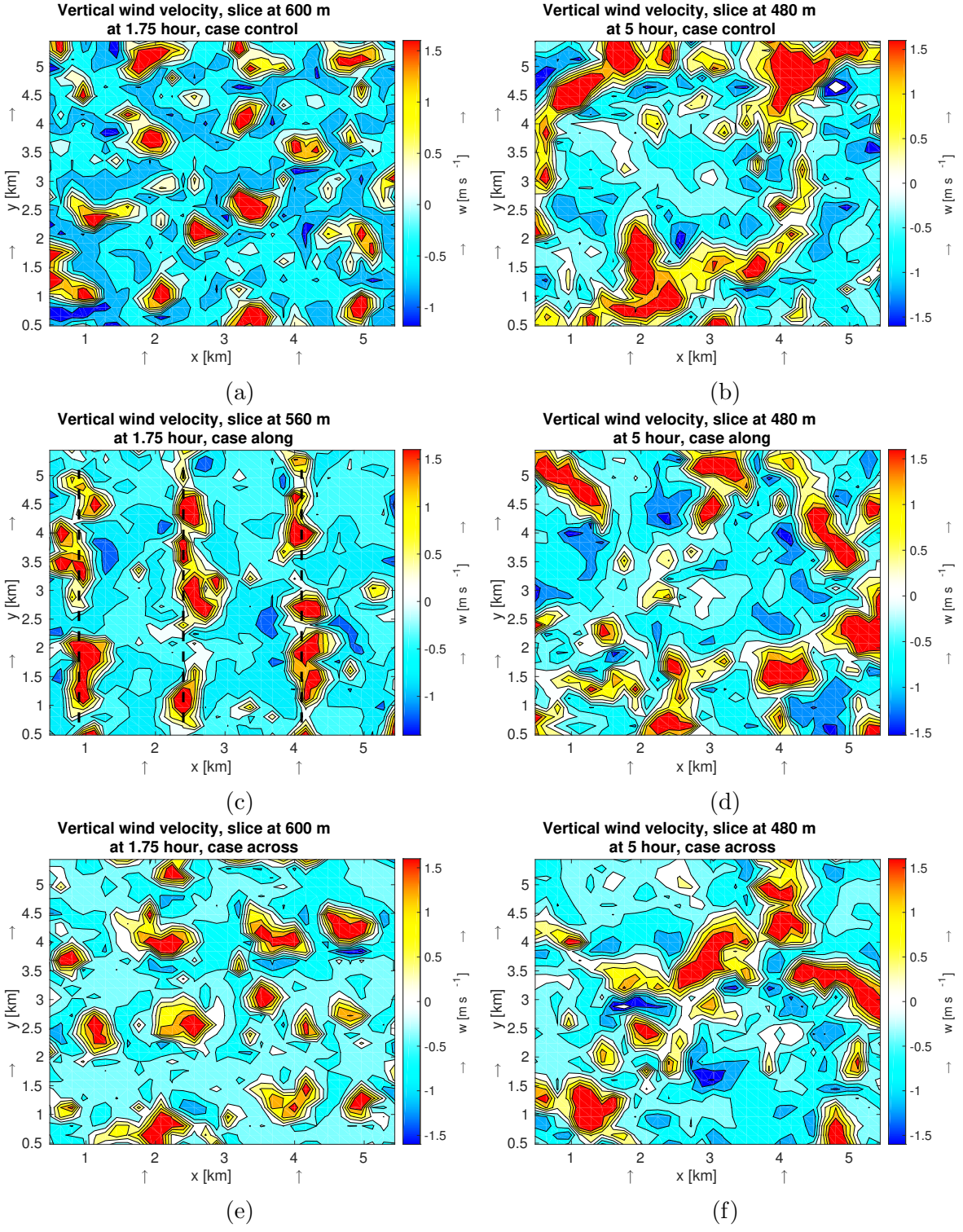

Figure 5.10: A detail of the horizontal cross-section is showing vertical velocity in the horizontal slice at the **top of the ML** over heterogeneous surface in the scenario with a weak wind shear.
Arrows (↑) indicate the mean wind direction and dashed lines (- -) indicate the organised convective structures.

5.4.2 The Impact of the Size of Heterogeneity under Strong Wind Forcing

Studies of the air-sea interaction in Labrador Sea region have shown that high winds often coincide with regions where convection regularly occurs (Moore et al., 2014). A partial sea-ice cover is also present in some of these areas (Fang and Wallace, 1994). While the spatial extend of patches of ice floes and patches of open water can greatly vary in scales up to few kilometres (Inoue et al., 2005b), this section investigates the impact of the size of heterogeneity on developing CBL in high wind shear cases.

The impact of the size of temperature heterogeneities 'across' and 'chessboard' in high winds-shear cases is analogous to the impact in the control scenario (4.2.3). For more details, see Appendix. On the other hand, the surface temperature heterogeneities of the type **'along'** alters the development of the CBL in high wind shear scenarios in a slightly different way than in the control scenario (4.2.1). The stripes of temperature anomalies oriented along the mean wind direction lead to formation of organised structure of convective rolls (see figure 5.11). This not only accelerates the upward growth of CBL but exhibits some additional effects. While the 'wind2' is dominated by high wind shear in the lower troposphere (see section 5.2), forced eddies improve the downward transport of momentum, leading to higher mean wind velocity in the ML. During the 1–2 hour after t_0, the velocity in the mean wind direction in the homogeneous case is exceeded by 0.5 m s^{-1} in the case with heterogeneities of the size $d_{(\mathrm{h})} = 1600\,\mathrm{m}$ and by more than 1 m s^{-1} in the case with heterogeneities of the size $d_{(\mathrm{h})} = 3200\,\mathrm{m}$ (see figure 5.12b).

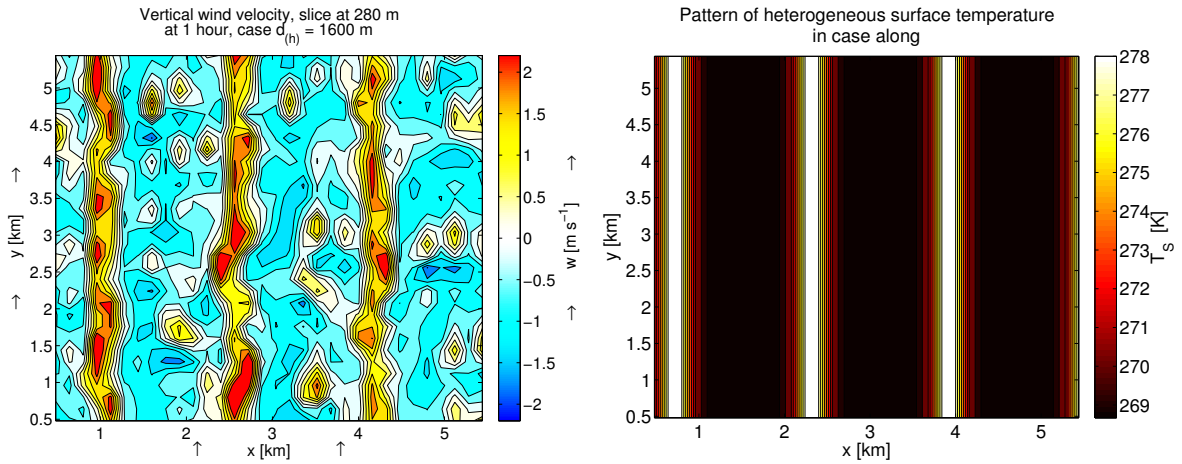

(a) (b)

Figure 5.11: A detail of the horizontal cross-section is showing vertical velocity in the **middle of the ML** over heterogeneous surface along in the scenario with strong wind shear and the underlying pattern of surface temperature heterogeneities.

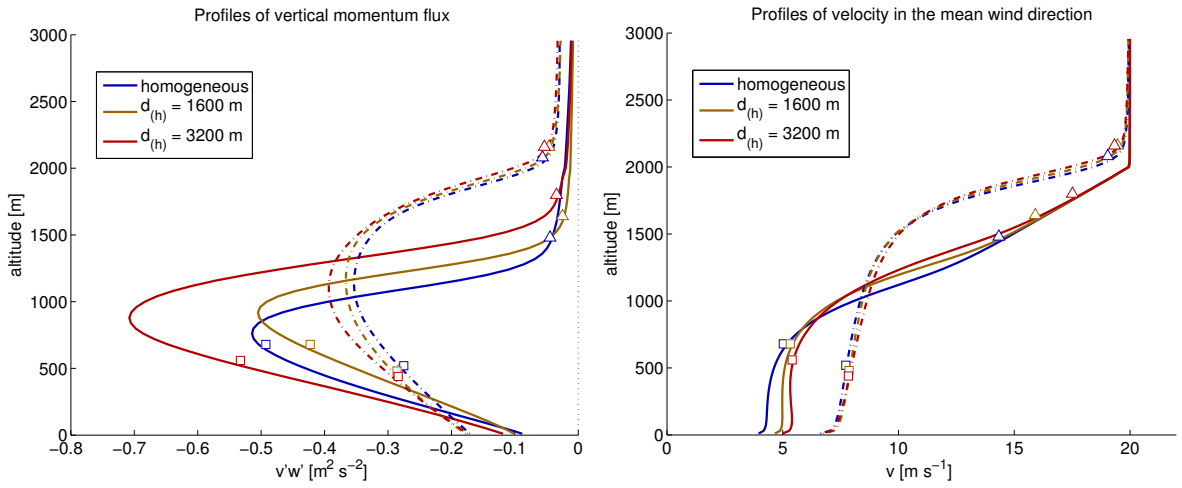

(a) (b)

Figure 5.12: The vertical kinematic flux of heat and moisture in scenarios with stronger initial stratification.
The symbol □ marks the altitude of cloud base, the symbol △ the altitude of cloud tops. The full line (—) marks the profile at 1.5–1.75 hour while the dash-dotted line (− · −) marks the profile at 2–3 hour.

Due to more localised transport of moisture, clouds start forming earlier in the runs with heterogeneities. Furthermore, in the case ($d_{(\mathrm{h})} = 3200\,\mathrm{m}$), clouds bases are generally located up to 100 m lower than in the homogeneous case or case with smaller anomalies. Clouds follow a clear cloud-street pattern in both cases with heterogeneity (not shown) Despite the clear differences in the spatial structure, the overall distribution of updraughts and downdraughts (see 3.4.2 and 3.4.3) does not significantly differ between the cases. Runs with heterogeneities exhibit slightly higher spread in perturbation of the potential temperature and moisture (at altitude 170 m and 360 m), however the vertical velocity distributions are similar. Furthermore, there are no significant differences in the amount of the heat and moisture transported by strong updraughts. Nevertheless, the heterogeneities of the type 'along' tend to alter the overall properties of the CBL. Both lead to a lower convective velocity scale w_* by approximately 15 % against the control run. The difference between the control and the run ($d_{(\mathrm{h})} = 1600\,\mathrm{m}$) disappears soon after 1 hour, while in the case ($d_{(\mathrm{h})} = 3200\,\mathrm{m}$) maintains the difference until the hour 2.

After the deepening of the CuL and the development of the active cumuli cores during the second hour, the differences between the model runs starts decreasing. Similarly to the results of analysis of the runs with the heterogeneities in the control scenario (4.2.3) the forcing by active cumuli clouds acts against the structures forced by heterogeneous surface forcing. However, in this scenario, the run with heterogeneity size ($d_{(\mathrm{h})} = 3200\,\mathrm{m}$) is affected as well. The clear structure of cloud streets disappear by the time 3 hour.

The next step is to evaluate domain-averaged timeseries of vertical fluxes of the LH, the SH and the momentum. The differences in the vertical SH flux between the runs are relatively small, the timeseries differ in oscillations while the smoothed values are within less than 1 % after 2 hour. While the differences in the vertical LH fluxes between the homogeneous run and runs with heterogeneities are by approximately 25 % higher during 1–2 hour, they later decrease to about 10 % both for the recording at the surface and in the upper part of the ML (see figure 5.13b). The differences in the values of fluxes between the run with ($d_{(\mathrm{h})} = 1600\,\mathrm{m}$) and ($d_{(\mathrm{h})} = 3200\,\mathrm{m}$) are relatively small and mostly diminish during the third hour.

While the depth of the ML is estimated during the 3–5 hour to be $z_i = 500 - 600\,\mathrm{m}$ during the 3-4 hour, the estimation of the total ABL height is $z_{\mathrm{bl}} = 2000 - 2100\,\mathrm{m}$ during the same time period. These values are in the intervals

$$4 < \frac{d_{(\mathrm{h})}}{z_i} < 6, \qquad 1.5 < \frac{d_{(\mathrm{h})}}{z_{\mathrm{bl}}} < 2, \tag{5.1}$$

that is according to the previous study (Patton et al., 2005), the case when the effect of surface heterogeneous forcing is the strongest. for the case $d_{(\mathrm{h})} = 3200\,\mathrm{m}$ (previously discussed in 4.2.3). However the effect of the heterogeneous surface forcing has mostly disappeared and the differences between the case $d_{(\mathrm{h})} = 3200\,\mathrm{m}$ and $d_{(\mathrm{h})} = 1600\,\mathrm{m}$ are almost negligible This stands in the contrast with the prediction that the effect of the heterogeneity would be strongest for the heterogeneity size of the ration (1.5, 2)to the ABL depth These results show that the forcing by active cumuli clouds and strong wind shear override even the effect of 'ideal' surface heterogeneous forcing.

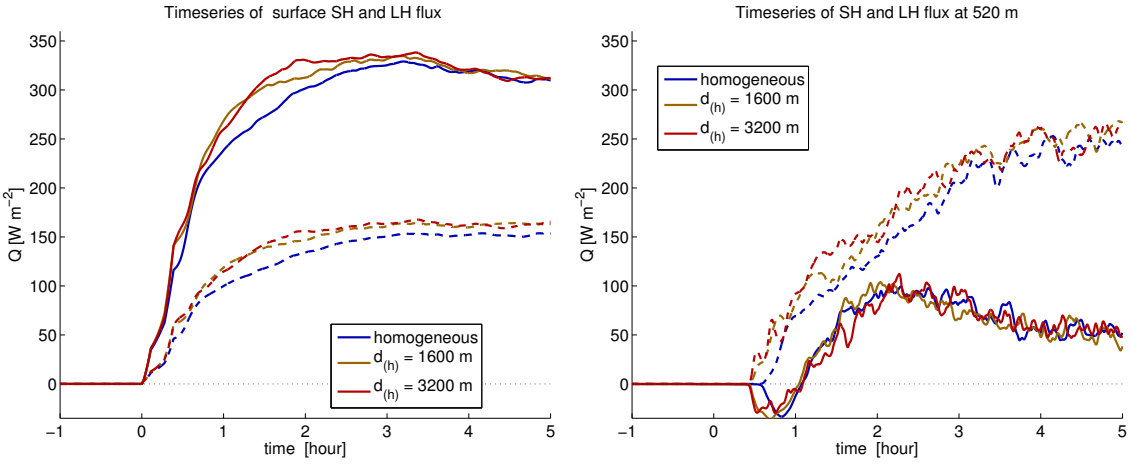

(a) (b)

Figure 5.13: The effect of heterogeneity size in high wind forcing on the surface SH and LH flux and on the SH and LH flux at the altitude 520 m.
The full line (—) marks the SH flux and the dashed (- -) marks the LH flux.

In summary, the analysis of runs with heterogeneities in the scenarios with high wind shear has revealed that the impact the depends on the type of heterogeneity. While the surface temperature pattern 'across' and 'chessboard' leads just to slightly increased mixing in the developing convection, the type 'along' exhibit a significant influence on a developing CBL. This type of the pattern drives the forced convective rolls in the first 2 hours after t_0. Unlike in the control scenario, larger size of the heterogeneity leads to an increased wind velocity in the ML. The thickening of the cloud layer again leads to an increase in the top-driven mixing by deep cumuli clouds, the effect of heterogeneous surface forcing on the structure of CBL quickly diminishes. Surface heterogeneities also exhibit a persisting influence on the surface LH flux. The increase in the surface LH flux does not significantly differ between the runs with $d_{(\mathrm{h})} = 1600\,\mathrm{m}$ and $d_{(\mathrm{h})} = 3200\,\mathrm{m}$ 'along' heterogeneities.

5.4.3 The Impact of the Size of Heterogeneity under Very Strong Wind Forcing

Although the previous pars showed the impact of high wind shear, it is reasonable to ask whether the influence of heterogeneities would disappear in case of a stronger wind shear. Therefore, the impact of the combination of the wind shear and the heterogeneous surface forcing is further investigated in in scenario **'wind3'**, i.e. in the scenario where the wind forcing linearly increases up to the extreme value $30\,\mathrm{ms}^{-1}$ This value of wind shear is not very common, yet it is still well bellow values occasionally observed in some areas of Northern Atlantic (Renfrew and Moore, 1999).

The stripes of temperature anomalies located along the mean wind direction again drive the formation of forced rolls. These forced rolls significantly speed-up the growth of the CBL. During the first two hours, the ABL height is in the runs with heterogeneities significantly higher than in the case with homogeneous surface. The estimated z_{cb} in the case $d_{(\mathrm{h})} = 3200\,\mathrm{m}$ exceeds the homogeneous case by 300–500 m at the end of the first hour. The downward transport of momentum facilitated by forced eddies lead to high differences in the mean wind velocity between the runs with heterogeneities and the homogeneous surface (see figure 5.14b). The mean wind velocity in the cases $d_{(\mathrm{h})} = 3200\,\mathrm{m}$ exceeds the mean wind velocity in the 'homogeneous' case by more than $1.5\,\mathrm{m\,s}^{-1}$ in the time interval 1.25–1.75 hour. Cloud bases in the case $d_{(\mathrm{h})} = 3200\,\mathrm{m}$ are not only forming lower, but some of the glaciated clouds start apparently in the surface convective layer. This phenomenon is caused by condensation in large updraughts columns that are the part of large forced rolls. Examples of this near-surface condensation were observed in flows off the ice edge in Baltic Sea (Brümmer, 2002).

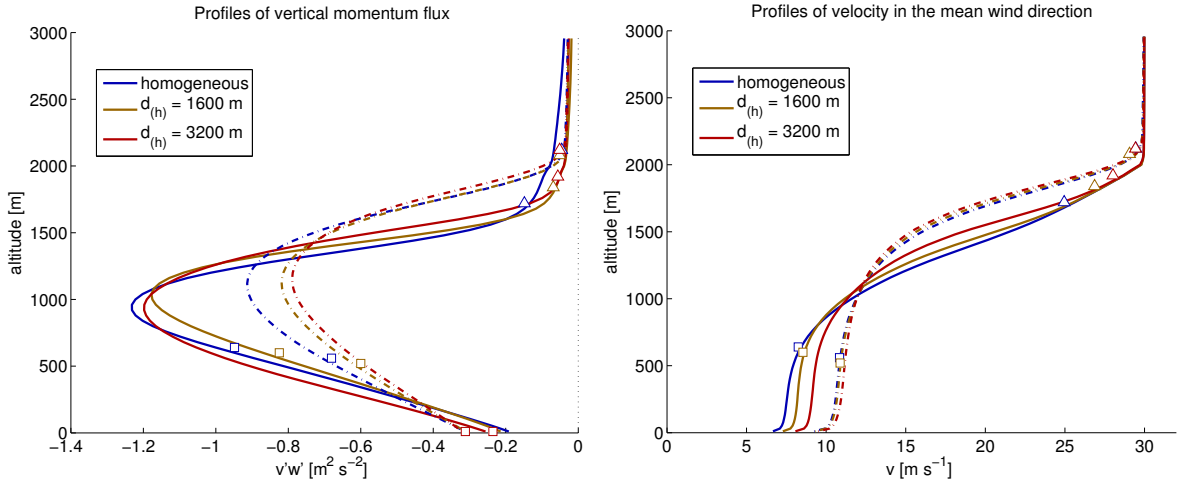

(a) (b)

Figure 5.14: The vertical kinematic flux of heat and moisture in scenarios with stronger initial stratification.
The full line (—) marks the profile at 1.5–1.75 hour while $(- \cdot -)$ marks the profile at 2–3 hour.

In the cases with heterogeneity, clouds again form a clear street patterns. These patterns are similar to the patterns in scenario 'wind2'. However, there are differences in the horizontal displacement of the cloud tops due to increased wind shear (see again figure 5.6a). The abrupt growth of cumuli clouds continues and active cumuli cores form during 1.5–2 hour. The top forcing by cumulus clouds then again leads to changes in the spatial structure of clouds and updraughts. The differences between the model runs starts diminishing.

The results of the domain-averaged timeseries of vertical fluxes of the LH, the SH and the momentum are consistent with the results for 'wind2' 5.4.3. The differences in the vertical fluxes of moisture between the homogeneous run and runs with heterogeneities are about 25 % during 1–2 hour, they later decrease to about 10 % both for the recording at the surface and at the top of ML (see figure 5.15) The differences in the values of fluxes between the run with ($d_{(\mathrm{h})} = 1600\,\mathrm{m}$) and ($d_{(\mathrm{h})} = 3200\,\mathrm{m}$) within ML do not exceed 10 % in the first 2 hours. After 2 hour, they fall bellow 3 %.

The ABL height in the case $d_{(\mathrm{h})} = 3200\,\mathrm{m}$ grows during the 1–3 hour from 1700 m to 2200 m. Therefore, values of the ratio $\frac{d_{(\mathrm{h})}}{z_{\mathrm{bl}}}$ are during this whole time period in the interval (1.5, 2). However, this time period includes both the stage when the differences between the runs are highest as well as the stage when the differences quickly diminish. This further supports the findings of the previous section (5.4.3) that the effect of the heterogeneous surface forcing is in high wind-shear cases diminished by the forcing by cumuli clouds.

In essences, the analysis of the impact of surface temperature heterogeneity of the type 'along' in the scenario 'wind3' further supports the findings of the previous section. A larger size of the heterogeneity leads in first 2 hours to a faster growth of the CBL and increased wind velocity in the ML. Differences start diminishing due to forcing by active cumuli clouds, however runs with heterogeneity still maintain a slightly higher LH flux than the homogeneous case. The increase in the surface LH flux does not significantly differ between the runs with $d_{(\mathrm{h})} = 1600\,\mathrm{m}$ and $d_{(\mathrm{h})} = 3200\,\mathrm{m}$ 'along' heterogeneities. The main difference in comparison with scenario 'wind2' is that large heterogeneities lead to an increased condensation within the ML and formation of scattered glaciated clouds low above the surface during the first 1.5 hour.

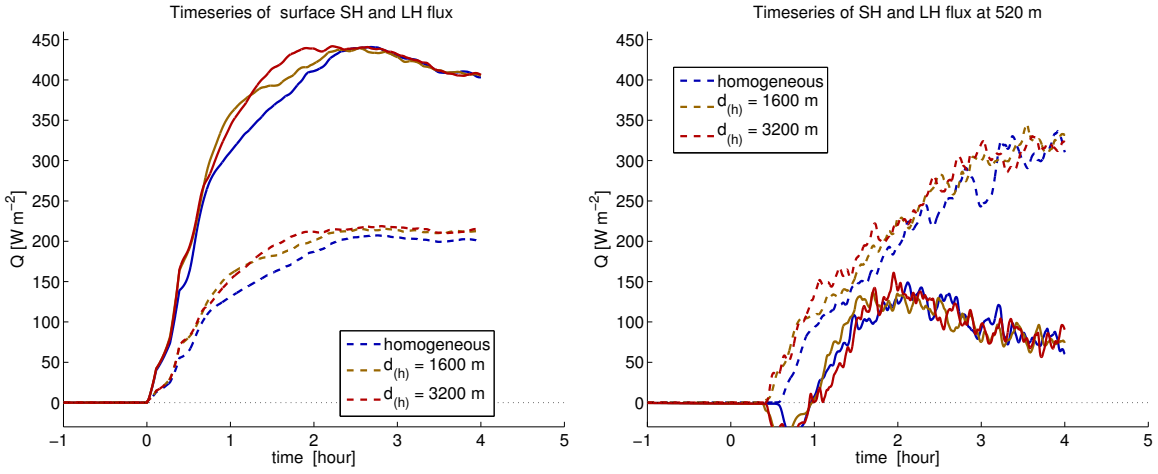

(a) (b)

Figure 5.15: The effect of heterogeneity size in high wind forcing on the timeseries of surface SH and LH flux and on the SH and LH flux at the altitude 520 m in a scenario a very high wind forcing.
The full line (—) marks the SH flux and the dashed (- -) marks the LH flux.

5.5 Impact of Stratification on the Heterogeneous Surface Forcing

The analysis of CAO has already showed that top forcing by the cumuli clouds leads to the diminishing of the effect of surface heterogeneous forcing (see parts 5.4). However an increased stratification in the troposphere leads to a qualitatively different CBL that is not topped by the CuL (general description in 5.3.1) Therefore, it is important to investigate how a different top-forcing interacts with the heterogeneous surface forcing. This part of the chapter first presents the analysis of model runs with surface temperature heterogeneities in scenarios with increased stratification of the lower troposphere. Later, the impact of the wind shear in scenarios with increased stratification is investigated.

5.5.1 Scenarios with Stronger Stratification and Homogeneous surface

Scenarios with increased initial stratification, have undergone rapid formation of the CBL after the increase of the surface temperature, with warm plumes penetrating up to 100–200 metres and larger organised thermals forming by the 0.45 hour followed by a very slow deepening to height 600 m in 'strat4', 700 m in 'strat2' and 1000 m in 'strat3' Due to increased stratification of the initial potential temperature profile, the depth of the CBL grows more slowly than in the control scenario, but the potential temperature rises faster (see again figure 5.4). This further leads to a smaller difference in the surface temperature gradient, and consequently lower surface SH and LH flux. An abrupt increase in surface fluxes during the transition is later followed by a stagnation. Unlike in the control case, the surface SH flux not only stagnates, but also gradually decreases in scenarios 'strat2', 'wind2-strat2' and 'strat4'.

Scattered clouds appear at the top of the boundary layer, however they do not form continuous layers. Unlike in the case of the control scenario, the ML is not divided from the free atmosphere by CuL.An entrainment occurs at the top of the CBL and a clear capping inversion with a high potential temperature gradient develops in 'strat2' and 'strat3' cases.

The depth of clouds in 'strat2' and 'strat3' does not exceed 400 metres. The upper part of the clouds are mostly liquid and the amount of ice increases towards the bottom, with a number of ice particles scattered in below the cloud bases. This phenomena was in the previous study of cold clouds (Forbes and Ahlgrimm, 2014) accounted to aggregated ice particles falling below.

The vertical structure of the troposphere further differs from the control scenario. Wind velocity in the main direction is nearly constant in most of the ML and cloud shear is confined to cloud tops (see figure 5.16a). Both the variance in the wind component along and the variance across the mean wind follow similar vertical profiles. Maxima in velocity variance are generally reached by the surface and in the bottom part of clouds (in 'strat4' at the top of ML'), followed by a sharp decline above. Maxima in the vertical velocity variance are reached in the lower half of ML (below 200-300 m), similarly to 'control'. However variance in the vertical velocity steeply decrease by the top of CBL, unlike in the control scenario with active cumuli clouds (see figure 4.5b).

Profiles of the vertical kinematic fluxes of heat and moisture (see figure 5.17) follow simple linear shape in the mid 80 % of the boundary layer, in a good agreement with the

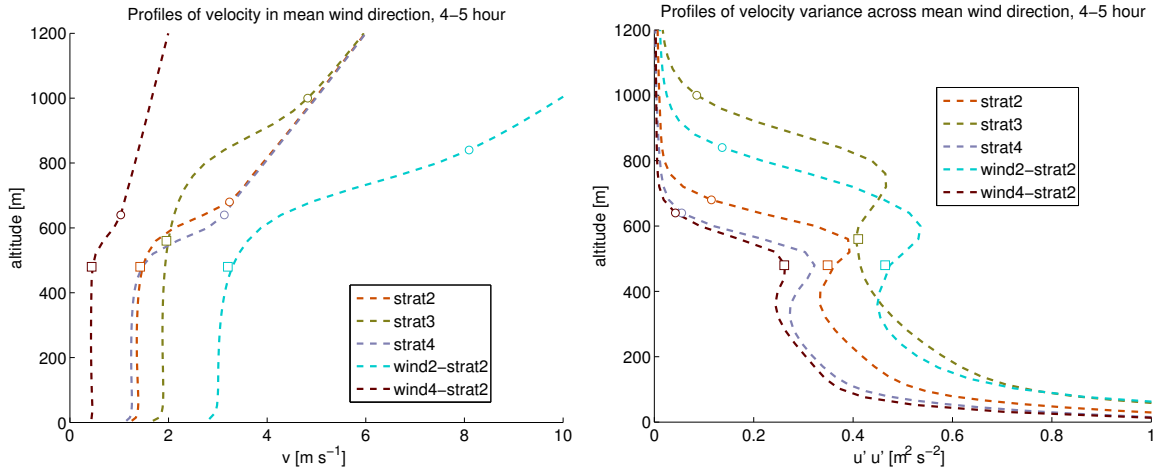

(a) (b)

Figure 5.16: Vertical profiles of mean velocity and variance in the velocity across the mean wind direction. The symbol □ marks the altitude of cloud base and the symbol ○ indicate the top of the CBL.

similarity theory for mixed layer (Cheinet and Siebesma, 2009). At the top they decline deep into negative numbers indicating a downward flux of the heat and moisture in the capping inversion. This phenomena is explained by the combination of the turbulent entrainment with the strong temperature and humidity inversion.

The analysis of updraughts and downdraughts (3.4.3) reveals that majority of strong updraughts are warm. Unlike in the control case, the positive temperature perturbations in strong updraughts often do not exceed perturbations in the majority of weak warm downdraughts. Despite that, strong updraughts play a decisive role in the transport of heat and moisture. For example in the scenario 'strat2', strong updraughts facilitated 60 – 90 % of the kinematic heat flux in ML from the hour 2 onwards.

To sum up, the idealised scenarios investigated in this chapter represent a wide palette of cold air outbreaks. All scenarios exhibit quick formation of a shallow CBL at the bottom of the troposphere, followed by the propagation of the IBL upwards. Further development of the scenarios diverge both in the rate of CBL growth as well as in the qualitative properties of the CBL. Scenarios with a weaker stratification undergo a formation of the CuL in the upper part of the CBL. On the other hand, scenarios with a stronger stratification exhibit a formation of strong entrainment layer in the upper part of the CBL. Some of these scenarios remain nearly cloud free (strat4), in others a shallow cloud layer is formed. The contribution of strong updraughts to the transport of heat and moisture is more pronounced in scenarios with increased stratification.

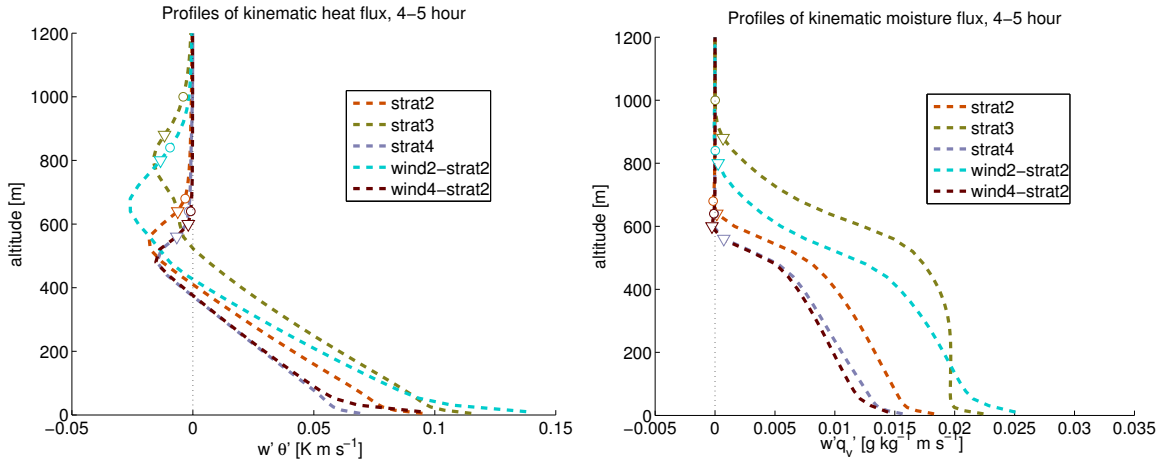

(a) (b)

Figure 5.17: The vertical kinematic flux of heat and moisture in scenarios with stronger initial stratification. The symbol ▽ indicates the top of the ML and the symbol ○ indicates the top of the CBL.

5.5.2 Heterogeneous Surface in Strongly Stratified Scenario

The scenario 'strat2' presents an interesting case of CAO starting with a strongly stratified lower troposphere and leading to a ML topped with shallow stratocumulus clouds (see figure 5.5c) and a strong entrainment layer above. This section then shows how is the CBL in the strongly stratified scenario modified by different types of surface heterogeneity.

Three runs with different types of surface heterogeneity ('along, 'across', 'chessboard') of the size $d_{(\mathrm{h})} = 1600\,\mathrm{m}$ and the temperature scale $\delta_{(\mathrm{h})}T = 7\,\mathrm{K}$ are compared against the run with homogeneous surface temperature. During the first half hour after t_0, heterogeneous surface forcing in the 'across' case facilitates the fastest development of plumes. The kinematic heat flux is up to an order of magnitude higher than in the 'homogeneous' case and by more than 30 % higher than in the case 'along'. While the stripes of anomalies located across the mean wind flow greatly increase the mixing in a shallow CBL, this phenomenon is relatively short-lived. As the IBL grows over 200 m, the stripes of temperature anomalies generally act against the formation of larger eddies and rolls. On the other hands, stripes of temperature anomalies along the mean wind force the formation of rolls parallel to the direction of the wind (see figure 5.18).

At the beginning of the second hour, ML deepens in all four cases and the differences mostly vanish. Passive tracer propagate slightly higher in the case 'along' due to organised forced rolls, however the differences are relatively small. Scattered clouds appear in all cases during the third hour, thought the subsequent growth of clouds is faster in the case 'along', followed by the case 'across'. Case 'along' exhibited a clear pattern of cloud streets located over positive anomalies in surface temperatures (see figure 5.18)

Although the horizontal scale of heterogeneous pattern (1600 m) is smaller than in many previous studies (Gryschka et al., 2014), a clear pattern of convective rolls is maintained well beyond the time 5 hour.

The runs 'across' and 'chessboard' do not exhibit any organised pattern of clouds, Although each case shows a slightly different spatial organisation of updraughts and downdraughts, the differences in the overall distributions of vertical wind velocities and perturbations in the potential temperature are relatively small. The case 'along' exhibit higher w_u, velocity of strong updraughts, particularly in the upper part of the ML. It generally exceeds values for other 3 runs by 20-50 %. This difference in the vertical velocities is caused by forced eddies over the anomalies oriented along the mean wind direction. On the other hand, the velocities of strong updraught in case 'chessboard' and 'across' do not significantly differ from the homogeneous case.

However in all four cases, strong updraughts facilitate a dominant part of the vertical transport of heat and moisture. The ratio of the vertical kinematic heat flux by strong updraughts to the total vertical kinematic heat flux is almost always above 60 % The ratio can occasionally exceeds 100 %, i.e. the vertical transport in the remaining 95 % is actually negative. For the vertical kinematic flux of moisture, the ratio of the contribution by strong updraughts also attains values than in the control scenario, generally between 30 % and 50 %. Both these ratios are slightly higher than in the control scenario (see figure 4.14). In indicates that in case of a strong stratification over the ML, well defined strong updraughts in convective roll facilitate majority of the vertical transport heat and significant portion of transport of moisture.

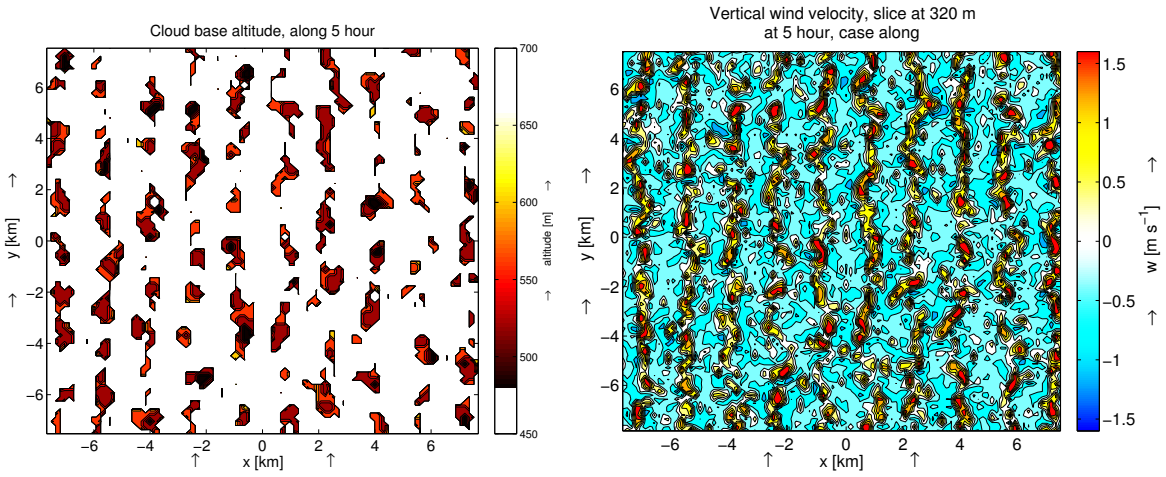

(a) (b)

Figure 5.18: The height of clouds and the cross-section of the vertical velocity in the **middle of the ML** over heterogeneous surface of the type 'along'.
Arrows (↑) indicate the mean wind direction.

The analysis of fluxes averaged over the horizontal extent of the domain reveals a significant impact of the heterogeneities on the vertical SH and LH flux. The timeseries of the SH heat mostly vary in oscillations. If smoothed by the averaging window, values do not vary between the cases by more than 3 %. On the other hand, the LH in the convective regime is always higher in the runs with heterogeneities (see figure 5.19a). At the recording altitude 170 m, LH flux in the case 'across' is by 10–12 % higher than in the 'homogeneous' case. In the 'along' case, it is even 12–15 % higher. Furthermore, at altitude 360 m, the 'along' case exceeds the LH flux of the 'homogeneous' case by almost 20 % (see figure 5.19b). The further analysis of the timeseries of vertical fluxes reveals also other differences between the model runs. In LH and SH flux timeseries at lower recording altitudes (45 m, 170 m and 360 m), there are generally higher oscillations in the case 'across'.

These large differences in the LH flux can be explained by the presence of forced rolls (Gryschka et al., 2014) that improve the transport of the moist air up from the warm patches and allows to reach higher vertical wind velocities in organised updraughts. Differences in the vertical SH flux remain relatively small mostly due to high stratification above the CBL. Unlike in the control scenario, a local increase in a SH flux does not lead to a growth of a cumulus on the top of a thermal, but to an increase in the potential temperature at the top of ML and in the entrainment layer. Descending updraughts are then warmer and the surface sensible heat flux decreases.

On the other hand, a temporary increase in LH flux at the surface leads only to a slight increase in humidity. Since the air at the bottom of ML is relatively far from saturation, the subsequent decrease in LH flux at the surface would be just negligible. Furthermore, the strong inversion layer at the top of the CBL does not allow the formation of a layer of active cumuli clouds. In the absence of the CuL, the cloud entrainment is still driven by convective rolls. Therefore the top of the CBL generally does not act against the surface forcing.

To sum up, the impact of surface temperature inhomogeneities in the scenario with strongly stratified lower troposphere is qualitatively different from the impact in the control scenario. Due to the strong inversion layer and the top of the CBL and the absence of CuL, the effect of heterogeneous surface forcing is not diminished by the cloud-top forcing. Each run maintains its specific properties at least for 5 hours. In the run 'along', a clear structure of forced rolls oriented along the mean wind directions is maintained. Model run differ in values of LH flux at the surface and at the recording altitudes within the ML. Unlike in the control scenario, this differences in the surface LH flux are maintained not only in the run 'along', but also in the run 'across'. On the other hand, differences in SH flux between the runs are generally smaller than in the control case. The orientation of anomalies in run 'across' leads to higher oscillation for

both LH and SH flux at the surface, as well as at altitudes in lower half of the ML.

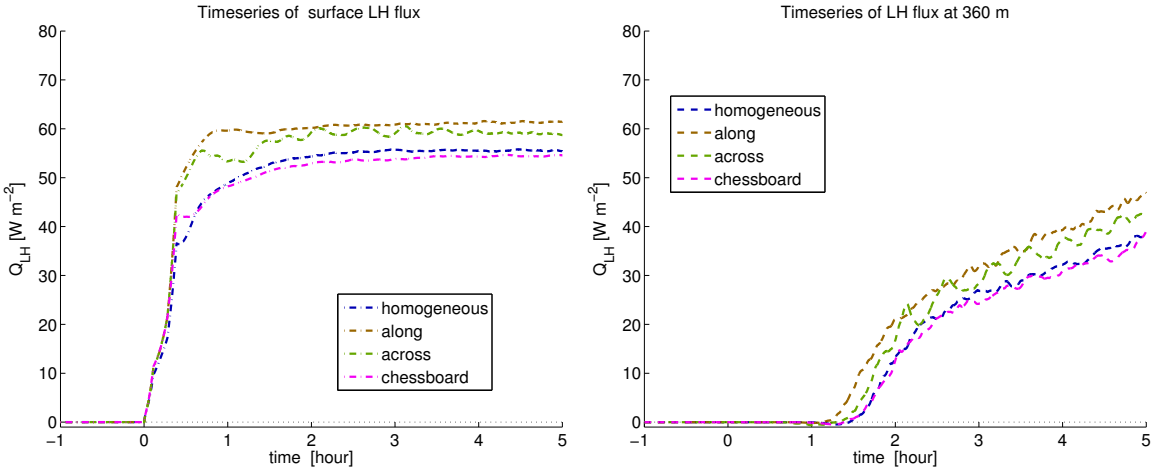

(a) (b)

Figure 5.19: The effect of heterogeneity type on the timeseries of the surface LH flux and the LH flux at the altitude 520 m in the scenario 'strat2'.

5.5.3 Size of Anomalies in Strongly Stratified Scenario

Previous idealised model studies of atmospheric boundary layer with heterogeneous surface conditions have often investigated how does the effect of the surface forcing depends on the spatial extend of the heterogeneity (Huang and Margulis, 2013). The study of Patton et al. (2005) indicated a ratio between the depth of the boundary layer and the wavelength of the heterogeneous pattern where the effect of the heterogeneous forcing is the strongest. Similar results were obtained by Heerwarden et al. (2014). However, model scenarios investigated in these studies usually started with a semi-stationary CBL (as was discussed in 4.3). Furthermore, it was generally not taken into account how are the results influenced by the stratification in the lower troposphere.

While the thickness of gradually growing CBL in scenarios with increased stratification is usually between 400 and 900 m, the ratio of the ML height to the spatial extent of temperature anomalies in MIZ is higher than in the scenarios with the weaker initial stratification. Since the previous section 5.5.2 has demonstrated that the impact of the surface heterogeneity does not diminish in stratified scenarios, it is important to investigate whether this property is not dependent on the size of the heterogeneity. Therefore, the study of the developing CBL in the conditions of strong stratification continues with the comparison of model runs with different spatial extent of the heterogeneity in the surface temperature.

The analysis of the impact of modifying the size of heterogeneous patterns 'across' and chessboard' unveils just a minor quantitative differences between runs with the different setting of the size. While the impact of the heterogeneous pattern 'across' and 'chessboard' in the stratified scenario is generally limited to the lower part of the ML (established in 5.5.2) this section is further going to focus on the impact of modifying the size of the heterogeneity 'along'.

The investigation of convective patterns show that runs with the heterogeneities along the mean wind direction with $d_{(\mathrm{h})} > 400\,\mathrm{m}$ tend to maintain the organised structure of forced convective rolls. Due to organised convection, theses runs exhibit a clear structure of cloud streets (see example in figure 5.20). The height of cloud tops generally does not vary between the runs. Domain-averaged timeseries of vertical SH and LH fluxes then exhibit some interesting trends. As has been already established in previous section, the heterogeneity 'along' increases the surface flux. The effect of a larger size of the heterogeneity is just minor (see 5.21a). However timeseries of the LH flux at higher altitudes within the ML show much larger differences between the runs (see the example in figure 5.21b). This indicates that although the larger heterogeneities do not increase the surface flux, the improve the upward transport of moisture. In the presence of strong inversion above the ML, these large differences in LH flux generally leads to an increased generation of clouds.

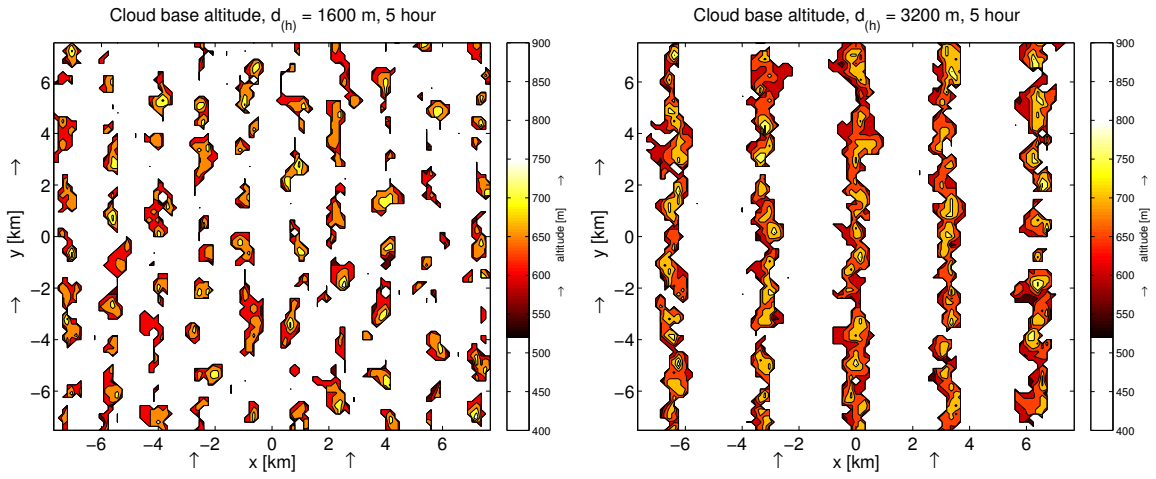

Figure 5.20: The height of clouds tops over the heterogeneous surface patterns of the type 'along'.
Arrows (↑) indicate the mean wind direction.

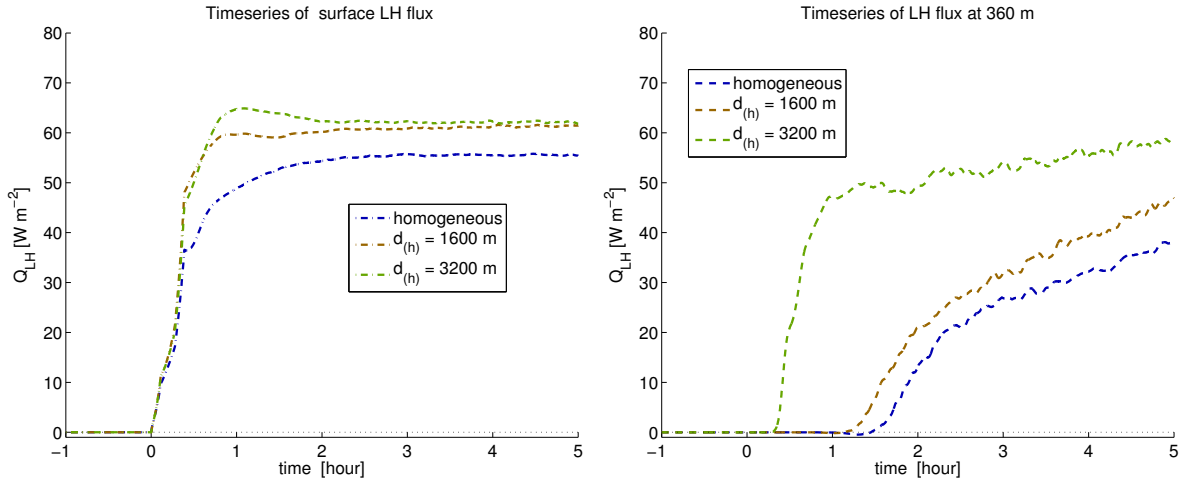

(a) (b)

Figure 5.21: The effect of heterogeneity type on the timeseries of the surface LH flux and the LH flux at the altitude 520 m in the scenario strat2'.

In essence, adjusting the size heterogeneities in surface temperatures generally lead to just minor impact on the surface SH and LH flux. However increasing the size of 'along' type of heterogeneity can modify the properties of the rest of the ML. Larger heterogeneities lead to an increase in the LH flux upward and a increased amount of cloud water.

5.5.4 The Combination of Stratification and Wind Shear

The previous sections have investigated the impact of heterogeneous surface forcing in scenarios with different surface stratification, however all of them maintained the same large scale wind forcing. Field observations of CAO cases described stratocumulus-topped CBL with wind speeds lower than as well as wind speed as high as. To reflect these possibilities, the impact of surface heterogeneities should be compared between strongly stratified scenarios with a different strength of winds. This section is therefore going to focus on the analysis of runs with heterogeneities in scenarios 'wind4-strat2', 'strat2' and 'wind2-strat2'.

In all three scenarios, heterogeneities of the type 'across' and 'chessboard' accelerate the formation of larger plumes and the upward propagation of the IBL during the first hour. In runs with heterogeneities 'along', the orientation of the temperature anomalies along the mean wind direction drives the formation of forced rolls. The development of CBL in 'wind4-strat2' and 'wind2-strat2' with surface heterogeneities generally follows same trends as in 'strat2', albeit with some minor differences. With a goal to better explain these differences, we focus on the results on heterogeneity of the patter type

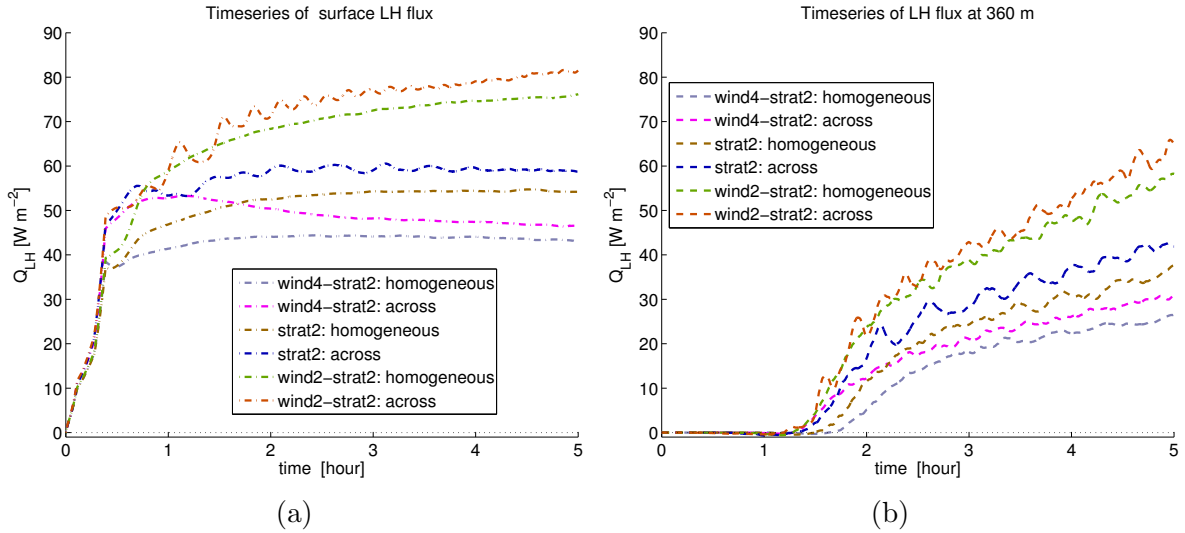

Figure 5.22: The impact of heterogeneity on the LH flux in scenarios with varying wind shear.

'across' of the temperature scale $\delta_{(\mathrm{h})} = 7\,\mathrm{K}$ and the size $d_{(\mathrm{h})} = 1600\,\mathrm{m}$.

Runs with the heterogeneity exhibit higher LH flux at the surface and at recording altitudes within the ML (see figure 5.22). The relative increase in the LH flux caused by the heterogeneity 'across' is then displayed in figure 5.23. It clearly shows that the impact of 'across' heterogeneity is more pronounced during the first two hours of the CBL growth. The telative impact in 'strat2' is temporary exceeded by 'wind4-strat2' during the time period 0.75–2 hour The relative impact in LH flux is lowest in the scenario 'wind2-strat4'. A similar, albeit weaker effect was found also in the case of the heterogeneity 'chessboard' (not shown here).

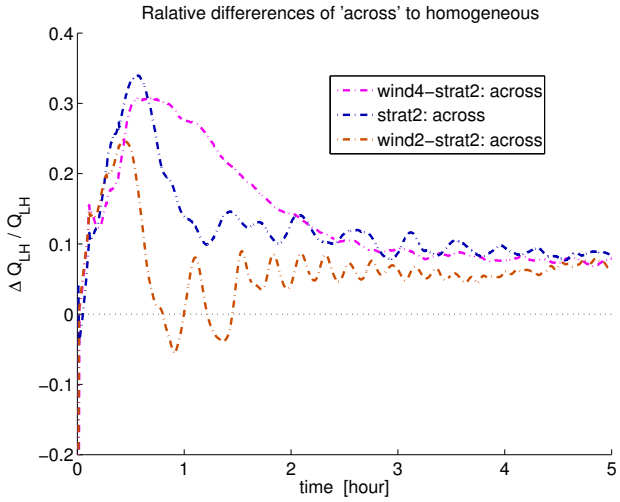

Figure 5.23: The relative increase in the surface LH flux due to heterogeneity 'across'

To sum up, increased wind velocity forcing in a CAO scenarios with high stratification leads to a *decreased impact* of anomalies 'across' and 'chessboard' during the first two hours of CBL growth. The differences in the latent heat flux between the runs with heterogeneities and the 'homogeneous' is generally smaller in scenarios with an increased wind forcing.

5.6 Discussion

Since this study has taken a slightly unusual approach to the investigation of heterogeneous surface forcing, this part of the chapter is going to address possible limitations in the model setting as well as in model results. The question of the model sensitivity to the horizontal and the vertical resolution has been already discussed in (3.6). While there is a possibility that scenarios with increased stratification might be more sensitive to resolution, this issues was also investigated. For details, see the results of sensitivity testing in the Appendix.

One of the main question in this study was the selection of the set of the idealised model scenarios. The main requirements was to represent a large palette of possible tropospheric conditions in CAO upwind of the MIZ while at the same time keeping the setting relatively simple. Since trial runs of control scenario presented the CAO case with an abrupt growth of clouds, the other scenarios were set with an increased stratification in the lower troposphere. The main purpose of the scenario 'strat4' is to represent mean winter temperature profile in the sub-Arctic areas. The comparison of model scenarios (5.3) shows that they cover both CBL with CuL and boundary layer topped by stratocumulus or nearly cloud free. Therefore, model scenarios account for at least two types of ABL as per classification of both ECMWF IFS and MetUM.

The other factor that might have an impact on the development of the CBL is setting of microphysical properties used by the model. Model result regarding cloud formation in the Arctic should be always view with caution. The intercomparison of various LES of the Arctic mixed-phase clouds (Ovchinnikov et al., 2014) showed that the ice particle size can play a significant role. Numerical models generally tend to underestimate ice water path and overestimated liquid water path (Morrison et al., 2009) (Klein et al., 2009). Furthermore, modelled clouds are often thinner and displaced downward (Tjernström et al., 2008). Nevertheless, the presence of mixed-phase stratucumulus alone plays an important role in the turbulent mixing. (Solomon et al., 2014).

The apparent limitation of this study is that the setting of the growth of the surface temperature with time remains the same as in the control case. However, introducing other settings of the mean surface temperature would be adding extra degree of free-

dom into the set of scenarios and would require a number of additional runs. Generally speaking, adjusting the mean surface temperature would mostly lead to an increase of decrease in the temperature gradient at the surface and therefore to an increased or decreased surface fluxes. It would also modify the relative ratio of temperature anomalies to the surface temperature gradient. However, the same effect is already achieved by adjusting $\delta_{(\mathrm{h})}T$, the temperature scale of anomalies. Nevertheless, the model scenario with a slower growth in the surface temperatures was run for the purpose of sensitivity testing. The results of the scenario did not show a qualitatively different development of the CBL. The results are briefly described in the Appendix.

Due to different settings of the wind forcing and the initial stratification, there is a high variability how far off the edge of sea ice has the observed air parcel travelled. Particularly with regard to the strong wind forcing in the scenario 'wind3', it is relevant to ask whether such a long MIZ is actually realistic. However, most of the wind shear is contained in the CuL, placing the estimated velocity of the ML parcel see 3.4.1 in the scenario 'wind' between 7.9 m s^{-1} during the formation of cloud and 11.8 m s^{-1} later. The total distance travelled by parcel within ML is therefore 129–137 km, which is still consistent with the usual length of MIZ 30–150 km (Claussen, 1991).

There are also other issues with the scenario 'wind3'. Since the mean wind velocity is gradually increasing within the ML 5.6a it does not follow the constant wind velocity profile expected by Monin-Obukhov (M-O) theory (Cheinet and Siebesma, 2009). While previous studies of the ABL over an ice-free Arctic fjord found that M-O theory is applicable in moderate and strong winds (Kilpeläinen and Sjöblom, 2010), the wind-shear within the ML in the scenario 'wind3' suggests that there should be an upper bound in the applicable wind velocities. In addition, issues with the applicability of the M-O theory in higher wind-shear scenarios have also dissuaded us from applying the similarity dimensionless scaling (Stull, 1988). The impact of heterogeneous surface forcing is instead listed with respect to the 'homogeneous' run of the same scenario.

In a number of studies, the effect of surface heterogeneities was increasing with higher stability (Grossman et al., 2005) However, these studies generally examined scenarios where a CBL did not develop, or where where the instability was relatively weak (Mahrt and Khelif, 2010). On contrary, other study has found a decrease in the effect of heterogeneities with an increase in the stratification (Mahrt, 2000). Generally speaking, it has proved rather difficult to separate the effect of the ratio of the heterogeneity size to boundary layer depth and the effect of increased stratification. In the "optimal" ratio between the heterogeneity size and the CBL depth, fluxes usually reach maxima (Patton et al., 2005). Further growth then results in result into the decrease in this ratio and possibly transition into the different turbulent regime (Heerwarden et al., 2014). Now, considering an increased stratification in the lower troposphere, there effect on the

growth of the CBL could be viewed in two different way. On one hand, it puts poses an obstacle to further vertical growth of a CBL. On the other hand, this may allow to maintain favourable ration between the size of the heterogeneity and the boundary layer depth for a longer period of time.

Previous studies of a CAO over a MIZ showed the temperature heterogeneities might be important factor in the formation of cloud rolls (Gryschka et al., 2008) (Liu et al., 2006). However, our study has shown that different pattern types lead to qualitatively different impact on the developing CAO. The formation of well-organised convective roll was identified only in the case of heterogeneities 'along' the direction of the wind. Therefore without an information about the orientation of surface temperature anomalies in MIZ, it would be rather difficult to predict the impact of sea-ice heterogeneity. However, previous studies of remote sea-ice sensing have shown that leads in Arctic generally tend to be aligned in the direction of prevailing geostrophic wind (Barry et al., 1989). Therefore, the development of cloud rolls is likely in cases of CAO where the wind follows the direction of the recent geostrophic winds.

5.7 Conclusion

This study has addressed the impact of the heterogeneous surface forcing in surface temperatures in a wide set of cold-air outbreak scenarios. It continued from the findings of the previous chapter and extended the scope of the study on idealised scenarios with a different setting of the wind shear and the initial temperature profile in the lower troposphere. Two main points of the hypothesis were:

- *A stronger wind forcing leads to a weaker effect of the heterogeneity in surface temperatures*
  In our study, the weaker effect was indicated (5.4.2) for scenarios with friction velocity above $u_* > 0.3$.

- *An increased stratification alters the effect of the heterogeneity in surface temperatures.*

  - Stronger impact of the heterogeneity on the LH flux and weaker impact on the SH flux 5.5.2.
  - Weaker impact on the size of heterogeneity on the SH flux (see figure 5.19).
  - The structures of convective rolls forced by the surface heterogeneity is maintained for longer 5.5.2.

The novel approach of this study involves introducing three three distinctive *types of heterogeneous pattern* in surface temperatures into selected idealised scenarios. While the selection of idealised scenarios is supposed to reflect the conditions in cold-air outbreaks events, the adjusted properties of the troposphere are: the large scale wind forcing and the initial stratification in the lower troposphere. All model scenarios start with the initially stable stratified atmospheric boundary layer. The result of different scenarios are compared and the impact of heterogeneities in each scenario analysed by comparing runs with the different setting of the surface heterogeneity.

First and foremost, the results have again shown that there are qualitative differences in the effects of different types of heterogeneous patter. The heterogeneities of the pattern types 'across' and 'chessboard' mostly modify the developing plumes in the early stages of convection. After the formation of mixed layer, their main impact is slightly increased surface latent heat flux. The heterogeneities of the pattern type 'along' modify the structure of the mixed layer and drive the formation of convective rolls. Although some studies found an increase in sensible heat flux due to patches of the surface temperature (Avissar and Schmidt, 1998) (Górska et al., 2008), our study indicated that the impact of surface heterogeneities of the sensible heat flux was just minor (not exceeding 2–3 %).

With regard to the initial stratification, an increase in the initial stratification can qualitatively alter the effect of the surface heterogeneous forcing. The model results have shown a clear differences between *two stratification regimes* — the weaker stratification that permits the development of cumulus layer and the stronger stratification that leads to boundary layer that remains clear or topped with stratocumuli clouds. In the regime with the weaker stratification, the effect of surface heterogeneities on the height and structure of the boundary layer generally diminished with the thickening of the cumulus layer. The cloud-top forcing by active cumulus cores and entrainment leads pose dominant effect on the resulting convective structures in the CBL. On the other hand, in the regime of stronger stratification, the effect of surface heterogeneities on the structure of boundary layer is mostly maintained. This is particularly demonstrated by the effect of the heterogeneity 'along'. The stripes of temperature anomalies drives the formation of distinctive forced cloud rolls (Gryschka et al., 2014). The previous chapter showed that the structure of these rolls disappears soon after the formation cumuli layer. However in the absence of cloud-top forcing by cumulus cores and entrainment, forced rolls persist well beyond 5 hour. Model results generally agree that inhomogeneities in the surface present favourable conditions for roll convection (Gryschka et al., 2008).

The first point of the hypothesis, the issues of the impact of an increased wind forcing, is separately addressed in both stratification regimes. In the scenarios without the cumulus layer, the increased wind velocity in the mixed layer leads to a *decreased impact*

of anomalies 'across' and 'chessboard'. The differences in the latent heat flux between the runs with heterogeneities and the 'homogeneous' run was smaller in scenarios with an increased wind forcing. The impact of the increased wind velocity in case of heterogeneity 'along' did not exhibit any clear trends.

In the scenarios with the weaker initial stratification, the results again slightly differ for each heterogeneity type. During the first hour, runs with heterogeneities 'across' and 'chessboard' exhibit a faster growth in the scenario with a weak wind shear The comparison of scenarios with other wind forcing do not reveal any specific trends. The heterogeneity 'along' drives the formation of of cloud rolls. Resulting differences between the run with heterogeneity 'along' and the 'homogeneous' run are higher in the scenarios with increased wind forcing. The impact of heterogeneities on the structure of CBL disappears in majority of scenarios after the formation of CuL. The effects of all three types of heterogeneities are then limited to an increased values in the surface latent heat flux. These values generally do not differ between the scenarios with 10, 20 and 30 $\mathrm{m/s^{-1}}$ Therefore, we conclude that in the regime with cumulus layer, increased wind forcing does not lead to a decrease in the effect of the heterogeneities. On contrary, it can actually lead to its increase. This indicates that findings of previous LES studies of the impact of heterogeneous forcing (Grossman et al., 2005) and (Avissar and Schmidt, 1998) are often limited to specific atmospheric conditions and size of heterogeneities.

Furthermore, the combination of the high wind forcing and the surface heterogeneities 'along' exhibited a specific influence on the development of the ABL. Before the formation of the CuL, heterogeneity of the type 'along' leads to a higher mean wind velocity in the mixed layer. This phenomenon is caused by forced convective rolls that improve downward transport of momentum. After the thickening of the CuL, these forced convective rolls diminish and the difference in mean wind velocity disappears.

The evaluation of updraughts and downdraught has further extended the findings of the previous chapter. The distribution of the vertical wind velocities within the ML is not normal in any of the model runs evaluated. Furthermore, the approximation by normal distribution mostly results into an underestimation of the kinetic energy of updraughts. These results are generally consistent over the whole set of model results. The evaluation of the heat and moisture flux by strong updraught has then unveiled a clear differences between the model scenarios. In the scenarios with the stronger stratification, the ratio of the heat and moisture transport facilitated by strong updraught is significantly higher than in the runs with a weaker stratification This finding is consistent with the previous modelling study of updraughts in CBL (Hellsten et al., 2013). Moreover, the heterogeneities of the type 'along' lead to a higher ratio of the heat and moisture transport by strong updraughts in strongly stratified scenarios. These phenomena can be explained by the more organised structure of strong updraughts in the absence of

the additional turbulence by cumuli clouds. The implication of these findings for the parametrization schemes are going to be further addressed in the Chapter 6.

Due to the large number of scenarios investigated, we have not presented results of the analysis of residua in flux timeseries. Since these results are relatively complicated, they were rather placed in the appendix. The analysis of the gravity was also not included in this chapter. However the main reason was that none of the model scenarios exhibited differences in the power spectra in the upper atmosphere between the model runs with the different heterogeneous patterns.

Findings of this study improve our understanding of the impact of heterogeneity in surface temperatures on the convective boundary later. Presented results further extend the findings of the previous chapter on a wider palette of cold air outbreaks. Model results further serve for an adjustment of parametrization schemes presented in the Chapter 6. Since all model runs presented so far were based on some idealised setting, the link to real weather conditions should be addressed. Therefore, the following chapter is going to focus on a selected case of an observed cold-air outbreak.

Chapter 6

Case Studies

Although an idealised large eddy simulation (LES) provides a valuable tool for understanding the development of the atmospheric boundary layer (ABL), it might seem slightly disconnected from "real" weather scenarios. Idealised LES model scenarios are usually designed to represent some observed weather phenomena, however a number of simplifications are introduced both in the initial conditions as well as in the forcings applied. On the one hand, various simplifications in the model setting allow us to clearly define model scenarios and examine the impact of modifying some of the model parameters (see chapter 4). On the other hand, the model might not correctly capture the inner variability within the ABL. Furthermore, simplifications in the setting of surface conditions often ignore some feedback loops in the physical processes (see discussion on surface fluxes in 4.3). In a *case study*, LES model runs are instead directly based on a previously observed weather scenario. Therefore, a case study provides an opportunity to compare the model results with the observational data.

The main purpose of this chapter is to extend the scope of this thesis to an observed cold-air outbreak (CAO). Although there was an extended LES study of the impact of MIZ heterogeneities on a developing CAO (Gryschka et al., 2014), it lacks a comparison with airborne data. A number of other case studies used mesoscale models (i.e. not eddy resolving) instead of a LES. These were, for example, studies of Pagowski and Moore (2001) and Wacker et al. (2005). There have been a number of LES case studies that focused on the heterogeneity in surface conditions, however they were usually concerned with the atmosphere in mid-latitudes and tropics. Bertoldi et al. (2013) performed an interesting LES study and compared it with airborne observations, however the lower troposphere was mostly neutrally stratified. This was also the study of heterogeneous surface patches by Maronga et al. (2014). Studies of the heterogeneity over deserts in Central Asia (Li et al., 2011) and the Sahara (Huang et al., 2010) whitch were concerned with much deeper ABL than in a CAO.

As a suitable example for our case study, we chose CAO that occurred over a marginal sea-ice zone (MIZ) during the ACCACIA field campaign in spring 2013. The main aims of this case study are:

- Investigate the impact of heterogeneous surface conditions in a specific CAO case.
- Compare the model results with airborne data.
- Analyse the likely variability due to uncertainty in surface conditions.

The approach applied in the preparations of this case study is inspired by the previous case studies of Kosovic and Curry (2000) on turbulent boundary layer and by Klein et al. (2009) on the impact of microphysics parametrization . Since the main goal of this chapter is to assess a likely impact of the spatial heterogeneity in surface temperature, a small ensemble of model runs is constructed — each run follows a different setting of surface conditions. The *control run* of each set is based exclusively on the data extracted from regional NWP used during the campaign. Three separate sets with different initial positions are constructed with the aim to cover the horizontal variability in CAO. Furthermore, they provide a better opportunity for comparison with the airborne data.

This chapter first explains the choice of the CAO case, the flight mission **B760** that took place on 21 March 2013. It will continue with the description of the datasets available for this study (6.1). This is followed by the methodology. Firstly, it explains the construction of the sets of modified runs. Secondly, it provides a clear overview of model settings (6.2.2). The specific aspect of the methods are then further described and explained. Results of the case study then consist of the analysis of model runs (6.3.2) and their comparison with the airborne observations (6.3.3).

6.1 Data

The *Aerosol-Cloud Coupling And Climate Interactions in the Arctic* (ACCACIA) field campaign took place in 2013 over the seas surrounding Svalbard. The main purpose of the campaign was to measure concentrations of different aerosol particles in the Arctic and investigate the interaction between the aerosols, boundary layer structures, and low level clouds (Young et al., 2016b). The purpose of this part of the chapter is to provide a basic description of the observed CAO case and introduce the datasets used in this case study. Firstly, we briefly review the main specifics of the ACCACIA flight campaign. Secondly, we focus on a chosen CAO case. The following paragraphs then focus on the airborne observations (6.1.3), the NWP forecast used during the campaign (6.1.4), and satellite observations of sea-ice.

6.1.1 ACCACIA

ACCACIA is a research project focusing on studying the interactions between clouds and aerosols in Arctic. One of the goals of the project is to improve the understanding of the effect of aerosols and other processes on the low-level clouds in Arctic (Carslaw et al., 2015). Field campaigns took place in spring and summer 2013. It involved observations from a research ship and two research aircraft: Facility for Airborne Atmospheric Measurements (FAAM) BAe-146 and the British Antarctic Survey MASIN Twin Otter (ACCACIA, 2013). The part of the campaign in spring 2013 consisted of a number of flight missions over sea-ice and MIZs in the seas around Svalbard (see figure 6.1 for an overview). The planning of the flight missions was enhanced by the specialised regional NWP forecast performed with the MetUM (Met Office, 2014).

The ACCACIA project has so far achieved interesting results on iodine particles in the Arctic (Allan et al., 2015) as well as on the distribution of other aerosols in the Arctic (Young et al., 2016a). Furthermore, the project provided detailed measurements of spring time stratocumulus clouds (Lloyed et al., 2015). It also provided new results for studies on the momentum flux over MIZs (Elvidge et al., 2016).

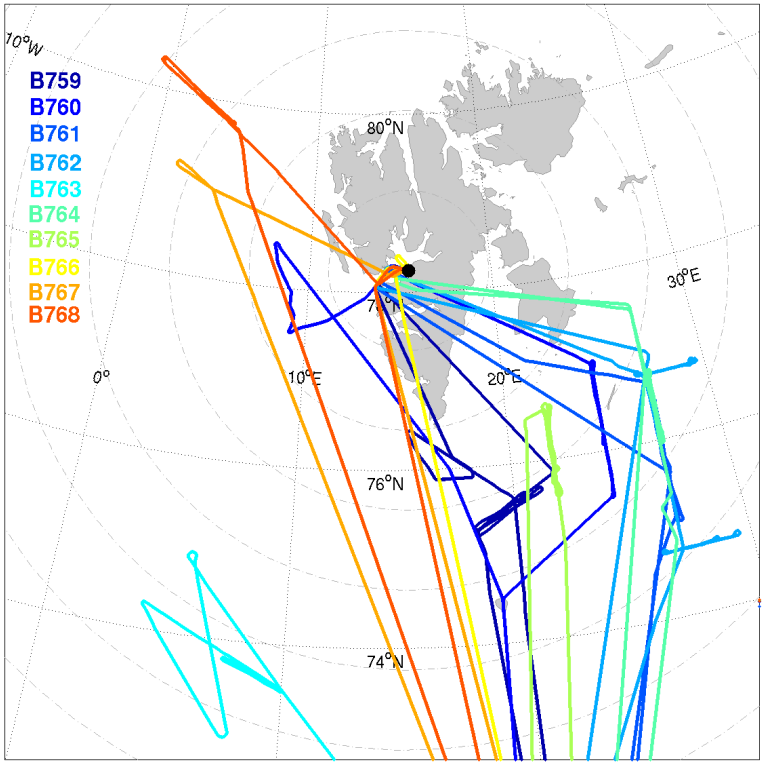

Figure 6.1: The trajectories of flight missions during the spring season of the ACCCACIA field campaign. Reproduced from the Quicklookbook of the ACCACIA project FAAM et al. (2015).

ACCACIA field campaigns provided a few opportunities for an observation of a CAO over a MIZ. After a careful consideration, we chose the CAO case observed during the FAAM flight B760. In the following paragraph, we are going to justify our choice and describe this CAO case.

6.1.2 Chosen Flight Day

The main reasons for the choice of the flight day 21 March 2013 is the availability of turbulent measurements over a MIZ. The mesoscale weather conditions are schematically shown in the figure 6.2a. A mass of cold air was advected from the inner Arctic over the MIZ that is located in Barents Sea. While most of the air mass is strongly stratified, the warm surface in the MIZ (see figure 6.4) lead to the formation of a CBL. This then continued deepening in the downwind direction. While the area over the MIZ was mostly cloud free, there were uuper level clouds at the end of the MIZ and low level clouds were forming further downwind over open water. The transition on the cumulus-caped boundary layer was observed further downwind. The cumulus topped CBL was indicated in the forecast, as well as in the satellite and airborne data.

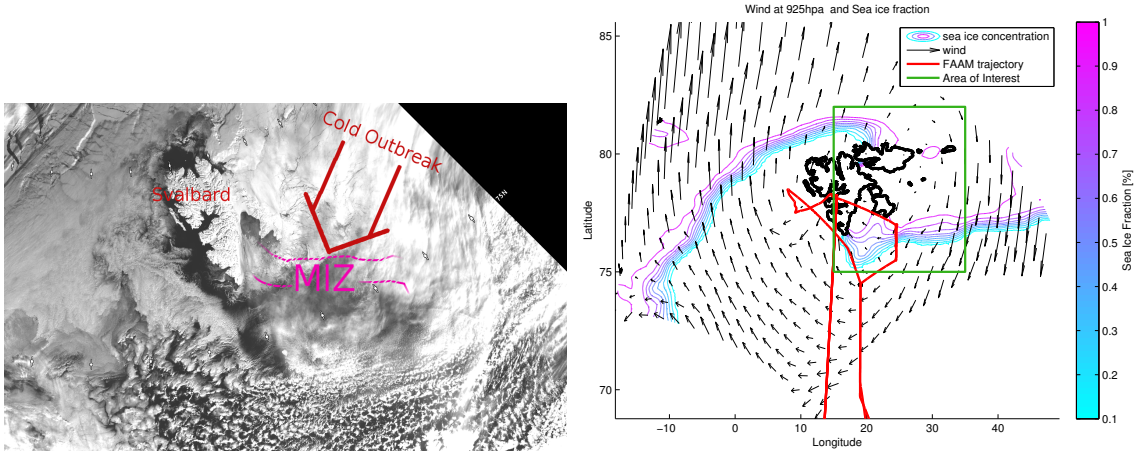

(a) annotated satellite image (b) NWP forecast of MetUM.

Figure 6.2: Overview of the CAO case on 21 March 2013 in the area East from Svalbard that was observed during the FAAM flight mission B760. Sea-ice fraction and wind vectors derived from the NWP forecast are shown in **(b)**. The trajectory of the FAAM research aircraft is added.

This flight mission consisted of a number of profiles and horizontal flight legs in areas both East and West of Svalbard. However, the other flight legs are not relevant for this study. Our wider area of interest consists of the area Southeast of Svalbard (see figure 6.2b). The main focus is then on the part of MIZ in vicinity of the stack of three horizontal flight legs through a developing CBL (marked in bold in the figure 6.4) and

upwind from them. For the details on flight legs, see table 6.2. The time interval of interest spanned from 6:00 until 16:00 on 21 March 2013 .

	leg 7	leg 8	leg 9
starting time (UTC) [s]	13:30	13:56	14:27
starting position	24.5° E 76.9° N	24.5° E 75.5° N	24.61° E 77.0° N
ending position	24.5° E 75.5° N	24.5° E 77.0° N	24.5° E 76.05° N
average altitude [m]	108.0	181.2	303.1
average aircraft speed [$\mathrm{m\,s^{-1}}$]	101.3	101.7	103.8

Table 6.2: Overview of flight legs in the area of interest

6.1.3 Airborne Observations

The flight mission on 21 March 2013 was performed by the FAAM aircraft. This aircraft has participated in a number of research flights over the last two decades. For the ACCACIA field campaign, it was equipped with a number of state-of the art science instruments. In the following paragraphs, we briefly describe the airborne data that were used in this case study. For further details on the instrument specification, we refer to documentation on the FAAM website (FAAM, 2017).

- An essential part of the airborne measurements is the recording of the positions of the aircraft. FAAM utilises *GPS-aided Inertial Navigation system* that provides longitude, latitude, altitude and velocity data. This navigational system is comprised of an Applanix POS AV 510 system, designed explicitly for the geo-referencing of airborne sensor data. The high frequency outputs of this system are sampled as 32 Hz for the data recording.

- The basic recording of the temperature was performed with the *Rosemount/Goodrich type 102 Total Air Temperature probes*. It generally consists of two probes. One is enclosed in the de-iced housing while the other one is non de-iced. The temperature data are sampled at 32 Hz.

- The main source of the data on humidity was the *General Eastern GE 1011B Chilled Mirror Hygrometer*. This instrument provides 4 Hz recordings of the dew-point temperature.

- A turbulent measurements were enabled by FAAM CORE 5-hole turbulence probe. The location of the probe in the tip of the aircraft allows it to measure the incident

airflow and 3-D wind components. The data output from the turbulent probe is combined with the filtered output from the Inertial navigation system (Petersen and Renfrew, 2009). The turbulent measurements are in the end sampled at 32 Hz.

- The FAAM aircraft was further equipped with a number of instrument for sampling aerosol concentrations as well as advanced instruments for cloud microphysics. Although those data were essential to the success of the ACCACIA flight campaign, they are not relevant for this case study.

All of the listed instruments were recording in the flight legs 7, 8 and 9 of the mission B760. No severe instrument conditions were reported. A pre-processing of the instrument outputs performed by FAAM specialists did not indicate any significant errors in the data apart from isolated error values in the flight leg 8. As the non-deiced probe stayed ice-free in listed flight legs (see figure 6.3), we use this timeseries in the further calculation of thermodynamic variables.

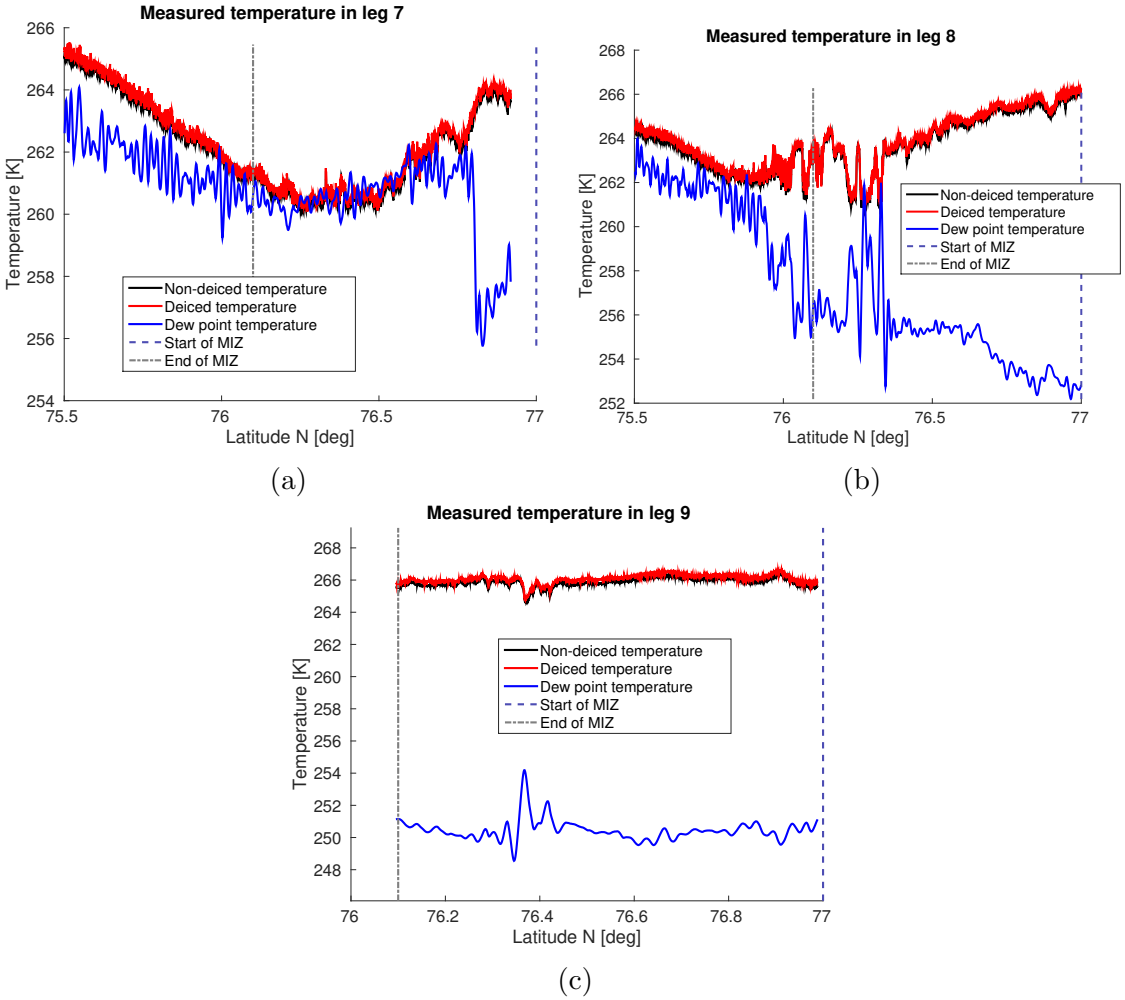

Figure 6.3: The series of temperature and the dew point temperature derived from the airborne observations in the flight legs 7, 8 and 9. The added vertical lines mark the latitudes between which is the aircraft flying above the MIZ (as derived from the MetUM forecast and the aircraft trajectory).

6.1.4 Operational NWP Data

The availability of a cutting edge NWP weather forecast is essential for planning of flight missions (Renfrew et al., 1999). The ACCACIA flight campaign used the specialised regional NWP forecast (Met Office, 2014) from the Met Office Unified Model (MetUM). It allowed researchers to decide which days would be suitable for observing specific phenomena and to propose the mission flight path. Furthermore, the NWP forecast allowed an identification of some of the observed atmospheric phenomena in the later data analysis.

The specialised regional forecast was performed with the operational version of the MetUM. The computational domain span from the longitude 23° W to 23° E and from 70° N to 82° N and in the vertical direction from the surface up to the pressure level 100 hPa. While the region was located in the vicinity of the north pole, the computations were performed on a non-standard grid where the pole was shifted to the position 154.8° N° for the purpose of avoiding various computational issues (Randall et al., 1998). In the rotated coordinate system, the horizontal resolution was 0.036 degree. This translates as approximately 4 km in the target area. The boundary layer was parametrized by the standard MetUM scheme (see 1.1.1 for the description).

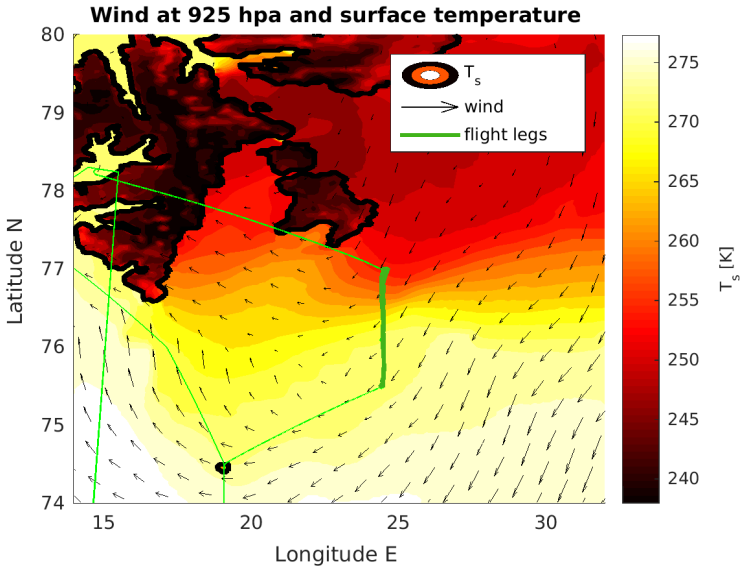

Figure 6.4: The surface temperature during the FAAM flight mission B760 on 21 March 2013. The surface temperature and wind vectors were derived from MetUM forecast.

The NWP simulation used for the chosen mission B760 started with the initial conditions at 00:00 on 21 March 2013. The model outputs consisted of the fields of prognostic variables and various model diagnostics. They were produced every 3 hour. Although the outputs included a number of diagnostics such as cloud types and the long-wave

radiation at the top of the atmosphere, the data on ABL were quite limited. The diagnostics of the ABL type and the diagnostics of the ABL depth were provided, however the estimation of the vertical fluxes of heat and moisture in the ABL were not included.

6.1.5 Sea-Ice Data

While this case study is focused on the impact of surface conditions in the MIZ on the CAO, further attention is given to the data on MIZ. For this purpose, we compare the distribution of the sea-ice in the MetUM forecast with the observational data. In this part of the thesis, we describe the sea-ice observations and the main implications for the NWP.

High-resolution satellite observations of the sea-ice fraction are obtained from the AMSR2 Sea Ice Maps (Spreen et al., 2008). The sea-ice map for 21 March 2013 in the figure 6.5a shows a wide extent of the MIZ southeast of Svalbard with a number of smaller areas of open water . The comparison of sea-ice fraction in MetUM with the observations reveals that the southward extent of the MIZ is underestimated (see figure 6.5b). Furthermore, the concentration of the ice within the MIZ in the area upwind from the flight legs is also underestimated.

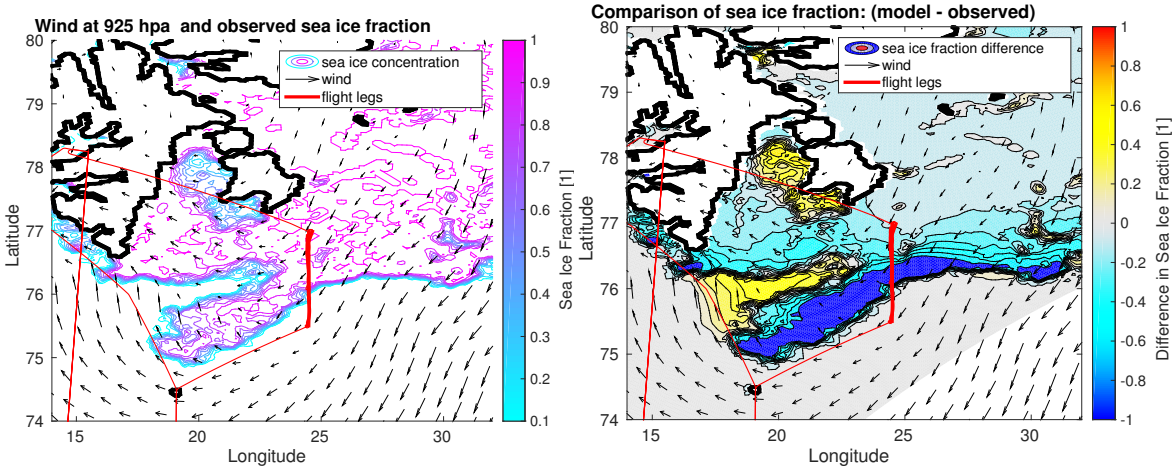

(a) observational data

(b) The observed sea-ice fraction subtracted from the sea-ice fraction used in the MetUM regional forecast.

Figure 6.5: The comparison of the observed of the sea-ice fraction on 21 March 2013 and the prediction of the sea-ice fraction used in the MetUM regional forecast.

Since the MetUM uses a different surface parametrization of surface fluxes for the sea-ice surface (Lock and Edwards, 2013), underestimation of the sea-ice extent might lead to the overestimation of surface fluxes. Furthermore, the underestimation of the

sea-ice extent might also lead to incorrect evaluation of the aerodynamic surface roughness. While there are significant differences in the sea-ice fraction between the MetUM and the AMSR2 data, we further employ the observational data in the construction of surface heterogeneities for the case model runs in 6.2.6.

6.2 Methods for Case Studies

The construction of this case study was inspired by the study of Kosovic and Curry (2000) and the M-PACE comparison study (Klein et al., 2009). The former study motivated the construction of the set of runs, while the later served mostly as a guideline how to set the model based on NWP forecasts and observations of a CAO case. While the model runs presented in the previous result chapters introduced idealised initial and boundary conditions, the case study would employ conditions derived from a NWP forecast. Therefore, it requires a substantial adjustment to the methodology presented in 3.2.

In this part of the chapter, we first explain the main principle of the framework for case simulations. Then we provide the overview of model setting. The following sections then focus on specific parts of the methodology. The methods for the evaluation of the model runs remain essentially the same as for idealised model scenarios (3.4). The main part of the analysis is again performed for the interval of model runs when larger CBL eddies are fully in the resolved regime (see 3.2.4 for clarification). The interval of the model run when the larger CBL eddies are properly resolved is again determined by a comparison of resolved portion and subgrid portion of the vertical fluxes (see 3.5.3). Additional methods are then introduced for the comparison between the model results and the airborne data (6.2.7).

6.2.1 Framework for Case Study

Since the main goal is to assess the likely impact of the heterogeneous surface forcing, a small ensemble of model runs is constructed — each run follows a different setting of surface conditions. The *control run* is set exclusively on the data extracted from the specialised MetUM forecast used during the campaign. Although the MetUM forecast includes the estimated sea-ice fraction, it does not provide information on the structure of ice floes within the MIZ. Therefore, the control run assumes homogeneous surface conditions, similarly to control runs described in 3.2 and 5.2.

Same initial conditions and the large scale wind forcing are applied in other runs. However the setting of the surface temperature is modified by adding spatial heterogeneity over the MIZ. In addition, we should consider the form drag produced by ice floes

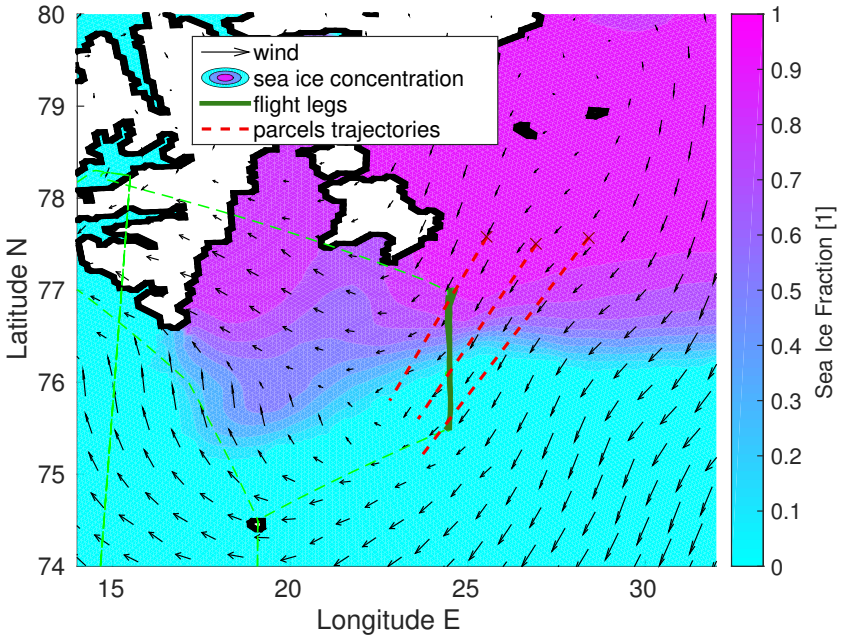

Figure 6.6: The location of the flight legs of the FAAM flight mission B760 on 21 March 2013 and the trajectories of modelled parcels. The sea-ice fraction and wind vectors were derived from MetUM forecast.

within the MIZ. While the MIZ is expected to influence the air friction (Lüpkes and Gryanik, 2015), it would be reasonable to include it in the analysis of the variability in the MIZ (Carper and Porté-Agel, 2007). Furthermore, it would allow us to compare the relative influence of form drag and the influence of surface temperature heterogeneities on a developing CBL. Therefore, the resulting ensemble consists of the following runs:

1. **control run** with variable surface roughness and albedo set accordingly to UM forecast; surface is locally homogeneous
2. modified runs according to **MetUM forecast** setting
   (a) surface roughness adjusted based on sea-ice fraction
   (b) heterogeneous surface based on sea-ice fraction
3. modified runs according to **observations** of sea-surface temperature and sea-ice fraction
   (a) homogeneous surface temperature, surface roughness based on sea-ice fraction
   (b) heterogeneous surface temperature based on sea-ice fraction
   (c) heterogeneous surface temperature and surface roughness based on sea-ice fraction

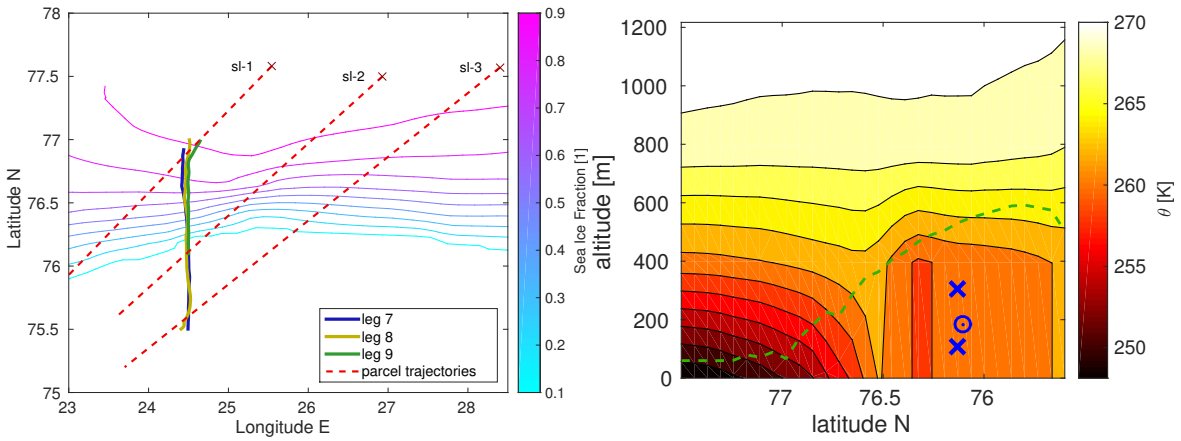

(a) (b)

Figure 6.7: The location of the flight legs of the FAAM flight mission B760 on 21 March 2013 and the trajectories of modelled parcels. **(a)** shows the location of flight legs against the sea-ice fraction in the MIZ while **(b)** compares altitudes of flight legs against the vertical structure of the troposphere in sl-2. Green line indicates the boundary layer height. The sea-ice fraction and potential temperature were derived from the MetUM forecast.

The framework is further extended with the aim to represent the mesoscale variability within the CAO and to provide a comparison between the model and airborne data: Three different Quasi-Lagrangian model parcels (see 1.5 for explanation) are considered. We denote them **sl-1**, **sl-2** and **sl-3** for clarity. The parcels are projected to move approximately along the direction of the synoptic-scale geostrophic wind. Their initial positions (see table 6.4) are located approximately on an East-West line with a longitude spacing of 1.5 degree. They are chosen in the way that the Quasi-Lagrangian parcels trajectories starting from these positions intersect the aircraft legs in the sector of flight legs 7, 8, 9 (see figure 6.6). Moreover, the intersections occur at specific part of the flight legs. The trajectory of the parcel sl-1 intersect flight legs over the early part of the MIZ, while parcel trajectories sl-2 and sl-3 intersect flight legs further downwind over the MIZ and the open sea respectively (see figures 6.7a and 6.7b). Therefore, each of these three sets of model runs should provide us with data for the comparison with airborne observations at different stages of the CBL development.

6.2.2 Overview of Model Setting

The case study requires a cautious setting of the model runs. With an intention to maintain clarity and allow for reproducibility in future studies, all the scenario & model settings are defined in the following tables. The first and the second table defines the setting of control runs. The following tables then define setting of modified runs in each set.

The following tables are designed in a way to provide a clear overview. The left column list a model properties and the central column defines its setting. The third column then provides a reference to the following parts of this chapter that offers a detailed description and the explanation of these settings. Finally the rightmost columns refers to the part of the software where is the setting implement. The names of LEM code segments start with the symbol * and the names of LEM namelists starts with the & symbol. Notwithstanding, the exact implementation in the idealised scenarios in LEM code is not included in this chapter. Due to its technical character and overall size, it is instead located in the Appendix.

property		setting	details	set in
domain	width in x	16 km	3.2.4	runfile
	length in y	16 km	3.2.4	runfile
	depth	12 km	3.2.1	&GRID
resolution				
	horizontal	160 m, in both directions x and y		runfile
	vertical	altitude [m] / spacing [m]: 7500–12000 / 100; 2500–7500 / 100; 100–2500 / 40; 0–100 / 10	2.3.1	&GRID
grid	type	Arakawa-C in horizontal, Lorenz in vertical	2.6	
	size	100 x 100 x 126		runfile
subgrid model		LEM subgrid model based on S-L theory	2.4	&SUBMODEL
microphysics		LEM 3-phase cloud microphysics precipitation: rain, snow, graupel	6.2.3	*PRAMETR
radiation				
	• solar	Edwards-Slingo radiation code	6.2.3	*PRAMETR
	• long-wave	radiation update every 5 timesteps	6.2.3	* &INPUT
		sub-arctic winter profiles for upper atmosphere	6.2.3	*CALC_LEVS
numerics		• maximum advective CFL number 0.2	2.6	&NUMERICS
		• maximum viscous CFL number 0.2		
		• P–W advection scheme for momentum	2.6	*PRAMETR
		• ULTIMATE advection scheme for scalars	2.6	*PRAMETR
		• initialisation by perturbations in wind velocity	3.2.5	* START

Table 6.3: Overview of model setting — computational setting of control scenario

property	setting	details	set in
initial positions	<table><tr><td></td><td colspan="3">parcels</td></tr><tr><td></td><td>sl-1</td><td>sl-2</td><td>sl-3</td></tr><tr><td>Longitude (East)</td><td>25.54</td><td>26.93</td><td>28.4</td></tr><tr><td>Latitude (North)</td><td>77.58</td><td>77.50</td><td>77.57</td></tr></table>	6.2.1	
azimuth of the trajectory	<table><tr><td></td><td>sl-1</td><td>sl-2</td><td>sl-3</td></tr><tr><td>azimuth [deg]</td><td>237.0</td><td>240.3</td><td>243.2</td></tr></table>	6.2.1	
initial conditions	Potential temperature, humidity and wind velocity follows values at 06:00, 21 March 2016 from MetUM forecast	6.2.5	&INITPROF
dynamics	Coriolis parameter for 77° North		&DYNAMICS
forcing	large scale wind forcing in both directions derived from the forecast along the trajectory	6.2.4	forcing file
boundary conditions			
• top	rigid boundary, no subsidence, stress-free for horizontal velocities with damping layer 2 km deep, located above 10 km	3.2.4	&DAMPNML
• lateral	periodic boundary	2.3.1	
• bottom	rigid boundary, with surface model, reference surface pressure 1004 hPa	6.2.3	&INPUT
surface model	based Monin-Obukhov theory, prescribed surface roughness length and values for surface temperature and humidity	2.5	*PRAMETR
	roughness length derived from the forecast	6.2.6	&INPUT
surface albedo	derived from the forecast		&RADCNTL
surface humidity	saturated surface	3.2.1	*PRAMETR
surface temperature	derived from the forecast	6.2.6	&INPUT
reference profile	temperature reference profiles at the beginning are derived from the forecast along the trajectory	6.2.5	&THPROF

Table 6.4: Overview of model setting — control runs

'40 m' horizontal resolution				
property		setting	details	set in
resolution				
	horizontal	40 m, in both directions x and y	3.2.4	runfile
domain	width in x	4800 m	3.2.4	runfile
	length in y	4800 m		runfile
	height	12 km	3.2.1	&GRID
grid	size	120 x 120 x 126		runfile

Table 6.5: Overview of model setting — model runs with increased horizontal resolution

heterogeneity in surface temperatures			
property	setting	details	set in
types	**along**: stripes along wind; **across**: stripes across wind; **chessboard**: chessboard pattern	3.3	update code
spatial scales	size of the square block of the pattern ($d_{(\mathrm{h})}$): 1600 m → 40 m and 160 m; 3200 m → 160 m	3.3.2	update code
temperature scales	maximum scale of a positive anomaly $\delta_{(\mathrm{h})}T = 3$ K	3.3.2	&INPUT
time development	Defined by the equation 6.7 dependent on the values of surface temperature and sea-ice fraction extracted from: MetUM forecast; sea-ice observations	6.2.6	&INPUT

Table 6.6: Overview of model setting — model runs with modified surface conditions

modified surface roughness			
property	setting	details	set in
surface roughness	Defined by the equation 6.11 dependent on the values of sea-ice fraction extracted from: MetUM forecast; sea-ice observations	6.2.6	&INPUT

Table 6.7: Overview of model setting — model runs with modified surface roughness

6.2.3 General Setting

The setting of the physical properties in the model generally follows the setting of the control run in 3.2 The following paragraphs focus on the aspects of the model setting that differ from idealised model runs or otherwise require further explanation.

The downwind development of the CAO is again simulated with the help of Quasi-Lagrangian approach of Szoeke and Bretherton (2004). For detailed description and justification, see 3.2.3. The Quasi-Lagrangian parcels move into the area over the MIZ at least 6 hours after the front of the CAO has passed. This allows us to avoid the issues with the secondary circulation at the CAO front that might otherwise invalidate the Quasi-Lagrangian approach (Skyllingstad and Edson, 2009). The effect of lateral advection is neglected after a careful consideration due to homogeneity in prognostic variables in the lateral direction (see 6.2.4 for details).

While the CAO we are studying occurred around the spring equinox, the atmosphere was receiving solar irradiation for most of the modelled time interval. Although the incoming SW radiation is weaker than the OLR, it might effect the properties of shallow stratiform clouds (Slingo and Schrecker, 1982). As we do not want to neglect the effect of SW on newly formed clouds, the code for SW radiation in LEM (2.3) is switched on. We further consider the radiation properties of the atmosphere above the model domain. Since the CAO case is taking place at the beginning of the spring, the upper atmosphere is again represented by the McClatchey profile for the subarctic winter (McClatchey et al., 1971).

6.2.4 Large Scale Forcing

The setting of the large scale wind forcing in this study is motivated by the M-PACE comparison study (Klein et al., 2009) where the large scale forcing were derived from a NWP forecast. In our case study, the large scale forcing is based on the consecutive steps of the MetUM regional forecast. In the following paragraphs, we describe the whole process step by step. Then we also address the issue of differential advection.

Firstly, we interpolate the values of wind velocity on the slice along the parcel trajectory. The interpolation in the horizontal direction is performed on each vertical level separately. Since the grid is not equidistant, we employ the tri-scattered interpolation technique (Amidror, 2002). While this method is already implemented in Matlab as the function `TriScatteredInterp`, we simply call it on the set of gridpoints at each horizontal level and then connect the outputs together. The advantage of this approach over applying tri-scattered interpolation on the whole field is the effective use of the memory. We repeat this approach for each MetUM timestep within the interval of interest.

Secondly, we decompose the wind velocity into the component parallel to the direction of the parcel trajectory and perpendicular to it.While the wind velocity is stored in eastward and northward component, a simple linear transformation suffices. The new decomposition into the parallel component v and the perpendicular component u of wind is therefore obtained as:

$$\begin{pmatrix} u \\ v \end{pmatrix} = \begin{pmatrix} \cos\alpha & \sin\alpha \\ -\sin\alpha & \cos\alpha \end{pmatrix} \cdot \begin{pmatrix} u_{\mathrm{E}} \\ u_{\mathrm{N}} \end{pmatrix} \tag{6.1}$$

where u_{E} is the eastward wind component, u_{N} is the northward wind component, and α is the azimuth of the parcel trajectory. The advantage of this choice of the wind components is that the horizontal wind vector (u, v) is consistent with the right-handed Cartesian coordinate system (x, y, z) in the LES grid.

Thirdly, we evaluate the resulting wind field (see figure 6.8). The large scale forcing in the direction parallel with the trajectory is approximately constant with time. This simplifies the transformation of the spatially-dependent wind forcing on the time-dependent forcing required in the LEM. We reclaim that the horizontal mean of wind velocity in ML is approximately constant within the ML (Stull, 1988, p.450) and that the distance travelled by a parcel since some reference point t_0 can be expressed as

$$s(t) = \int_{t_0}^{t} \bar{v}(\tilde{t}, z_i)\, \mathrm{d}\tilde{t} \tag{6.2}$$

where z_i is the ML height and $\bar{v}$ is the horizontal mean of wind velocity in the direction of the parcel trajectory (see 3.4.1). The time interval Δt_j required by the Quasi-Lagrangian parcel to travel between two points on the trajectory (denoted s_{j+1} and s_j) is then approximated as

$$\Delta t_j \approx \frac{s_{j+1} - s_j}{\bar{v}(s_{j+1}, z_i)} \tag{6.3}$$

where $\bar{v}(s_{j+1}, z_i)$ is the mean wind velocity in the direction of the parcel trajectory between the points s_{j+1} and s_j. The time coordinate of Quasi-Lagrangian parcel therefore yields

$$t_n \approx t_{\mathrm{INI}} + \sum_{j=0}^{n-1} \frac{s_{j+1} - s_j}{\bar{v}(s_{j+1}, z_i)} \tag{6.4}$$

where t_{INI} is the initial time (6:00 on 21 March).

In the stratified troposphere over the sea-ice, $\bar{v}(s_{j+1}, z_i)$ was replaced with the mean velocity at the indicated boundary layer top. A further testing revealed that values of t_n are generally not sensitive to the exact choice of sampling s_j in (6.4), as long as it is

on the same order of magnitude as MetUM horizontal resolution or finer. Furthermore, replacing the s_{j+1} with s_j also does not lead to significant changes in t_n.

Finally, we construct the wind forcing for the LEM. The wind forcing v_f in the direction parallel to parcel trajectory yields

$$v_f(t_j,\, z) = v(t_j,\, s_j,\, z), \tag{6.5}$$

for all points s_j on the trajectory and all altitudes z within the LEM domain. The changes in the wind velocity component in the direction perpendicular to the parcel trajectory should be then included as an additional large-scale forcing (Szoeke and Bretherton, 2004). The calculation of u_f, wind forcing in the perpendicular direction, is analogous to (6.5).The forcing in both wind directions is then included in the LEM setup as forcing files (Gray and Petch, 2004). The exact setting of the wind forcing is provided in the Appendix.

The effect of the differential advection should be considered. While the NWP data are available, the advection of the environmental air into the Quasi-Lagrangian parcel can be included following the work of Richardson et al. (2007). However, the NWP forecast show relatively small differences in the direction perpendicular to the wind trajectory. Furthermore, the potential temperature and humidity are approximately homogeneous in the horizontal direction above the ABL. Therefore, we neglect the effect of the horizontal advection of the environmental air by the perpendicular wind component. This approach is consistent with the previous studies of CAOs by Muller et al. (1999) and Skyllingstad and Edson (2009).

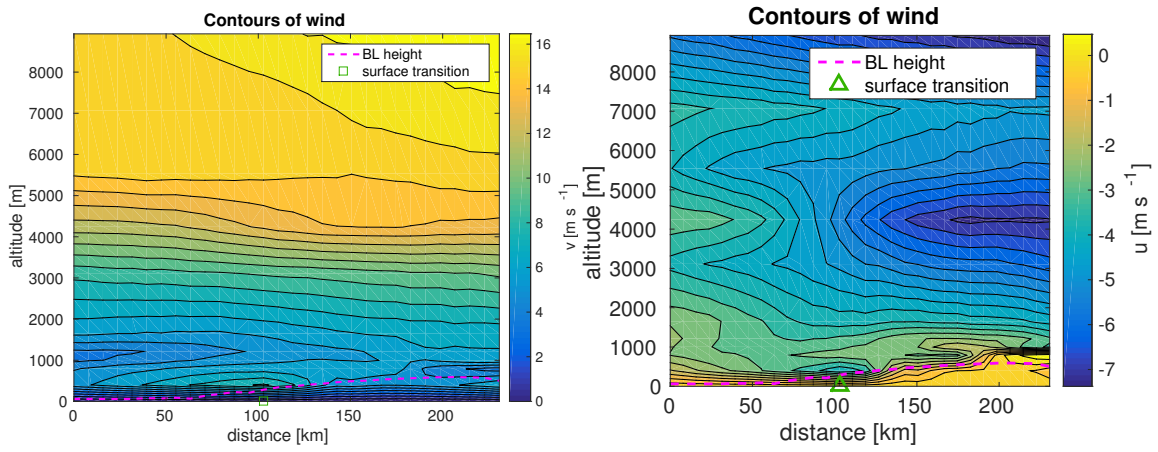

(a) wind in the direction parallel to the trajectory

(b) wind in the direction perpendicular to the trajectory

Figure 6.8: The cross-section of wind forcing in the vertical slice following the parcel sl-2.
The small square indicates the start of the MIZ in MetUM forecast.

6.2.5 Initial Conditions

Initial conditions in a number of case studies followed the data obtained from soundings (Desai et al., 2006) or from the dropsondes released from an observational aircraft (Huang et al., 2010). Unfortunately, neither of these is available in our CAO case. Although a number of dropsondes were used during the ACCACIA flight missions, none of them was released during the flight mission B760. With an aim to accurately represent the vertical structure of the troposphere over ice in this CAO case, the initial conditions for each parcel are instead extracted from the MetUM regional forecast.

The evaluation of the initial conditions again requires additional processing of the MetUM forecast data. The interpolation of the potential temperature and humidity follows the approach from 6.2.4. However unlike the large-scale forcing on pressure levels, the initial conditions are required on altitude levels. Therefore, said variables are in addition linearly interpolated in the vertical direction on fixed altitudes. The vertical profiles of potential temperature, humidity and both wind components at the start of the slice in the first time step are then inserted as the initial conditions into the case model run. The rest of the slice is then used for further comparison with LEM results.

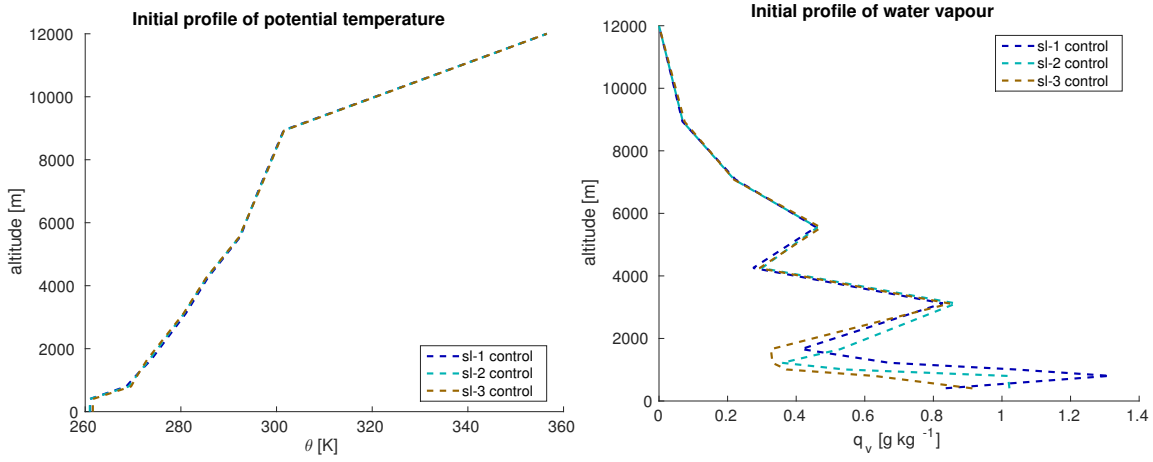

(a) initial potential temperature profiles (b) initial water vapour content profiles

Figure 6.9: Initial conditions in potential temperature and water vapour content of for all three sets or runs.
(Note: Profiles of potential temperature are virtually almost the same)

6.2.6 Surface Conditions

The important part of the model scenario is the description of the surface forcing. This is also the only aspect in which the runs in the same set differ from each other. The following paragraphs describe the setting of the mean surface temperature and the setting of heterogeneities in surface temperature. The effect of the form drag on the surface

exchange in the MIZ is also taken into account. Due to significant differences between the ice-fraction in the MetUM forecast and the observational data, we employ them separately in the setting of model runs. In the following paragraphs, we first define the surface properties in the control run. Then we define the setting of heterogeneity in surface conditions. Finally we define the modification of surface roughness.

The time dependent setting of surface temperature and aerodynamic roughness in the control run of each parcel is directly derived from the MetUM forecast. This approach is similar to the approach on deriving wind velocities in 6.2.4. The values of surface properties from the forecast dataset are first interpolated on the parcel trajectory. We again employ tri-scattered interpolation in the horizontal layer of the surface. The linear interpolation is then used in the time coordinate. The time-dependent values of surface temperature $T_{s,\,c}$, aerodynamic surface roughness $z_{0,\,c}$ and the surface albedo $al_{s,\,c}$ for the control run are then derived as

$$\begin{aligned} T_{s,\,c}(t_j) &= T_s(t_j,\, s_j), \\ z_{0,\,c}(t_j) &= z_0(t_j,\, s_j), \\ al_{s,\,c}(t_j) &= al_s(t_j,\, s_j) \end{aligned} \tag{6.6}$$

where T_s, z_0 and al_s are the respective values on the line interpolated from the MetUM dataset. While the MetUM forecast does not provide data on the aerodynamic surface roughness for scalars, we set them to the same values as $z_{0,\,c}$ for simplicity (Derbyshire et al., 2004).

Since the description of the size and shape of floes within the MIZ is not available, we use a semi-idealised setting similar to 3.3.2. All three types of the pattern of heterogeneity are considered. The surface temperature $T_{s,\,(\mathrm{h})}$ in the runs with heterogeneity should represent conditions in the MIZ. Therefore, we expect it to fulfil the following criteria:

- $T_{s,\,(\mathrm{h})}$ is homogeneous over the contiguous sea-ice and open sea-water.
- The mean value of $T_{s,\,(\mathrm{h})}$ is the same as $T_{s,\,c}$ in the control run.
- The MIZ is not colder than the ice further upwind. Therefoe, the $T_{s,\,(\mathrm{h})}$ in the patches of negative anomalies is always greater or equal than T_s over sea-ice surface upwind.
- The water in MIZ is not warmer than on the open sea. Therefore, $T_{s,\,(\mathrm{h})}$ in the patches of positive anomalies is always lesser of equal than T_s over open water downwind.
- The difference between T_s in the patches of negative anomalies and the mean T_s in MIZ should reach $\delta_{(\mathrm{h})}T$ if possible.

The values of surface temperature anomalies are therefore dependent on $T_{s,\,c}$ and sea-ice fraction c_{ic}. The spatial scales 1600 m and 3200 m are tested. The temperature scale $\delta_{(\mathrm{h})}T$ of anomalies is set to 3 K (which was the middle value in the idealised model runs).

Before we introduce the heterogeneity in surface temperatures, we obtain the sea-ice fraction $c_{\mathrm{ic}}(s_j)$ at each point of the trajectory by interpolating from the MetUM dataset (note: c_{ic} is constant with time in the dataset). We find indices

- $j_{c,0}$ — the first point where $c_{\mathrm{ic}}(p_j) < 1$ and $T_{s,\,c}(t_j)$ is rising.
- $j_{c,3}$ — the last point where $c_{\mathrm{ic}}(p_j) \gg 0$
- $j_{c,1}$ — the last point where $T_{s,\,c}(t_j) < T_{s,\,c}(t_{j_{c,0}}) + \delta_{(\mathrm{h})}T$
- $j_{c,2}$ — the first point where $T_{s,\,c}(t_j) > T_{s,\,c}(t_{j_{c,1}}) - \delta_{(\mathrm{h})}T$

The surface temperature $T_{s,\,(\mathrm{h})^+}$ over the patches of positive anomaly is then defined as:

$$T_{s,\,(\mathrm{h})^+}\,(t_j) \;=\; \begin{cases} T_{s,\,c}\,(t_j) & j < j_{c,0} \\ T_{s,\,c}\,(t_j) + \dfrac{s_j - s_{j_{c,0}}}{s_{j_{c,1}} - s_{j_{c,0}}}\,\delta_{(\mathrm{h})}T & j \in \left[j_{c,0},\, j_{c,1}\right) \\ T_{s,\,c}\,(t_j) + \;\delta_{(\mathrm{h})}T & j \in \left[j_{c,1},\, j_{c,2}\right] \\ T_{s,\,c}\,(t_j) + \dfrac{s_{j_{c,3}} - s_j}{s_{j_{c,3}} - s_{j_{c,2}}}\,\delta_{(\mathrm{h})}T & j \in \left(j_{c,2},\, j_{c,3}\right] \\ T_{s,\,c}\,(t_j) & j > j_{c,3} \end{cases} \tag{6.7}$$

The similar approach is then applied in the construction of model runs based on the observational sea-ice data. The only difference is that $c_{\mathrm{ic}}(s_j)$ is derived from the observational dataset for 20 March 2013 (see 6.1.5 for description of the AMSR2 dataset).

In the modification of surface roughness, we take into account the increase in the surface roughness due to the additional drag in the MIZ (Elvidge et al., 2016). The neutral drag coefficient over a mixture of sea-ice and water is usually formulated as

$$C_{\mathrm{dn}} = (1 - c_{\mathrm{ic}})\,C_{\mathrm{d,w}} + c_{\mathrm{ic}}\,C_{\mathrm{d,ic}} + C_{\mathrm{d,f}}, \tag{6.8}$$

where $C_{\mathrm{d,w}}$ is the drag coefficient over open open water, $C_{\mathrm{d,ic}}$ is the drag coefficient over packed sea-ice and $C_{\mathrm{d,f}}$, is the form drag (Lüpkes and Birnbaum, 2005). The form drag accounts for the drag caused by large roughness elements such Shao and Yang (2008) such as edges of ice floes and other obstacles in the packed ice. Lüpkes et al. (2012)

proposed the a number of set of drag parametrization for MIZ that were extensively tested in the sea-ice exchange models (Tsamados et al., 2014). Since the distribution of ice floes sizes in the MIZ in the area of interest is not known fully, we apply the parametrization formula:

$$C_{\mathrm{d,f}} = \frac{c_e}{2\,\kappa}\left(\frac{\ln\left(h_f/z_{0,\mathrm{w}}\right)}{\ln\left(z_1/z_{0,\mathrm{w}}\right)}\right)^2 \left(1-c_{\mathrm{ic}}\right)_f^{\beta}\, c_{\mathrm{ic}}, \tag{6.9}$$

where κ is von Kármán constant, z_1 is the height at which the drag coefficient is calculated, $z_{0,\mathrm{w}}$ is the aerodynamic surface roughness over water, h_f is the parameter representing the vertical extent of ice floes, here set to 0.41 m, $c_e = 0.3$ is the parameter representing the drag exchange, and β_f is the parameter representing the floe size distribution, here set to 1 (Lüpkes et al., 2012).

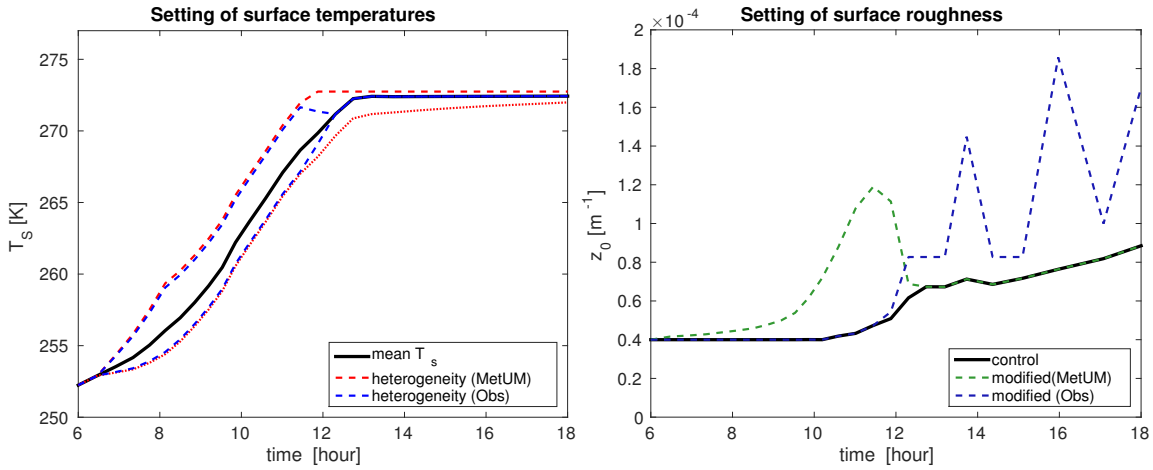

(a) (b)

Figure 6.10: The setting of the surface time-dependent forcing for modified runs in the set for the parcel sl-2.

Since the LEM does not allow to insert drag coefficients directly, we need to express the increase in drag as an updated aerodynamic surface roughness length. We reclaim that in the neutral stratification, the relation between the drag coefficeint and the surface roughness yields (Stull, 1988):

$$C_{\mathrm{dn}} = \kappa^2 \left(\ln\left(z_1/z_0\right)\right)^{-2}, \tag{6.10}$$

where we combine this equation with (6.8) and (6.9). After a number of simple algebraic

operations, we obtain the explicit formula for the updated value of z_0:

$$\widetilde{z_0} = z_1 \exp\left(\frac{-\ln\left(\frac{z_1}{z_{0,\mathrm{ic}}}\right)\ln\left(\frac{z_1}{z_{0,\mathrm{w}}}\right)}{\sqrt{(1-c_{\mathrm{ic}})\left(\ln\left(\frac{z_1}{z_{0,\mathrm{w}}}\right)\right)^2 + c_{\mathrm{ic}}\left(\ln\left(\frac{z_1}{z_{0,\mathrm{ic}}}\right)\right)^2 + \frac{c_{\mathrm{ic}}\, c_e\, (1-c_{\mathrm{ic}})^{\beta} f}{2\,\kappa}\left(\ln\left(\frac{h_f}{z_{0,\mathrm{w}}}\right)\ln\left(\frac{z_1}{z_{0,\mathrm{w}}}\right)\right)^2}} \right) \tag{6.11}$$

Since we want to maintain a smooth transitions between the MIZ and both sea-ice and open water, we set $z_{0,\mathrm{ic}}$ and $z_{0,\mathrm{w}}$ to values from MetUM forecast over the sea-ice, respectively over open water.

6.2.7 Methods for the Analysis of Airborne Data

In this part of the methodology, we briefly introduce the methods for the analysis of airborne data. Firstly, we explain the basic quality control. Secondly, we describe the eddy-covariance method for the estimation of vertical fluxes.

Core instruments on aircraft are measuring wide variety of physical properties of surrounding atmospheric environment. Some sensitive instruments get occasionally iced or otherwise compromised due to severe atmospheric conditions. Therefore, we have to pay a lot of attention to pre-processing of data, removing corrupted datapoints from timeseries. An extensive quality control of recorded time series was proposed by French et al. (2007). This process can be summarised as (Petersen and Renfrew, 2009):

- Evaluate the power spectra of the along-wind velocity component, temperature and water vapour content. In the inertial subrange, the spectra should follow a well defined power law decay slope of -5/3 with respect to the wavenumber.
- Calculate the covariances of vertical velocity and along-wind velocity, temperature and water vapour content. The linear cumulative sum should exhibit a near constant slope over the entire flight leg.
- The cospectra of the covariances should not have power at wavenumber smaller than 10^{-4} m^{-1}.

The vertical fluxes of heat and moisture in the area of flight legs are estimated by the eddy–covariance method. The flight legs are first divided into runs of a fixed length (also called "data window" in some studies (Stull, 1988)). We denote θ', q'_v, $u'_{\mathrm{E}}, u'_{\mathrm{E}}, w'$ the perturbations in the potential temperature, water vapour, and three wind components. They are calculated in each run by the standard procedure of subtracting the mean

value from recorded values . The vertical kinematic fluxes of temperature and moisture, denoted $\overline{(w'\,\theta')}$, $\overline{(w'\,q'_v)}$, are then evaluated in each run.

The choice of the length of the run and the explicit computational technique is often questioned. In the analysis of time series from ships, meteorological masts, the processing of the data often included detrended and smoothing (Moncrieff et al., 2004). However this approach is less common in airborne measurement. The choice of the length of the runs is motivated by *the need for runs to be long enough to cover several wavelengths of the turbulence but at the same time short enough to provide sampling over a homogeneous surface* (Petersen and Renfrew, 2009). Studies of the vertical fluxes over MIZ and open water often used run lengths between 9 km and 12 km. This was also applied in the study of momentum fluxes during the ACCACIA by Elvidge et al. (2016). However for flight legs in B760, a shorter runs are preferable due to the structure of the MIZ. Here we therefore divide flight legs into runs of the length 4000 m following the guidelines of Gioli et al. (2004) on aircraft-based eddy covariance fluxes.

6.3 Results

Since the previous result chapters have already examined the impact of different types of surface heterogeneity under diverse atmospheric conditions, the main aim of this chapter was to expand the scope of the study to an observed CAO scenario. Instead of repeating step by step the description of model results presented in Chapter 4, this chapter would rather focus on the overall effect of the heterogeneous surface forcing and new findings that differ from previous results. Firstly, we compare the CBL in the controls runs for sl-1, sl-2 and sl-3. Secondly, we focus on the comparison of the impact of heterogeneous surface forcing. Finally we compare the model results with the processed airborne observations.

6.3.1 Results of Control Runs

The increase in the surface temperature over the MIZ leads to a rapid development of the CBL. The formation and the growth of the CBL is clearly shown in all three control runs. A further increase in the surface temperature then leads to a rapid warming and deepening of the CBL. By the downwind distance 50 km from the edge of ice, the ABL depth reaches the depth 550 m. Further increase in the ABL depth is then relatively slow due to higher stratification above the CBL. This stage of the CAO development also shows a gradual increase in the humidity.

The vertical structure of the lower troposphere shows that CBL consist mostly of

the well-mixed ML. The top of the CBL is occupied by a relatively strong entrainment layer. Convective rolls develop during the deepening of the CBL in all three control runs. The axis of newly formed convective rolls is pointing approximately 20° from the direction of the mean wind (see figure 6.12a). This is in a good agreement with previous studies observational and model studies on CAO that found that axis are usually pointing 15° to 20° left from the direction of the geostrophic wind (Atkinson and Zhang, 1996).

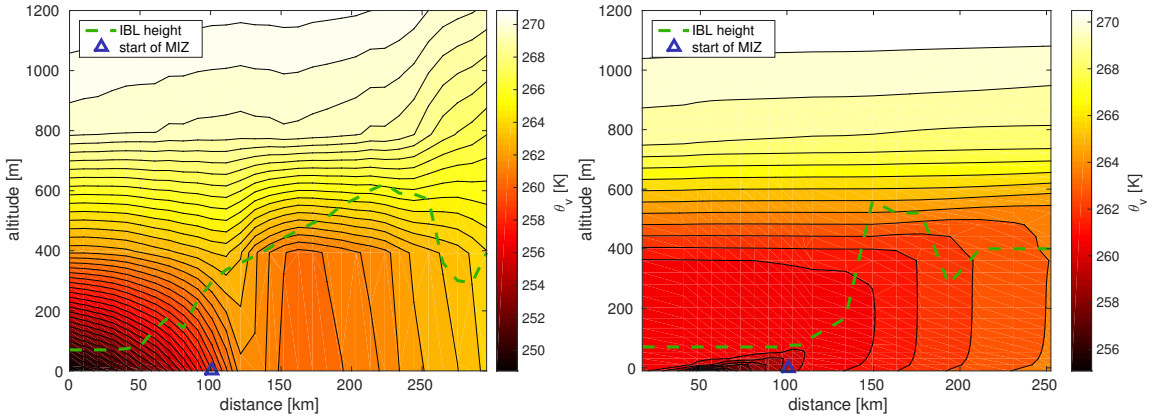

(a) In the forecast (b) In the LEM control run

Figure 6.11: The basic comparison of the virtual potential temperature in the atmospheric conditions on 21 March 2013 in the vertical slice following the parcel sl-2 between the MetUM forecast and the LEM model values. The small triangle indicates the start of the MIZ.
The comparison below 300 m is complicated by lack of output layers in the MetUM.

The comparison of the LEM with the MetUM forecast is slightly complicated by the lack of the data within the ABL. Due to the setting of MetUM grid, only a part of the lowest MetUM model level is within the CBL. Therefore, it does not provide enough data for the comparison of the vertical structure with the LEM. This also explains why most of the increase in potential temperature and humidity in the CBL is not shown in the cross-sections obtained from UM (see figure 6.11). Moreover, the forecast dataset does not include the diagnostics of the vertical transport in the ABL and the entrainment. However, the classification of the boundary layer type and the boundary layer depth generally agrees with the LEM model results.

6.3.2 Impact of the Surface Modification

Previous chapters have shown the impact of heterogeneity in surface temperatures on the development of CAO . In this part of the case chapter, we analyse the effect of surface heterogeneity in each slice of this case scenario. The main focus is on the vertical structure of the CBL and the vertical fluxes of heat and moisture. Firstly, we address possible qualitative differences between model runs. Secondly, we describe the main dif-

ferences between the runs with surface heterogeneity and the control run for each parcel trajectory. Then we compare the impact of different settings of surface heterogeneity in relative terms. This is followed by a further comparison the effect of heterogeneity in surface temperatures with the effect of the modification of the surface roughness.

All model runs show the formation and the growth of the CBL. All the modified runs in each set show warming and the deepening of the CBL that is similar to the development in the control run of the set. While the surface properties of model runs in the set vary, the model runs can differ in the distance travelled by the parcel during the model time. Although the modification of surface roughness and the surface heterogeneity affect the wind velocity, the differences in the resulting mean wind velocity are relatively small. The difference between runs with modified surface in the set and the control run does not exceed 0.15 m s^{-1}. The resulting differences in the downwind distance travelled by parcel reach maxima 740 m for runs with modified surface roughness and 600 m for runs with surface heterogeneity. While these differences are relatively small in comparison with the downwind distance travelled by parcels, it is safe to assume that model outputs from the same model time can be directly compared.

The heterogeneity in surface temperatures affect the distribution of updraughts and downdraughts in the ML (see 4.2.1). The surface fluxes of heat and moisture mostly follows the structure of surface heterogeneities. The heterogeneous surface forcing of the type 'across' and 'chessboard' lead to changes in the velocity variance. However, their effect of the structure of the CBL is otherwise relatively weak. Vertical fluxes of heat and moisture and moisture in runs with heterogeneity 'across' and 'chessboard' are slightly higher than in the control run. However these differences do not exceed 5 % percent of fluxes (see figure 6.13).

The impact of the heterogeneous surface forcing on the structure of the CBL is strongest in the case **along**. A clear organisation of updraughts is demonstrated on the cross-section of wind velocities in the middle of the ML (see figure 6.12) The pattern of surface temperatures drives the structure of growing convective rolls. Unlike in the control runs, the axis of convective rolls are parallel to the direction of the mean wind. These results are in agreement with previous studies that showed the convective rolls can be forced by surface heterogeneities (Gryschka et al., 2008). However, this organised convection does not strictly follow the pattern of surface heterogeneities. In the runs with heterogeneity type along and the block width $d_{(\mathrm{h})} = 3200$ m the convective rolls attain the similar width as in the runs with the block width $d_{(\mathrm{h})} = 1600$ m.

With the stagnation of the growth of the CBL and the thickening of the entrainment layer, the organised structure of cloud rolls mostly diminish. The axis of convective rolls veer off and attains similar direction as in the control run of each set. This stands in

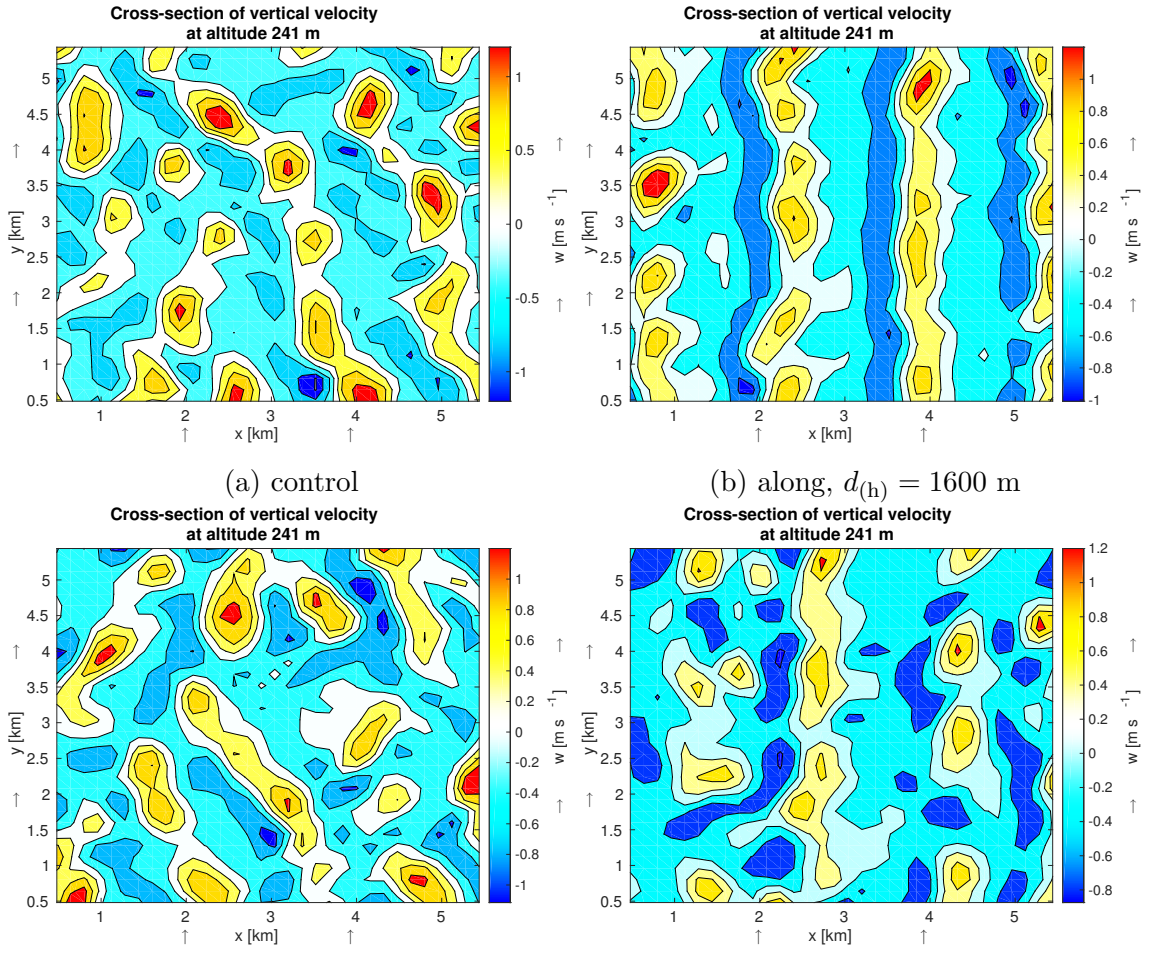

(a) control

(b) along, $d_{(\mathrm{h})} = 1600$ m

(c) across, $d_{(\mathrm{h})} = 1600$ m

(d) along, $d_{(\mathrm{h})} = 3200$ m

Figure 6.12: The comparison of roll structure between different runs with surface heterogeneity. The comparison is made for chosen runs from the set sl-3 at the downwind distance 60 km from the start of the MIZ when the ML depth reaches 500 m. Contour-plots show the vertical wind velocity at the cross-section in the middle of the ML. The arrows on sides indicate the direction of the large-scale wind.

a contrast with the findings of the chapter on idealised model runs. The organisation of rolls forced by the surface heterogeneity in idealised scenarios disappeared mostly due to the forcing of the cumuli clouds (see 4.2.1). However, in the case model run of the slice sl-3, the effect is diminished with the thickening of the entrainment layer. The results for the sl-1 and sl-2 are similar.

The runs with the modified surface roughness exhibit a similar structure of convective rolls as the control run. The modification of the surface roughness for the form drag also leads to a slight increase in vertical fluxes of heat and moisture. Nevertheless, the increase in the vertical fluxes is nearly an order of magnitude lower than in the case of runs with heterogeneity in surface temperature. The effect is stronger in the case of surface modification based on the observations of sea-ice where the MIZ is significantly longer. Still, the effect on the overall properties of the CBL is almost negligible.

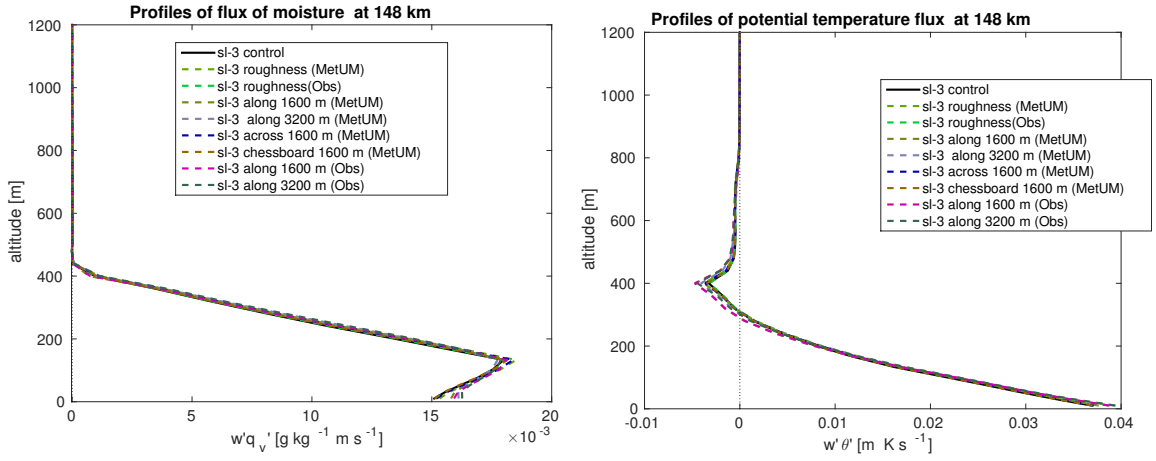

(a) (b)

Figure 6.13: The comparison of vertical fluxes between model runs in the set sl-3. The kinematic flux of temperature and the kinematic flux of moisture are evaluated approximately 60 km from the start of MIZ (148 km from the run initial point)

In summary, the impact of the modification of surface properties in the case scenario is limited. The effect of adding heterogeneous surface forcing in surface temperatures is generally stronger then the effect of adding the form drag. The heterogeneity of the surface temperatures of the type across and chessboard affect the spatial distribution of surface fluxes, however they do not show any significant impact on the structure of the ML. On the other hand, heterogeneity of the type 'along' drives the formation of forced convective rolls. However the effect of this surface forcing is later diminished.

6.3.3 Comparison with Airborne Measurements

An important part of the evaluation of the case is the comparison of model results with the airborne observations. Firstly, we briefly describe the values of thermodynamic variables observed in flight legs. Secondly, vertical fluxes of heat and moisture estimated from the airborne data and compare them with the vertical fluxes in model runs. Finally, we asses the spread in values both in the model and airborne data.

The FAAM airborne measurement show the changing structure in the lower troposphere above the MIZ. The timeseries of thermodynamic variables obtained from legs 7 and 8 exhibit an increase in the dew point temperature and the absolute temperatures in the areas further from the ice edge (see figures 6.3a and 6.3b). This is consistent with the increase of the temperature and the humidity in the CBL predicted by model runs.

However, there are significant difference between the leg 9 (altitude $\approx$ 300 m) and model results. The series of potential temperature and humidity show relatively small

changes along the flight leg. There is no indication of a propagating boundary layer. Although the MetUM forecast and the LEM runs show that the intersection of the flight leg 9 with the sl-2 should be at least 150 m bellow the top of the top of the CBL (see figure 6.7b), this is not indicated in the observational data. The observational data suggest that the flight leg 9 was above the CBL and therefore that models overestimate the growth of the CBL.

The turbulent measurements from the airborne instruments were processed to estimate the vertical fluxes of heat and moisture. There is a relatively high spread in fluxes from airborne measurements, particularly in the area over over the middle of the MIZ. In this area, there are also significant differences between the neighbouring runs. The modelled vertical fluxes of the intersection of sl-2 with flight legs are generally higher than the fluxes estimated from airborne data. This particularly applies to $\overline{w'\theta'}$, the vertical kinematic heat flux of temperature (see figure 6.14). The estimated fluxes in leg 7 at the intersection with the sl-2 are close to 0, followed by an increase in fluxes further south (i.e. downwind). The values in fluxes on the intersection with sl-3 generally agrees. This would again suggest that the ML propagates through the flight leg further south. The estimated fluxes in leg 8 show negative values at the intersection with sl-2. This indicates the presence of the entrainment layer, however at altitude that is 250 m lower than in model runs.

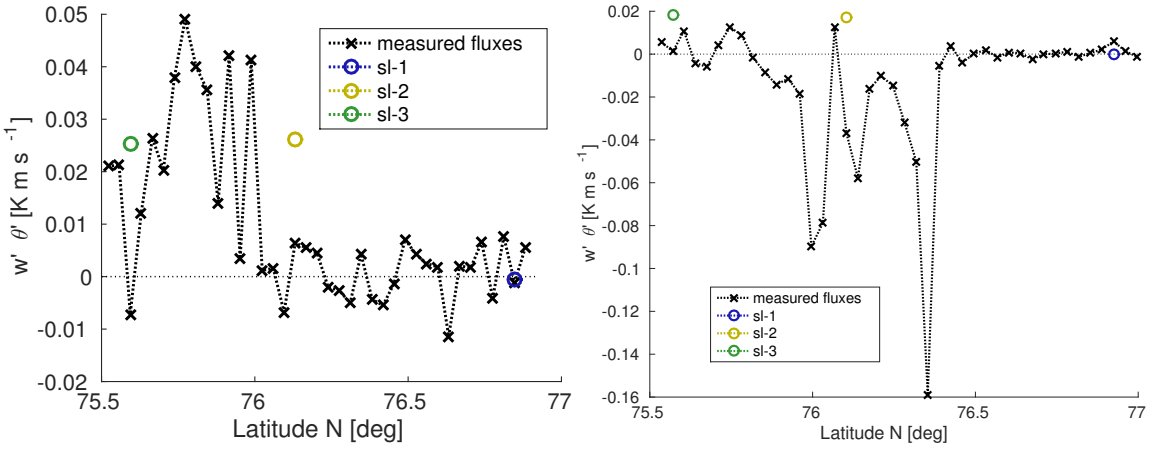

(a) leg 7 (b) leg 8

Figure 6.14: The comparison of vertical fluxes between model runs in the set sl-3. The kinematic flux of temperature and the kinematic flux of moisture are evaluated approximately 60 km from the start of MIZ (148 km from the run initial point)

To account for the variability in the boundary layer caused by the uncertainty in surface heterogeneity in roughness, we evaluate the sub-mesoscale variability in model runs (see 3.4.4). Only the sl-2 and sl-3 sets are included in this part of the analysis since the model runs in sl-1 are not yet at the fully-resolved regime (see 6.2 and 2.3.1) on the intersection of sl-1 with flight legs. The subdomain sets of the whole ensemble set are

then compared with the estimated fluxes from flight legs. The comparison reveals that spread min–max envelope of the whole ensemble set sl-2 is relatively low and does not cover the fluxes estimated from airborne data. As figures 6.15 show, the vertical kinematic heat flux is outside of the min–max envelope of the set sl–2. Since the envelopes of the subdomains in the ensemble set does not cover the estimated fluxes, it is shown that values of estimated fluxes cannot be explained by the modified surface conditions nor the sub-mesoscale variability.

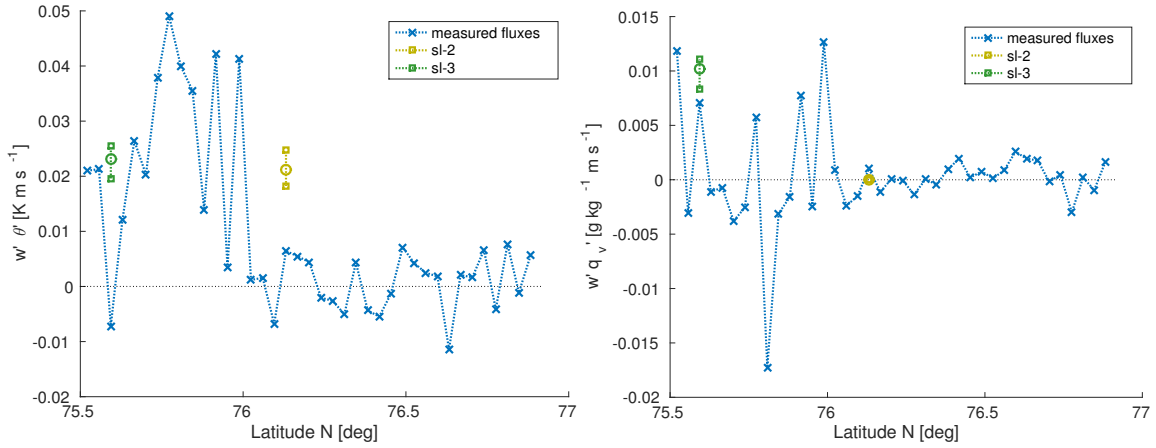

(a) kinematic flux of potential temperature (b) kinematic flux of water vapour

Figure 6.15: The comparison of vertical fluxes in the flight leg 7 with the model ensemble sets. The model data show the min–max envelope of the whole ensemble sets for the sub-mesoscale variations in the vertical fluxes.

In summary, the comparison of model runs with the airborne data showed differences in the boundary layer depth in the area of interest. Both model and observational data show a growing CBL, however they disagree on the growth of the boundary layer downwind. Since the spread in the flux values between the model runs with modified surface conditions does not cover the fluxes from observations, the difference between the airborne observations and models cannot be explained by the heterogeneity in surface temperature in MIZ nor by the increase in surface roughness. This further implies that the difference is caused by some other part of the model conditions.

6.4 Conclusions

In this case study, we have investigated the possible impact of the surface conditions within the MIZ on the developing CAO observed on 21 March 2016 during the ACCACIA field campaign. The novelty of this study lies in the construction of the ensemble set of runs with modified surface conditions — heterogeneity in surface temperature and the increased surface roughness. This approach is applied to three different starting

positions to account for the mesoscale variability in conditions within the CAO. The setting of the scenario is based on the NWP regional forecast performed by MetUM and the observations of sea-ice cover. Results of model runs are further compared with the airborne observations from the FAAM aircraft.

The growth of the CBL in the LEM model runs generally agree with the MetUM forecast. However the comparison of model results with airborne data shows that the model runs overestimate the boundary layer depth over the MIZ. While the vertical fluxes of heat and moisture further downwind generally agree, it is indicated that the boundary layer growth in the model is overestimated. This difference between the airborne observations and models cannot be explained by the mild heterogeneity in surface temperature in MIZ nor by the increase in surface roughness (see 6.3.3). However we do not have sufficient data to say which part of the MetUM surface conditions is responsible for this difference.

Furthermore, there is much higher spread in the vertical fluxes of heat and moisture in the aircraft measurements than in the in the model results. The values of $\overline{(w'\,\theta')}$, $\overline{(w'\,q'_v)}$ estimated by the eddy-covariance method (6.2.7) show particularly high spread in values over the MIZ. The sub-mesoscale variability in fluxes estimated from model results was significantly smaller. This applied even when the spread in each ensemble set was considered. These results imply that there was another factor influencing the variability in the vertical transport over the MIZ which was not accounted for in the setting of our ensemble spread.

If we consider the CAO scenario defined by the MetUM forecast without the airborne data, we can draw further conclusions about the impact of the heterogeneities in surface temperatures. The heterogeneity in surface temperatures alters the structure of developing convective rolls. While the axis of growing convective rolls in the control run are pointing approximately 20° from the mean wind direction, the convective rolls in the case of heterogeneity along generally follow the direction of heterogeneities (6.3.2). This agree both with the previous studies (Gryschka et al., 2008) and the results of idealised model scenarios (4.2.1).

The impact of heterogeneity on the structure of convective rolls is diminishing downwind with the thickening of the entrainment layer. This stands in contrast with the findings of the chapter on idealised model runs. The organisation of rolls forced by the surface heterogeneity in idealised scenarios disappeared mostly due to the forcing of the cumuli clouds. In this case study, the effect of heterogeneity diminished in the presence of stronger winds above the CBL and strong entrainment. This generally agrees with finding of Sühring et al. (2014) and Mahrt (2000).

The anomalies in surface temperature oriented along the direction of the mean wind lead to the increase in vertical fluxes of heat and moisture (6.3.2). However this increase does not exceed 5 % within the mixed layer. Still, this effect is usually an order of magnitude higher than the increase in vertical fluxes due increased surface roughness over surface heterogeneity. The influence of heterogeneity in surface temperature in the resulting vertical transport of heat and moisture in the CBL are generally lower than in the idealised model scenarios. This suggest that the additional forcing generally decrease the effect of the heterogeneity.

Chapter 7

Conclusions

This thesis has analysed the variability within the cold air outbreaks (CAO). The main focus was on the impact of heterogeneous surface temperatures on the developing convective boundary layer (CBL) in a cold air outbreak (CAO). The study then aimed to investigate the structure of the convective boundary layer and provide implications for the boundary layer parametrization schemes. Therefore, the thesis focused on the analysis of vertical fluxes of heat, moisture and momentum, as well as on the variation in their values. The main research questions of this thesis (stated in 1.4) were:

- Does a local structure of the marginal sea-ice zone (MIZ) plays a significant role in the developing CBL during a CAO event?
- Does a heterogeneity introduce more variability in the behaviour of the CBL?
- What is the impact of modifying the properties of the heterogeneous surface and the troposphere?
  Where the properties of the heterogeneous surface were:
  - the **temperature scale** - difference between the anomalies and the mean values,
  - the spatial **size** of the pattern;

  and the modified properties of the troposphere were:
  - wind forcing in the lower troposphere,
  - initial stratification in the lower troposphere.

The main novelty of this thesis lies in:

- Firstly, introducing three different patterns of heterogeneity in surface temperature to represent the surface conditions in MIZ;

- Secondly, investigating both the spatial and temporal variability in the developing CBL.

This chapter is first going to summarise the chapters of the thesis (7.1) and subsequently address these main questions (7.2). Then it will explain the implications for the parametrization of CBL (7.3). Part 7.4 will present known caveats of the study. There are also ways how to further extend the findings of this thesis. The unfinished research tasks and suggestion for new research directions are discussed in part 7.5.

7.1 Summary of Chapters

The Chapter 1 explained the motivation behind this study. Firstly, it introduced the topic of importance of parametrizing small-scale processes and parametrizing the underlying variability in weather. Secondly, it explained the significance of the phenomenon of cold-air outbreak and justified. The chapter further narrowed the topic on the study of the impact of the spatial heterogeneity in surface temperature. This was followed by the overview of thesis aims and the introduction to the methodology.

Chapter 2 focused exclusively on the theory behind the modelling software employed - The Met Office Large Eddy Model. Firstly, it explained the choice of LEM for this study. Secondly, it described the main dynamical core of the model. Then it the specific parts of the theory that were particularly relevant with respect to this study.

The methodology was presented in Chapter 3. Firstly, it provided the overview of model setting. Secondly, it described the main properties of the model scenario and justified the applicability of the model framework. Thirdly, it introduced the spatial heterogeneity in surface temperatures. The rest of the chapter then dealt with the methods for the analysis of the model output.

The first result chapter, Chapter 4 focused on the analysis of variability in a control scenario. It has demonstrated that the surface temperature heterogeneities plays an important role in the formation of convective rolls and cloud streets. Overall, the heterogeneous surface conditions modify the properties of the atmospheric boundary layer. These results stand in a good agreement with many other studies such as (Kang et al., 2007), (Maronga et al., 2014) or (Beyrich and Mengelkamp, 2006). The impact of heterogenities on the variability of the convective boundary layer was compared against the control set and the conclusion were drawn about the impact of the heterogeneous forcing on both spatial and temporal variability.

The chapter has further addressed the impact of modifying the temperature scale and

the size of the heterogeneity. It has shown how changing of the size of the heterogeneous pattern leads to slightly different effect for each type of the heterogeneous pattern. The chapter has also investigated the impact of a heterogeneity that was diminishing with time. It was shown that the impacts of heterogeneity persists beyond the removal of the heterogeneity, diminishing slowly over time.

The second result chapter, Chapter 5 , then extended the scope of the study on idealised scenarios with a different setting of the wind shear and the initial temperature profile in the lower troposphere. The model results have shown a clear differences between *two stratification regimes* — the weaker stratification that permits the development of cumulus layer and the stronger stratification that leads to boundary layer that remains clear or topped with stratocumuli clouds.

In case of weaker stratification, a thick cumulus layer develops. It was demonstrated that the formation of active cumuli cores then leads to an increase in the turbulent kinetic energy. This *top-driven forcing contributes to the decline* in the impact of the surface forcing. The effects of all three types of heterogeneities are then limited to an increased values in the surface latent heat flux. These values generally do not differ between the scenarios with different wind forcing. In the regime of stronger stratification that inhibits formation of cumuli clouds, the effect of surface heterogeneities on the structure of boundary layer is mostly maintained. The effect was particularly strong for the heterogeneity type where temperature anomalies are oriented along the winds. In this case, stripes of temperature anomalies drive the formation of distinctive forced cloud rolls.

Chapter 6, based on case studies, analysed a weak cold-air outbreak that was observed during the ACCACIA field campaign on 21 March 2013. It has shown that the heterogeneous forcing in the MIZ would lead to differences in a developing convective boundary layer. The further comparison with airborne observations showed that there is generally higher variability in observed fluxes than in the model. The comparison with model ensemble implied that this variability in observed fluxes could not be explained by heterogeneities up to 3 km in the MIZ or by increased surface roughness.

7.2 Main Conclusions

In this section, we directly address the main research question of the thesis.

Does a local structure of the marginal sea-ice zone (MIZ) plays a significant role in the developing CBL during a CAO event?
True, introducing heterogeneous surface forcing in surface temperature affect the development of the convective boundary layer. The impact depends on the type of the heterogeneity that was introduced (see 4.2.1). This was further demonstrated in scenarios with a different setting of the properties of a lower troposphere.

Does a heterogeneity introduce more variability in the behaviour of the CBL?
Inconclusive. The heterogeneous surface forcing has slightly increased the spatial variability on a sub-mesoscale. However these differences were not deemed significant.
Vertical fluxes of the latent heat have shown higher temporary oscillation for the heterogeneity of the type 'across'. Further analysis of timeseries than revealed that in case of latent heat flux, these oscillations exhibit stronger autocorrelation than for other types of the heterogeneities. However differences in the sensible heat flux did not exhibit a clear trend.

What is the impact of modifying the properties of the heterogeneous surface and the troposphere?
One of the most influential factors is the **initial stratification**. An increase in the initial stratification can qualitatively alter the effect of the surface heterogeneous forcing. As was already stressed in 7.1, model results have shown a clear differences between *two stratification regimes*. In a stronger stratification that inhibits formation of cumuli clouds, the effect of surface heterogeneities on the structure of boundary layer is mostly maintained. The differences in the values of surface fluxes of latent heat usually stay constant.

The weaker stratification that permits the development of cumulus layer lead into a reduction in the effect of heterogeneity within 1 hour after the development of active cumuli cores.

The effect of a weaker **wind forcing** allowed to propagate the pattern of heterogeneities higher up into the atmosphere. The effect of a stronger wind forcing was dependent was on the combination of the type of heterogeneity and a stratification of the lower troposphere. In a stronger stratification, an increase in the wind velocity decreased the effect of the heterogeneity of types 'across' and 'chessboard'. In the weaker initial stratification, the increase in the wind forcing increased the effect of heterogeneities 'along',

Increasing the **temperature scale** of the heterogeneity generally lead to a stronger effect of the heterogeneity. This effect was consistent amongst all three heterogeneous patters examined. However, even a relatively high temperature difference of $\delta_{(\mathrm{h})}T = 7\,\mathrm{K}$ was not sufficient to overcome the effect of wind and the entrainment. This particularly applies for the heterogeneity of the type 'across' and 'chessboard'.

Decreasing the spatial **size** of the pattern generally lead to a faster development of a convective boundary layer. However, the subsequent growth was usually slower. The effect of the increased size of the heterogeneity lead to some qualitative changes, that were explained in 4.2.3 and 5.4.2. In case of the heterogeneity type with the stripes along the mean wind direction, pattern of the size $d_{(\mathrm{h})} = 3200\,\mathrm{m}$ not only forced the formation of cloud streets along the mean wind, but also maintained the organisation of cloud streets along the mean wind. This agrees with the findings of some other studies that there is no blending height for larger scale heterogeneities (Sühring and Raasch, 2013).

7.3 Implication for Parametrization

The improvements in the parametrization in NWP have been one of the main motivations behind this study (1.1). While the previous section summarised the general findings of this study, this section focuses on the findings that bears direct implications for the parametrization schemes.

The analysis of updraught has revealed that the distribution of vertical velocities in the convective boundary layer is generally skewed towards negative values. The approximation of wind velocities by normal distribution results might often result into an incorrect estimation of the kinetic energy of updraughts (4.1.2). That bears some unfortunate implications for eddy-diffusivity mass-flux (EDMF) schemes (Huang et al., 2013) implemented in a number of meteorological models including ECMWF IFS (Watson et al., 2015). The analysis of updraught showed that the assumption of normal distribution in vertical velocities might lead to a bias in the kinetic energy of updraughts.

Furthermore, figure 4.12 showed the bias in the values of estimated updraughts changes with the altitude. The numerical results in this study suggest that the lowest bias would be achieved for EDMF scheme initiated over the top of surface layer at 135–170 m. These results is generally not affected by size or the temperature scale of the heterogeneity. Similar estimation was performed also for runs with modified wind forcing and initial stratification in the lower troposphere, but generally lead to similar results.

These results pose some concerns for the representation of the effect of CAO in currently used EDMF schemes. Even if the surface parametrization in a forecast model is well calibrated, E_w in EDMF scheme would be underestimated or overestimated based on the altitude of the model level where EDMF algorithm is initiated.

The evaluation of the heat and moisture flux by strong updraught has then unveiled a clear differences between the model scenarios with modified initial stratification. In the scenarios with the stronger stratification, the ratio of the heat and moisture transport facilitated by strong updraught is significantly higher than in the runs with a weaker stratification This finding is consistent with the previous modelling study of updraughts in CBL (Hellsten et al., 2013).

Regarding cases with an increased stratification in the lower troposphere, the heterogeneities of the type 'along' (i.e. stripes of anomalies oriented along the direction of the wind) lead to a higher ratio of the heat and moisture transport by strong updraughts. This difference is mostly caused by more organised structure of strong updraughts in the absence of the additional turbulence by cumuli clouds. Ratios of the kinematic heat and moisture flux in cases with the heterogeneity of the 'along' type were in the middle part of the boundary by 10–15 % higher than in cases with other types of the heterogeneity. This suggest thay surface heterogeneity might actually require an adjustment in the parametrization schemes.

7.4 Caveats

Despite the best efforts to analyse the research questions thoughtfully and precisely, the study has also its caveats and shortcomings. This section therefore address known caveats of the study and proposes possible countermeasures.

A very limiting factor in the current set-up of LEM is the treatment of aerosols and cloud microphysics. The model of cloud microphysics in LEM has undergone very little changes since 1998 (Gray et al., 2004). The distribution of cloud water droplets follows single-moment scheme, described solely by the water mixing ratio. The distributions of hydrometeors are treated by double-moment schemes (Gray and Petch, 2004, p.17-18). Furthermore, aerosols are treated as passive aerosols only and therefore their concentrations do not interact with cloud formation.

The other limiting factor was the setting the grid resolution. Increasing the model resolution and model domain size soon encountered memory issue in a single-core computations. Due to the original purpose of the LEM, its multicore processing scripts are optimised for a specific type of Met Office computers (Gray and Petch, 2004, p.7) and

therefore relatively complicated to adjust for the computing cluster available during the study.

There were also ongoing issues with the bugs in LEM model code. Some model setting unfortunately lead to conflicts during the model compilation and often resulted in physically implausible model results. These issue were finally overcome, however lead to significant time constrains in finishing this study.

7.5 Future Work

While this study has answered a number of research questions, it has also yielded some new ones. Due to a limited time and number of technical obstacles encountered, some of the research direction were stopped half-way to new discoveries due to time constrains. While it would be nice to further continue in the exploration of this interesting topis, this part of the thesis suggest possible ways how to continue in future and extend the finding of this thesis.

The first apparent expansion of this study will be implementation of heterogeneous surface conditions in the successor software to the LEM. This will allow to investigate the impact of heterogeneity in model domains with a larger size and a higher resolution. Perhaps the second expansion of this study will be further evaluation of case model studies. The ACCACIA flight campaign provided a number of airborne observation in cold outbreak cases.

The other logical step in the expansion of this study will be an a comparison of the impact of heterogeneous surface forcing in different LES software packages. This would also allow to investigate whether LEM model with a clouds developing over surface heterogeneities are affected by the setting of the schemes for cloud microphysics.

Bibliography

Abel, S. J., and B. J. Shipway (2007). *A comparison of cloud-resolving model simulations of trade wind cumulus with aircraft observations taken during RICO*. Quarterly Journal of the Royal Meteorological Soc., **133**, pp. 781–794.

ACCACIA (2013). *The ACCACIA project website*. NCAS, accessed on 12 March 2017, `https://www.ncas.ac.uk/index.php/en/currentnews/archived-news-2013/545-aerosol-cloud-coupling-and-climate-interactions-in-the-arctic`

Agee, E. M., and S. R. Gilbert (1989). *An aircraft investigation of mesoscale convection over Lake Michigan during the 10 January 1984 cold air outbreak*. Journal of the Atmospheric Sciences, **46** (13), pp. 1877–1897.

Agee, E., and A. Gluhovsky (1999). *LES model sensitivities to domains, grids, and large-eddy timescales*. Journal of the atmospheric sciences, **56** (4), pp. 599–604.

Alexeev, V. A., I. Esau, I. V. Polyakov, S. J. Byam, and S. Sorokina (2012). *Vertical structure of recent Arctic warming from observed data and reanalysis products*. Climatic Change, **111** (2), pp. 215–239.

Allan, J.D., Williams, P.I., Najera, J., Whitehead, J.D., Flynn, M.J., Taylor, J.W., Liu, D., Darbyshire, E., Carpenter, L.J., Chance, R., and S.J. Andrews (2015). *Iodine observed in new particle formation events in the Arctic atmosphere during ACCACIA*. Atmospheric Chemistry and Physics, **15** (10), pp. 5599–5609.

Alpers, W., W. K. Wong, K.-F. Dagestad, P. W. Chan. (2012). *A northerly winter monsoon surge over the South China Sea studied by remote sensing and a numerical model*. International Journal of Remote Sensing, **33** (23), pp. 7361–7381.

Ament, F., and C. Simmer (2006). *Improved representation of land-surface heterogeneity in a non-hydrostatic numerical weather prediction model*. Boundary-layer meteorology, **121** (1), pp. 153–174.

Amidror, I. (2002). *Scattered data interpolation methods for electronic imaging systems: a survey*. Journal of Electronic Imaging. **11** (2), pp. 157–176.

Andreas, E. L. (1987). *A theory for the scalar roughness and the scalar transfer coefficients over snow and sea ice*. Boundary-Layer Meteorology, **38** (1–2), pp. 159–184.

Andren, A., Brown, A. R., Mason, P. J., Graf, J., Schumann, U., Moeng, C. H., and F. T. Nieuwstadt (1994). *Large-eddy simulation of a neutrally stratified boundary layer: A comparison of four computer codes*. Quarterly Journal of the Royal Meteorological Society, **120** (520), pp. 1457–1484.

Arakawa, A., and V. R. Lamb (1977). *Computational design of the basic dynamical processes of the UCLA general circulation model*. Methods of Computational Physics **17**. New York: Academic Press. pp. 173–265.

Arnal, M., and R. Friedrich (1992). *On the effects of spatial resolution and subgrid-scale modeling in the large eddy simulation of a recirculating flow*. In Proceedings of the Ninth GAMM-Conference on Numerical Methods in Fluid Mechanics. Vieweg+Teubner Verlag. pp. 3–13.

Atkinson, B. W., and J. W. Zhang (1996). *Mesoscale shallow convection in the atmosphere*. Reviews of Geophysics, **34** (4), 403–431.

Avissar, R., and T. Schmidt (1998). *An evaluation of the scale at which ground-surface heat flux patchiness affects the convective boundary layer using large-eddy simulations.* Journal of the Atmospheric Sciences **55**, pp. 2666–2689.

Barry, R. G., M. W. Miles, M. W., Cianflone, R. C., Scharfen, G., and R. C. Schnell (1989). *Characteristics of Arctic sea ice from remote-sensing data and their relationship to atmospheric processes.* Ann. Glaciol, **12**, pp. 9–15.

Barton, N. P., Klein, S. A., and J. S. Boyle (2014). *On the Contribution of Longwave Radiation to Global Climate Model Biases in Arctic Lower Tropospheric Stability.* Journal of Climate, **27**, pp. 7250–7269.

Beare, R. J., Macvean,M. K., Holtslag, A. A. M., Cuxart, J., Esau, I., Golaz, J. C., Jimenez, M. A., Khairoutdinov, M., Kosovic, B., Lewellen, D., Lund, T. S., Lundquist, J. K., Mccabe, A., Moene, A. F., Noh, Y., Siegfried Raasch, S., Sullivan, P., (2006). *An Intercomparison of Large-Eddy Simulations of the Stable Boundary Layer.* Boundary-Layer Meteorology, Volume **118** (2), pp. 247–272.

Beljaars, A. C. M., and A. A. M. Holtslag (1991). *Flux parameterization over land surfaces for atmospheric models.* Journal of Applied Meteorology, **30** (3),pp. 327–341.

Beljaars, A. C. M.(1994). *The parametrization of surface fluxes in large-scale models under free convection.* Quarterly Journal of the Royal Meteorological Soc. **121**, pp. 255–270.

Bengtsson, L., Körnich, H., Källén, E., and G. Svensson (2011). *Large-scale dynamical response to subgrid-scale organization provided by cellular automata.* Journal of the Atmospheric Sciences, **68** (12), pp. 3132–3144.

Bengtsson, L., Steinheimer, M., Bechtold, P., and J. F. Geleyn (2013). *A stochastic parametrization for deep convection using cellular automata.* Quarterly Journal of the Royal Meteorological Soc., **139** (675), pp. 1533–1543.

Berg, L. K., and R. B. Stull (2004). *Parameterization of Joint Frequency Distributions of Potential Temperature and Water Vapor Mixing Ratio in the Daytime Convective Boundary Layer.* Journal of the Atmospheric Sciences **61** (7), pp. 813–828.

Berner, J., (2005). *Linking Nonlinearity and non-Gaussianity by the Fokker-Planck equation and the associated nonlinear stochastic model.* Journal of the Atmospheric Sciences , **62**, pp. 2098–2117.

Berner J., T. Jung and T. N. Palmer (2012). *Systematic Error Model Error: The Impact of Increased Horizontal Resolution versus Improved Stochastic and Deterministic Parameterizations.* In AGU Fall Meeting Abstracts, **1**, p. 01.

Bertoldi, G., W. P. Kustas, and J. D. Albertson. (2013) *Evaluating Source Area Contributions from Aircraft Flux Measurements Over Heterogeneous Land Using Large-Eddy Simulation.* Boundary-Layer Meteorology **147** (2), pp. 261–279.

Betts, A. K. (1976). *Modeling subcloud layer structure and interaction with a shallow cumulus layer.* Journal of the Atmospheric Sciences, **33** (12), pp. 2363–2382.

Beyrich, F., and H. Mengelkamp (2006). *Evaporation over a heterogeneous land surface: EVA_GRIPS and the LITFASS-2003 experiment: an overview.* Boundary-Layer Meteorol, **121**, pp. 5–32.

Bian, L., Y. Ma, Ch. Lu and X. Ling (2013). *The vertical structure of the atmospheric boundary layer over the central Arctic Ocean.* Acta Oceanologica Sinica, October 2013, **32** (10), pp. 34–40.

Birch, C. E., D. J. Parker, J. H. Marsham, G. M. Devine (2012). *The effect of orography and surface albedo on stratification in the summertime Saharan boundary layer: Dynamics and implications for dust transport.* Journal of Geophysical Research, **117**.

Blyth, A. M., Cooper, W. A., and J. B. Jensen (1988). *A Study of the Source of Entrained Air in Montana Cumuli.* Journal of the Atmospheric Sciences, **45** (24).

Blyth, A. M. (1993). *Entrainment in Cumulus Clouds*. Journal of applied meteorology, **32**, pp. 626–631

Bogenschutz, P. A., and S. K. Krueger (2013). *A simplified PDF parameterization of subgrid-scale clouds and turbulence for cloud-resolving models*. J. Adv. Model. Earth Syst., **5**, pp. 195–211.

Boris, J. P., F. F. Grinstein, E. S. Oran, and R. L. Kolbe (1992). *New insights into large eddy simulation*. Fluid dynamics research. **10** (4-6), pp. 199–228.

Boutle, I.A., J. E. J. Eyre, and A. P. Lock (2014). *Seamless Stratocumulus Simulation across the Turbulent Gray Zone*. Monthly Weather Review, **142**, pp. 1655–1668.

Bou-Zeid, E., C. Meneveau, and M. B. Parlange (2004). *Large-eddy simulation of neutral atmospheric boundary layer flow over heterogeneous surfaces: Blending height and effective surface roughness*. Water Resources Research, **40**, W02505,

Box, G. E. P., and Jenkins, G. (1976). *Time Series Analysis: Forecasting and Control, revisited edition*, Holden-Day.

Braam, M., J. V.-G. de Arellano, M. Górska (2011). *Boundary Layer Characteristics over Homogeneous and Heterogeneous Surfaces Simulated by MM5 and DALES*. Journal of Applied Meteorology and Climatology, **50** (6), pp. 1372–1386.

Brooks, I. M., and A. M. Fowler (2012). *An evaluation of boundary-layer depth, inversion and entrainment parameters by large-eddy simulation*. Boundary-Layer Meteorology, **142**, pp. 245–263.

Brooks, I.M., and A. M. Fowler (2007). *A new measure of entrainment zone structure*. Geophys Res Lett **34**, (L16808).

Brooks, I. M., Andreas, E. L., McFiggans, G., Anguelova, M.D., and C, O'Dowd (2011). *Primary Marine Aerosol Fluxes*. Bulletin of the American Meteorological Society, **92**, pp. 489–491.

Brown, A. R., Derbyshire, S. H., and P. J. Mason (1994). *Large-eddy simulation of stable atmospheric boundary layers with a revised stochastic subgrid model*. Quarterly Journal of the Royal Meteorological Soc., **120** (520), pp. 1485–1512.

Brown, A. R. (1999). *Large-eddy simulation and parametrization of the effects of shear on shallow cumulus convection*. Boundary-Layer Meteorology, **91** (1). pp. 65–80.

Brown, A. R. (1999). *The Sensitivity of Large-Eddy Simulations of Shallow Cumulus Convection to Resolution and Subgrid Model*. Quarterly Journal of Royal Meteorological Soc., **125**, pp. 469–482.

Brown, A. R., Cederwall, R. T., Chlond, A., Duynkerke, P. G., Golaz, J.-C., Khairoutdinov, M., Lewellen, D. C., Lock, A. P., MacVean, M. K., Moeng, C.-H., Neggers, R. A. J., Siebesma, A. P., and Stevens, B. (2002). *Large-eddy simulation of the diurnal cycle of shallow cumulus convection over land*. Quarterly Journal of the Royal Meteorological Soc., **128**, pp. 1075–1093.

Brown, A. R., Beare, R. J., Edwards, J. M., Lock, A. P., Keogh, S. J., Milton, S. F., and D. N. Walters (2008). *Upgrades to the boundary-layer scheme in the Met Office numerical weather prediction model*. Boundary-Layer Meteorology, **128**, pp. 117–132.

Brümmer, B. (1996). *Boundary-layer modification in wintertime cold-air outbreaks from the Arctic sea ice*. Boundary-Layer Meteorology **80** (1–2), pp. 109–125

Brümmer, B. (1997). *Boundary Layer Mass, Water, and Heat Budgets in Wintertime Cold-Air Outbreaks from the Arctic Sea Ice*. Monthly Weather Review, **125**, pp. 1824–1837.

Brümmer, B. (1999). *Roll and Cell Convection in Wintertime Arctic Cold-Air Outbreaks*. Journal of the Atmospheric Sciences, **56**, pp. 2613–2636.

Brümmer, B. (2002). *Temporal and spatial variability of surface fluxes over the ice edge*

zone in the northern Baltic Sea. Journal of Geophysical Research, **107**, Number C8.

Buizza, R., Milleer, M., and T. N. Palmer (1999). *Stochastic representation of model uncertainties in the ECMWF ensemble prediction system*, Quarterly Journal of the Royal Meteorological Soc., **125**, pp. 2887–2908.

Bull, J,M, and S. H. Derbyshire (1990). *Numerical solution of the surface layer equations*. Turbulence and Diffusion Note, No. 197.

Businger, J. A., Wyngaard, J. C., Izumi,Y and E. F. Bradley (1971). *Flux-Profile Relationships in the Atmospheric Surface Layer*. Journal of the Atmospheric Sciences, **28**, pp. 181–189.

Cai, X. M., M. Nasrullah, Y. Huang (2004). *Fumigation of pollutants into a growing convective boundary layer over an inhomogeneous surface: a large eddy simulation*. Atmospheric Environment, **38**, pp. 3605–3616.

Caldwell, P., and C. S. Bretherton (2009). *Large Eddy Simulation of the Diurnal Cycle in Southeast Pacific Stratocumulus*. Journal of the Atmospheric Sciences, **66** (2), pp. 432–449.

Canuto, V. M., and Y. Cheng (1997). *Determination of the Smagorinsky-Lilly constant CS*. Physics of Fluids, **9**, pp. 1368–1378.

Carper, M. A., F. Porté-Agel (2007). *Subfilter-scale Fluxes over a Surface Roughness Transition. Part I: Measured Fluxes and Energy Transfer Rates*. Boundary-Layer Meteorology, **126**, pp. 157–179.

Carper, M. A., F. Porté-Agel (2008). *Subfilter-Scale Fluxes over a Surface Roughness Transition. Part II: A priori Study of Large-Eddy Simulation Models*. Boundary-Layer Meteorology, **127**, pp. 73–95.

Carslaw, K.S., Pringle, K., Mann, G., Reddington, C., Brooks, I.M., Mulcahy, J., Young, G., Allan, J.D., Liu, D., Trembath, J. and A. Dean (2015). *Understanding the Processes Controlling Aerosol-Cloud Interactions in the Arctic Marine Boundary Layer*. In AGU Fall Meeting Abstracts.

Casella, G., and R. L. Berger (2002). *Statistical Inference. Second edition*. Duxbury, Pacific Grove

Caughey, S. J., Kitchen, M., and J. R. Leighton (1983). *Turbulence structure in convective boundary layers and implications for diffusion*. Boundary-Layer Meteorology, **25** (4), pp. 345–352.

Cha, Y.-M., H.-W. Lee, and S.-H. Lee (2011). *Impacts of the High-Resolution Sea Surface Temperature Distribution on Modeled Snowfall Formation over the Yellow Sea during a Cold-Air Outbreak*. Wea. Forecasting, **26**, pp. 487–503.

Chamorro, L. P., and F. Porté-Agel (2010). *Wind-tunnel study of surface boundary conditions for large-eddy simulation of turbulent flow past a rough-to-smooth surface transition*. Journal of Turbulence, **11**, N1.

Chapman, W. L., Welch, W. J., and Bowman, K. P. (1994). *Arctic sea ice variability: Model sensitivities and a multidecadal*. Journal of Geophysical Research, **99** (C1), pp. 919–935.

Chasnov, J. R. (1991). *Simulation of the Kolmogorov inertial subrange using an improved subgrid model*. Physics of Fluids, A3, pp. 188–200.

Chechin, D. C., C. Lüpkes, I. A. Repina and V. M. Gryanik (2013). *Idealized dry quasi 2-D mesoscale simulations of cold-air outbreaks over the marginal sea ice zone with fine and coarse resolution*. Journal of Geophysical Research: Atmospheres **118** (10), jgrd 118 (16), pp. 8787–8813.

Cheinet, S. (2003). *A Multiple Mass-Flux Parameterization for the Surface-Generated Convection. Part I: Dry Plumes*. Journal of the Atmospheric Sciences, **60** (18), pp. 2313-2327.

Cheinet, S., and A. P. Siebesma, (2009). *Variability of Local Structure Parameters in the Convective Boundary Layer*. Journal of the Atmospheric Sciences, **66**, pp. 1002–1017.

Chen, F., R. Avissar (1994). *The impact of land-surface wetness heterogeneity on mesoscale heat fluxes*. Journal of Applied Meteorology and Climatology, **33**, pp. 1323–1340

Cheng, W. Y. Y., and W. R. Cotton, (2004). *Sensitivity of a Cloud-Resolving Simulation of the Genesis of a Mesoscale Convective System to Horizontal Heterogeneities in Soil Moisture Initialization*. Journal of Hydrometeorology, **5**, pp. 934–958

Cheng, A., K.-M. Xu, and B. Stevens (2010). *Effects of Resolution on the Simulation of Boundary-layer Clouds and the Partition of Kinetic Energy to Subgrid Scales*. Journal of Advances in Modeling Earth Systems, **2**, 3.

Chasmer, L., Barr, A., Hopkinson, C., McCaughey, H., Treitz, P., Black, A., and A. Shashkov (2009). *Scaling and assessment of GPP from MODIS using a combination of airborne lidar and eddy covariance measurements over jack pine forests*. Remote Sensing of Environment, **113** (1), pp. 82–93.

Ching, J., R. Rotunno, M. LeMone, A. Martilli, B. Kosovic, P. A. Jimenez, and J. Dudhia, (2014). *Convectively Induced Secondary Circulations in Fine-Grid Mesoscale Numerical Weather Prediction Models*. Monthly Weather Review, **142**, pp. 3284–3302.

Chou, S. H., and D. Atlas (1982). *Satellite estimates of ocean-air heat fluxes during cold air outbreaks*. Monthly Weather Review, **110** (10), pp. 1434–1450.

Chou, S.-H., and M. P. Ferguson (1991). *Heat fluxes and roll circulations over the western Gulf Stream during an intense cold-air outbreak*. Boundary-Layer Meteorology, **55**, pp. 255–281.

Chou, S.-H., J. Zimmerman. (1989). *Bivariate conditional sampling of buoyancy flux during an intense cold-air outbreak*. Boundary-Layer Meteorology, **46**, pp. 93–112.

Chung, M. G., D., Nuijens, L., Stevens, B., Teixeira, J. (2011). *On the fidelity of large-eddy simulation of shallow precipitating cumulus convection* , Monthly Weather Review, **139** (9), pp. 2918–2939.

Claussen, M. (1991). *Local advection processes in the surface layer of the marginal ice zone*. Boundary-Layer Meteorology, **54** (1), pp. 1–27.

Chlond, A. (1992). *Three-dimensional simulation of cloud street development during a cold air outbreak*. Boundary Layer Meteorological, **58**, pp. 161–200.

Comiso, J. C., and A. L. Gordon, A. L. (1987). *Recurring polynyas over the Cosmonaut Sea and the Maud Rise. Journal of Geophysical Research: Oceans*, **92** (C3), pp. 2819–2833.

Cooper, K. A., Hjelmfelt, M. R., Derickson, R. G. , Kristovich, D. A. R., and N. F. Laird, (2000). *Numerical Simulation of Transitions in Boundary Layer Convective Structures in a Lake-Effect Snow Event*. Monthly Weather Review, **128**, pp. 3283–3295.

Courant, R.; Friedrichs, K.; Lewy, H. (1967). [1928]. *On the partial difference equations of mathematical physics*. IBM Journal of Research and Development, **11** (2), pp. 215–234.

Courault, D. , P. Drobinski, Y. Brunet, P. Lacarrere and C. Talbot, (2007). *Impact of surface heterogeneity on a buoyancy-driven convective boundary layer in light winds*. Boundary-Layer Meteorology, **124** (3), pp. 383-403.

Couvreux, F., F. Hourdin, and C. Rio, (2010) *Resolved versus parametrized boundary-layer plumes. Part I: A parametrization-oriented conditional sampling in large-eddy simulations*. Boundary-Layer Meteorology, **134**, pp. 441–458.

Craig, G., and H.-R. Cho (1988). *Cumulus Heating and CISK in the Extratropical Atmosphere. Part I: Polar Lows and Comma Clouds*. Journal of the Atmospheric

Sciences, **45**, pp. 2622–2640.

Craig,G. C., and B. G. Cohen (2006). *Fluctuations in an Equilibrium Convective Ensemble. Part I: Theoretical Formulation*, Journal of the Atmospheric Sciences, Volume **63** (8). pp. 1996–2004, http://ejournals.ebsco.com/direct.asp?ArticleID=47DC94807508AC271F05

Crum, T. D., Stull, R. B., and E. W. Eloranta (1987). *Coincident lidar and aircraft observations of entrainment into thermals and mixed layers*. Journal of climate and applied meteorology, **26** (7), pp. 774–788.

Crum, T. D., and R. B. Stull (1987). *Field measurements of the amount of surface layer air versus height in the entrainment zone*. Journal of the atmospheric sciences, **44** (19), pp. 2743–2753.

Cullen, M. J. P. (1993). *The unified forecast/climate model*. Meteorological Magazine, **122** (1449), pp. 81–94.

Daly, C. (1877). *English Arctic Expedition*. The North American Review, **124** (255), pp. 229–245.

Deardorff, J. W. (1971). *On the magnitude of the subgrid scale eddy coefficient*. Journal of Computational Physics, **7** (1), pp. 120–133.

Deardorff, J. W. (1974). *Three-dimensional numerical study of the height and mean structure of a heated planetary boundary layer*. Boundary-Layer Meteorology, **7** (1), pp. 81–106.

Deardorff, J. W., and G. E. Willis (1985). *Further results from a laboratory model of the convective planetary boundary layer*. Boundary-Layer Meteorology, **32** (3), pp. 205–236.

Denmead, O. T., Raupach, M. R., Dunin, F. X., Cleugh, H. A., and R. Leuning (1996). *Boundary layer budgets for regional estimates of scalar fluxes*. Global Change Biology, **2** (3), pp. 255–264.

Derbyshire, S. H. (1990). *Nieuwstadt's stable boundary layer revisited*. Quarterly Journal of the Royal Meteorological Soc., **116**, pp. 127–158.

Derbyshire, S. H. (1994). *A "balanced" approach to stable boundary layer dynamics*. Journal of the atmospheric sciences, **51** (23), pp. 3486–3504.

Derbyshire, S. H., Beau, I., Bechtold, P., Grandpeix, J.-Y., Piriou, J.-M., Redelsperger, J.-L., and P. M. M. Soares, (2004). *Sensitivity of moist convection to environmental humidity*. Quarterly Journal of the Royal Meteorological Soc., **130**, pp. 3055–3079.

Desai, A.R. , K. J. Davis, C. J. Senff, S. Ismail, E. V. Browell, D. R. Stauffer, B. P. Reen. (2006). *A Case Study on the Effects of Heterogeneous Soil Moisture on Mesoscale Boundary-Layer Structure in the Southern Great Plains, U.S.A. Part I: Simple Prognostic Model*. Boundary-Layer Meteorology, **119**, pp. 195–238.

Desjardins, R. L., MacPherson, J. I., Schuepp, P. H., and F. Karanja (1989). *An evaluation of aircraft flux measurements of CO2, water vapor and sensible heat*. In Boundary Layer Studies and Applications, Springer Netherlands. pp. 55–69.

Dörnbrack, A. (1997). *Broadening of convective cells*. Quarterly Journal of the Royal Meteorological Soc., **123**, pp. 829–847.

Dosio, A., Vilà-Guerau de Arellano, J., Holtslag, A. A., and P. J. Builtjes (2003). *Dispersion of a passive tracer in buoyancy-and shear-driven boundary layers*. Journal of Applied Meteorology, **42** (8), pp. 1116–1130.

Draper, N.R.; Smith, H. (1998). *Applied Regression Analysis* (3rd ed.). John Wiley.

Durran, D. R. (1989). *Improving the anelastic approximation*. Journal of the atmospheric sciences, **46** (11), pp. 1453-1461.

Dyer, A. J. (1974). *A review of flux-profile relationships*. Boundary-Layer Meteorology,

7 (3), pp. 363–372.

Ebner L., D. Schröder and G. Heinemann (2011). *Impact of Laptev Sea flaw polynyas on the atmospheric boundary layer and ice production using idealized mesoscale simulations*. Polar Research, 2011, **30** (0), pp. 1–16

Edwards, J. M., and Slingo, A. (1996). *Studies with a flexible new radiation code. I: Choosing a configuration for a large-scale model*. Quarterly Journal of the Royal Meteorological Soc., **122** (531), pp. 689–719.

Efimov, V. V., and D. A. Yarovaya (2014). *Numerical simulation of air convection in the atmosphere during the invasion of cold air over the Black Sea*. Izvestiya, Atmospheric and Oceanic Physics, **50** (6), pp. 610–620.

Einaudi, F., and Finnigan, J. J. (1981). *The interaction between an internal gravity wave and the planetary boundary layer. Part I: The linear analysis*. Quarterly Journal of the Royal Meteorological Soc., **107**, pp. 793–806.

Elperin, T., N. Kleeorin, I. Rogachevskii, S. S. Zilitinkevich (2006). *Tangling Turbulence and Semi-Organized Structures in Convective Boundary Layers*. Boundary-Layer Meteorology, **119**, pp. 449–472.

Elvidge, A. D., Renfrew, I. A., Weiss, A. I., Brooks, I. M., Lachlan-Cope, T. A., and J. C. King (2016). *Observations of surface momentum exchange over the marginal ice zone and recommendations for its parametrisation*. Atmospheric Chemistry and Physics, **16** (3), pp. 1545-1563.

Esau, I. N. (2007). *Amplification of turbulent exchange over wide Arctic leads: Large-eddy simulation study*. Journal of Geophysical Research, 112, D08109.

Etling, D., and Brown, R. A. (1993). *Roll vortices in the planetary boundary layer: A review*. Boundary-Layer Meteorology, **65** (3), pp. 215-248.

Facility for Airborne Atmospheric Measurements; Natural Environment Research Council; Met Office (2015). *FAAM B760 ACCACIA flight, number 2: Airborne atmospheric measurements from core and non-core instrument suites on board the BAE-146 aircraft*. NCAS British Atmospheric Data Centre, cited on 12 March 2017. `http://catalogue.ceda.ac.uk/uuid/62170082a19844f5ab5a8caec5147dc5`

Facility for Airborne Atmospheric Measurements (2017). Official website of the-Facility for Airborne Atmospheric Measurements. accessed on 12 march 2017 `http://www.faam.ac.uk/index.php/science-instruments`

Fang, Z., and J. M. Wallace (1994). *Arctic Sea Ice Variability on a Timescale of Weeks and Its Relation to Atmospheric Forcing*. Journal of Climate, 7, pp. 1897–1914.

Fedorovich, E., and R. Conzemius (2008). *Effects of wind shear on the atmospheric convective boundary layer structure and evolution*. Acta Geophysica, **56**, pp. 114–141.

Ferrier, B. S. (1994). *A double-moment multiple-phase four-class bulk ice scheme. Part I: Description*. Journal of the Atmospheric Sciences, **51** (2), pp. 249-280.

Ferrier, B. S., Tao, W. K., and Simpson, J. (1995). *A double-moment multiple-phase four-class bulk ice scheme. Part II: Simulations of convective storms in different large-scale environments and comparisons with other bulk parameterizations*. Journal of the atmospheric sciences, **52** (8), pp. 1001–1033.

Fesquet, C., S. Dupont, P. Drobinski, T. Dubos, C. Barthlott (2009). *Impact of terrain heterogeneity on coherent structure properties: numerical approach*. Boundary-Layer Meteorolology, 133, pp. 71–92

Feynman, R. P. (1965) *'The Development of the Space-Time View of Quantum Electrodynamics'*, Nobel Prize Lecture (11 Dec 1965). Collected in Stig Lundqvist, Nobel Lectures: Physics, 1963-1970

Finnigan, J. J., and Einaudi, F. (1981). *The interaction between an internal gravity wave and the planetary boundary layer. Part II: Effect of the wave on the turbulence*

structure. Quarterly Journal of the Royal Meteorological Soc., **107**, pp. 807–832.

Flatau, P.J. (1989). *The CSU-RAMS cloud microphysics module: General theory and code documentation*. Department of Atmospheric Science, Colorado State University

Fletcher, J., Mason, S., and C. Jakob (2016). *The Climatology, Meteorology, and Boundary Layer Structure of Marine Cold Air Outbreaks in Both Hemispheres*. Journal of Climate, **29** (6), pp. 1999–2014

Forbes, R. M., and M. Ahlgrimm, (2014). *On the Representation of High-Latitude Boundary Layer Mixed-Phase Cloud in the ECMWF Global Model*. Monthly Weather Review, **142**, pp. 3425–3445.

French, J. R., Drennan, W. M., Zhang, J. A., and P. G. Black (2007). *Turbulent fluxes in the hurricane boundary layer. Part I: Momentum flux*. Journal of the atmospheric sciences, **64** (4), pp. 1089–1102.

Fritts, D. C., and M. J. Alexander (2003). *Gravity wave dynamics and effects in the middle atmosphere*. Rev. Geophysical, **41** (1), 3,

Fritts, D. C., S. L. Vadas, K. Wan, and J. A. Werne (2005). *ean and variable forcing of the middle atmosphere by gravity waves*. Journal of Atmospheric and Solar-Terrestrial Physics, 2006, 68, 3-5, pp. 247-265

Gal-Chen, T. (1982). *Errors in fixed and moving frame of references: Applications for conventional and Doppler radar analysis*. Journal of the Atmospheric Sciences, **39** (10), pp. 2279–2300.

Galperin, B., Sukoriansky, S., and N. Dikovskaya (2010). *Geophysical flows with anisotropic turbulence and dispersive waves: flows with a β-effect*. Ocean Dynamics, **60** (2), pp. 427-441.

Gerbush, M. R., D. A. R. Kristovich, and N. F. Laird, (2008). *Mesoscale Boundary Layer and Heat Flux Variations over Pack Ice–Covered Lake Erie*. J. Appl. Meteorological Climatol., 47, pp. 668–682.

Gibbs J. A., and E. Fedorovich (2014). *Comparison of Convective Boundary Layer Velocity Spectra Retrieved from Large- Eddy-Simulation and Weather Research and Forecasting Model Data*. Journal of Applied Meteorology and Climatology, **53** (2),pp. 377–394.

Gibert F. , J. Cuesta, J-I. Yano, N. Arnault, P. H. Flamant. (2007) *On the Correlation between Convective Plume Updrafts and Downdrafts, Lidar Reflectivity and Depolarization Ratio*. Boundary-Layer Meteorology 125, pp. 553-573.

Gioli, B., Miglietta, F., De Martino, B., Hutjes, R. W., Dolman, H. A., Lindroth, A., Schumacher, M., Sanz, M J., Manca, G., Peressotti, A., and E. J. Dumas (2004). *Comparison between tower and aircraft-based eddy covariance fluxes in five European regions*. Agricultural and Forest Meteorology, **127** (1), pp. 1–16.

Glazunov, A. V., and V. P. Dymnikov (2013). *Spatial spectra and characteristic horizontal scales of temperature and velocity fluctuations in the convective boundary layer of the atmosphere*. Izvestiya, Atmospheric and Oceanic Physics, **49** (1), pp. 33–54.

Górska M., J. V.-G. de Arellano, M. A. LeMone and C. C. van Heerwaarden (2008). *Mean and Flux Horizontal Variability of Virtual Potential Temperature, Moisture, and Carbon Dioxide: Aircraft Observations and LES Study*. Monthly Weather Review, 2008, Volume **136** (11), pp. 4435–4451

Gossard, E., and W. Munk (1954). *On gravity waves in the atmosphere*. Journal of Meteorology, **11** (4), pp. 259–269.

Grabon, J.S., K. J. Davis, C. Kiemle andf G. Ehret (2010). *Airborne lidar observations of the transition zone between the convective boundary layer and free atmosphere during the international H2O Project(IHOP) in 2002*. Boundary-Layer Meteorol, **134**, pp. 61–83

Grachev, A. A. ,E. L Andreas, Ch. W. Fairall, P. S. Guest, P. O. G. Persson (2013). *The Critical Richardson Number and Limits of Applicability of Local Similarity Theory in the Stable Boundary Layer*. Boundary-Layer Meteorology, **147** (1), pp. 51-82

Gray, M. E. B. , A. R. Brown, A. P. Lock, J. Petch (2004). *Version 2.3 Of The Met Office Large Eddy Model: Part III. Software Documentation*, Met Office

Gray, M. E. B. , J. Petch, S. H. Derbyshire, A. R. Brown, A. P. Lock, H. A. Swann and P. R. A. Brown (2004). *Version 2.3 Of The Met Office Large Eddy Model: Part II. Scientific Documentation*, Met Office

Gray, M. E. B. , J. Petch (2004). *Version 2.3 Of The Met Office Large Eddy Model: Part I. User Documentation*, Met Office

Gregory, D., and P. R. Rowntree (1990). *A mass flux convection scheme with representation of cloud ensemble characteristics and stability-dependent closure*. Monthly Weather Review, **118** (7), pp. 1483–1506.

Grossman, R.L, and A. K. Betts, (1990). *Air–Sea Interaction during an Extreme Cold Air Outbreak from the Eastern Coast of the United States*. Monthly Weather Review, **118**, pp. 324–342.

Grossman, R. L., Yates, D., LeMone, M. A., Wesely, M. L., and J. Song (2005). *Observed effects of horizontal radiative surface temperature variations on the atmosphere over a midwest watershed during CASES 97*, Journal of Geophysical Res., **110**, D06117.

Grunwald, J.,Kalthoff, N. , Corsmeier, U., and F. Fiedler (1996). *Comparison of areally averaged turbulent fluxes over non-homogeneous terrain: results from the EFEDA-field experiment*. Boundary-Layer Meteorology, **77** (2), pp. 105-134.

Gryschka, M., and S. Raasch (2005). *Roll convection during a cold air outbreak: A large eddy simulation with stationary model domain*. Geophysical Research Letters, **32** (14), L14805,

Gryschka, M., C. Drüe, D. Etling, and S. Raasch (2008). *On the influence of sea-ice inhomogeneities onto roll convection in cold-air outbreaks*.Geophysical Research Letters, **35**, L23804,

Gryschka, M., J. Fricke, and S. Raasch (2014). *On the impact of forced roll convection on vertical turbulent transport in cold air outbreaks*. Journal of Geophysical Research: Atmospheres, **119**, 12, pp. 513–532.

Gupta, M., D. G. Barber, R. K. Scharien, and D. Isleifson (2014). *Detection and classification of surface roughness in an Arctic marginal sea ice zone*. Hydrol. Process., 28, pp. 599–609.

Hacker, J.P. (2010). *Spatial and Temporal Scales of Boundary Layer Wind Predictability in Response to Small-Amplitude Land Surface Uncertainty*. Journal of the Atmospheric Sciences, **67**, pp. 217–233.

Harten, A. (1983). *High resolution schemes for hyperbolic conservation laws*. J. Computational Physics, **49**, pp. 357–393.

Hartmann, J., Albers, F., and S. Argentini (1999). *Arctic radiation and turbulence interaction study:(artist)*. Berichte zur Polarforschung (Reports on Polar Research), 305.

He, L., V. Y. Ivanov, G. Bohrer, K. D. Maurer, C. S. Vogel, and M. Moghaddam (2014). *Effects of fine-scale soil moisture and canopy heterogeneity on energy and water fluxes in a northern temperate mixed forest*. Agricultural and Forest Meteorology, 184, pp. 243-256.

Hebeler, F., R. S. Purves and S. S. R. Jamieson (2008). *The impact of parametric uncertainty and topographic error in ice-sheet modelling*. Journal of Glaciology **54** (188), pp. 899-919.

Heerwaarden, C. C., and J. V. Guerau de Arellano, 2008: Relative Humidity as an

Indicator for Cloud Formation over Heterogeneous Land Surfaces. Journal of the Atmospheric Sciences, 65, 3263–3277.

Heinemann, G., and M. Kerschgens. (2005). *Comparison of methods for area-averaging surface energy fluxes over heterogeneous land surfaces using high-resolution non-hydrostatic simulations*. International Journal of Climatology, 25, pp. 379–403.

Heerwaarden, C. C. v., J. P. Mellado, and A. De Lozar, (2014) *Scaling Laws for the Heterogeneously Heated Free Convective Boundary Layer*. Journal of the Atmospheric Sciences, 71, pp. 3975–4000.

Hellsten, A., and S. Zilitinkevich (2013). *Role of convective structures and background turbulence in the dry convective boundary layer*. Boundary-Layer Meteorology, 149, pp. 323–353.

Hintz, M., S. Lennartz-Sassinek, S. Liu, and Y. Shao (2014). *Quantification of land-surface heterogeneity via entropy spectrum method*. Journal of Geophysical Research Atmos., 119, pp. 8764–8777.

Holdaway, D., Thuburn, J., and Wood, N. (2013). *Comparison of Lorenz and Charney–Phillips vertical discretisations for dynamics–boundary layer coupling*. Part I: Steady states. Quarterly Journal of the Royal Meteorological Soc., 139: 1073–1086.

Holland, P. R., N. Bruneau, C. Enright, M. Losch, N. T. Kurtz, and R. Kwok (2014). *Modeled Trends in Antarctic Sea Ice Thickness*. Journal of Climate, 27, pp. 3784–3801.

Holloway, G., and T. Sou (2002): *Has Arctic Sea Ice Rapidly Thinned?*. Journal of Climate, 15, pp. 1691–1701.

Holtslag, A. A. M., and H. A. R. De Bruin (1988). *Applied modeling of the nighttime surface energy balance over land*. Journal of Applied Meteorology, **27** (6), pp. 689–704.

Holtslag, A. A. M., and C.-H. Moeng (1991). *Eddy diffusivity and countergradient transport in the convective atmospheric boundary layer*. Journal of the Atmospheric Sciences ,**48**, pp. 1690–1698.

Jiang, H., and W. R. Cotton, (2000). *Large Eddy Simulation of Shallow Cumulus Convection during BOMEX: Sensitivity to Microphysics and Radiation*. Journal of the Atmospheric Sciences, 57, pp. 582–594.

Hollinger, D. Y., and A. D. Richardson (2005). *Uncertainty in eddy covariance measurements and its application to physiological models*. Tree physiology, **25** (7), pp. 873–885.

Holton, J. R., and G. J. Hakim (2012). *An introduction to dynamic meteorology*. (88). Academic press.

Hosannah, N., and E. G. Jorge (2014). *Impacts of Aerosol Particle Size Distribution and Land Cover Land Use on Precipitation in a Coastal Urban Environment Using a Cloud-Resolving Mesoscale Model*. Advances in Meteorology

Huang, H.-Y., and S. A.Margulis (2013). *Impact of soil moisture heterogeneity length scale and gradients on daytime coupled land-cloudy boundary layer interactions*. Hydrological Processes, 27: pp. 1988–2003.

Huang, Q. , J. H. Marsham, D. J. Parker, W. Tian and C. M. Grams (2010). *Simulations of the effects of surface heat flux anomalies on stratification, convective growth, and vertical transport within the Saharan boundary layer*. Journal of Geophysical Research 115.

Huang, H.-Y., A. Hall, and J. Teixeira (2013). *Evaluation of the WRF PBL Parameterizations for Marine Boundary Layer Clouds: Cumulus and Stratocumulus*. Monthly Weather Review, 141, pp. 2265–2271

Hudson, R. D. (1987). *Multiyear sea ice floe distribution in the Canadian Arctic Ocean*. Journal of Geophysical Research: Oceans, **92** (C13), pp. 14663-14669.

Hunt, J. C. R. (1988). *Length scales in stably stratified turbulent flows and their use in*

turbulence models. Stably stratified flow and dense gas dispersion, pp. 285–321.

Hunt, J.C.R, G.J. Shutts, and S.H. Derbyshire (1996) *Stably stratified flows in meteorology*. Dynamics of Atmospheres and Oceans **23** (1-4), pp. 63–79.

IFS Documentation – Cy40r1, Operational implementation 22 November 2013, Part IV: Physical Processes, retrieved on 29 January 2014 from `http://old.ecmwf.int/research/ifsdocs/CY40r1/`

IFS Documentation – Cy40r1, Operational implementation 22 November 2013, Part V: Ensemble Prediction System, retrieved on 29 January 2014 from `http://old.ecmwf.int/research/ifsdocs/CY40r1/`

Inoue, J., Ono, J., Tachibana, Y., Honda, M., Iwamoto, K., Fujiyoshi, Y., and K. Takeuchi (2003) *Characteristics of Heat Transfer over the Ice-Covered Sea of Okhotsk During Cold Air Outbreaks*. J. Meteorol. Soc. Japan, 8110571067

Inoue, J., M. Wakatsuchi and Y. Fujiyoshi (2004). *Ice floe distribution in the Sea of Okhotsk in the period when sea-ice extent is advancing*. Geophysical Research Letters, 2004, **31** (20), l20303, pp. 1–4

Inoue, J., M. Kawashima, Y. Fujiyoshi and M. Yoshizaki (2005). *Aircraft observations of air-mass modification upstream of the Sea of Japan during cold-air outbreaks*. Journal of the Meteorological Soc. of Japan. Ser. II, **83** (2), pp. 189–200.

Inoue, J., M. Kawashima, Y. Fujiyoshi and M. Wakatsuchi (2005). *Aircraft Observations of Air-mass Modification Over the Sea of Okhotsk during Sea-ice Growth*. Boundary-Layer Meteorology, **117** (1), pp. 111–129.

Inoue, M., Matheou, G., and J. Teixeira (2014). *LES of a Spatially Developing Atmospheric Boundary Layer: Application of a Fringe Method for the Stratocumulus to Shallow Cumulus Cloud Transition*. Monthly Weather Review **142** (9), pp. 3418–3424.

Jacobitz,F. G., Rogers, M. M., and J. H. Ferziger (2005). *Waves in stably stratified turbulent flow*. Journal of Turbulence, **6**, N32.

Jiménez, M. A., and J. CUXART (2006). *Study of the Probability Density Functions From a Large-Eddy Simulation for a Stably Stratified Boundary Layer*. Boundary-Layer Meteorology **118** (2), pp. 401–420.

Johnson, R. H. (1978). *Characteristic Structure and Growth of the Nonprecipitating Cumulus Layer over South Florida*. Monthly Weather Review, 106, pp. 1495–1504.

Johnson, D. (1997). *The triangular distribution as a proxy for the beta distribution in risk analysis*. Journal of the Royal Statistical Society: Series D (The Statistician), **46** (3), pp. 387–398.

Kanak, K. M., Lilly, D. K., and J. T. Snow (2000). *The formation of vertical vortices in the convective boundary layer. Quarterly Journal of the Royal Meteorological Soc.*. **126** (569), pp. 2789–2810.

Kang, S. L.,K. J. Davis and M. LeMone (2007). *Observations of the ABL structures over a heterogeneous land surface during IHOP_2002*. J Hydrometeorology. **8**, pp. 221–244.

Kang, S. L., and K. J. Davis (2008). *The effects of mesoscale surface heterogeneity on the fair-weather convective atmospheric boundary layer*. Journal of the Atmospheric Sciences, **65**, pp.3197–3213

Kang, S-L. (2009) *Temporal Oscillations in the Convective Boundary Layer Forced by Mesoscale Surface Heat-Flux Variations*. Boundary-Layer Meteorology, **132**, 59-81.

Kang, S.-L., and G. H. Bryan (2011.) *A Large-Eddy Simulation Study of Moist Convection Initiation over Heterogeneous Surface Fluxes*. Monthly Weather Review **139**:9, pp. 2901-2917.

Kang, S-L., and D. H. Lenschow (2014). *Temporal Evolution of Low-Level Winds Induced by Two-dimensional Mesoscale Surface Heat-Flux Heterogeneity*. Boundary-Layer

Meteorology, **151**, pp. 501–529.

Kang, S-L., J-H. Ryu (2016). *Response of moist convection to multi-scale surface flux heterogeneity*. Quarterly Journal of the Royal Meteorological Soc., **142** (698), pp. 2180–2193.

Kerman, B.R. (1974). *An energy budget for waves and turbulence within an inversion*. Boundary-Layer Meteorology **6** (3-4), pp. 443–458.

Kershaw, R. (1995). *Parametrization of momentum transport by convectively generated gravity*, Quarterly Journal of the Royal Meteorological Soc. , **121**, pp. 1023–1040.

Khairoutdinov, M. F., Krueger, S. K., Moeng, C. H., Bogenschutz, P. A., and D. A. Randall (2009). *Large-eddy simulation of maritime deep tropical convection*. Journal of Advances in Modeling Earth Systems, **1** (4).

Kilpeläinen, T. , T. Vihma, M. Manninen, A. Sjöblom, E. Jakobson, T. Palo and M. Maturilli (2012). *Modelling the vertical structure of the atmospheric boundary layer over Arctic fjords in Svalbard*. Quarterly Journal of the Royal Meteorological Soc., **138** (668), pp. 1867–1883.

Kilpeläinen, T., and A. Sjöblom (2010). *Momentum and Sensible Heat Exchange in an Ice-Free Arctic Fjord*. Boundary-Layer Meteorology. **134** (1), pp. 109–130.

Kirkil G, Mirocha JD, Chow FK, Bou-Zeid E (2012). *Implementation and evaluation of dynamic subfilter-scale stress models for large-eddy simulation using WRF*. Mon Weather Rev 140:266—28

Klaassen, G. P., and T. L. Clark (1985). *Dynamics of the cloud-environment interface and entrainment in small cumuli: Two-dimensional simulations in the absence of ambient shear*. Journal of the atmospheric sciences, **42** (23), pp. 2621–2642.

Klein, S. A., McCoy, R. B., Morrison, H., Ackerman, A. S., Avramov, A., Boer, G. d., Chen, M., Cole, J. N. S., Del Genio, A. D., Falk, M., Foster, M. J., Fridlind, A., Golaz, J.-C., Hashino, T., Harrington, J. Y., Hoose, C., Khairoutdinov, M. F., Larson, V. E., Liu, X., Luo, Y., McFarquhar, G. M., Menon, S., Neggers, R. A. J., Park, S., Poellot, M. R., Schmidt, J. M., Sednev, I., Shipway, B. J., Shupe, M. D., Spangenberg, D. A., Sud, Y. C., Turner, D. D., Veron, D. E., Salzen, K. v., Walker, G. K., Wang, Z., Wolf, A. B., Xie, S., Xu, K.-M., Yang, F., and G. Zhang (2009). *Intercomparison of model simulations of mixed-phase clouds observed during the ARM Mixed-Phase Arctic Cloud Experiment. I: single-layer cloud*. Quarterly Journal of the Royal Meteorological Soc., 135, pp. 979–1002.

Köhler, M., Ahlgrimm, M., and A. Beljaars (2011). *Unified treatment of dry convective stratocumulus-topped boundary layers in the ECMWF model*. Quarterly Journal of the Royal Meteorological Soc., **137**, pp. 43–57.

Kosovic, B., and J. A. Curry (2000). *A large eddy simulation study of a quasi-steady, stably stratified atmospheric boundary layer*. Journal of the atmospheric sciences, **57** (8), pp. 1052–1068.

Kottmeier, C., and R. Hartig (1990). *Winter observations of the atmosphere over Antarctic sea ice*. Journal of Geophysical Res.,**95** (D10), pp. 16551–16560.

Krasnopolsky, V. M. , M. S. Fox-rabinovitz , A. A. Belochitski (2013). *Using Ensemble of Neural Networks to Learn Stochastic Convection Parameterizations for Climate and Numerical Weather Prediction Models from Data Simulated by a Cloud Resolving Model*. Advances in Artificial Neural Systems, (2013), 5.

Kristovich, D. A. (1993). *Mean circulations of boundary-layer rolls in lake-effect snow storms*. Boundary-Layer Meteorology, **63** (3), pp. 293–315.

Kure, S., Kavvas, M. L., Ohara, N., and Jang, S. (2010). *Upscaling of coupled land surface process modeling for heterogeneous landscapes: Stochastic approach*. Journal of Hydrologic Engineering, 16(12), pp. 1017–1029.

Kwok, R. (2014). *Declassified high-resolution visible imagery for Arctic sea ice investigations: An overview*. Remote Sensing of Environment, **142**, pp. 44–56.

Lane, T. P., and M. W. Moncrieff (2010). *Characterization of Momentum Transport Associated with Organized Moist Convection and Gravity Waves*. Journal of the Atmospheric Sciences, 67, pp. 3208–3225.

Van Leer, B. (1974). *Towards the ultimate conservative difference scheme. II. Monotonicity and conservation combined in a second-order scheme*. J. Comput. Phys., **14** , pp. 361–370

Margaret A. LeMone, M. A., R. L. Grossman, F. Chen, K. Ikeda, and D. Yates (2003). *Choosing the Averaging Interval for Comparison of Observed and Modeled Fluxes along Aircraft Transects over a Heterogeneous Surface*. J. Hydrometeor, 4, pp. 179–195.

LeMone, M. A., F. Chen, J. G. Alfieri, M. Tewari, B. Geerts, Q. Miao, R. L. Grossman, and R. L. Coulter, (2007). *Influence of Land Cover and Soil Moisture on the Horizontal Distribution of Sensible and Latent Heat Fluxes in Southeast Kansas during IHOP_2002 and CASES-97*. J. Hydrometeor, 8, pp. 68–87.

Lenschow, D. H. (1970). *Airplane Measurements of Planetary Boundary Layer Structure*,J. Appl. Meteorological **9**, pp. 874–884.

Leonard, A. (1975). *Energy cascade in large-eddy simulations of turbulent fluid flows*. Advances in Geophysics, **18**, pp. 237-248.

Leonard, B. P. (1979). *A stable and accurate convective modelling procedure based on quadratic upstream interpolation*. Computer methods in applied mechanics and engineering, **19** (1), pp. 59-98

Leonard, B. P. (1991). *The ULTIMATE conservative difference scheme applied to unsteady one-dimensional advection*. Computer Methods in Applied Mechanics and Engineering, **88** (1), 17-74.

Leonard, B. P., MacVean, M. K., and Lock, A. P. (1993). *Positivity-preserving numerical schemes for multidimensional advection*. NASA STI/Recon Technical Report N, 93, 27091.

Letzel, M. O., and S. Raasch (2003). *Large Eddy Simulation of Thermally Induced Oscillations in the Convective Boundary Layer*. Journal of the Atmospheric Sciences, 60, pp. 2328–2341.

Li, X. , M. Charron ; L. Spacek, G. Candille (2008). *A regional ensemble prediction system based on moist targeted singular vectors and stochastic parameter perturbations*, Monthly Weather Review, 2008, 136(2). pp. 443-462.

Li, W., S. Lü, S. Fu, X. Meng, H. C. Nnamchi. (2011) *Numerical simulation of fluxes generated by inhomogeneities of the underlying surface over the Jinta Oasis in Northwestern China*. Advances in Atmospheric Sciences 28, pp. 887–906

Lilly, D. K. (1966). *On the application of the eddy viscosity concept in the inertial sub-range of turbulence*. National Center for Atmospheric Research.

Lilly DK (1967). *The representation of small-scale turbulence in numerical experiments*. IBM Scientific Comuting Symposium on Environmental Sciences, White Plains, pp. 195–210.

Lilly, D. K. (1968). *Models of cloud-topped mixed layers under a strong inversion*. Quarterly Journal of the Royal Meteorological Soc., **94** (401), pp. 292–309.

Lin, Y. L., Farley, R. D., and Orville, H. D. (1983). *Bulk parameterization of the snow field in a cloud model*. Journal of Climate and Applied Meteorology, **22** (6), pp. 1065–1092.

Lin, J. W. B., and J. D. Neelin (2003). *Toward stochastic deep convective parameterization in general circulation models*. Geophysical research letters, **30** (4). 11.

Lindsay, R. W., and D. A. Rothrock (1995). *Arctic sea ice leads from advanced very high resolution radiometer images*. Journal of Geophysical Research: Oceans, **100** (C3), pp. 4533–4544.

Liu, A. Q., G. W. K. Moore, K. Tsuboki, and I. A. Renfrew (2004). *A high-resolution simulation of convective roll clouds during a cold-air outbreak.*Geophysical Research Letters, 31, L03101.

Liu, A. Q., Moore, G. W. K., Tsuboki, K., and I. A. Renfrew (2006). *The Effect of the Sea-ice Zone on the Development of Boundary-layer Roll Clouds During Cold Air Outbreaks,*Boundary-Layer Meteorology, Volume **118** (3), pp. 557–581.

Liu, G. , J. Sun, L. Yin (2011). *Turbulence Characteristics of the Shear-Free Convective Boundary Layer Driven by Heterogeneous Surface Heating*. Boundary-Layer Meteorology 140, pp. 57–71.

Liu Z., Axel Schweiger, and Ron Lindsay, (2015). *Observations and Modeling of Atmospheric Profiles in the Arctic Seasonal Ice Zone*. Monthly Weather Review, 143, pp. 39–53

Liu, Y., Key, J., and r. Mahoney (2016). *Sea and Freshwater Ice Concentration from VIIRS on Suomi NPP and the Future JPSS Satellites*, Remote Sensing, **8** (6), 523.

Lloyd, G., Choularton, T. W., Bower, K. N., Crosier, J., Jones, H., Dorsey, J. R., M. W. Gallagher1, P. Connolly, A. C. R. Kirchgaessner and T. Lachlan-Cope, (2015). *Observations and comparisons of cloud microphysical properties in spring and summertime Arctic stratocumulus clouds during the ACCACIA campaign*. Atmospheric Chemistry and Physics, **15** (7), pp. 3719-3737.

Lock, A. (2000). *A parameterization of turbulent mixing in convective cloud-capped boundary layers derived from large-eddy similations*. World meteorological organization-publications-wmo TD, pp. 33–41.

Lock, A. P., A. R/ Brown, M. R. Bush, G. M. Martin, R. N. B. Smith (2000) *A new boundary layer mixing scheme. Part I: Scheme description and single-column model tests*, Monthly Weather Review, 2000, **128** (9). pp. 3187-3199

Lock A., J. Edwards (2013). *Unified Model Documentation Paper 24, The Parametrization of Boundary Layer Processes, Unified Model Version: 8.6*. Met Office

Lorenz, E. N. (1963). *Deterministic nonperiodic flow*. Journal of the Atmospheric Sciences, 20(2), pp. 130-141

Love, M. D., and Leslie, D. C. (1979). *Studies of Subgrid Modelling with Classical Closures and Burgers' Equation. In Turbulent Shear Flows I*. Springer Berlin Heidelberg. pp. 353–369.

Lüpkes, C., and G. Birnbaum (2005). *Surface drag in the Arctic marginal sea-ice zone: a comparison of different parameterisation concepts*. Boundary-layer meteorology, **117** (2), pp. 179-211.

Lüpkes, C., Gryanik, V. M., Witha,B., Gryschka, M., Raasch, S., and T. Gollnik (2008).*Modeling convection over arctic leads with LES and a non-eddy-resolving microscale model*, Journal of Geophysical Research, **113**, C9

Lüpkes, C., Gryanik, V. M., Hartmann, J., and E. L. Andreas (2012). *A parametrization, based on sea ice morphology, of the neutral atmospheric drag coefficients for weather prediction and climate models*. Journal of Geophysical Research: Atmospheres (1984–2012), **117** (D13).

Lüpkes, C., and V. M. Gryanik, (2015). *A stability-dependent parametrization of transfer coefficients for momentum and heat over polar sea ice to be used in climate models*. Journal of Geophysical Research: Atmospheres, **120** (2), pp. 552–581.

Magnusdottir, G., C. Deser, and R. Saravanan (2004). *The effects of North Atlantic SST and sea ice anomalies on the winter circulation in CCM3. Part I: Main features and*

storm track characteristics of the response. Journal of Climate, **17** (5), pp. 857–876.

Mahrt, L. (1979). *Penetrative convection at the top of a growing boundary layer*. Quarterly Journal of the Royal Meteorological Soc., **105** (444), pp. 469–485.

Mahrt, L., and J. Paumier (1984). *Heat transport in the atmospheric boundary layer*. Journal of the Atmospheric Sciences, **41** (21), pp. 3061–3075.

Mahrt, L. (2000). *Surface heterogeneity and vertical structure of the boundary layer*. Boundary-Layer Meteorol 96, pp. 33–62

Mahrt, L., and D. Khelif (2010) *Heat fluxes over weak SST heterogeneity* Journal: Journal of Geophysical Research, 2010, **115**, D11

Mäkiranta, E. , T. Vihma, A. Sjöblom and E-M. Tastula (2011). *Observations and Modelling of the Atmospheric Boundary Layer Over Sea-Ice in a Svalbard Fjord*. Boundary-Layer Meteorology, 2011, Volume **140**, (1), pp. 105–123

Mann, J., and D. H. Lenschow (1994). *Errors in airborne flux measurements*. Journal of Geophysical Research: Atmospheres, **99** (D7), pp. 14519-14526.

Maronga, B., and S. Raasch (2013). *Large-eddy simulations of surface heterogeneity effects on the convective boundary layer during the LITFASS-2003 experiment*. Boundary-Layer Meteorol 146:17–44

Maronga B. (2014). *Monin–Obukhov Similarity Functions for the Structure Parameters of Temperature and Humidity in the Unstable Surface Layer: Results from High-Resolution Large-Eddy Simulations*. Journal of the Atmospheric Sciences, 71, pp. 716–733.

Maronga, B. , O. K. Hartogensis, S. Raasch and F. Beyrich (2014). *The Effect of Surface Heterogeneity on the Structure Parameters of Temperature and Specific Humidity: A Large-Eddy Simulation Case Study for the LITFASS-2003 Experiment*. Boundary-Layer Meteorology, **153** (3), pp. 441-470.

Marshall, J., Andersson, A., Bates, N., Dewar, W., Doney, S., Edson, J., and other coauthors from the Climode group (2009). *The CLIMODE field campaign: Observing the cycle of convection and restratification over the Gulf Stream*. Bulletin of the American Meteorological Soc., **90** (9), pp. 1337–1335.

R. H. Maryon. (1989). *The effect of grid resolution upon the numerical modelling of the convective boundary layer*. Boundary-Layer Meteorology 46:1-2, pp. 69-91.

Mason, P. J., and N. S. Callen (1986). *On the magnitude of the subgrid-scale eddy coefficient in large-eddy simulations of turbulent channel flow*. Journal of Fluid Mechanics, 162, pp. 439–462.

Mason, P.J. (1989). *Large-Eddy Simulation of the Convective Atmospheric Boundary Layer*. Journal of the Atmospheric. Sciences, **46**, pp. 1492–1516.

Mason, P. J., and S. H. Derbyshire (1990). *Large-eddy simulation of the stably-stratified atmospheric boundary layer*. Boundary-layer meteorology, **53** (1-2), pp. 117–162.

Mason, P.J., and D. J. Thomson (1992). *Stochastic backscatter in large-eddy simulations of boundary layers*. Journal of Fluid Mechanics, **242**, pp. 51–78.

Mason, P. J. (1994). *Large-eddy simulation: A critical review of the technique*. Quarterly Journal of the Royal Meteorological Soc., 120, pp. 1–26.

Mason, P. J., and A. R. Brown (1994). *The sensitivity of large-eddy simulations of turbulent shear flow to subgrid models*. Boundary-Layer Meteorology, 70, pp. 133–150.

Mason, P. J., and A. R. Brown, (1999). *On Subgrid Models and Filter Operations in Large Eddy Simulations*. Journal of the Atmospheric Sciences, 56, pp. 2101–2114.

Matheou, G., D. Chung, L. Nuijens, B. Stevens and J. Teixeira (2011). *On the Fidelity of Large-Eddy Simulation of Shallow Precipitating Cumulus Convection*. Monthly Weather Review, 139, pp. 2918–2939.

McClatchey, R.A., R.W. Fenn, J.E.A. Selby, F.E. Volz and J.S. Garing (1971). *Optical Properties of the Atmosphere (Revisited)*, Air Force Cambridge Research Laboratories L.G. Hanscom Field, Bedford, Massachusetts.

Melfi, S.H., and Stephen P. Palm (2012). *Estimating the Orientation and Spacing of Midlatitude Linear Convective Boundary Layer Features: Cloud Streets*. Journal of the Atmospheric Sciences, 69, pp. 352–364.

Meneveau, C., T.S. Lund, and W.H. Cabot (1996). *A Lagrangian dynamic subgrid-scale model of turbulence*. Journal of Fluid Mechanics, **319**, pp. 353–385.

Met Office (2014). *ACCACIA: Met Office UM Model output*. NCAS British Atmospheric Data Centre, cited on 12 March 2017. `http://catalogue.ceda.ac.uk/uuid/f3d2c9b53e34271de53e3a3802cc6689`

Meylan, M., V. M. Squire, and C. Fox (1997). *Towards realism in modeling ocean wave behavior in marginal ice zones*. Journal of Geophysical Res, 102, pp. 22–981.

Miller, N. E., and R. Stoll (2013). *Surface Heterogeneity Effects on Regional-Scale Fluxes in the Stable Boundary Layer: Aerodynamic Roughness Length Transitions*. Boundary-Layer Meteorology 149, pp. 277–301.

Michioka, T., A. Sato and K. Sada (2013). *Large-eddy simulation coupled to mesoscale meteorological model for gas dispersion in an urban district*. Atmospheric Environment, August, 2013, **75** (10), p. 153.

Moncrieff, J., Clement, R., Finnigan, J., and T. Meyers (2004). *Averaging, detrending, and filtering of eddy covariance time series*. Handbook of micrometeorology. Springer Netherlands. pp. 7–31

Monin, A. S., and A. M. F. Obukhov (1954). *Basic laws of turbulent mixing in the surface layer of the atmosphere*. Contrib. Geophys. Inst. Acad. Sci. USSR, **151** (163), e187.

Monin, A. S., and A. M. Yaglom (1971). *Statistical fluid mechanics, volume II: Mechanics of turbulence*. The MIT Press.

Moore, G. W. K., R. S. Pickart, I. A. Renfrew, and K. Våge (2014). *What causes the location of the air-sea turbulent heat flux maximum over the Labrador Sea?*. Geophysical Res. Lett., 41, pp. 3628–3635.

Morille, Y., Haeffelin, M., Drobinski, P., and J. Pelon (2007). *STRAT: an automated algorithm to retrieve the vertical structure of the atmosphere from single channel lidar data*. J. Atmospheric Oceanicic Technology, **24**, pp. 761–775.

Morrison, H., McCoy, R. B., Klein, S. A., Xie, S., Luo, Y., Avramov, A., Chen, M., Cole, J. N. S., Falk, M., Foster, M. J., Del Genio, A. D., Harrington, J. Y., Hoose, C., Khairoutdinov, M. F., Larson, V. E., Liu, X., McFarquhar, G. M., Poellot, M. R., von Salzen, K., Shipway, B. J., Shupe, M. D., Sud, Y. C., Turner, D. D., Veron, D. E., Walker, G. K., Wang, Z., Wolf, A. B., Xu, K.-M., Yang, F., and Zhang, G. (2009). *Intercomparison of model simulations of mixed-phase clouds observed during the ARM Mixed-Phase Arctic Cloud Experiment. II: Multilayer cloud*. Quarterly Journal of the Royal Meteorological Soc., **135**, pp. 1003–1019.

Muller, G., and A. Chlond (1996). *Three-dimensional numerical study of cell broadening during cold-air outbreaks*. Bound. -Layer Meteorological, **81** (3–4), pp. 289–323.

Muller, G., Brummer, B., and W. Alpers (1999). *Roll convection within an Arctic cold-air outbreak: Interpretation of in situ aircraft measurements and spaceborne SAR imagery by a three-dimensional atmospheric model*. Mon. Weather Rev., **127** (3), pp. 363–380.

Muñoz-Esparza, D., Kosović, B., García-Sánchez,C., van Beeck, J., (2014). *Nesting Turbulence in an Offshore Convective Boundary Layer Using Large-Eddy Simulations*. Boundary-Layer Meteorology, **151** (3), pp. 453

Murphy, J. J. (1860). *On Great Fluctuations of Temperature in the Arctic Winter*. Proceedings of the Royal Soc. of London, **11**, pp. 309-312.

Nappo, C. J. (2013). *An introduction to atmospheric gravity waves*. Academic Press.

NERC. *Development of a Met Office NERC cloud model (MONC)*, `http://gtr.rcuk.ac.uk/project/F1023ACF-76FF-4AD4-8E22-BA4A74451AD0`, retrieved on 5 October 2014

O'Brien, J. J. (1970). *A note on the vertical structure of the eddy exchange coefficient in the planetary boundary layer*. Journal of the Atmospheric Sciences, **27** (8), pp. 1213–1215.

Olsson, P. Q., and J. Y. Harrington (2000). *Dynamics and energetics of the cloudy boundary layer in simulations of off-ice flow in the marginal ice zone*. Journal of Geophysical Res., **105** (D9), pp. 11889–11899.

Oppenheim, A.V., Schafer, R.W., and Buck J.R. (1999). *Discrete-Time Signal Processing*, 2nd ed, Englewoods Cliffs, Nj: Prentice-Hall

Orrell, D. (1999). *A shadow of a doubt: Model error, uncertainty, and shadowing in nonlinear dynamical systems*. (Doctoral dissertation, PhD Thesis), University of Oxford.

Ovchinnikov, M., A. S. Ackerman, A. Avramov, A. Cheng, J. Fan, A. M. Fridlind, S. Ghan, J. Harringto, C. Hoose, A. Korolev, G. M. McFarquhar, H. Morrison, M. Paukert, J. Savre, B. J. Shipway, M. D. Shupe, A. Solomon and K. Sulia (2014). *Intercomparison of large-eddy simulations of Arctic mixed-phase clouds: Importance of ice size distribution assumptions*, Journal of Advances in Modeling Earth Systems, 6, pp. 223–248,

Pagowski, M., and G. W. K. Moore, (2001). *A Numerical Study of an Extreme Cold-Air Outbreak over the Labrador Sea: Sea Ice, Air–Sea Interaction, and Development of Polar Lows*. Monthly Weather Review, 129, pp. 47–72.

Palmer, T. N. (2001). *A nonlinear dynamical perspective on model error: A proposal for non-local stochastic-dynamic parametrization in weather and climate prediction models*. Quarterly Journal of the Royal Meteorological Soc., **127**, pp. 279–304.

Palmer, T.N., GJ Shutts, R Hagedorn, FJ Doblas-Reyes, T Jung and M. Leutbecher, (2005). *Representing model uncertainty in weather and climate prediction*, Annual Review Earth Planetary Sci, **33**, pp. 163-93.

Palmer, T. N., Buizza, R., Doblas-Reyes, F., Jung, T., Leutbecher, M., Shutts, G. J., M. Steinheimer and A. Weisheimer (2009). *Stochastic parametrization and model uncertainty*. ECMWF Research Department Technical Memorandum, ECMWF, Reading (598), 42.

Palmer, T. N. (2012). *Towards the probabilistic Earth-system simulator: a vision for the future of climate and weather prediction*, Quarterly Journal of the Royal Meteorological Soc., **138**: 841–861.

Panofsky, H. A. (1963). *Determination of stress from wind and temperature measurements*. Quarterly Journal of the Royal Meteorological Society, **89** (379), pp. 85–94.

Papritz, L., S. Pfahl, H. Sodemann and H. Wernli. (2014) *A Climatology of Cold Air Outbreaks and Their Impact on Air–Sea Heat Fluxes in the High-Latitude South Pacific*. Journal of Climate **28** (1), pp. 342-364.

Patton, E. G., Peter P. Sullivan, and Chin-Hoh Moeng, (2005). *The Influence of Idealized Heterogeneity on Wet and Dry Planetary Boundary Layers Coupled to the Land Surface*. Journal of the Atmospheric Sciences, 62, pp. 2078–2097

Paulson, C. A. (1970) *The mathematical representation of wind speed and temperature profiles in the unstable atmospheric surface layer*. Journal of Applied Meteorology, **9** (6), pp. 857–861.

G. Persson, P. O., Hare, J. E., Fairall, C. W., and Otto, W. D. (2005). *Air–sea interaction processes in warm and cold sectors of extratropical cyclonic storms observed during FASTEX*, Quarterly Journal of the Royal Meteorological Soc., **131**, pp. 877–912.

Petch, J. C. (1998). *Improved radiative transfer calculations from information provided by bulk microphysical schemes*. Journal of the Atmospheric Sciences, **55** (10), pp. 1846–1858.

Petersen, GN, Renfrew, IA and Moore, GWK (2009). *An overview of barrier winds off southeastern Greenland during the Greenland Flow Distortion experiment*. Quarterly Journal of the Royal Meteorological Soc., **135** (645). pp. 1950–1967.

Petersen, G. N., and I. A. Renfrew (2009). *Aircraft-based observations of air–sea fluxes over Denmark Strait and the Irminger Sea during high wind speed conditions*. Quarterly Journal of the Royal Meteorological Society, **135** (645), pp. 2030–2045.

Perovich, D. K., and K. F. Jones (2014). *The seasonal evolution of sea ice floe size distribution*. Journal of Geophysical Research: Oceans, **119** (12), pp. 8767–8777.

Piacsek, S. A., and Williams, G. P. (1970). *Conservation properties of convection difference schemes*. Journal of Computational Physics, 6, pp. 392–405.

Pitteway, M. L. V., and C. O. Hines (1963). *The Viscous Damping of Atmospheric Gravity Waves*. Canadian Journal of Physics, **41** (12), pp. 1935–1948.

Igor V. Polyakov, I. V., R. V. Bekryaev, G. V. Alekseev, U. S. Bhatt, R. L. Colony, M. A. Johnson, A. P. Maskshtas, and D. Walsh, (2003). *Variability and Trends of Air Temperature and Pressure in the Maritime Arctic, 1875–2000*. Journal of Climate, 16, pp. 2067–2077.

Pope, S. B. (2004). *Ten questions concerning the large-eddy simulation of turbulent flows*. New journal of Physics, **6** (1), 35.

Porson, A., Price, J., Lock, A., Clark, P., (2011). *Radiation Fog. Part II: Large-Eddy Simulations in Very Stable Conditions*. Boundary-Layer Meteorology, 2011, **139** (2), pp. 193-224.

Prabha, T. V., Karipot, A., and M. W. Binford (2007). *Characteristics of secondary circulations over an inhomogeneous surface simulated with large-eddy simulation*. Boundary-Layer Meteorology **123** (2), pp. 239–261.

Press, W. H., Teukolsky, S.A, Vetterling, W.T., Flannery, B. P. (2007). *Numerical recipes 3rd edition: The art of scientific computing*. Cambridge University Press.

Priestley, C. H. B., and W. C. Swinbank (1947). *Vertical transport of heat by turbulence in the atmosphere*. In Proceedings of the Royal Society of London A: Mathematical, Physical and Engineering Sciences, **189** (1019), pp. 543–561.

Priestley, M. B. (1982). *Spectral analysis and time series*. London, New York: Academic Press.

Putrasahan, D. A., Miller, A. J., and H. Seo (2013). *Isolating mesoscale coupled ocean–atmosphere interactions in the Kuroshio Extension region*. Dynamics of Atmospheres and Oceans **63**, pp. 60-78.

Randall, D., Curry, J., Battisti, D., Flato, G., Grumbine, R., Hakkinen, S., Martinson, D., Preller, R., Walsh, J. and Weatherly, J., (1998). *Status of and outlook for large-scale modeling of atmosphere–ice–ocean interactions in the Arctic*. Bulletin of the American Meteorological Society, **79** (2), pp. 197–219.

Raupach, M. R. (1993). *The averaging of surface flux densities in heterogeneous landscapes*. IAHS publication, pp. 343-343.

Renfrew, I. A., Moore, G. W. K., Holt, T. R., Chang, S. W., and P. Guest (1999). *Mesoscale forecasting during a field program: Meteorological support of the Labrador Sea Deep Convection Experiment*. Bulletin of the American Meteorological Soc.,

80 (4), pp. 605–620.

Renfrew I. A., and G. W. K. Moore, (1999) *An Extreme Cold-Air Outbreak over the Labrador Sea: Roll Vortices and Air–Sea Interaction.* Monthly Weather Review, 127, pp. 2379–2394.

Renfrew, IA ; King, JC, (2000). *A simple model of the convective internal boundary layer and its application to surface heat flux estimates within polynyas*, Boundary-layer Meteorology, 2000, **94** (3). pp. 335-356

Renfrew, I. A., G. W. K. Moore, P. S.Guest, and K. Bumke (2002). *A comparison of surface layer and surface turbulent flux observations over the Labrador Sea with ECMWF analyses and NCEP reanalyses.* Journal of Physical Oceanography, **32** (2), pp. 383–400.

Renfrew, I.A., Petersen, G.N., Outten, S., Sproson, D., Moore, G.W.K., Hay, C., Ohigashi, T., Zhang, S., Kristjánsson, J.E., Føre, I. and H. Ólafsson (2008). *The Greenland flow distortion experiment.* Bulletin of the American Meteorological Society, **89** (9), pp. 1307–1324.

Richardson, Y. P., Droegemeier, K. K., and R. P. Davies-Jones (2007). *The influence of horizontal environmental variability on numerically simulated convective storms. Part I: Variations in vertical shear.* Monthly Weather Review, 135(10), pp. 3429–3455.

Roe, P.L, E. Engquist, S. Osher, R.J.C. Sommerville (1985) *Large Scale Computations In Fluid Mechanics (2nd Edition).* Lectures in Applied Mathematics, Vol. 22, American Mathematical Society, Providence, RI , Pt. 2, pp. 163–193.

de Roode, S. R., Duynkerke, P. G., and H. J. J. Jonker (2004). *Large-Eddy Simulation: How Large is Large Enough?.* Journal of the Atmospheric Sciences, 2004, **61** (4), pp. 403–415.

de Rooy, W. C., P. Bechtold, K. Fröhlich, C. Hohenegger, H. Jonker, D. Mironov, P. A. Siebesma, A., J. Teixeira, and J.-I. Yano (2013). *Entrainment and detrainment in cumulus convection: an overview.* Quarterly Journal of the Royal Meteorological Soc., 139, pp. 1–19.

Rothrock, D. A., and A. S. Thorndike (1984). *Measuring the sea ice floe size distribution.* Journal of Geophysical Research: Oceans, **89** (C4), pp. 6477-6486.

Roy, S. B., C. P. Weaver, D. S. NOLAN, and R. Avissar (2003). *A preferred scale for landscape forced mesoscale circulations?: GEWEX Continental-Scale International Project, Part 3 (GCIP3).* Journal of geophysical research, **108** (D22), GCP15-1.

Rutledge, S. A., and Hobbs, P. (1983). *The mesoscale and microscale structure and organization of clouds and precipitation in midlatitude cyclones. VIII: A model for the "seeder-feeder" process in warm-frontal rainbands.* Journal of the Atmospheric Sciences, **40** (5), 1185–1206.

Rutledge, S. A., and Hobbs, P. V. (1984). *The mesoscale and microscale structure and organization of clouds and precipitation in midlatitude cyclones. XII: A diagnostic modeling study of precipitation development in narrow cold-frontal rainbands.* Journal of the Atmospheric Sciences, **41** (20), 2949–2972.

Salhi, A., and C. Cambon (1997). *An analysis of rotating shear flow using linear theory and DNS and LES results.* Journal of Fluid Mechanics, **347**, pp. 171–195.

Savage, S. B. (1995). Marginal ice zone dynamics modelled by computer simulations involving floe collisions. In Mobile particulate systems, Springer Netherlands, pp. 305–330.

Savijärvi, H. I. (2012). *Cold air outbreaks over high-latitude sea gulfs.* Tellus A, Dynamic Meteorology and Oceanography, **64**, 12244

Schlatter, P., and Örlü, R. (2010). *Assessment of direct numerical simulation data of turbulent boundary layers.* Journal of Fluid Mechanics, **659**, pp. 116–126.

Schemm, C. E. (1974). *A three-dimensional numerical study of turbulence in homogeneous and convectively unstable fluids*. Ph.D. Thesis Princeton University, NJ.

Schröder, D., T. Vihma, A. Kerber, and B. Brümmer (2003). *On the parameterization of turbulent surface fluxes over heterogeneous sea ice surfaces*. Journal of Geophysical Research, **108**, 3195.

Schröter, M., S. Raasch, and H. Jansen, (2005). *Cell Broadening Revisited: Results from High-Resolution Large-Eddy Simulations of Cold Air Outbreaks*. Journal of the Atmospheric Sciences, **62**, pp. 2023–2032.

Sedlar, J., and Shupe, M. D. (2005). *Characteristic nature of vertical motions observed in Arctic mixed-phase stratocumulus*. Atmospheric Chemistry Physics, **14**, pp. 3461–3478.

Shao, Y., M. Sogalla, M. Kerschgens, and W. Brücher (2001). *Effects of land-surface heterogeneity upon surface fluxes and turbulent conditions*. Meteorology and Atmospheric Physics, **78** (3-4), pp. 157–181.

Shao, Y. , S. Liu, J. H. Schween, S. Crewell (2013). *Large-Eddy Atmosphere–Land-Surface Modelling over Heterogeneous Surfaces: Model Development and Comparison with Measurements*. Boundary-Layer Meteorology, **148**, pp. 333–356.

Shapiro, L. G., and Stockman, G. C (2001). *Computer Vision*,. Prentice Hall, 2001

Shaw, N. (1928). *Arctic Weather of April 15-16, 1928: With Some Observations on Polar Weather in Relation to the General Circulation*. Geographical Review, **18** (4), pp. 556–566.

Shen, S., and M. Y.Leclerc, (1995). *How large must surface inhomogeneities be before they influence the convective boundary layer structure? A case study*. Quarterly Journal of the Royal Meteorological Soc., **121**, pp. 1209–1228.

Shao, Y., and Y. Yang (2008). *A theory for drag partition over rough surfaces*. Journal of Geophysical Research: Earth Surface, **113** (F2).

Shin, H. H., and S-Y. Hong, (2013). *Analysis of Resolved and Parameterized Vertical Transports in Convective Boundary Layers at Gray-Zone Resolutions*. Journal of the Atmospheric Sciences, **70**, pp. 3248–3261.

Shin, H. H., and S-Y. Hong, (2015). *Representation of the Subgrid-Scale Turbulent Transport in Convective Boundary Layers at Gray-Zone Resolutions*. Monthly Weather Review, **143**, pp. 250–271.

Shinoda, T., Higuchi, A., Tsuboki, K., Hiyama, T,, Tanaka, H.,Endo, S., Minda, H., Uyeda, H., and K. Nakamura (2009). *Structure of Convective Circulation in the Atmospheric Boundary Layer over the Northwestern Pacific Ocean under a Subtropical High*. Journal of the Meteorological Soc. of Japan, **87** (6), pp. 979–996.

Shutts, G. J., and T. N. Palmer (2007). *Convective Forcing Fluctuations in a Cloud-Resolving Model: Relevance to the Stochastic Parameterization Problem*. Journal of Climate, **20**, pp. 187–202.

Siebesma, P., and Teixeira, J. (2000). *An advection-diffusion scheme for the convective boundary layer: description and 1d-results*. In: Proceeding 14th Symposium on Boundary Layers and Turbulence, Am. Meteorological Soc.

Siebesma, A. P., C. S. Bretherton, A. Brown, A. Chlond, J. Cuxart, P. G. Duynkerke, H. Jiang, M. Khairoutdinov, D. Lewellen, C. H. Moeng, E. Sanchez, B. Stevens, and D. E. Stevens (2003). *A Large Eddy Simulation Intercomparison Study of Shallow Cumulus Convection*. Journal of the Atmospheric Sciences, **60**, pp. 1201–1219.

Siebesma, A. P., P. M. M. Soares, and J. Teixeira (2007). *A Combined Eddy-Diffusivity Mass-Flux Approach for the Convective Boundary Layer*. Journal of the Atmospheric Sciences, 64, pp. 1230–1248.

Siebesma A. P., and J. W. M. Cuijpers, (1995). *Evaluation of parametric assumptions for shallow cumulus convection*. Journal of the Atmospheric Science, **52**, pp. 650–666.

Sigmond, M., J. C. Fyfe, G. M. Flato, V. V. Kharin, and W. J. Merryfield (2013). *Seasonal forecast skill of Arctic sea ice area in a dynamical forecast system*,Geophysical Research Letters, **40**, pp. 529–534.

Skyllingstad E.D., and J. B. Edson, (2009): *Large-Eddy Simulation of Moist Convection during a Cold Air Outbreak over the Gulf Stream*. Journal of the Atmospheric Sciences, **66**, pp. 1274–1293.

Slingo, A., and H. M. Schrecker (1982). *On the shortwave radiative properties of stratiform water clouds*. Quarterly Journal of the Royal Meteorological Soc., **108**, pp. 407–426.

Smagorinsky, J. (1963). *General circulation experiments with the primitive equations: I. The basic experiment*. Monthly weather review, **91** (3), pp. 99–164.

Small, R. J., Xie, S-P., Wang, Y., Esbensen, S. K., and D. Vickers (2005). *Numerical Simulation of Boundary Layer Structure and Cross-Equatorial Flow in the Eastern Pacific*. Journal of the Atmospheric Sciences **62** (6), pp. 1812–1830.

Smith, L. A. (2001). *Disentangling uncertainty and error: on the predictability of nonlinear systems*. in: Nonlinear dynamics and statistics. Birkhäuser Boston, pp. 31–64.

Song, X., and L. Yu. (2012) *High-Latitude Contribution to Global Variability of Air–Sea Sensible Heat Flux*. Journal of Climate **25** (10), pp. 3515-3531.

Solomon, A., M. D. Shupe, O. Persson, H. Morrison, T. Yamaguchi, P. M. Caldwell, and G. de Boer (2014). *The Sensitivity of Springtime Arctic Mixed-Phase Stratocumulus Clouds to Surface-Layer and Cloud-Top Inversion-Layer Moisture Sources*. Journal of the Atmospheric Sciences, **71**, pp. 574–595.

Spreen, G., Kaleschke, L., and G. Heygster (2008). *Sea ice remote sensing using AMSR-E 89 GHz channels*. J. Geophys. Res., **113**, C02S03. available at `http://www.iup.uni-bremen.de:8084/amsr2/amsr2.html`

Steinfeld, G., S. Raasch and T. Markkanen. (2008) *Footprints in Homogeneously and Heterogeneously Driven Boundary Layers Derived from a Lagrangian Stochastic Particle Model Embedded into Large-Eddy Simulation*. Boundary-Layer Meteorology, **129**, pp. 225–248.

Stevens, B., Moeng, C.H., Ackerman, A.S., Bretherton, C.S., Chlond, A., de Roode, S., Edwards, J., Golaz, J.C., Jiang, H., Khairoutdinov, M., and M.P. Kirkpatrick (2005). *Evaluation of large-eddy simulations via observations of nocturnal marine stratocumulus*. Monthly weather review, **133** (6), pp.1443–1462.

Stewart, R. W. (1969). *Turbulence and waves in a stratified atmosphere*. Radio Science, **4** (12), pp. 1269–1278.

Stoll R., F. Porté-Agel. (2009). *Surface Heterogeneity Effects on Regional-Scale Fluxes in Stable Boundary Layers: Surface Temperature Transitions*. Journal of the Atmospheric Sciences, **66** (2), pp. 412–431.

Streten, N. A. (1973). *Satellite observations of the summer decay of the Antarctic sea-ice*. Arch. Meteorological Geophysical Bioklimatol., Ser. A, **22** (1), pp. 119–134.

Strunin, M. A., and T. Hiyama (2005). *Spectral Structure of Small-Scale Turbulent and Mesoscale Fluxes in the Atmospheric Boundary Layer over a Thermally Inhomogeneous Land Surface*. Boundary-Layer Meteorology, **117** (3), pp. 479–510.

Stull, R. B. (1985): *A Fair-Weather Cumulus Cloud Classification Scheme for Mixed-Layer Studies*. Journal of Applied Meteorology and Climatology, 24, pp. 49–56.

Stull R. B. (1988). *An Introduction to Boundary Layer Meteorology*. Kluwer Academic Publishers, Dodrecht

Sühring M, and S. Raasch(2013). *Heterogeneity-induced heat-flux patterns in the convective boundary layer: can they be detected from observations and is there a blending height? - A large-eddy simulation study for the LITFASS-2003 experiment.* Boundary-Layer Meteorol **148** pp. 309–331

Sühring, M. , Maronga, B., Herbort, F., and S. Raasch(2014). *On the Effect of Surface Heat-Flux Heterogeneities on the Mixed-Layer-Top Entrainment.* Boundary-Layer Meteorology, Volume **151** (3), pp. 531-556.

Sullivan, P. P., Moeng, C. H., Stevens, B., Lenschow, D. H., and S. D. Mayor (1998). *Structure of the entrainment zone capping the convective atmospheric boundary layer.* Journal of the Atmospheric Sciences, **55** (19), pp. 3042–3064.

Sušelj K., J. Teixiera, and G. Matheou (2012). *Eddy Diffusivity/Mass Flux and Shallow Cumulus Boundary Layer: An Updraft PDF Multiple Mass Flux Scheme.* Journal of the Atmospheric Sciences, **69** (5), (May 2012). pp. 1513–1533.

Sušelj, K., J. Teixeira and D. Chung (2013). *A Unified Model for Moist Convective Boundary Layers Based on a Stochastic Eddy-Diffusivity/Mass-Flux Parameterization.* Journal of the Atmospheric Sciences, 70, pp. 1929–1953.

de Szoeke, S. P., and C. S. Bretherton (2004). *Quasi-Lagrangian large eddy simulations of cross-equatorial flow in the east Pacific atmospheric boundary layer.* Journal of the atmospheric sciences, **61** (15), pp.1837–1858.

de Szoeke, S. P., Bretherton, C. S., Bond, N. A., Cronin, M. F., and B. M. Morley (2005). *EPIC 95° W Observations of the Eastern Pacific Atmospheric Boundary Layer from the Cold Tongue to the ITCZ.* Journal of the Atmospheric Sciences, **62** (2), pp. 426–442.

Talbot, C., Bou-Zeid, E., Smith, J. (2012). *Nested Mesoscale Large-Eddy Simulations with WRF: Performance in Real Test Cases.* Journal of Hydrometeorology, **13** (5), pp. 1421–1444

Taylor, G. R., and Baker, M. B. (1991). *Entrainment and detrainment in cumulus clouds.* Journal of the atmospheric sciences, **48** (1), pp. 112–121.

Teixeira, J, and C. A. Reynolds, (2008). *Stochastic nature of physical parameterizations in ensemble prediction: A Stochastic convection approach*; Monthly Weather Review, 2008, **136** (2). pp. 483-496.

Tennant, W. J., Shutts, G. J., Arribas, A., and S. A. Thompson(2011). *Using a stochastic kinetic energy backscatter scheme to improve MOGREPS probabilistic forecast skill.* Monthly Weather Review, **139** (4), pp. 1190–1206.

Thuburn, J. (1997). *TVD Schemes, Positive Schemes, and the Universal Limiter.* Monthly Weather Review, 125, pp. 1990–1993.

Tisler, P., T. Vihma, G. Müller and Brümmer (2008), *Modelling of warm-air advection over Arctic sea ice.* Tellus A, 60, pp. 775–788.

Tjernström,. M. , Joseph Sedlar, and Matthew D. Shupe, (2008). *How Well Do Regional Climate Models Reproduce Radiation and Clouds in the Arctic? An Evaluation of ARCMIP Simulations.* Journal of Applied Meteorology and Climatology, 47, pp. 2405–2422.

Tjernström, M., T. Mauritsen (2009)/ *Mesoscale Variability in the Summer Arctic Boundary Layer.* Boundary-Layer Meteorology **130**, pp. 383–406.

Tjernström, M., and R. G. Graversen (2009). *The vertical structure of the lower Arctic troposphere analysed from observations and the ERA-40 reanalysis.* Quarterly Journal of the Royal Meteorological Soc., 135 (639), pp. 431-443.

Toyota, T., Takatsuji, S., and M. Nakayama (2006). *Characteristics of sea ice floe size distribution in the seasonal ice zone.* Geophysical Research Letters, **33** (2), L02616.

Toyota, T., Haas, C., T., and Tamura (2011). *Size distribution and shape properties of*

relatively small sea-ice floes in the Antarctic marginal ice zone in late winter. Deep Sea Research Part II: Topical Studies in Oceanography, **58** (9), pp. 1182–1193.

Troen, I., and L. Mahrt (1986). *A simple model of the atmospheric boundary layer; sensitivity to surface evaporation*. Boundary-Layer Meteorology, **37**, pp. 129–148.

Tsamados, M., Feltham, D. L., Schroeder, D., Flocco, D., Farrell, S. L., Kurtz, N., Laxon, S. W., and S. Bacon (2014). *Impact of Variable Atmospheric and Oceanic Form Drag on Simulations of Arctic Sea Ice*. J. Phys. Oceanogr., **44**, pp. 1329–1353.

Tsay, S. C., K. Stamnes, and K. Jayaweera (1989). *Radiative energy budget in the cloudy and hazy Arctic*. Journal of the atmospheric sciences, **46** (7), pp. 1002–1018.

Tukey, J. W. (1977). *"Box-and-Whisker Plots." §2C in Exploratory Data Analysis*. Reading, MA: Addison-Wesley, pp. 39-43,

Verlinde, J., Harrington, J.Y., Yannuzzi, V.T., Avramov, A., Greenberg, S., Richardson, S.J., Bahrmann, C.P., McFarquhar, G.M., Zhang, G., Johnson, N., and M.R. Poellot (2007). *The Mixed-Phase Arctic Cloud Experiment (M-PACE)*. Bulletin American Meteorological Soc., **88** (2), pp. 205–221.

Vickers, D., and L. Mahrt(2003). *The Cospectral Gap and Turbulent Flux Calculations*. J. Atmos. Oceanic Technol., **20**, pp. 660–672.

Vihma, T., Hartmann, J., and C. Lüpkes (2003). *A case study of an on-ice air flow over the Arctic marginal sea-ice zone*. Boundary-layer meteorology, **107** (1), pp. 189–217.

Vihma, T., Lüpkes, C., Hartmann, J., and H. Savijärvi (2005). *Observations and modelling of cold-air advection over Arctic sea ice*. Boundary-layer meteorology, **117** (2), pp. 275–300.

Vihma, T. (2014). *Effects of Arctic Sea Ice Decline on Weather and Climate: A Review*. Surveys in Geophysics 35, pp. 1175-1214.

Vincent, C. L., Hahmann, A. N., and . C. Kelly (2012). *Idealized Mesoscale Model Simulations of Open Cellular Convection Over the Sea*. Boundary-Layer Meteorology, **142** (1), pp. 103–121

Vogelezang, D. H. P., and A. A. M. Holtslag (1996). *Evaluation and model impacts of alternative boundary-layer height formulations*. Boundary-Layer Meteorology, **81** (3-4), pp. 245-269.

Wacker, U., K. V. Jayaraman Potty, C. Lüpkes, J. Hartmann and M. Raschendorfer (2005). *A Case Study on a Polar Cold Air Outbreak over Fram Strait using a Mesoscale Weather Prediction Model*. Boundary-Layer Meteorology 117, pp. 301–336.

Wai, M-K. M. (1988). *Modeling the effects of the spatially varying sea surface temperature on the marine atmospheric boundary layer*. Journal of Applied Meteorology, **27** (1), pp. 5-19.

Walsh, J. E., Phillips, A. S., Portis, D. H., and W. L. Chapman (2001). *Extreme cold outbreaks in the United States and Europe, 1948-99*. Journal of Climate, **14** (12), pp. 2642-2658.

Wang, Q., Danilov, S., Jung, T., Kaleschke, L., and A. Wernecke (2016) *Sea ice leads in the Arctic Ocean: Model assessment, interannual variability and trends*. Geophysical Research Letters, **43** (13), pp. 7019–7027.

Walko, R. L., Cotton, W. R., and R. A. Pielke (1992). *Large-eddy simulations of the effects of hilly terrain on the convective boundary layer*. Boundary-Layer Meteorology, **58** (1-2), pp. 133–150.

Watson, P. A. G., H. M. Christensen, and T. N. Palmer, (2015). *Does the ECMWF IFS Convection Parameterization with Stochastic Physics Correctly Reproduce Relationships between Convection and the Large-Scale State?*. Journal of the Atmospheric Sciences, 72, pp. 236–242.

Weinbrecht, S., and Raasch, S. (2001). *High-resolution simulations of the turbulent flow in the vicinity of an Arctic lead*. Journal of Geophysical Research: Oceans, **106** (C11), pp. 27035–27046.

Weinbrecht, S ; Mason, PJ, (2008). *Stochastic backscatter for cloud-resolving models. Part I: Implementation and testing in a dry convective boundary layer*, Journal Of The Atmospheric Sciences, **65** (1). pp. 123–139.

Weisstein, E. W. *"Box-and-Whisker Plot."* From MathWorld–A Wolfram Web Resource. , available at `http://mathworld.wolfram.com/Box-and-WhiskerPlot.html`, retrieved on 31 August 2015

Weisheimer, A., T. N. Palmer, and F. J. Doblas-Reyes (2011). *Assessment of representations of model uncertainty in monthly and seasonal forecast ensembles*. Geophysical Research Letters, **38**, L16703.

Weisheimer, A., S. Corti, T. Palmer and Vitart, F. (2014). *On the impact of stochastic parametrisations in the ECMWF seasonal forecasting system*. In EGU General Assembly Conference Abstracts, **16**, p. 4481.

Welch, P.D. (1967). *The use of fast Fourier Transform for the Estiimation of Power Spectra: A Method Based on Time Averaging Over Short, Modified Periodogramsd*, IEEE Transactions on Audio and Electroacoustics, vol. AU-15, pp. 70–73.

Wells, H., Webster, S., and A. Brown (2005). *The effect of rotation on the pressure drag force produced by flow around long mountain ridges*. Quarterly Journal of the Royal Meteorological Society, **131** (608), pp. 1321–1338.

Dean W. Wichern (1973). *The Behaviour of the Sample Autocorrelation Function for an Integrated Moving Average Process*. Biometrika **60** (2), pp. 235-239

Williams, T. D., Bennetts, L. G., Squire, V. A., Dumont, D., and L. Bertino (2013). *Wave–ice interactions in the marginal ice zone. Part 2: Numerical implementation and sensitivity studies along 1D transects of the ocean surface*. Ocean Modelling, **71**, pp. 92–101.

Winstead, N. S., T. D. Sikora, D. R. Thompson, and P. D. Mourad (2002). *Direct Influence of Gravity Waves on Surface-Layer Stress during a Cold Air Outbreak, as shown by Synthetic Aperture Radar*. Monthly Weather Review, 130, pp. 2764–2776.

Witek, M.L., J. Teixeira, and G. Matheou (2011). *An eddy diffusivity-mass flux approach to the vertical transport of turbulent kinetic energy in convective boundary layers*. Journal of the Atmospheric Sciences, **68** (10), pp. 2385–2394.

Wyant, M. C., Bretherton, C. S., Rand, H. A., and D. E. Stevens (1997). *Numerical simulations and a conceptual model for the stratocumulus to trade cumulus transition*. Journal of the Atmospheric Sciences, **54**, pp. 168–192.

Yamamoto, M. (2012). *Mesoscale structures of two types of cold-air outbreaks over the East China Sea and the effect of coastal sea surface temperature*. Meteorology and Atmospheric Physics, 115, pp. 89–112.

Yang, X.-Y., and X. Yuan (2014). *The Early Winter Sea Ice Variability under the Recent Arctic Climate Shift*. Journal of Climate, 27, pp. 5092–5110.

Yates, D.Y., Fei Chen, and Haruyasu Nagai, (2003). *Land Surface Heterogeneity in the Cooperative Atmosphere Surface Exchange Study (CASES-97). Part II: Analysis of Spatial Heterogeneity and Its Scaling*. Journal of Hydrometeorology , 4, pp. 219–234

Yoshiki, M., and K. Sato (2000). *A statistical study of gravity waves in the polar regions based on operational radiosonde data*, Journal of Geophysical Res., **105** (D14), pp. 17995–18011.

Young, G. S., Kristovich, D. A., Hjelmfelt, M. R., and R. C. Foster (2002). *Supplement to Rolls, Streets, Waves, and More*. Bulletin of the American Meteorological Soc., **83** (7), 1001–1001.

Young, G., Jones, H.M., Darbyshire, E., Baustian, K.J., McQuaid, J.B., Bower, K.N.,

Connolly, P.J., Gallagher, M.W., and T.W. Choularton (2016). *Size-segregated compositional analysis of aerosol particles collected in the European Arctic during the ACCACIA campaign*. Atmospheric Chemistry and Physics, **16** (6), pp. 4063–4079.

Young, G., Jones, H.M., Choularton, T.W., Crosier, J., Bower, K.N., Gallagher, M.W., Davies, R.S., Renfrew, I.A., Elvidge, A.D., Darbyshire, E. and F. Marenco (2016). *Observed microphysical changes in Arctic mixed-phase clouds when transitioning from sea ice to open ocean*. Atmospheric Chemistry and Physics, **16** (21), p. 13945.

Zacharias, S., M. Reyers, J. G. Pinto, J. H. Schween and S. C. Kerschgens (2012). *Heat and moisture budgets from airborne measurements and high-resolution model simulations*. Meteorology and Atmospheric Physics, **117** (1,2), pp. 47–61

Zhang, N., Q. L. Williams, and H. Liu (2010). *Effects of land-surface heterogeneity on numerical simulations of mesoscale atmospheric boundary layer processes*. Theoretical and applied climatology, **102** (3-4), pp. 307–317.

Zhang, Q., Skjetne, R., Metrikin, I., and S. Løset (2015). *Image processing for ice floe analyses in broken-ice model testing*. Cold Regions Science and Technology, **111**, pp. 27–38.

Zuidema P., Baker,B. , Han, Y., Intrieri, J., Key, J., Lawson, P., Matrosov, S., Shupe, M., Stone, R., and T. Uttal, (2005). *An Arctic Springtime Mixed-Phase Cloudy Boundary Layer Observed during SHEBA*. Journal of the Atmospheric Sciences, **62**, pp. 160–176

Zurn-Birkhimer, S. M., Agee, E. M., and Z. Sorbjan (2005). *Convective Structures in a Cold Air Outbreak over Lake Michigan during Lake-ICE*. Journal of the Atmospheric Sciences **62** (7), pp. 2414–2432.

Index

Appendix A

List of LEM Runs

The first appendix presents the list of the model runs. For each run, there is a corresponding runfile. The filename is:
`<name>.txt` Each runfile consists of the lines difining the basis LEM setting as well as definition of which namelists and code updates are used. The format of namelists is a *Fortran namelist* while the format of the code updates mostly follows the standart *Fortran95*.

The runfiles, namelist and code updates for idealised LEM runs are included in the folder:
`./appendices/lem_files/cao_idelised/`
Similarly, the namelist and code updates for idealised LEM runs are included in the folder `./appendices/lem_files/cao_idelised/`

Both the list of case runs and the list of idealised runs include just the relavant model runs. The trial runs, test runs, and failed runs are not included.

A.1 List of Case Runs

The model runs generally follows the setting defined in 6.2.2, unless stated otherwise.

no.	name	parcel	setting
3101	case_b760_sl1mod1_control__val0	sl1	control
3102	case_b760_sl1mod2_rough_um__val2	sl1	surface roughness adjusted based on MetUM
3103	case_b760_sl1mod3_rough_ice__val2	sl1	surface roughness adjusted based on observations
3104	case_b760_sl1mod4_het_surf_um_al10_val3	sl1	heterogeneity 'along' $\delta\_(\mathrm{h})T = 3\,\mathrm{K}$, $d\_(\mathrm{h}) = 1600$ m, based on MetUM

no.	name	parcel	setting
3105	case_b760_sl1mod5_het_surf_um_al20_val3	sl1	heterogeneity 'along' δ_(h)T = 3 K, d_(h) = 3200 m, based on MetUM
3106	case_b760_sl2mod1_control__val0	sl2	control
3107	case_b760_sl2mod2_rough_um__val2	sl2	surface roughness adjusted based on MetUM
3108	case_b760_sl2mod3_rough_ice__val2	sl2	surface roughness adjusted based on observations
3109	case_b760_sl2mod4_het_surf_um_al10_val3	sl2	heterogeneity 'along' δ_(h)T = 3 K, d_(h) = 1600 m, based on MetUM
3110	case_b760_sl2mod5_het_surf_um_ac10_val3	sl2	heterogeneity 'across' δ_(h)T = 3 K, d_(h) = 1600 m, based on MetUM
3111	case_b760_sl2mod6_het_surf_um_ch10_val3	sl2	heterogeneity 'chessboard' δ_(h)T = 3 K, d_(h) = 1600 m, based on MetUM
3112	case_b760_sl2mod7_het_surf_um_al20_val3	sl2	heterogeneity 'along' δ_(h)T = 3 K, d_(h) = 3200 m, based on MetUM
3113	case_b760_sl3mod1_control__val0	sl3	control
3114	case_b760_sl3mod2_rough_um__val2	sl3	surface roughness adjusted based on MetUM
3116	case_b760_sl3mod3_rough_ice__val2	sl3	surface roughness adjusted based on observations
3117	case_b760_sl3mod4_het_surf_um_al10_val3	sl3	heterogeneity 'along' δ_(h)T = 3 K, d_(h) = 1600 m, based on MetUM
3118	case_b760_sl3mod5_het_surf_um_ac10_val3	sl3	heterogeneity 'across' δ_(h)T = 3 K, d_(h) = 1600 m, based on MetUM
3118	case_b760_sl3mod6_het_surf_um_ch10_val3	sl3	heterogeneity 'chessboard' δ_(h)T = 3 K, d_(h) = 1600 m, based on MetUM
3119	case_b760_sl3mod7_het_surf_um_al20_val3	sl3	heterogeneity 'along' δ_(h)T = 3 K, d_(h) = 3200 m, based on MetUM
3120	case_b760_sl3mod8_het_surf_ice_al10_val3	sl3	heterogeneity 'along' δ_(h)T = 3 K, d_(h) = 1600 m, based on observations
3121	case_b760_sl3mod9_het_surf_ice_al20_val3	sl3	heterogeneity 'along' δ_(h)T = 3 K, d_(h) = 3200 m, based on observations

A.2 List of Idealised Runs

The model runs generally follows the setting defined in 3.1, unless stated otherwise.

no.	name	type	setting
0952	cao_test_control_03	control	control run
0957	cao_test_control_03		additional run with control setting
0961	cao_tests_rh85	sensitivity	initial humidity increased to $RH = 85$ %
1101	cao_test_control_03		part of control set
1115	cao_test_long_03	sensitivity	increased duration of run, control scenario
1211	cao_strat2_03	stratification	stratification 'strat2', homogeneous surface
1212	cao_strat2_resh40_lowdom_03	sensitivity	stratification 'strat2', lower domain, horizontal resolution $\Delta x = 40$ m
1213	cao_strat2_long_03	sensitivity	stratification 'strat2', increased duration of run,
1214	cao_strat2_s2_03	combination	stratification 'strat2', wind shear 'wind2'
1215	cao_strat2_s4_03	combination	stratification 'strat2', wind shear 'wind4'
1216	cao_strat4_s2_03	combination	stratification 'strat4', wind shear 'wind2'
1217	cao_strat4_s2_03	combination	same as 1216
1224	cao_strat4_s2_03_3a10h07	combination	stratification 'strat4', wind shear 'wind2', heterogeneity 'persistent' 'along' $\delta\_(\mathrm{h})T = 7\,\mathrm{K}$, $d\_(\mathrm{h}) = 1600$ m
1226	cao_strat2_s4_03_3a10h03	combination	stratification 'strat2', wind shear 'wind4', heterogeneity 'persistent' 'along' $\delta\_(\mathrm{h})T = 3\,\mathrm{K}$, $d\_(\mathrm{h}) = 1600$ m
1227	cao_strat4_s4_03_3a10h03	combination	stratification 'strat4', wind shear 'wind4', heterogeneity 'persistent' 'along' $\delta\_(\mathrm{h})T = 3\,\mathrm{K}$, $d\_(\mathrm{h}) = 1600$ m
1228	cao_strat4_s2_03_3a10h03	combination	stratification 'strat2', wind shear 'wind2', heterogeneity 'persistent' 'along' $\delta\_(\mathrm{h})T = 3\,\mathrm{K}$, $d\_(\mathrm{h}) = 1600$ m
1321	cao_s2_03	wind shear	wind shear 'wind2', homogeneous surface
1322	cao_s2_03_3a10h03	wind shear	wind shear 'wind2', heterogeneity 'persistent' 'along' $\delta\_(\mathrm{h})T = 3\,\mathrm{K}$, $d\_(\mathrm{h}) = 1600$ m
1323	cao_s2_03_3a10h07	wind shear	wind shear 'wind2', heterogeneity 'persistent' 'along' $\delta\_(\mathrm{h})T = 7\,\mathrm{K}$, $d\_(\mathrm{h}) = 1600$ m
1324	cao_s2_03_3a20h07	wind shear	wind shear 'wind2', heterogeneity 'persistent' 'along' $\delta\_(\mathrm{h})T = 7\,\mathrm{K}$, $d\_(\mathrm{h}) = 3200$ m
1331	cao_s3_03	wind shear	wind shear 'wind3', homogeneous surface
1332	cao_s3_03_3a10h07	wind shear	wind shear 'wind3', heterogeneity 'persistent' 'along' $\delta\_(\mathrm{h})T = 7\,\mathrm{K}$, $d\_(\mathrm{h}) = 1600$ m
1333	cao_s3_03_3a20h07	wind shear	wind shear 'wind3', heterogeneity 'persistent' 'along' $\delta\_(\mathrm{h})T = 7\,\mathrm{K}$, $d\_(\mathrm{h}) = 3200$ m
1340	cao_s4_03	wind shear	wind shear 'wind4', homogeneous surface
1341	cao_s4_03_3a10h01	wind shear	wind shear 'wind4', heterogeneity 'persistent' 'along' $\delta\_(\mathrm{h})T = 1\,\mathrm{K}$, $d\_(\mathrm{h}) = 1600$ m
1342	cao_s4_03_3a10h03	wind shear	wind shear 'wind4', heterogeneity 'persistent' 'along' $\delta\_(\mathrm{h})T = 3\,\mathrm{K}$, $d\_(\mathrm{h}) = 1600$ m
1343	cao_s4_03_3a10h07	wind shear	wind shear 'wind4', heterogeneity 'persistent' 'along' $\delta\_(\mathrm{h})T = 7\,\mathrm{K}$, $d\_(\mathrm{h}) = 1600$ m

no.	name	type	setting
1344	cao_s4_03_3a20h03	wind shear	wind shear 'wind4', heterogeneity 'persistent' 'along' $\delta\_(h)T = 3\,K$, $d\_(h) = 3200$ m
1345	cao_s4_03_3a20h07	wind shear	wind shear 'wind4', heterogeneity 'persistent' 'along' $\delta\_(h)T = 7\,K$, $d\_(h) = 3200$ m
1346	cao_s4_03_3c10h03	wind shear	wind shear 'wind4', heterogeneity 'persistent' 'across' $\delta\_(h)T = 3\,K$, $d\_(h) = 1600$ m
1347	cao_s4_03_3c20h03	wind shear	wind shear 'wind4', heterogeneity 'persistent' 'across' $\delta\_(h)T = 3\,K$, $d\_(h) = 3200$ m
1348	cao_s4_03_2a10h03	wind shear	wind shear 'wind4', heterogeneity 'persistent' 'along' $\delta\_(h)T = 3\,K$, $d\_(h) = 1600$ m
1349	cao_s4_03_2a20h03	wind shear	wind shear 'wind4', heterogeneity 'persistent' 'along' $\delta\_(h)T = 3\,K$, $d\_(h) = 3200$ m
1351	cao_test_03_3a10h01		heterogeneity 'persistent' 'along' $\delta\_(h)T = 1\,K$, $d\_(h) = 1600$ m
1352	cao_test_03_3a10h03		heterogeneity 'persistent' 'along' $\delta\_(h)T = 3\,K$, $d\_(h) = 1600$ m
1353	cao_test_03_3a10h07		heterogeneity 'persistent' 'along' $\delta\_(h)T = 7\,K$, $d\_(h) = 1600$ m
1365	cao_test_het16r3_vres01	sensitivity	vertical resolution 'vres01'
1366	cao_test_het16r3_vres2	sensitivity	vertical resolution 'vres2'
1401	cao_test_het16r3control		additional run with control setting
1402	cao_test_het16r3_ac10dh03		heterogeneity 'diminishing' 'across' $\delta\_(h)T = 3\,K$, $d\_(h) = 1600$ m,
1403	cao_test_het16r3_al10dh03		heterogeneity 'diminishing' 'along' $\delta\_(h)T = 3\,K$, $d\_(h) = 1600$ m,
1404	cao_test_het16r3_al20dh03		heterogeneity 'diminishing' 'along' $\delta\_(h)T = 3\,K$, $d\_(h) = 3200$ m,
1405	cao_test_het16r3_ch10dh03		heterogeneity 'diminishing' 'chessboard' $\delta\_(h)T = 3\,K$, $d\_(h) = 1600$ m,
1406	cao_test_het16r3_l2	sensitivity	slower increase in surface temperature
1407	cao_test_het16r3_ac10dh03_l2	sensitivity	slower increase in surface temperature, heterogeneity 'diminishing' 'across' $\delta\_(h)T = 3\,K$, $d\_(h) = 1600$ m,
1408	cao_test_het16r3_al10dh03_l2	sensitivity	lower increase in surface temperature, heterogeneity 'diminishing' 'along' $\delta\_(h)T = 3\,K$, $d\_(h) = 1600$ m,
1409	cao_test_het16r3_al20dh03_l2	sensitivity	lower increase in surface temperature, heterogeneity 'diminishing' 'along' $\delta\_(h)T = 3\,K$, $d\_(h) = 3200$ m,
1410	cao_test_het16r3_ch10dh03_l2	sensitivity	lower increase in surface temperature, heterogeneity 'diminishing' 'chessboard' $\delta\_(h)T = 3\,K$, $d\_(h) = 1600$ m,
1411	cao_test_het16r3_vz0	sensitivity	longer tranisition, adjusted surface roughness
1412	cao_test_het16r3_l2_vz0	sensitivity	longer tranisition, adjusted surface roughness
1603	cao_strat2_het16r3_ch10h07_03	stratification	stratification 'strat2', heterogeneity 'diminishing' 'chessboard' $\delta\_(h)T = 7\,K$, $d\_(h) = 1600$ m
1604	ao_strat2_het16r3_ch20h07_03	stratification	stratification 'strat2', heterogeneity 'diminishing' 'chessboard' $\delta\_(h)T = 7\,K$, $d\_(h) = 3200$ m

no.	name	type	setting
1612	cao_strat2_het16r3_al20h03_hres40_03	stratification	stratification 'strat2', heterogeneity 'persistent' 'along' δ_(h)T = 3 K, d_(h) = 800 m, horizontal resolution Δx = 40 m
1613	cao_strat2_het16r3_al40h03_hres40_03	stratification	stratification 'strat2', heterogeneity 'persistent' 'along' δ_(h)T = 3 K, d_(h) = 1600 m, horizontal resolution Δx = 40 m
1614	cao_strat2_het16r3_al40h07_hres40_03	stratification	stratification 'strat2', heterogeneity 'persistent' 'along' δ_(h)T = 7 K, d_(h) = 1600 m, horizontal resolution Δx = 40 m
1615	cao_strat2_het16r3_ch20h03_hres40_03	stratification	stratification 'strat2', heterogeneity 'persistent' 'chessboard' δ_(h)T = 3 K, d_(h) = 800 m, horizontal resolution Δx = 40 m
1616	cao_strat2_het16r3_ch40h03_hres40_03	stratification	stratification 'strat2', heterogeneity 'persistent' 'chessboard' δ_(h)T = 3 K, d_(h) = 1600 m, horizontal resolution Δx = 40 m
1617	cao_strat4_het16r3_h0_hres40_03	stratification	stratification 'strat4', homogeneous surface, horizontal resolution Δx = 40 m
1618	cao_strat4_het16r3_al10h03_hres40_03	stratification	stratification 'strat4', heterogeneity 'persistent' 'along' δ_(h)T = 3 K, d_(h) = 400 m, horizontal resolution Δx = 40 m
1619	cao_strat4_het16r3_al20h03_hres40_03	stratification	stratification 'strat4', heterogeneity 'persistent' 'along' δ_(h)T = 3 K, d_(h) = 800 m, horizontal resolution Δx = 40 m
1620	cao_strat4_het16r3_al40h03_hres40_03	stratification	stratification 'strat4', heterogeneity 'persistent' 'along' δ_(h)T = 3 K, d_(h) = 1600 m, horizontal resolution Δx = 40 m
1621	cao_strat4_het16r3_al40h07_hres40_03	stratification	stratification 'strat4', heterogeneity 'persistent' 'along' δ_(h)T = 7 K, d_(h) = 1600 m, horizontal resolution Δx = 40 m
1622	cao_s2_strat2_het16r3_h0_03	combination	stratification 'strat2', wind shear 'wind2', homogeneous surface
1623	cao_s2_strat2_het16r3_ac10h07_03	combination	stratification 'strat2', wind shear 'wind2', heterogeneity 'persistent' 'across' δ_(h)T = 7 K, d_(h) = 1600 m
1624	cao_s2_strat2_het16r3_ch10h07_03	combination	stratification 'strat2', wind shear 'wind2', heterogeneity 'persistent' 'chessboard' δ_(h)T = 7 K, d_(h) = 1600 m
1625	cao_s2_strat2_het16r3_al20h07_03	combination	stratification 'strat2', wind shear 'wind2', heterogeneity 'persistent' 'along' δ_(h)T = 7 K, d_(h) = 3200 m
1626	cao_strat3_het16r3_h0_03	stratification	stratification 'strat3', homogeneous surface
1627	cao_strat3_het16r3_al10h07_03	stratification	stratification 'strat3', heterogeneity 'persistent' 'along' δ_(h)T = 7 K, d_(h) = 1600 m
1628	cao_strat3_het16r3_ac10h07_03	stratification	stratification 'strat3', heterogeneity 'persistent' 'across' δ_(h)T = 7 K, d_(h) = 1600 m
1629	cao_strat3_het16r3_ch10h07_03	stratification	stratification 'strat3', heterogeneity 'persistent' 'chessboard' δ_(h)T = 7 K, d_(h) = 1600 m
1630	cao_strat3_het16r3_al20h07_03	stratification	stratification 'strat3', heterogeneity 'persistent' 'along' δ_(h)T = 7 K, d_(h) = 3200 m

no.	name	type	setting
1631	cao_strat4_het16r3_h0_03	stratification	stratification 'strat4', homogeneous surface
1632	cao_strat4_het16r3_al10h07_03	stratification	stratification 'strat4', heterogeneity 'persistent' 'along' δ_(h)$T = 7\,\mathrm{K}$, d_(h) = 1600 m
1633	cao_strat4_het16r3_ac10h07_03	stratification	stratification 'strat4', heterogeneity 'persistent' 'across' δ_(h)$T = 7\,\mathrm{K}$, d_(h) = 1600 m
1634	cao_strat4_het16r3_ch10h07_03	stratification	stratification 'strat4', heterogeneity 'persistent' 'chessboard' δ_(h)$T = 7\,\mathrm{K}$, d_(h) = 1600 m
1635	cao_strat4_het16r3_ch20h07_03	stratification	stratification 'strat4', heterogeneity 'persistent' 'chessboard' δ_(h)$T = 7\,\mathrm{K}$, d_(h) = 3200 m
1636	cao_strat4_het16r3_al20h07_03	stratification	same as 1635
1637	cao_strat5_het16r3_h0_03	stratification	stratification 'strat5', homogeneous surface
1638	cao_strat5_het16r3_al10h07_03	stratification	stratification 'strat5', heterogeneity 'persistent' 'along' δ_(h)$T = 7\,\mathrm{K}$, d_(h) = 1600 m
1639	cao_strat5_het16r3_ac10h07_03	stratification	stratification 'strat5', heterogeneity 'persistent' 'across' δ_(h)$T = 7\,\mathrm{K}$, d_(h) = 1600 m
1640	cao_strat5_het16r3_ch10h07_03	stratification	stratification 'strat5', heterogeneity 'persistent' 'chessboard' δ_(h)$T = 7\,\mathrm{K}$, d_(h) = 1600 m
1641	cao_strat5_het16r3_al20h07_03	stratification	stratification 'strat5', heterogeneity 'persistent' 'along' δ_(h)$T = 7\,\mathrm{K}$, d_(h) = 3200 m
1642	cao_s2_het16r3_ac10h07_03	wind shear	wind shear 'wind2', heterogeneity 'persistent' 'across' δ_(h)$T = 7\,\mathrm{K}$, d_(h) = 1600 m
1643	cao_s2_het16r3_ch10h07_03	wind shear	wind shear 'wind2', heterogeneity 'persistent' 'chessboard' δ_(h)$T = 7\,\mathrm{K}$, d_(h) = 1600 m
1644	cao_s3_het16r3_ac10h07_03	wind shear	wind shear 'wind3', heterogeneity 'persistent' 'across' δ_(h)$T = 7\,\mathrm{K}$, d_(h) = 1600 m
1645	cao_s3_het16r3_ch10h07_03	wind shear	wind shear 'wind3', heterogeneity 'persistent' 'chessboard' δ_(h)$T = 7\,\mathrm{K}$, d_(h) = 1600 m
1646	cao_strat2_het16r3_ch10h07_03	stratification	stratification 'strat2', heterogeneity 'persistent' 'chessboard' δ_(h)$T = 7\,\mathrm{K}$, d_(h) = 1600 m
1647	cao_strat2_het16r3_ch20h07_03	stratification	stratification 'strat2', heterogeneity 'persistent' 'chessboard' δ_(h)$T = 7\,\mathrm{K}$, d_(h) = 3200 m
1648	cao_s2_strat2_het16r3_al10h07_03	combination	stratification 'strat2', wind shear 'wind2', heterogeneity 'persistent' 'along' δ_(h)$T = 7\,\mathrm{K}$, d_(h) = 1600 m
1649	cao_s4_strat2_het16r3_h0_03	combination	stratification 'strat2', wind shear 'wind4'
1651	cao_s4_strat2_het16r3_al10h07_03	combination	stratification 'strat2', wind shear 'wind4', heterogeneity 'persistent' 'along' δ_(h)$T = 7\,\mathrm{K}$, d_(h) = 1600 m
1652	cao_s4_strat2_het16r3_ac10h07_03	combination	stratification 'strat2', wind shear 'wind4', heterogeneity 'persistent' 'across' δ_(h)$T = 7\,\mathrm{K}$, d_(h) = 1600 m
1653	cao_s4_strat2_het16r3_ch10h07_03	combination	stratification 'strat2', wind shear 'wind4', heterogeneity 'persistent' 'chessboard' δ_(h)$T = 7\,\mathrm{K}$, d_(h) = 1600 m
1654	cao_strat4_het16r3_al20h07_03	stratification	startification 'strat4', heterogeneity 'persistent' 'along' δ_(h)$T = 7\,\mathrm{K}$, d_(h) = 3200 m

no.	name	type	setting
1655	cao_s4_het16r3_h0_03	wind shear	wind shear 'wind4'
1656	cao_s4_het16r3_al10h07_03	wind shear	wind shear 'wind4', heterogeneity 'persistent' 'along' $\delta_{-}(\mathrm{h})T = 7\,\mathrm{K}$, $d_{-}(\mathrm{h}) = 1600$ m
1657	cao_s4_het16r3_ac10h07_03	wind shear	wind shear 'wind4', heterogeneity 'persistent' 'across' $\delta_{-}(\mathrm{h})T = 7\,\mathrm{K}$, $d_{-}(\mathrm{h}) = 1600$ m
1658	cao_s4_het16r3_ch10h07_03	wind shear	wind shear 'wind4', heterogeneity 'persistent' 'chessboard' $\delta_{-}(\mathrm{h})T = 7\,\mathrm{K}$, $d_{-}(\mathrm{h}) = 1600$ m
1659	cao_s4_het16r3_al20h07_03	wind shear	wind shear 'wind4', heterogeneity 'persistent' 'along' $\delta_{-}(\mathrm{h})T = 7\,\mathrm{K}$, $d_{-}(\mathrm{h}) = 3200$ m
1660	cao_s4_het16r3_ch20h07_03	wind shear	wind shear 'wind4', heterogeneity 'persistent' 'chessboard' $\delta_{-}(\mathrm{h})T = 7\,\mathrm{K}$, $d_{-}(\mathrm{h}) = 3200$ m
1661	cao_s3_het16r3_al10h07_03	wind shear	wind shear 'wind3', heterogeneity 'persistent' 'along' $\delta_{-}(\mathrm{h})T = 7\,\mathrm{K}$, $d_{-}(\mathrm{h}) = 1600$ m
1662	cao_s3_het16r3_al20h07_03	wind shear	wind shear 'wind3', heterogeneity 'persistent' 'along' $\delta_{-}(\mathrm{h})T = 7\,\mathrm{K}$, $d_{-}(\mathrm{h}) = 3200$ m
2600	cao_test_het16r3_control_v00		additional run with control setting
2601	cao_test_het16r3_control_v01	sensitivity	larger domain - grid 120x120
2602	cao_test_het16r3_hres80	sensitivity	coarse resolution, $\Delta x = 320$ m, grid 120x120
2603	cao_test_het16r3_hres40	sensitivity	coarse resolution, $\Delta x = 480$ m, grid 120x120
2604	cao_test_het16r3_hres80	sensitivity	increased resolution, $\Delta x = 80$ m, grid 120x120
2605	cao_test_het16r3_hres40	sensitivity	increased resolution, $\Delta x = 40$ m, grid 120x120
2606	cao_test_het16r3_al10dh03_v01	sensitivity,	heterogeneity 'dimininishing' 'along' $\delta_{-}(\mathrm{h})T = 3\,d_{-}(\mathrm{h}) = 1600$ m
2607	cao_test_het16r3_al20dh03_v01	sensitivity	heterogeneity 'dimininishing' 'along' $\delta_{-}(\mathrm{h})T = 3\,d_{-}(\mathrm{h}) = 3200$ m
2608	cao_test_het16r3_al20dh03_v01	sensitivity	same as 2607
2609	cao_test_het16r3_al20dh03_hres80	sensitivity	heterogeneity 'dimininishing' 'along' $\delta_{-}(\mathrm{h})T = 3\,\mathrm{K}$, $d_{-}(\mathrm{h}) = 1600$ m, horizontal resolution $\Delta x = 80$ m
2610	cao_test_het16r3_al40dh03_hres40	sensitivity	heterogeneity 'dimininishing' 'along' $\delta_{-}(\mathrm{h})T = 3\,\mathrm{K}$, $d_{-}(\mathrm{h}) = 1600$ m, horizontal resolution $\Delta x = 40$ m
2701	cao_test_het16r3_control_v00		additional run with control setting
2702	cao_test_het16r3_low01_v00		
2703	cao_test_het16r3_low01do01_v00	sensitivity	smaller vertical and horizontal extend of the domain
2704	cao_test_het16r3_low01_hr02_v00	sensitivity	test of very fine horizontal resolution, $\Delta x = 10$ m, smaller domain
2705	cao_test_het16r3_low01_hr02vr02_v00	sensitivity	very fine resolution, $\Delta x = 10$ m, smaller domain
2706	cao_test_het16r3_low01_hr02vr03_v00	sensitivity	extra fine resolution, $\Delta x = 6$ m, smaller domain
2707	cao_test_het16r3_low01_hr02vr04_v00	sensitivity	increased horizontal and vertical resolution
2708	cao_test_het16r3_low01_hr02vr04_v00	sensitivity	same as 2705
2708	cao_test_het16r3_low01_hr02vr04_v00	sensitivity	same as 2707
2710	cao_test_het16r3_control_v00		additional run with control setting
2711	cao_test_het16r3_low01_hr02vr04_v00s	sensitivity	fine resolution, smaller domain extent

Appendix B

Derivation of expressions

B.1 Kinetic Energy of Strong Updraughts

The part of the methods on the analysis of updraughts (3.4.2) provided a comparison between the estimated properties of strong updraughts in EDMF schemes and the quantities directly sampled from the model. This part of the appendix provides the derivation of the formula (3.9) for the kinetic energy of strong updraught estimated by EDMF schemes.

We want to compute the portion of the kinetic energy caused by the the vertical velocity in strong updraughts, i.e.

$$E_{w,u} = \int \tfrac{1}{2}\, w \, \mathrm{d}P(w) \tag{B.1}$$

where $w_u^{(a_u)}$ is the upper a_u-quantile of the distribution of vertical velocites.

Some EDMF schemes assumes that vertical velocity follows the normal distribution, i.e.

$$w \;\sim\; \mathcal{N}\big(0, \sigma_w^2\big),$$

where σ_w^2 is the variance in vertical velocities. The set of strong updraughts can be then expresses as

$$w_u \;=\; \big\{ w \;:\; w \geq \mathsf{z}_{(1-a_u)}\, \sigma_w \big\} \tag{B.2}$$

where $\mathsf{z}_{(1-a_u)}$ is the inverse a_u-quantile of the standard normal distribution. Recalling the pdf of normal distribution, the kinetic energy of strong updraughts yields:

$$E_{w,u} = \int_{\left\{\, w \,:\, w \geq \mathsf{z}_{(1-a_u)}\ \sigma_w \right\}} \frac{1}{2}\, w^2\, \frac{1}{\sqrt{2\,\pi\,\sigma_w^2}} \exp\left(\frac{-\,w^2}{2\,\sigma_w^2}\right)\, \mathrm{d}w$$

$$\left\{ \begin{array}{lll} \text{substitution} & s & = \frac{w}{\sigma_w} \\ & \mathrm{d}s & = \frac{1}{\sigma_w}\,\mathrm{d}w \end{array} \right\}$$

$$= \frac{1}{2} \int_{s \geq \mathsf{z}_{(1-a_u)}} s^2\, \sigma_w^2\, \frac{1}{\sqrt{2\,\pi\,\sigma_w^2}} \exp\left(\frac{-\,s^2\,\sigma_w^2}{2\,\sigma_w^2}\right)\, \sigma_w\, \mathrm{d}s$$

$$= \frac{\sigma_w^2}{2} \int_{s \geq \mathsf{z}_{(1-a_u)}} \frac{1}{\sqrt{2\,\pi}} \exp\left(\frac{-\,s^2}{2}\right)\, \mathrm{d}s$$

$$\left\{ \begin{array}{llll} \text{per partes} & & & \\ a & = s & a' & = 1 \\ b & = -\exp\left(\frac{-s^2}{2}\right) & b' & = s\exp\left(\frac{-s^2}{2}\right) \end{array} \right\} \tag{B.3}$$

$$= \frac{\sigma_w^2}{2} \left(\left[-\frac{1}{\sqrt{2\,\pi}}\, s \exp\left(\frac{-s^2}{2}\right) \right]_{\mathsf{z}_{(1-a_u)}}^{+\infty} - \frac{1}{\sqrt{2\,\pi}} \int_{s \geq \mathsf{z}_{(1-a_u)}} -\exp\left(\frac{-s^2}{2}\right)\, \mathrm{d}s \right)$$

$$= \frac{\sigma_w^2}{2} \left(\frac{\mathsf{z}_{(1-a_u)}}{\sqrt{2\,\pi}} \exp\left(\frac{-\left(\mathsf{z}_{(1-a_u)}\right)^2}{2}\right) + \left(1 - \underbrace{\phi_{\mathcal{N}}(\mathsf{z}_{(1-a_u)})}_{=1-a_u \text{ by definition}}\right) \right)$$

$$= \frac{\sigma_w^2}{2} \left(\frac{\mathsf{z}_{(1-a_u)}}{\sqrt{2\,\pi}} \exp\left(\frac{-\left(\mathsf{z}_{1(1-a_u)}\right)^2}{2}\right) + a_u \right)$$

where $\phi_{\mathcal{N}}(x)$ is the cumulative distribution function of the standard normal distribution.

B.2 Form Drag

The paramaterization of the surface drag over the mix of sea-ice and water in 6.2.6 is provided in the form of the formula for the surface exchange coefficient. Since LEM requires an input in the form of aerodynamic surface roughness z_0, we derive the formula 6.11 for the apparent aerodynamic surface roughness. This part of the appendix provides the justification of this formula.

The neutral drag coefficient over a mixture of sea-ice and water is usually formulated

as

$$C_{\mathrm{dn}} = (1 - c_{\mathrm{ic}})\, C_{\mathrm{d,w}} + c_{\mathrm{ic}}\, C_{\mathrm{d,ic}} + C_{\mathrm{d,f}}, \tag{B.4}$$

where $C_{\mathrm{d,w}}$ is the drag coefficient over open open water, $C_{\mathrm{d,ic}}$ is the drag coefficient over packed sea-ice and $C_{\mathrm{d,f}}$, is the form drag (Lüpkes and Birnbaum, 2005). Since the distribution of ice floes sizes in the MIZ in the area of interest is not known fully, we apply the parametrization formula:

$$C_{\mathrm{d,f}} = \frac{c_e}{2\,\kappa} \left(\frac{\ln\!\left(h_f / z_{0,\mathrm{w}}\right)}{\ln\!\left(z_1 / z_{0,\mathrm{w}}\right)} \right)^2 (1 - c_{\mathrm{ic}})^{\beta}_{f}\, c_{\mathrm{ic}}, \tag{B.5}$$

where κ is von Kármán constant, z_1 is the height at which the drag coefficient is calculated, $z_{0,\mathrm{w}}$ is the aerodynamic surface roughness over water, h_f is the parameter representing the vertical extent of ice floes, here set to 0.41 m, $c_e = 0.3$ is the parameter representing the drag exchange, and β_f is the parameter representing the floe size distribution, here set to 1 (Lüpkes et al., 2012). We reclaim that in the neutral stratification, the relation between the drag coefficient and the surface roughness yields (Stull, 1988):

$$C_{\mathrm{dn}} = \kappa^2 \left(\ln\!\left(z_1 / z_0\right)\right)^{-2}, \tag{B.6}$$

and insert this on the left hand side of the equation (B.4). We denote $\widetilde{z_0}$ the apparent value of the aerodynamic surface roughness. Combining it with (B.5), we derive

$$\begin{aligned}
\frac{\kappa}{\left(\ln\left(\frac{z_1}{\widetilde{z_0}}\right)\right)^2} &= \frac{(1-c_{\mathrm{ic}})\,\kappa}{\left(\ln\left(\frac{z_1}{z_{0,\mathrm{w}}}\right)\right)^2} + \frac{c_{\mathrm{ic}}\,\kappa}{\left(\ln\left(\frac{z_1}{z_{0,\mathrm{ic}}}\right)\right)^2} + \frac{c_e}{2\,\kappa} \left(\frac{\ln\!\left(\frac{h_f}{z_{0,\mathrm{w}}}\right)}{\ln\!\left(\frac{z_1}{z_{0,\mathrm{w}}}\right)} \right)^2 (1-c_{\mathrm{ic}})^{\beta_f}\, c_{\mathrm{ic}} \\
\left(\ln\left(\frac{z_1}{z_{0,\mathrm{w}}}\right) \ln\left(\frac{z_1}{z_{0,\mathrm{ic}}}\right)\right)^2 &= \left(\ln\left(\frac{z_1}{\widetilde{z_0}}\right)\right)^2 \Bigg((1-c_{\mathrm{ic}}) \left(\ln\left(\frac{z_1}{z_{0,ic}}\right)\right)^2 + c_{\mathrm{ic}} \left(\ln\left(\frac{z_1}{z_{0,\mathrm{w}}}\right)\right)^2 + \\
&\qquad \frac{c_e}{2\,\kappa^2} \left(\ln\!\left(\frac{h_f}{z_{0,\mathrm{w}}}\right) \ln\!\left(\frac{z_1}{z_{0,\mathrm{ic}}}\right)\right)^2 (1-c_{\mathrm{ic}})^{\beta_f}\, c_{\mathrm{ic}} \Bigg) \\
\left(\ln\left(\frac{z_1}{\widetilde{z_0}}\right)\right)^2 &= \frac{\left(\ln\!\left(\frac{z_1}{z_{0,\mathrm{ic}}}\right) \ln\!\left(\frac{z_1}{z_{0,\mathrm{w}}}\right)\right)^2}{(1-c_{\mathrm{ic}}) \left(\ln\!\left(\frac{z_1}{z_{0,\mathrm{w}}}\right)\right)^2 + c_{\mathrm{ic}} \left(\ln\!\left(\frac{z_1}{z_{0,\mathrm{ic}}}\right)\right)^2 + \frac{c_{\mathrm{ic}}\, c_e\, (1-c_{\mathrm{ic}})^{\beta_f}}{2\,\kappa} \left(\ln\!\left(\frac{h_f}{z_{0,\mathrm{w}}}\right) \ln\!\left(\frac{z_1}{z_{0,\mathrm{w}}}\right)\right)^2}
\end{aligned} \tag{B.7}$$

Since both sides of the equation are positive, we can apply the operation of square root. We expect that $z_1 >> z_{0,\mathrm{w}}$ and $z_1 >> z_{0,\mathrm{ic}}$, and therefore we keep only the positive root.

Finally we remove the logarithm from left hand side and obtain:

$$\widetilde{z_0} = z_1 \exp\left(\frac{-\ln\left(\frac{z_1}{z_{0,\mathrm{ic}}}\right)\ln\left(\frac{z_1}{z_{0,\mathrm{w}}}\right)}{\sqrt{(1-c_{\mathrm{ic}})\left(\ln\left(\frac{z_1}{z_{0,\mathrm{w}}}\right)\right)^2 + c_{\mathrm{ic}}\left(\ln\left(\frac{z_1}{z_{0,\mathrm{ic}}}\right)\right)^2 + \frac{c_{\mathrm{ic}}\,c_e\,(1-c_{\mathrm{ic}})^{\beta_f}}{2\,\kappa}\left(\ln\left(\frac{h_f}{z_{0,\mathrm{w}}}\right)\ln\left(\frac{z_1}{z_{0,\mathrm{w}}}\right)\right)^2}}\right) \tag{B.8}$$

which was to prove.

Appendix C

Further Results of Sensitivity Testing

An essential part of a model study is an extensive testing of the model sensitivity. While the main results of the sensitivity study were presented in 3.5 it was not possible to show all the relevant results. The impact of increasing the initial humidity was originally part of Sensitivity testing (Chapter 3). However, due to the increasing size of the chapter, it was moved to the appendix to C.1. The model runs with very fine resolution allowed to asses the performance of the subgrid scheme in the early steps of model runs. Further insight into the early development of the convective boundary layer is provided in the part

C.1 Diminishing Impact of Humidity

Since the humidity profile in the lower troposphere in Arctic plays a significant role in the development of the stratified boundary layer, its impact on model results is questioned as well. While the relative humidity in the lower troposphere in the control run is 60 % (see figure 3.1c), scenarios with initial profile of relative humidity increased to 80 % and 85 % were set up (see figure C.1).

A higher relative humidity in the initial conditions leads not only to an earlier development of the cloud layer, but also to slightly warmer CBL. The higher humidity and slightly higher potential temperature decreased the temperature gradient in the surface layer. Furthermore, the higher humidity of ambient air in the lower troposphere ushers smaller differences in the virtual potential temperature between the free

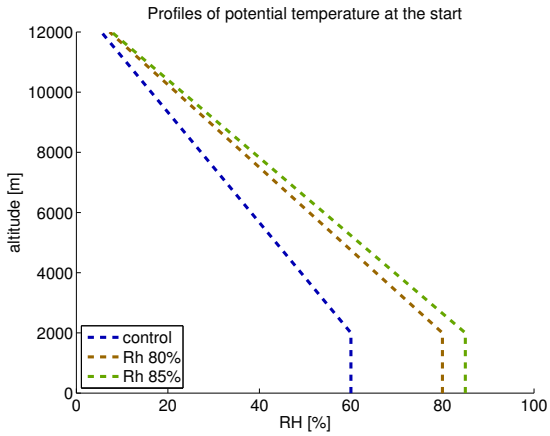

Figure C.1: The setting of initial profiles of relative humidity

atmosphere and the top of CBL, and thus
lowers differences in the buoyancy. This negative feedback slows down the development of the CBL. By the third hour hour, the vertical fluxes of heat and moisture in both runs with higher humidity are exceeded by the fluxes in the control case, as shown in the figure C.3b.

Although clouds in runs with increased humidity start forming earlier and at lower altitude, the cloud tops spans to the same height as in the control case (see again C.2). With the increase in the potential temperature of the ML, the cloud bases start rising and reach the same altitude as in the control case by the time 4 hour. During the second hour, runs with increased humidity also exhibit higher variance in specific humidity in the ML. On the other hand, the control run exhibit much higher variance in specific humidity in the cloud layer (see figure C.3a). This phenomena is caused by smaller differences in humidity between the air developing CBL and the ambient air entrained from above. The differences in the variance of specific humidity also disappear by 4 hour.

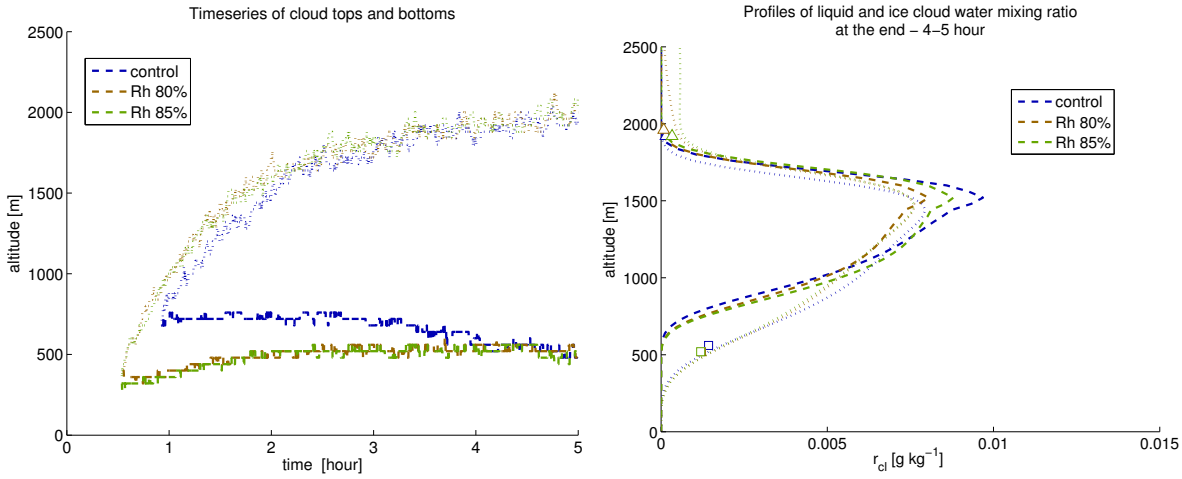

(a) (b)

Figure C.2: The sensitivity in the formation of clouds to the initial humidity.
The dashed line (−−) marks liquid cloud water, the dotted line (· · ·) ice cloud water. The symbol □ marks the altitude of cloud base, the symbol △ the altitude of cloud tops.

Due to the aforementioned negative feedback in forcing, the amount of cloud water increases at a slower rate then in the control run. During the 2–4 hour, the amount of cloud liquid water in the control run exceeds amounts in both run 'Rh 80 %' and run 'Rh 85 %'. Finally during the 4–5 hour, vertical profiles of liquid water mixing ratio do not differ by more than 10 %. Furthermore, timeseries of vertical fluxes of the momentum and the latent heat at all altitudes within CBL exhibit faster growth followed by a stagnation. During the 4–5 hour, values of fluxes are in the same interval as in the control case.
The analysis of flux residua reveals that values of autocorrelation for timeseries in runs

with higher humidity are higher than in the control case, however the difference is smaller than the spread in autocorrelation values between the cases with the different type of the surface heterogeneity.

In summary, the increase in the initial humidity does not lead to any qualitative changes in the developing CBL. findings of the sensitivity testing for humidity are in a good agreement with the previous research on mesoscale structures in CAO (Yamamoto, 2012) that stressed out the dominating influence of the SST on resulting specific humidity of air.

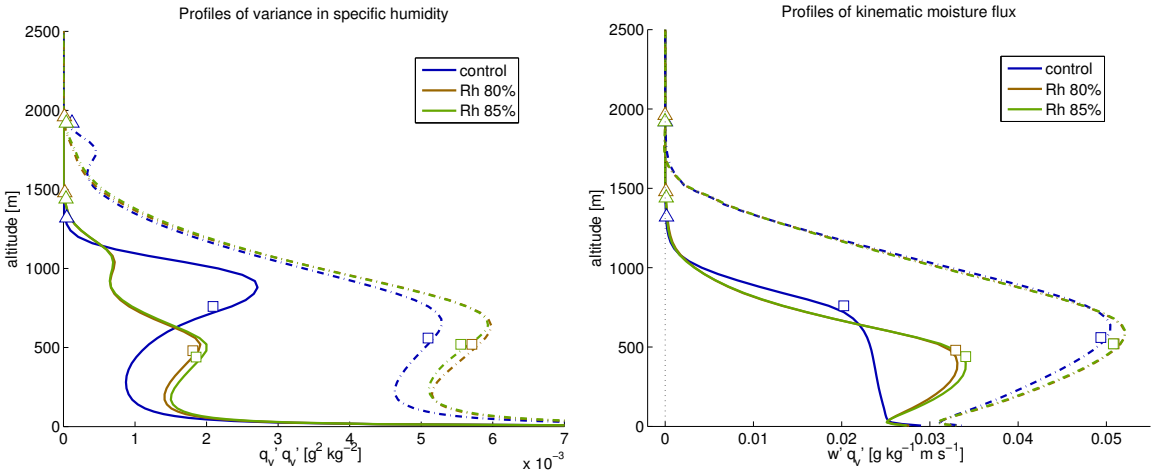

(a) (b)

Figure C.3: The negative feedback of initial humidity – variance in specific humidity and kinemtic moisture flux at different times. Full lines (–) show averaged profiles for 1.5–1.75 hour and dash-dotted lines (– · –·) show averaged profiles for 4–5 hours. The symbol □ marks the altitude of cloud base, the symbol △ the altitude of cloud tops.

C.2 Very fine resolution

The sensitivity testing of the runs with a very fine resolution was expained in 3.5.3. However it was not possible to show all the interesting results. In this part of the appendix, we would like to demonstrate the differences in the modelled structure of bottom part of the boundary layer between the control run and the run with extra fine resolution. Early convective plumes in the control run are not properly resolved. Most of the transport in the control run is parametrized. The run with extra fine resolution than clearly show the shape of convective plumes in the early convective boundary layer (see figure C.4).

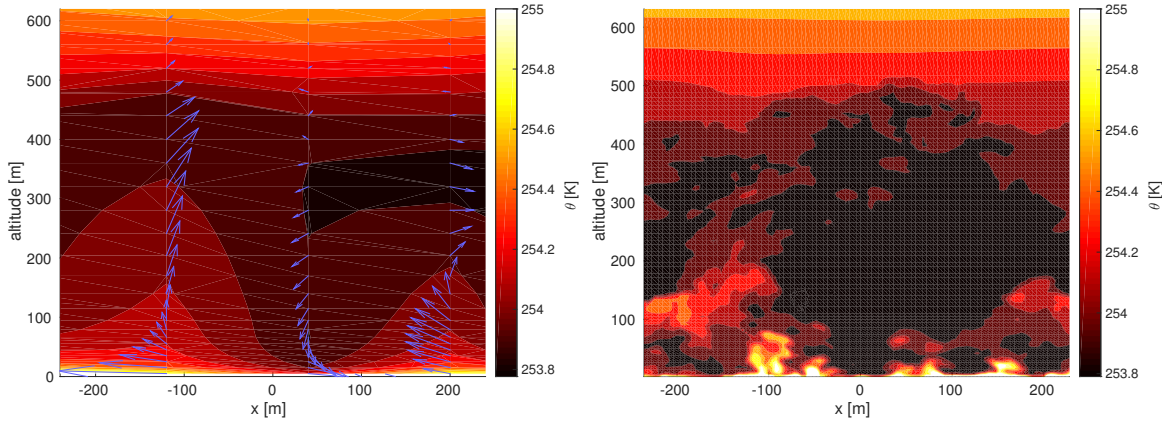

(a) control (b) extrafine resolution

Figure C.4: The comparison of control run and the run with extra fine resolution at the time 900 s after t_0. Vertical cross-section of the vertical structure shows the developing convective boundary layer. The run with the extra-fine resolution clearly shows the forming convective plumes
Arrows in the control run mark the direction of the wind.

Appendix D

Appendix C – Gravity Waves

The Analysis of gravity waves was originally part of chapter 3, 4 and 5. However, the results of the analysis did not show results that would be interesting enough. This part of the Appendix therefore presents the methods for the analysis of gravity waves and th

D.1 Introduction for Gravity Waves

As thermals of the developing CBL penetrates into stratified free atmosphere above, *gravity waves* are generated (Melfi and Palm, 2012). The gravity waves facilitate the transport of the momentum (Nappo, 2013) through the stratified layers above the boundary layer (Kerman, 1974). As they propagate higher into troposphere, they might reach resonance (Fritts and Alexander, 2003) at some altitudes. While the gravity waves travel within the stratified layer, they can alter the shear production in the troposphere (Finnigan and Einaudi, 1981), modify surface stress over water (Winstead et al., 2002), induce residual circulation and modulate the feedback of planetary waves (Fritts et al., 2005). Therefore, there is solid reason to analyse the gravity waves generated by a developing CBL in our idealised scenarios. In this part of the appendix, we are going to provide the methodology for the evaluation of the waves in the upper troposphere.

D.2 Methods for Gravity Waves

While areas of the free atmosphere with a high variance in vertical velocity might be an indication of gravity waves, wind fields in LEM outputs are further processed. If there is a repetitive wave pattern in a wind fields, it will show a response in the spectral decomposition of model wind fields. Still, a response in the upper atmosphere might be also caused by shear generated turbulence. In theory, air velocity in the in the upper atmosphere can be clearly decomposed into the part of advection, waves and turbulence (Einaudi and Finnigan, 1981). However, in the evaluation of model and observational data, the decomposition into the wave and the turbulent part pose quite a big issue. One

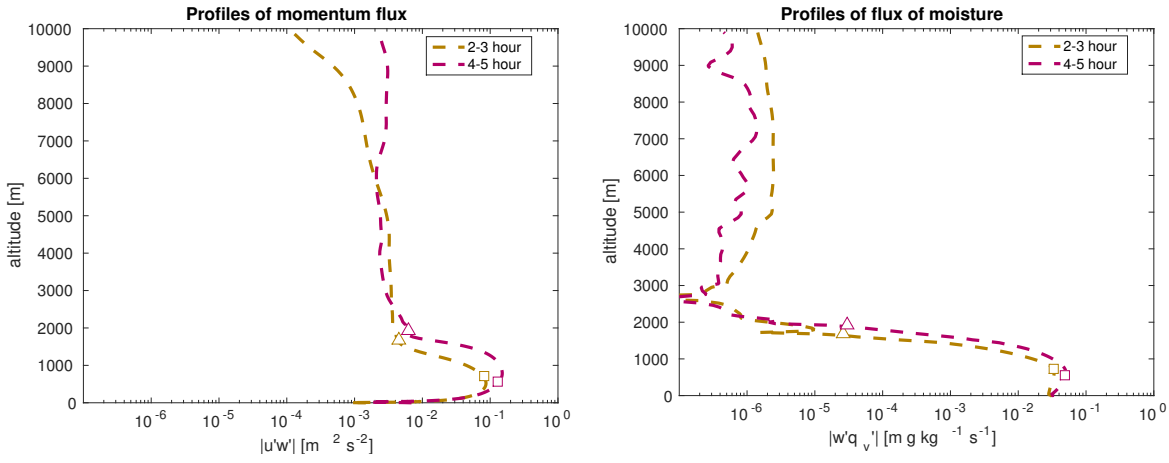

(a) (b)

Figure D.1: The comparison of mean profiles for the vertical flux of momentum and the vertical flux of moisture. Values of fluxes are taken in absolute values and plotted on logarithmic axis to better display the difference.

possibility is comparing the vertical momentum transport against the vertical transport of moisture and passive tracers, or rather lack of it. Since the waves transport the momentum but not scalar quantities, there should be a large difference in the vertical transport terms (Stewart, 1969). Nevertheless, there is no clear-cut difference between the waves and turbulence. Furthermore, a turbulence can be also generated by the breaking of gravity waves (Kerman, 1974) (Tjernström and Maueitsen, 2008). Despite all the progress in the analysis of gravity aves in recent decades (Galperin et al, 2010), there is no clear way how to separate the turbulent and wave part when they coexist (Jacobitz et al., 2005).

In this study, we will use the aforementioned suggestion of Stewart (1969) and compare the profiles of the vertical transport for moisture and momentum (see figure D.1). The part of the troposphere above clouds exhibit a sharp drop in the vertical fluxes of moisture while the momentum flux $\overline{u'w'}$ decreases just slightly. The momentum flux in the upper part of the atmosphere is 15 times lower than its maximum, but still reaches values similar close to the surface. While the values of the vertical fluxes of moisture are by 4 to 5 orders of magnitude lower than in the CBL, it could be considered an indicator of the likely present of the waves in the upper atmosphere. However, a further evaluation of spectral properties is preferable.

With an aim to analyse the spectral properties of the troposphere, horizontal slices are extracted from the model fields (see example from altitude 6496 m in figure D.2a) and their 2D power spectra are calculated by employing the Fast Fourier Transform in 2 Dimensions (Press et al., 2007, pp.631-636). Peaks in 2D spectra identify the wavelengths of dominant frequencies. To further process the prevailing wavelengths the 2 spectra

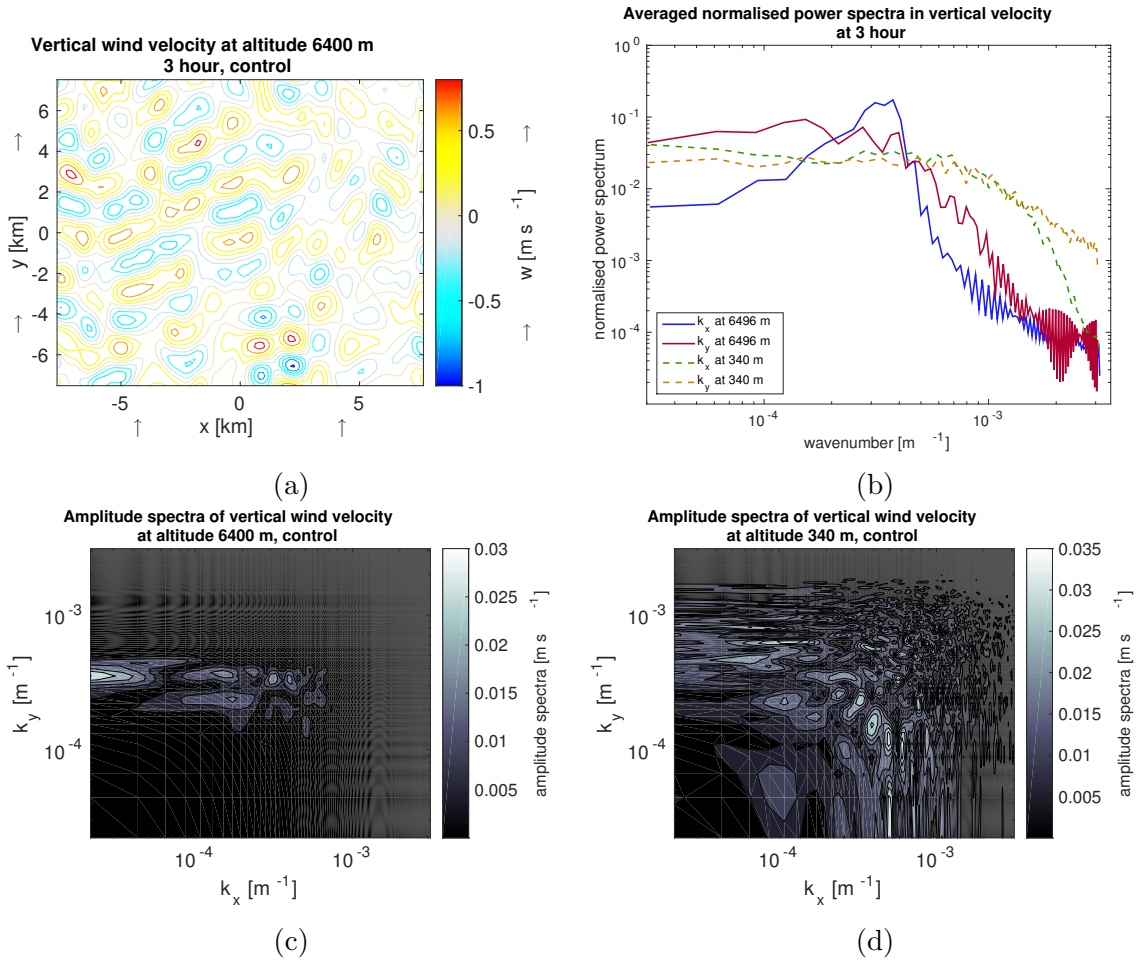

Figure D.2: Illustration of steps in the evaluation of gravity waves. Wind velocity are extracted from the chosen level in the upper troposphere **(a)** and 2D amplitude spectra are calculated **(c)**. The spectra in the middle of the ML stands in contrast **(d)**. Spectra at both altitudes are separately integrated over k_x and k_y to produce 1D spectra **(b)**.

are separately integrated along the x-axis and the y-axis. That allows us to look separately on the dominant wavenumbers in the direction along the mean wind and across it.

This approach is demonstrated on the comparison of spectra ow vertical wind velocity in the upper troposphere and in the CBL. For the upper atmosphere, we select an aforementioned slice from the altitude 6400 m. For the CBL, we select a slice approximately in the middle of ML. In our example, we can see a clear difference between the 2D spectra of these two slices (compare figures D.2c and D.2d). The evaluation of 1D spectra in x and y direction a clear difference (see figure D.2b). The spectra in the ML exhibit a steady line until approximately $5 \cdot 10^{-4}$, followed by a gradual decline for higher wavenumbers. This stands in a good agreement with previous studies (Roode et al., 2004). The spectra of vertical wind velocity in the upper atmosphere differ. Firstly, the decline in spectra is significantly sharper. Secondly, there is a clear differences between the spectral decomposition in the direction x and y. The spectra show a clear peak for a value of k_y between $2 \cdot 10^4$ and $4 \cdot 10^4$. This is consistent with the previous

observations and model studies of gravity waves (Gossard and Munk, 1954) (Yoshiki and Sato, 2000).

This peak in spectra will be discussed later (in Chapter 4). The choice of altitudes of horizontal slices used further in this study is constrained by two conditions. They should be high above the CBL to avoid a direct influence of convective overshoots but also well below the start of the damping layer (Kershaw, 1995). In our basic setting, the altitude 3150 m represents the mid-troposphere and the altitude 6400 m represents the upper troposphere.

D.3 Results

D.3.1 Gravity waves in Control Run

A growing CBL is not fully isolated from the rest of the troposphere. The turbulence in the boundary layer generates waves in the stratified layers above (Stull, 1988, 477). These waves then propagate further upwards and travel also horizontally (Lane and Moncrieff, 2010). The study of gravity waves is motivated by their effects, including the influence on surface stress (Winstead et al., 2002) and inducing residual circulation (Fritts et al., 2005). Case studies usually focus on situation over semi-stationary CBL, however the impact of a growing CBL should be questioned as well. This section investigates gravity waves generated by the developing CBL in the control set. The analysis of spectra follows the methods described in 2.5.5.

A high turbulent kinetic energy in the free atmosphere above the ABL (see again the figure 4.8b) indicates a likely presence of gravity waves. Two-dimensional spectral decomposition of the vertical velocity at chosen altitudes then shows a number of peaks in wavenumbers (see figure D.3).

Multiple peaks in the x-component between $0.1 \cdot 10^{-4}$ and $1.7 \cdot^1 0{-}4$ might indicate a complicated character of waves. Similarly, 2D spectra of potential temperature perturbations show high values for wavenumbers x-direction between $1.1 \cdot 10^{-4}$ and $1.5 \cdot 10^{-4}$ and wavenumbers in y-direction between $0.1 \cdot 10^{-4}$ and $1.7 \cdot 10^{-4}$.

While averaging the spectra in the y-component leads to approximately constant 1D spectra for lower wavenumbers in x-component with a decline for wavenumebers larger than $2 \cdot 10^{-4}$, averaging in the x-component reveals a single clear peak for the wavenumber k_y. During the third hour, peaks in spectra of vertical velocities at altitude 3200 m and 6400 m are achieved for $k_y = 3.8 \cdot 10^{-4}\,\mathrm{m}^{-1}$ and $k_y = 3.1 \cdot 10^{-4}\,\mathrm{m}^{-1}$ respectively. This indicates that gravity waves in the direction of the mean wind flow are of wavelengths

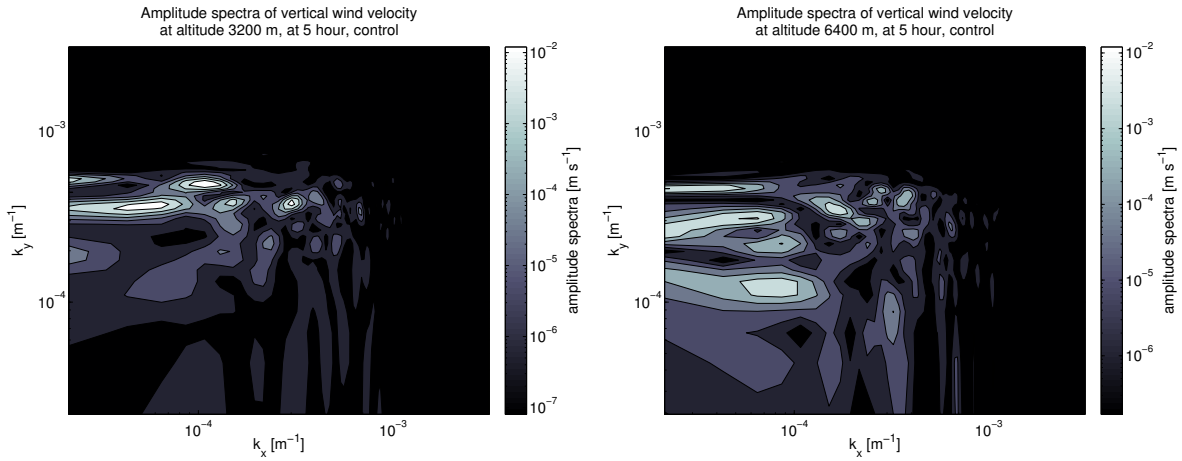

(a) (b)

Figure D.3: 2D amplitude spectra of the vertical velocity variance in the upper atmosphere at 5 hour

between 2.7 km and 3.2 km.

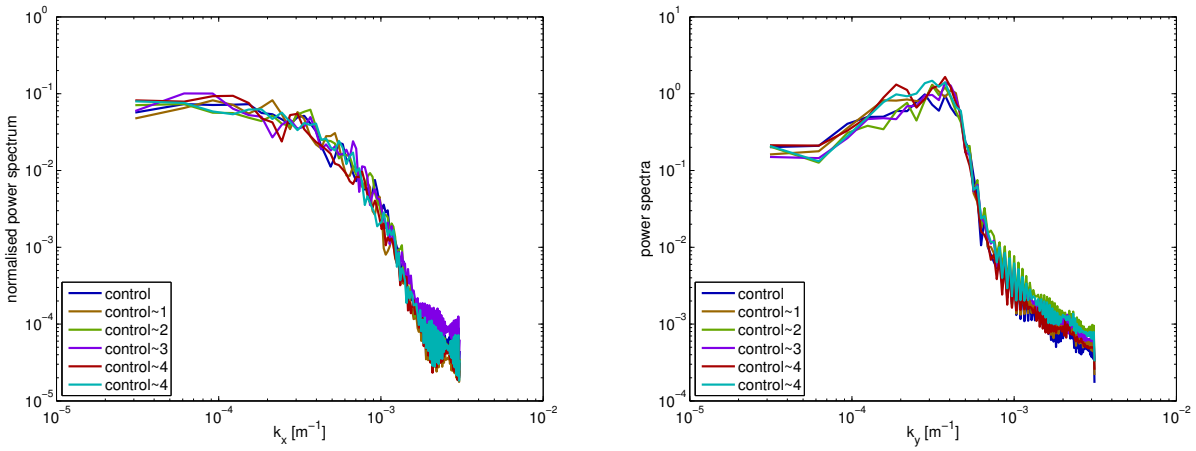

(a) (b)

Figure D.4: The spectra of the vertical wind velocity in the upper atmosphere at 5 hour for runs from the control set.

The comparison of the model runs (an example in figure D.5) does not show any significant differences in the resulting normalised power spectra estimations, implying that the temporary and spatial variations inside the CBL do not affect the resulting characteristic of the free atmosphere. The peak in each power spectra is surrounded by a drop in powers for lower wavenumbers as well as for higher ones. Furthermore, initially sharp decline for wavenumbers higher than $3.97 \cdot 10^{-4}\mathrm{m}^{-1}$ changes into a less steep decline for wavenumbers above $8.1 \cdot 10^{-4}\mathrm{m}^{-1}$. This further reinforces the hypothesis of well-defined gravity waves and smaller disturbances followed by an inertia cascade.

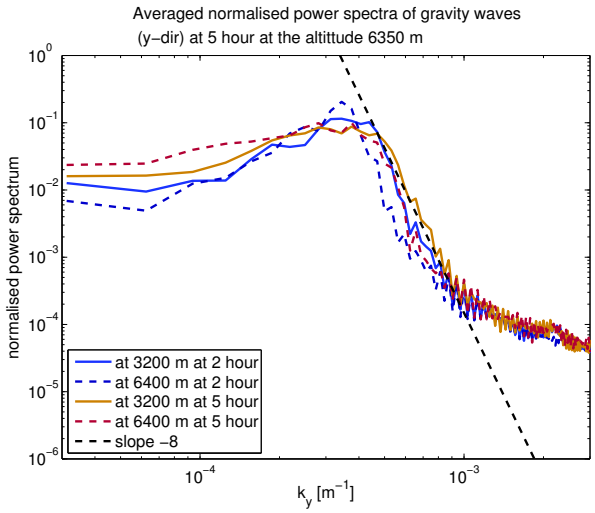

Figure D.5: The comparison of averaged k_y spectra in the upper troposphere for different times and runs

In summary, the analysis of stratified layer above the CBL has shown developing waves patterns in the upper troposphere. The patterns are dominated by waves aligned in the direction of the mean wind flow with the wavelengths between 2.7 and 3.2 km, indicating well defined gravity waves.

D.3.2 In Scenarios with Weak Wind Shear

An increased amount of kinetic energy is being transported into upper atmosphere in the scenarios with strong wind forcing. Repetitive pattern in vertical velocity is indicated already at 2 hour after the transition. Further analysis then reveals that while there are again relatively negligible differences in normalised power spectra for k_x, normalised power spectra for k_y clearly demonstrate the impact of increased wind shear. Peaks of spectra are shifted toward lower wavenumbers, $2 \cdot 10^{-4}$ for 'wind2' and $1.1 - -1.5 \cdot 10^{-4}$ for 'wind3'. The slope to lower higher wavenumbers is slightly less steep than in the control case, -6 against -7.

D.3.3 Scenarios with Stronger Stratification

The flux of momentum from the ML into upper atmosphere is in all 'strat#' scenarios weaker than in the control scenario, however that does not necessary imply the absence of gravity waves. Calculated 2D spectra of vertical velocity and potential temperature at altitudes clearly show multiple peaks for wavenumbers k_y between 10^{-4} and $3 \cdot 10^{-4}$. While normalised marginal spectra for wavenumber k_x return similar results as for control, there are differences in the marginal spectra for k_y. Peaks in the power spectra in strat-scenarios are at slightly lower wavenumbers than in the control scenario, The slope to lower wavenumbers is less steep than in the control scenario, indicating less distinct gravity waves compared with the background noise.